

12-2022

Deciphering Surfaces of Trans-Neptunian and Kuiper Belt Objects using Radiative Scattering Models, Machine Learning, and Laboratory Experiments

Al Emran
University of Arkansas, Fayetteville

Follow this and additional works at: <https://scholarworks.uark.edu/etd>



Part of the [Stars, Interstellar Medium and the Galaxy Commons](#), and the [The Sun and the Solar System Commons](#)

Citation

Emran, A. (2022). Deciphering Surfaces of Trans-Neptunian and Kuiper Belt Objects using Radiative Scattering Models, Machine Learning, and Laboratory Experiments. *Graduate Theses and Dissertations* Retrieved from <https://scholarworks.uark.edu/etd/4767>

This Dissertation is brought to you for free and open access by ScholarWorks@UARK. It has been accepted for inclusion in Graduate Theses and Dissertations by an authorized administrator of ScholarWorks@UARK. For more information, please contact scholar@uark.edu.

Deciphering Surfaces of Trans-Neptunian and Kuiper Belt Objects using Radiative
Scattering Models, Machine Learning, and Laboratory Experiments

A dissertation submitted in partial fulfillment
of the requirements for the degree of
Doctor of Philosophy in Space and Planetary Sciences

by

Al Emran
University of Dhaka
Bachelor of Science in Geography & Environment, 2012
University of Dhaka
Master of Science in Physical Geography & Environment, 2014
Auburn University
Master of Science in Geography, 2019

December 2022
University of Arkansas

This dissertation is approved for recommendation to the Graduate Council.

Vincent Chevrier, Ph.D.
Dissertation Director

Larry Roe, Ph.D.
Committee Member

William (Lin) Oliver III, Ph.D.
Committee Member

Jingyi Chen, Ph.D.
Committee Member

Abstract

Decoding surface-atmospheric interactions and volatile transport mechanisms on trans-Neptunian objects (TNOs) and Kuiper Belt objects (KBOs) involves an in-depth understanding of physical and thermal properties and spatial distribution of surface constituents – nitrogen (N_2), methane (CH_4), carbon monoxide (CO), and water (H_2O) ices. This thesis implements a combination of radiative scattering models, machine learning techniques, and laboratory experiments to investigate the uncertainties in grain size estimation of ices, the spatial distribution of surface compositions on Pluto, and the thermal properties of volatiles found on TNOs and KBOs. Radiative scattering models (Mie theory and Hapke approximations) were used to compare single scattering albedos of N_2 , CH_4 , and H_2O ices from their optical constants at near-infrared wavelengths (1 – 5 μm). Based on the results of *Chapters 2 and 3*, this thesis recommends using the Mie model for unknown spectra of outer solar system bodies in estimating grain sizes of surface ices. When using an approximation for radiative transfer models (RTMs), we recommend using the Hapke slab approximation model over the internal scattering model. In *Chapter 4*, this thesis utilizes near-infrared (NIR) spectral observations of the LEISA/Ralph instrument onboard NASA’s New Horizons spacecraft. Hyperspectral LEISA data were used to map the geographic distribution of ices on Pluto’s surface by implementing the principal component reduced Gaussian mixture model (PC-GMM), an unsupervised machine learning technique. The distribution of ices reveals a latitudinal pattern with distinct surface compositions of volatiles. The PC-GMM method was able to recognize local-scale variations in surface compositions of geological features. The mapped distribution of surface units and their compositions are consistent with existing literature and help in an improved understanding of the volatile transport mechanism on the dwarf planet. In *Chapter 5*, we propose a method to estimate thermal conductivity, volumetric heat capacity,

thermal diffusivity, and thermal inertia of N₂, CH₄, and CO ices, and mixtures thereof in a simulated laboratory setting at temperatures of 20 to 60 K – relevant to TNOs and KBOs. A new laboratory experimental facility – named the *Outer Solar System Astrophysics Lab (OSSAL)* – was built to implement the proposed method. This thesis provides detailed technical specifications of that laboratory with an emphasis on facilitating the design of similar cryogenic facilities in the future. Thus, this research was able to incorporate a set of methods, tools, and techniques for an improved understanding of ices found in the Kuiper Belt and to decipher surface-atmospheric interactions and volatile transport mechanisms on planetary bodies in the outer solar system.

©2022 by Al Emran
All Rights Reserved

Acknowledgments

In around 3.5 years, it took me 3 continents to finish this thesis while there is a saying that “it takes a village to get a PhD”. None of this work would have been accomplished without the guidance, patience, and assistance of my advisor Vincent F. Chevrier. He has been a great mentor with his invaluable guidance during my time here and his kind help with information and ideas that have provided me with organizational support in completing this thesis. I would also be thankful to other committee members – Larry Roe, William (Lin) Oliver III, and Jingyi Chen. Special gratitude also goes to my family members: parents [Nurul Islam and Mahmuda Khatun] and siblings [Asma Akter Sheuly, Mahbubul Alam, and Al Quium].

Next, I would like to thank the team members of NASA’s New Horizons spacecraft mission for targeting, collecting, and archiving LORRI, MVIC, and LEISA datasets used in this study. I am also grateful to Kevin Lyon, Stephen Tegler, Will Grundy, Walter Graupner Jr., Gregory Talley, Caitlin Ahrens, Matt Siegler, Jill McDonald, Pradeep Kumar, Hugh Churchill, and Hasan Doha for their support during the design and building of the cryogenic chamber and for formulating the method for measurement of thermal properties of ices.

I am grateful to all faculty, fellow graduate students, and staff in Space and Planetary Sciences at the University of Arkansas and to other people who helped me directly and indirectly to complete this thesis. Lastly, I would like to express my gratitude to all the reviewers for their invaluable insight and commentary on my papers.

Dedication

This dissertation is dedicated to my family. This work is also in honor of my motherland –
Bangladesh.

Table of Contents

Chapter 1: Introduction

1.1. Introduction	1
1.2. Surfaces of TNOs and KBOs	2
1.3. Atmospheres of TNOs and KBOs	3
1.4. Surface-atmospheric interaction and volatile transport	6
1.5. Rationale of this research	8
1.6. Organizations of chapters	11
1.7. Conclusion	12
1.8. References	13

Chapter 2: Uncertainty in Grain Size Estimations of volatiles on Trans-Neptunia Objects and Kuiper Belt Objects

Abstract	18
2.1. Introduction	19
2.2. Methods	21
2.2.1. Single scattering albedo	21
2.2.2. Optical constant	22
2.2.3. Mie calculation	23
2.2.4. Hapke slab and ISM calculations	23
2.3. Results	25
2.3.1. Calculated single scattering albedo	25
2.3.2. Discrepancies in grain size estimation	27
2.3.3. Effect of absorption coefficients	31
2.3.4. The interplay between albedo, absorption coefficient, and grain size	33

2.4. Discussion and conclusions	36
2.5. Appendix	39
2.6. Acknowledgements	39
2.7. References	40

Chapter 3: Discrepancy in Grain Size Estimation of H₂O Ice in the Outer Solar System

Abstract	44
3.1. Introduction	45
3.2. Methods	48
3.2.1. Optical constant	48
3.2.2. Single scattering albedo	49
3.2.3. Mie calculation	50
3.2.4. Hapke approximation models	51
3.3. Results	52
3.3.1. Calculated single scattering albedo	52
3.3.2. Relative grain size estimation	56
3.3.3. Characteristic absorption coefficients	65
3.4. Discussion	67
3.5. Conclusion	75
3.6. Acknowledgements	76
3.7. Software	76
3.8. Appendix	77
3.9. References	79

Chapter 4: Pluto's Surface Mapping using Unsupervised Learning from Near-Infrared Observations of LEISA/Ralph

Abstract	85
4.1. Introduction	86
4.2. Observations	91
4.3. Methodology	93
4.3.1. Principal component reduced Gaussian mixture model	94
4.4. Results	101
4.5. Discussion	123
4.6. Conclusion	129
4.7. Acknowledgements	131
4.8. Appendix	132
4.9. References	140

Chapter 5: The Outer Solar System Astrophysics Lab: A New Experimental Facility for Spectral and Thermal Investigations of Ices at Cryogenic Temperatures

Abstract	148
5.1. Introduction	149
5.2. Methods	156
5.2.1. Theory	157
5.2.2. Samples	158
5.3. Outer Solar System Astrophysics Lab	159
5.4. Experimental procedure	164
5.5. Uncertainty and mitigation of risk	166
5.6. Conclusion	168

5.7. Acknowledgements	169
5.8. Appendix	170
5.9. References	171
Chapter 6: Conclusion	
6.1. Summary and contributions	177
6.2. References	182

List of Figures

Chapter 1:

Fig. 1.1: Distribution of N_2 , CH_4 , and CO ices (left to right) on Pluto as derived from the Lisa Hardaway Infrared Mapping Spectrometer (LEISA) instrument a part of the Ralph instrument package (Reuter et al., 2008) onboard the New Horizons (Schmitt et al., 2017). The warmer colors indicate a higher concentration of volatiles. The N_2 distribution map was based on the integrated band depth of the $2.15 \mu m$ N_2 band, the CH_4 map was based on the state of CH_4 as determined by the CH_4 bands position index, and the CO map was based on the integrated band depth of the weak CO band at $1.58 \mu m$2

Fig. 1.2: Haze layer at the atmosphere of Pluto as seen by New Horizons spacecraft flyby in 2015. Image credit: NASA/Johns Hopkins University Applied Physics Laboratory/Southwest Research Institute (SwRI).4

Chapter 2:

Fig. 2.1: Plots for single scattering albedo of pure CH_4 at 39K (a), α - N_2 : CH_4 at 35K (b), and β - N_2 : CH_4 at 38K (c) for a grain $10 \mu m$ radius. The dashed solid line presents δ -Eddington corrected Mie, dashed yellow represents ISM, and the dotted green represents Hapke Slab results. The plots were smoothed using the *Savitzky-Golay* filter (Savitzky and Golay, 1964).27

Fig. 2.2: Grain sizes determined from the Hapke Slab (left column) and ISM (right column) using spectra calculated using the Mie model at different particle radii of 1, 10, 100, 1000 μm for pure CH_4 ice at 39K (top row), α - N_2 : CH_4 at 35K (middle row), and β - N_2 : CH_4 at 38K (bottom row). The resulting grain sizes are normalized to the input grain sizes. The plots were smoothed using the *Savitzky-Golay* filter (Savitzky and Golay, 1964).30

Fig. 2.3: Absorption coefficient of pure CH_4 ice at 39K (a), CH_4 saturated with α - N_2 ice at 35K (b), and CH_4 saturated with β - N_2 ice at 38K (c). Pure CH_4 has an absorption coefficient peak at $3.3 \mu m$. The absorption coefficient is much higher over the wavelength around $3.3 \mu m$ at 38K compared to 35K for CH_4 saturated with N_2 ices.32

Fig. 2.4: Plot of the single scattering albedo against absorption coefficient for pure CH_4 ice particle at 39K (left column), α - N_2 : CH_4 particle at 35K (middle column), and β - N_2 : CH_4 particle at 38K (right column). The subplots show the distribution of w at grain radii at 1 μm (upper row), 10 μm (2^{nd} row), 100 μm (3^{rd} row), and 1000 μm (bottom row). In all subplots, the scattering albedo from the Mie calculation (blue), ISM (yellow), and Hapke Slab (green). The Mie calculation follows two different paths due to the Rayleigh scattering effect at lower grain-size particles.35

Chapter 3:

Fig. 3.1: Calculated single scattering albedo plots for 10 μm radii particles of amorphous (left column) and crystalline (right column) H_2O ice at the NIR wavelengths. The subplots in the rows are the measurements at different temperatures where blue solid lines are δ -Eddington corrected Mie, green dotted lines are Hapke slab, and yellow dashed lines are ISM spectra.54

Fig. 3.2: Predicted relative gain sizes (normalized to the Mie prediction) using the Hapke slab (left column) and ISM (right column) calculated at particle radii of 1, 10, 100, and 1000 μm for amorphous H_2O ice, for temperatures ranging between 15 and 80 K.59

Fig. 3.3: Predicted relative gain sizes (normalized to the Mie prediction) using the Hapke slab (left column) and ISM (right column) calculated at particle radii of 1, 10, 100, and 1000 μm for crystalline H_2O ice, for temperatures ranging between 20 and 80 K.60

Fig. 3.4: Absorption coefficient of amorphous and crystalline H_2O ice at different temperatures over NIR wavelengths. Both phases of H_2O have a broad absorption coefficient peak of around 3.0 μm with a little shift toward shorter wavelengths by the Ia. Another absorption peak is seen at 4.5 μm for Ia while this peak shifts toward shorter wavelengths at 4.4 for Ic with much higher α values. The higher absorption peak for Ic compared to Ia at longer wavelengths is associated with the higher k values at these wavelengths.67

Chapter 4:

Fig. 4.1: Images of two LEISA cubes at a band of 2 μm and mosaics covering the entire Pluto disk, adopted from Schmitt et al. (2017). The image cubes are projected to a common orthographic viewing geometry appropriate to mid-time between scenes. The red line represents the overlapping line where the image cubes were cut and joined together side by side.93

Fig. 4.2: The first nine principal components from LEISA *REFF* data cubes. Up to four pc-axes, the disks show substantial surface information (covers 92.93% total variance of the data). The pc#5 and onward components show noisy data therefore the pc-axes #5 and higher were not considered in the analysis. Note: the assignment of “noisy” data was accomplished subjectively by visually analyzing if pc-axes can represent the underlying geomorphology of Pluto.100

Fig. 4.3: Long Range Reconnaissance Imager (LORRI) higher resolution (panchromatic) basemap projected to LEISA scenes (a). The LORRI base map is labeled with latitude (blue) & longitude (black) grid and formal & informal names of major geomorphic features. The red rectangles represent the reference locations in Fig. 4.9. Eight surface units were found on Pluto using PC-GMM (b). The surface units follow the latitudinal pattern and are consistent with broad geographic regions and geologic features. The north pole at Lowell Regio, Cthulhu Macula, Tombaugh Regio,

Sputnik Planitia and Venera Terra, and Pioneer Terra region show distinct surface units. The values in the legend indicate the assigned surface unit number. Note: the lower right region belongs to strongly shadowed areas and, thus, the pixels at these locations were excluded from the map (see the text for a detailed explanation)..102

Fig. 4.4: The probability plot of each surface unit at LESIA image pixel level using PC-GMM. The subplots are superposed on the LORRI base map. The probability scale ranges from 0 to 1, where higher values indicate a higher probability of the corresponding unit. We also refer the readers to Fig. 4A5 in the Appendix which shows that most of the surface units are dominated by pixels with higher probability values (close to 1).104

Fig. 4.5: The mean (red line) $\pm 1\sigma$ standard deviation (gray shade) I/F spectra of each surface unit on Pluto using PC-GMM. The spectra of the surface units in the subplots are labeled as C followed by the corresponding assigned surface unit number. The standard deviation of the I/F spectra shows varying degrees of closeness to the mean spectra at different wavelengths. All the classes (except the C7) exhibit a clear presence of CH₄ ice absorption bands with varying degrees of strength...107

Fig. 4.6: Post-classification probabilities of subunits for the region enriched with N₂ and CO region (#6; upper row) and the subunits for the H₂O-rich areas (#3; bottom row). The central part of Sputnik Planitia shows a distinct subunit while the southern SP and Venera Terra share common characteristics. H₂O ice at the Kiladze crater shows a difference from that of at Krun Macula. Refer to the histogram plot in Fig. 4A7 in the Appendix which shows that the post-class surface units of C3 and C6 are dominated by pixels with higher probability values.....110

Fig. 4.7: The generalized global compositional map of Pluto superposed on a higher resolution LORRI basemap. The compositions of the surface units are labeled to the corresponding unit. The asterisk (*) superscript appended to a component refers only to that component where * = larger grain/-rich material and ** = pure ice. The latitude and longitude are labeled as the blue and black grid, respectively. The values in the legend indicate the assigned surface unit number.113

Fig. 4.8: The average I/F spectra of the ten composite surface units. The colors of the spectra correspond to the colors of the surface unit in Fig. 4.7. The dashed vertical lines indicate N₂ absorption at 2.15 μm (red), CO absorption at 1.58 μm (green), CH₄:N₂ absorption at 1.69 μm (black), and H₂O absorption at 1.65 and 2.0 μm (blue). Note that the I/F values in the y-axis have offsets for clarity. For a higher resolution colored version of the figure, the readers are referred to the online version of the paper.....117

Fig. 4.9: The subset of the generalized surface map at mountains in the Cthulhu Macula (a), Kiladze crater (b), and Elliot crater (c). For the reference location, please see Fig. 4.1a.124

Fig. 4.10: Global-scale surface compositional distribution and inferred volatile transport directions (indicated by arrows) proposed in this study (a) and schematic view of the major ice distribution

and direction of nitrogen sublimation transport (b) explained by Protopapa et al. (2017). Figure (b) was adopted from Cruikshank et al. (2021) and Protopapa et al. (2017).....126

Fig. 4A1: The cumulative explained variance (left panel) and scree plot (right panel) of the PC axes. At four pc-axes, the plot shows 92.93% total variance of the data. The pc#5 and onward the plot shows a very gentle increase in the cumulative explained variance.....132

Fig. 4A2: Scaled AIC and BIC values at the different number of clusters. Both AIC and BIC show a similar trend as a function of the number of clusters. The plot shows the first local minima BIC (and AIC) value to be 8 and therefore was considered the optimal # of clusters in this study...134

Fig. 4A3: Observed and predicted density plot for different numbers of clusters using the PC-GMM algorithm. The observed data were the first 4 pc-axes used as the input data for GMM while the predicted data were simulated from the resulting GMM model parameter. The density for both observed and predicted data was calculated from multivariate kernel density estimates. The coefficient of the determination (R^2) for linear fit between the observed and predicted density for 8 GC solution is 0.96 – suggesting a good fit of the model.....135

Fig. 4A4: Pluto Nomenclature - the map showing the names of major provinces, geologic units, and features on Pluto. Credit: NASA/Johns Hopkins University Applied Physics Laboratory (JHU-APL)/ Southwest Research Institute (SwRI).....136

Fig. 4A5: The boxplot of the probabilities extracted from the pixels of corresponding classes (gaussian components). The median is shown by the line that divides the box into two parts while the left and right lines of the box represent the lower quartile (25%) and upper quartile (75%), respectively. The plot shows that most of the surface units are dominated by pixels with higher probability values (close to 1) – indicating the dominance of mostly pure pixels at each unit....137

Fig. 4A6: The mean (red line) $\pm 1\sigma$ standard deviation (gray shade) I/F spectra of each subunit for #6 (upper row) and #3 (lower row). The standard deviation of the I/F spectra shows varying degrees of closeness to the mean spectra.....138

Fig. 4A7: The histogram of the probabilities extracted from the pixels corresponding to each post class of C3 and C6 unit. The plot shows that the surface units are dominated by pixels with higher probability values (close to 1) – indicating the dominance of mostly pure pixels at each unit.....139

Chapter 5:

Fig. 5.1: The volumetric heat capacity and thermal inertia of solid N_2 ice at temperatures of 10 to 60 K (compiled data from Sagmiller and Hartwig, 2020) – relevant to TNO and KBO surfaces. The subplots exhibit an abrupt change in the volumetric heat capacity and thermal inertia trends at the α - β phase transition of N_2 ice at 35.6 K.....155

Fig. 5.2: Schematic diagram of the *Outer Solar System Astrophysics Lab* at the University of Arkansas. The chamber is 20" (50.8 cm) long by 12" (30.48 cm) in diameter in the outer dimension. The top and bottom of the cylindrical chamber hold 14" ConFlat (CF) flanges (1-fixed feed-thru, 1-rotating feed-thru) such that the lid of the chamber is the fixed feed-thru. The bottom flange adapter is the rotating feed-thru with a machined profile to mate with a CH-110LT 40K Cryocooler Series helium refrigerator system. The chamber has eight 2.75" CF ports, of which 4 are fixed feed-thru and the rest 4 are rotating feed-thru. The chamber drawing was adopted and subsequently modified from the official manufacture order at Kurt J. Lesker in Jefferson, PA. For a higher resolution version of the diagram, the readers are referred to the online version of the figure.....162

Fig. 5.3: Pictures of the Outer Solar System Astrophysics Lab at the Keck Laboratory for Planetary Simulations at the University of Arkansas. A CH-110 LT 40K Cryocooler Series helium refrigerator system is attached to the chamber with the bottom flange adapter. The chamber has eight CF ports, of which 4 are fixed feed-thru and the rest 4 are rotating feed-thru. A pressure gauge is connected to the chamber with a feed-thru (see Super Bee pressure gauge attached on the left side of the chamber). For measurement of temperature inside the chamber, a thermocouple feed-thru is also connected to the chamber. For a higher resolution version of the diagram, the readers are referred to the online version of the figure.....163

Fig. 5.4: The schematic diagram of the cell (mounted upon the cold tip of the cryocooler) in cross-section as seen from the side. Gas enters the cell via a fill tube. Glass windows for visual inspections of ice and the sapphire window for Raman and FTIR (reflectance spectroscopic) investigations. Thermometer T1 and T2 and heating wires H1 and H2 are used to monitor and control temperature, respectively. The DPHP sensor probe enters the cell from above.164

List of Tables

Chapter 2:

Table 2.1. Optical constant used in this study.	22
---	----

Chapter 3:

Table 3.1: Medians and their 16% quantile as a lower 1σ error bar and 84% quantile as an upper 1σ error bar of relative discrepancies in predicted grain sizes using the Hapke slab and ISM calculated at particle radii of 1, 10, 100, and 1000 μm for amorphous (a) and crystalline (b) H_2O ice at different temperatures.	58
--	----

Table 3A.1: The mean and $\pm 1\sigma$ standard deviation of relative discrepancies in predicted grain sizes using the Hapke slab and ISM calculated at different particle radii of 1, 10, 100, and 1000 μm for amorphous (a) and crystalline (b) H_2O ice at different temperatures.	77
--	----

Chapter 4:

Table 4.1. Details of the two LEISA scenes used in this study.....	92
---	----

Table 4.2: Summary of the characteristics and composition of the surface units.....	114
--	-----

Table 4.3: List of the spectral components used to characterize compositions and their surface units.....	118
--	-----

List of Abbreviations

AIC	Akaike Information Criterion
AU	Astronomical Units
BIC	Bayesian Information Criterion
C ₂ H ₆	Ethane
CF	Con Flat
CH ₄	Methane
CIRS	Composite Infrared Spectrometer
CO	Carbon Monoxide
CO ₂	Carbon Dioxide
DC	Direct-Current
DN	Digital Number
DPHP	Dual-Probe Heat-Pulse
FTIR	Fourier-Transform Infrared Spectroscopy
GC	Gaussian Component
GMM	Gaussian Mixture Model
H ₂ O	Water
HST	Hubble Space Telescope
I/F	Intensity Flux
ISISv3	Integrated Software for Imagers and Spectrometers
ISM	Internal Scattering Model
KB	Kuiper Belt
KBO	Kuiper Belt Object
LEISA	Linear Etalon Imaging Spectral Array

LORRI	Long Range Reconnaissance Imager
MVIC	Multispectral Visible Imaging Camera
N ₂	Nitrogen
NASA	National Aeronautics and Space Administration
NH ₃	Ammonia
NIR	Near infrared
PC	Principal Component
PCA	Principal Component Analysis
PC-GMM	Principal Component reduced Gaussian Mixture Model
PDS	Planetary Data System
PID	Proportional, Integral, and Derivative
RADF	Radiance Factor
RTM	Radiative Transfer Model
SP	Sputnik Planitia
SSA	Single Scattering Albedo
TI	Thermal Inertia
TNO	Trans-Neptunian Object
USGS	United States Geological Survey
UV	Ultra-violet
VIMS	Visible and Infrared Mapping Spectrometer
VIS	Visible

List of Published Chapters

Chapter 2:

Emran, A., and Chevrier, V. F., 2022. Uncertainty in Grain Size Estimation of Volatiles on Trans-Neptunian Objects and Kuiper Belt Objects. *The Astronomical Journal* 163, 196.

Chapter 3:

Emran, A., and Chevrier, V. F., 2022. Discrepancy in Grain Size Estimation of H₂O ice in the Outer Solar System, arXiv:2204.04192 [astro-ph], *Res. in Astronomy and Astrophysics* [under review].

Chapter 4:

Emran, A., Dalle Ore, C. M., Ahrens, C. J., Khan, M. K. H., Chevrier, V. F., and Cruikshank, D. P., 2022. Pluto's Surface Mapping using Unsupervised Learning from Near-Infrared Observations of LEISA/Ralph. *The Planetary Science Journal* [under revision].

Chapter 5:

Emran, A., and Chevrier, V. F., 2022. The Outer Solar System Astrophysics Lab: A New Experimental Facility for Spectral and Thermal Investigations of Ices at Cryogenic Temperatures [*To be submitted in Journal of Astronomical Instrumentation*].

Chapter 1

Introduction

1.1. Introduction

The solar system consists of three broad zones – (from the Sun) the inner rocky planets, the gas giants, and the Kuiper Belt of icy planetary bodies and dwarf planets. The Kuiper Belt is a vast region beyond the orbit of Neptune whose existence was first proposed by Kuiper (1951). The belt retains chemical, dynamic, and thermal fingerprints of the solar system's history (Schaller, 2010) because the celestial bodies in the belt are thought to be remnants of the early solar system (Barucci et al., 2005; Wu et al., 2013). While the inner boundary of the belt starts at the orbit of Neptune at around 30 astronomical units (AU), the inner main region might extend up to around 50 AU from the Sun (Stern and Colwell, 1997). The outer edge of the belt (in the main part), known as the scattered disk, is thought to extend nearly to a heliocentric distance of 1000 AU (Morbidelli and Brown, 2004 and references therein).

Millions of icy (solid) planetary bodies located in the outer fringe of the solar system, beyond the orbit of Neptune, are collectively referred to as Kuiper Belt objects (KBOs) or trans-Neptunian objects (TNOs; e.g., Barucci et al., 2005). The populations of KBOs and TNOs exhibit a wide variety of colors, from neutral to exceptionally red, in optical wavelength (Doressoundiram, 2004) and remarkably diverse albedos (Grundy et al., 2005). Pluto, a dwarf planet and the largest known trans-Neptunian object, is one of the fascinating outer solar system bodies in the Kuiper Belt. Triton, the largest moon of Neptune, is also considered as a KBO, which was captured by the gravity of its host planet (McKinnon and Leith, 1995; Agnor and Hamilton, 2006). Other larger objects, named or unnamed, in the Kuiper Belt, include dwarf planets Eris, Sedna, Makemake, Quaoar, 2007 OR10, etc. Albeit the typical TNOs and KBOs reside beyond the orbit of Neptune,

there are some KBOs, referred to as Centaurs, that have escaped from the Kuiper Belt and orbit among the giant classical planets (Schaller, 2010). Some of the Centaurs show the presence of their orbital activity around a heliocentric distance between 6 to 25 AU (Stern and Trafton, 2008).

1.2. Surfaces of TNOs and KBOs

Nitrogen (N_2), methane (CH_4), and carbon monoxide (CO) ices have been detected or inferred to be present on the surfaces of TNOs and KBOs such as Triton (Cruikshank et al., 1984, 1993). Pluto also reveals the presence of N_2 , CH_4 , and CO ices on its surface (Cruikshank et al., 1976; Owen et al., 1993; Schmitt et al., 2017; see Fig. 1.1). Though Pluto's surface hosts abundances of N_2 , CH_4 , and CO volatile ices, its largest moon Charon is a wholly different world (Grundy et al., 2016). Charon shows the presence of the inert components of water (H_2O) and ammonia (NH_3) ices on its surface (Grundy et al., 2016). Eris, a dwarf planet in the Kuiper Belt, exhibits a prevalence of N_2 and CH_4 ices on its surface (Dumas et al., 2007).

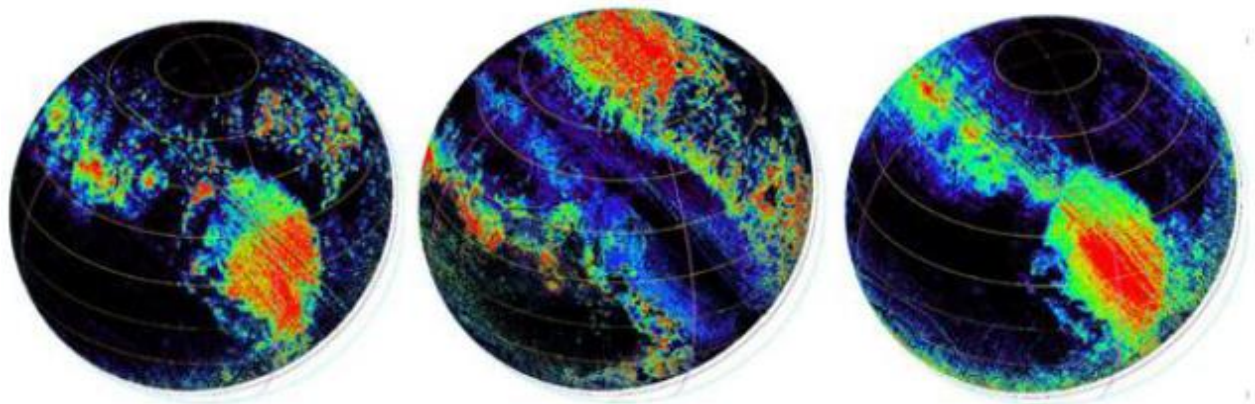


Fig. 1.1: Distribution of N_2 , CH_4 , and CO ices (left to right) on the surface of Pluto as derived from the Linear Etalon Imaging Spectral Array (LEISA) instrument a part of the Ralph instrument package (Reuter et al., 2008) onboard the New Horizons (Schmitt et al., 2017). The warmer colors indicate a higher concentration of volatiles. The N_2 distribution map (left panel) was based on the integrated band depth of the $2.15 \mu m$ N_2 band, the CH_4 map (middle panel) was based on the state of CH_4 as determined by the CH_4 bands position index, and the CO map (right panel) was based on the integrated band depth of the weak CO band at $1.58 \mu m$. The figure was adopted from Schmitt et al. (2017).

Besides the volatile materials of CH₄, N₂, and CO, Pluto's surface shows a photochemically formed organic hydrocarbon called tholins and a trace amount of ethane (C₂H₆) and H₂O ices (Cruikshank et al., 1976; Owen et al., 1993; Merlin, 2015). These various compositional mixtures are associated with some form of geological processes and seasonal interaction with the atmosphere of the dwarf planet (Bertrand and Forget, 2016). Though absent on Pluto, Triton's surface hosts carbon dioxide (CO₂) ice (Cruikshank et al., 1993; Grundy et al., 2016).

Eris shows a lot of similar characteristics to that of Pluto. Thus, besides the abundances of N₂ and CH₄ ices, Eris shows the presence of an intimate mixture of H₂O ice and tholins (Dumas et al., 2007). Visible (VIS) and near-infrared (NIR) spectra of Sedna, a dwarf planet in the Kuiper Belt, exhibit the presence of ices on its surfaces that are different from many other TNOs but have a resemblance to Triton – the presence of N₂ and CH₄ ices on Sedna's surface (Barucci et al., 2005). Heterogeneous ice mixtures of N₂, CH₄, and C₂H₆ have been reported on the surface of Makemake, a likely dwarf planet in the Kuiper Belt (Ortiz et al., 2012; Lim et al., 2010). Note that even though H₂O ice is most prevalent in the outer solar system and interstellar medium (Baragiola, 2003), it acts as non-volatile ice in the surface conditions of many outer solar system bodies.

1.3. Atmospheres of TNOs and KBOs

The atmosphere of a planetary body provides insight into the thermal evolution, origin, and surface-atmospheric interactions with the host planet (Stern and Trafton, 2008). The requirement of atmospheres on KBOs and TNOs includes gases or sublimation/evaporating materials present on the surface and having a source of energy to produce substantial vapor pressure from reservoir volatiles (Stern and Trafton, 2008). The presence of volatile ices on TNOs and KBOs suggests that

the vapor pressure supports a permanent or seasonal atmosphere in the larger bodies beyond or at the orbit of Neptune (Johnson et al., 2015).

Pluto has a tenuous atmosphere (Fig. 1.2) - composed mainly of volatile N_2 and trace amounts of CH_4 and CO (Stern et al., 2015; Gladstone et al., 2016). The climate model of Pluto indicates that, unlike Earth, the atmospheric temperatures on Pluto increase with altitude (Lellouch et al., 2009; Gladstone et al., 2016). Charon, the largest moon of Pluto, does not hold an atmosphere or holds an atmosphere that has far lower column abundance than Pluto's upper atmosphere as evident from the solar occultation total count rate data (Stern et al., 2015). Triton also possesses a thin tenuous molecular N_2 -rich atmosphere with a surface pressure of 1.5 – 1.9 Pa (15 – 19 μ bar), as evident from the Voyager 2 encounter data (Ingersoll, 1990), with a variety of other component species (Lellouch et al., 2010). CH_4 and CO gas abundances have also been detected in the atmosphere of Triton (Lellouch et al., 2010).

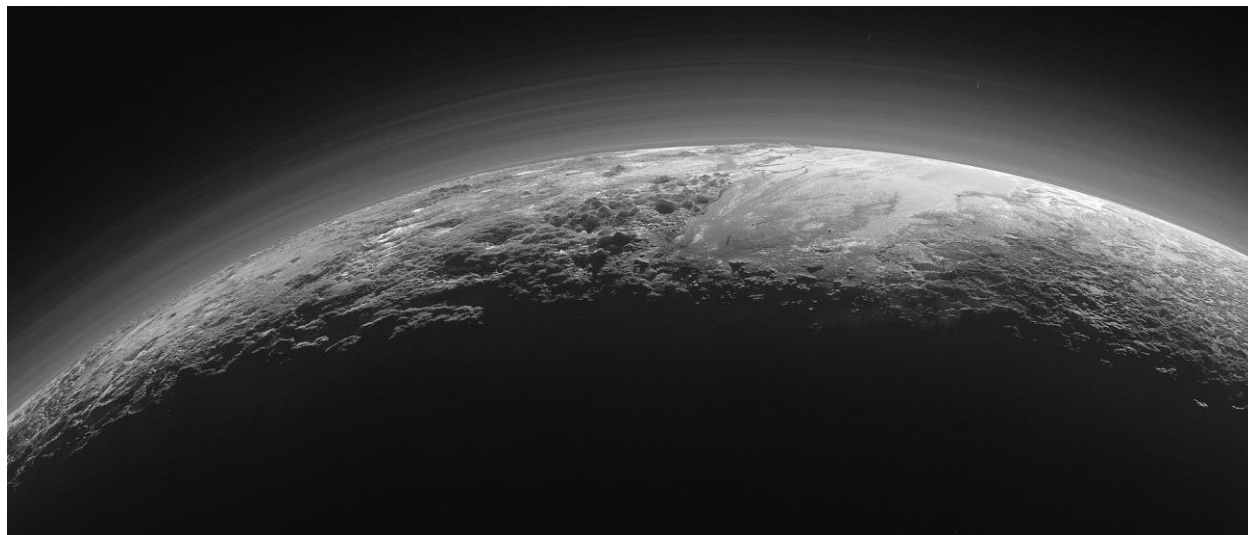


Fig. 1.2: Haze layer at the atmosphere of Pluto as seen by New Horizons spacecraft flyby in 2015. Image credit: National Aeronautics and Space Administration (NASA)/Johns Hopkins University Applied Physics Laboratory/Southwest Research Institute (SwRI).

Despite the discoveries of N_2 and CH_4 on Eris (Licandro et al., 2006; Dumas et al., 2007) and Sedna (Barucci et al., 2005), the presence of an atmosphere on these bodies is still not unambiguously clear. However, it is hypothesized that the surface volatile may support a seasonal thin atmosphere on Eris at perihelion – closer to the Sun or shorter heliocentric distances (Johnson et al., 2015). This seasonal atmosphere may freeze on the Eris's surface at aphelion or larger heliocentric distances (Dumas et al., 2007). Centaurs, residing around the orbits of the giant planets, enjoy an increased amount of solar insolation which results in the sublimation of volatiles (Stern and Trafton, 2008). Atmospheric phenomena on Centaurs were first observed in Centaur 2060, Chiron (Stern and Trafton, 2008). Chiron's surface may contain surface or near-surface volatiles, probably CO, in an uneven distribution and surface sources of atmospheric gases or particulates (Stern and Trafton, 2008).

In summary, the presence of an atmosphere on TNOs and KBOs depends on the sublimation pressure of ice, which is sensitive to the composition, mixing states, and temperatures of volatile ices (Young et al., 2020). Vapor pressure of N_2 , CH_4 , and CO volatile ices may rise to an atmosphere on KBOs and TNOs and, thus, the atmosphere is called a vapor pressure-supported atmosphere (Young et al., 2020). Among the TNOs and KBOs, Pluto and Triton have significant atmospheres and have been studied over the past decades extensively, so far, from ground-based observations e.g., occultations, spacecraft data (Voyager and New Horizons), spectroscopy, and modeling (Young et al., 2020). A summary of the surface and atmospheric properties of the eight largest TNOs and KBOs (Triton, Pluto, Charon, Eris, Sedna, Makemake, Quaoar, and 2007 OR10) in the Kuiper Belt is given in Johnson et al. (2015).

1.4. Surface-atmosphere interaction and volatile transport

The interactions between the surface and atmosphere of icy bodies of TNOs and KBOs happen through the exchange of matter and energy. These exchange mechanisms are expected to be complex in nature. Among the N_2 , CH_4 , and CO ices, N_2 is the most volatile component - it has the highest vapor pressure and sublimates first when heated by solar irradiation. Thus, the surface and atmospheric heating of TNOs and KBOs indicate that N_2 on the surface gets diffused and sublimates into the atmosphere eventually. The isothermality of volatiles is maintained by the latent heat exchange resulting in the deposition in the winter hemisphere where the net radiation is balanced (Trafton et al., 1998). Larger KBOs have significant mass-loss rates and consequently affect the surface morphologic features. On the other hand, significant precipitation of bright N_2 frost correlates with the higher albedo of the KBOs (Johnson et al., 2015). The volatiles on TNOs and KBOs function in various ways due to the nature of compositional mixtures and play important roles in the surface-atmospheric processes or interactions on the icy bodies (Grundy et al., 2016; Moore et al., 2016). However, the surface-atmospheric interactions are known, to some extent, for Pluto and Triton, thanks to the observational data of these bodies from the National Aeronautics and Space Administration (NASA)'s Voyager and New Horizons spacecraft missions.

The complex surface-atmospheric interactions influence volatile movements and morphologies on Pluto. The atmosphere of Pluto is composed of N_2 gas and is in solid-gas equilibrium condition with surface N_2 ice (e.g., Gladstone et al., 2016). Consequently, the movement of global ice distribution and N_2 condensation-sublimation influence the atmospheric circulation on the dwarf planet (Bertrand et al., 2020). A deep impact basin, Sputnik Planitia (SP), represents a powerful cold trap for the natural accumulation of volatile N_2 (and CO) ices due to its lower elevation corresponding to higher atmospheric pressure and condensation temperature (e.g., Bertrand and

Forget, 2016; Bertrand and Forget, 2017). The layers of global photochemical hazes are the result of interaction between the surface and atmosphere through the process of sublimation and condensation of N_2 (Cheng et al., 2017). Independently of N_2 ice distribution outside the Sputnik Planitia, the contemporary control of the general atmospheric circulation of the dwarf planet is dominated by its retrorotation (Bertrand et al., 2020). This unusual circulation regime explains the distribution of surface geological features and longitudinal asymmetry of ice distribution on Pluto as observed by New Horizon spacecraft data (Bertrand et al., 2020).

Although the geological evidence of surface-atmospheric interactions on Pluto can conveniently be observed, thanks to the New Horizons mission that provides a plethora of data, in the case of Triton the available data are not that much. Triton, and its host planet Neptune, was only visited by Voyager 2 spacecraft in 1989. However, like Pluto, Triton has a thin atmosphere composed mostly of volatile N_2 gas, vapor equilibrium with the surface ices, and other minor species (e.g., Lellouch et al., 2010). Like Mars, Triton has a well-structured global atmosphere equilibrium with surface frost (Ingersoll, 1990). The atmosphere of Triton is believed to have evolved from the outgassing of Triton's volcanic activity driven by seasonal solar heating. Ices are frozen on the surface of Triton which warms up, evaporates, and escapes into the lower atmosphere forming a thin atmospheric layer (Lellouch et al., 2010). The atmosphere also contains N_2 ice grains and makes haze layers (Lellouch et al., 2010).

The surface-atmospheric exchange of materials and energy are intricately associated with the constituent materials involved (N_2 , CH_4 , CO , and H_2O ices), their physical properties such as solid phases and grain sizes, the spatial distribution of ices on the surfaces, and their thermal states. On top of that, the mechanical strengths and thermal properties of planetary surfaces are directly influenced by the grain size of planetary regolith (Gundlach and Blum, 2013). Thus, an accurate

grain size estimation of the outer solar system bodies is important for an improved understanding of surface volatile transport and thermophysical modeling of planetary bodies. On KBOs and TNOs, the surface-atmospheric interaction is influenced by the diurnal and seasonal temperature changes over the orbital period of the planetary bodies. The diurnal and seasonal temperatures of planetary surfaces are directly controlled by thermal properties such as thermal conductivity, thermal diffusivity, and specific heat capacity, and more specifically the thermal inertia, of the surface materials (e.g., Wang et al., 2010).

The seasonal ice cycle on Pluto is influenced by the topography, albedo, emissivity of ice, and thermal conductivity of shallow and deep subsurface, which determines diurnal and seasonal thermal inertia (Bertrand and Forget, 2016). Surface thermal inertia together with topography and albedo controls the planetary energy exchange between surface and atmosphere and, thus, influences the atmosphere and the climate of a planetary body (MacKenzie et al., 2019). Seasonal thermal inertia is a key driver of the cycle of volatile N_2 , which is the major ice constituent of TNOs and KBOs (Bertrand and Forget, 2016). Thus, the surface volatile transport of the icy planetary bodies is influenced by the thermal characteristics of the surface volatile materials (Spencer and Moore, 1992). Understanding volatile transport mechanisms and ultimately the surface-atmospheric interactions, thus, warrant the accurate estimation of the thermal properties of the volatile surfaces of KBOs and TNOs.

1.5. Rationale of this research

As discussed above, the characteristics of ice are associated with surface geological processes and surface-atmospheric interactions, which are governed by physical characteristics such as grain size and thermal properties of surface constituents. Radiative transfer models (RTMs) have been used to characterize the composition and physical characteristics of outer solar system bodies

including KBOs and TNOs (e.g., Grundy and Fink, 1991; Dumas et al., 2007; Merlin et al., 2010; Tegler et al., 2010). For instance, the grain sizes of ices found in the outer solar system bodies are estimated by using the radiative scattering models (e.g., Mie theory) from the measurements of single scattering albedo (SSA).

Using the radiative model of Mie theory, single scattering albedo of spherical grains (simple geometries) can exactly be calculated from Maxwell's equations (Mie, 1908), if refractive indices and particle size are known. On the other hand, the approximation models of Hapke (1993), such as the equivalent slab model (Hapke slab) and internal scattering/scatterer model (ISM), are also widely used in calculating the single scattering albedo of different planetary bodies ranging from terrestrial to icy surfaces. However, wide discrepancies in the estimation of grain size have been reported for H₂O ice on Saturnian moons, such as Enceladus, using different radiative scattering models (Hansen, 2009). These uncertainties are due to the use of different single-scattering albedo calculations rather than a choice of using bidirectional scattering models (Hansen, 2009). Thus, it is reasonable to anticipate that the estimation of grain sizes of CH₄ and N₂ ices (pure and mixture) on TNO and KBO surfaces will have inconsistencies owing to the different scattering models used.

Hansen (2009) compared single scattering albedos using the optical constant data of crystalline H₂O ice at 110 K – relevant to Saturnian moons and other icy bodies. The temperatures at the far reach of the solar system in the Kuiper Belt, Oort cloud, and interstellar medium are much lower, and amorphous ice should dominate in these environments. Furthermore, while employing RTMs in the outer solar system bodies, there has been extensive use of optical constants of crystalline and/or amorphous phases of H₂O ice and a variety of scattering models. Thus, the uncertainty of the grain size estimation of amorphous and crystalline H₂O ice at temperatures analogous to the outer solar system and the interstellar medium (15 K – 80 K) using different scattering models is

warranted. Accordingly, two of the research sections of this thesis (*Chapters 2 and 3*) focus on assessing the discrepancies in grain size estimation of N₂, CH₄, and H₂O ices at the temperatures relevant to the icy bodies in the Kuiper Belt.

Mapping spatial abundance and geographic distribution of ices and their relationship with the geological features are imperative for an in-depth understanding of the volatile transport mechanism on icy bodies such as Pluto (Bertrand and Forget, 2016). Thus, the surface compositional abundance and geographic distribution of volatiles (N₂, CH₄, and CO) and non-volatiles (H₂O, tholins, etc.) on Pluto have thoroughly been reported in existing studies from the observations by instruments onboard the New Horizons spacecraft. However, existing studies in mapping surface ices on Pluto were mostly accomplished using band depth measurements of known ice species, spectral indices or indicators, or the implementation of complex radiative transfer models. The execution of these methods requires prior knowledge of representative surface ices, or needs the reflectance, or optical constants data of the end members (label data). In this research (*Chapter 4*), we use an unsupervised machine learning technique to map the geographic distribution of ices on Pluto's surface without any prior information or label data.

An accurate estimation of the spectral and thermal properties of ices is incredibly important for an in-depth understanding of surface-atmospheric mechanisms. Nevertheless, an estimation of the spectral and thermal properties of ices needs an experimental facility to investigate the intrinsic characteristics of volatiles at cryogenic temperatures. While laboratory data on spectral properties are, to some extent, available, the data on thermal properties are not widely available or poorly constrained. In this research (*Chapter 5*), we propose a method to estimate the thermal properties of N₂, CH₄, and CO ices, and the mixture thereof in a simulated laboratory setting at temperatures of 20 to 60 K – relevant to TNOs and KBOs. While the method is relatively new and has not been

tested in cryogenic temperature conditions yet, this thesis describes the detailed methodology, including the theory of the proposed method, which can be used to estimate the thermal properties of ices at cryogenic temperatures. To implement the method, we built a new experimental facility – named the *Outer Solar System Astrophysics Lab* – located at the University of Arkansas. The laboratory has facilities to experiment with spectral and thermal properties of volatile ices found on the surfaces of outer solar system bodies. We provide detailed technical specifications of the new experimental facility so that it can help as a guideline for building a similar cryogenic chamber in the future for scientific experiments on ices.

1.6. Organizations of chapters

This research consists of a total of six chapters including a combination of the implementation of radiative scattering models (*Chapters 2 and 3*), a machine learning technique (*Chapter 4*), and laboratory experiments (*Chapter 5*). In the Introduction (*Chapter 1*), the thesis introduces a holistic overview of parameters required for an in-depth understanding of surface-atmospheric interaction and the volatile transport mechanism of the TNOs and KBOs. In the Conclusion (*Chapter 6*), the thesis wraps up the summaries of all research chapters and describes the contributions this present work put forward to the science community. The complete outline of the dissertation involves:

- Introduction (*Chapter 1*)
- Uncertainty in grain size estimation of CH₄ and N₂ ices (*Chapter 2*)
- Discrepancy in grain size estimation of amorphous and crystalline H₂O ices (*Chapter 3*)
- Implementation of unsupervised learning on Pluto (*Chapter 4*)
- The proposed method for estimation of the thermal properties of ices and the detailed technical specifications of the new laboratory facility (*Chapter 5*), and
- Summary and conclusion (*Chapter 6*)

1.6.1. Primary Author Contribution

I hereby certify that over 51% of the work presented in this thesis was prepared and completed by the primary author, Al Emran. The percentage of the contribution within the provided research sections (*Chapters 2, 3, 4, and 5*) by the primary author is listed below while the rest of the percentages are awarded for intellectual contributions by listed coauthors corresponding research chapters.

- *Chapter 2: 95%*
- *Chapter 3: 95%*
- *Chapter 4: 85%*
- *Chapter 5: 95%*

1.7. Conclusion

Deciphering volatile transport and surface-atmospheric interactions on trans-Neptunian objects and Kuiper Belt objects needs an in-depth understanding of the physical and thermal properties of the constituent surface ices of these planetary bodies. In this dissertation, we present a holistic study of these physical and thermal properties of ices (both volatile and non-volatile) through the implementation of radiative scattering models to understand the discrepancies in the estimation of grain size of the ices, mapping a surface composition of a KBO using unsupervised machine learning techniques, and integrating a laboratory experimental aspect. Thus, this research incorporates a set of models, tools, and techniques used in planetary sciences for an improved understanding of the properties of surface ices found in the Kuiper Belt and deciphering the surface-atmospheric interactions on the planetary bodies in the outer reach of the solar system.

1.8. References

- Agnor, C.B., Hamilton, D.P., 2006. Neptune's capture of its moon Triton in a binary–planet gravitational encounter. *Nature* 441, 192–194. <https://doi.org/10.1038/nature04792>
- Baragiola, R.A., 2003. Water ice on outer solar system surfaces: Basic properties and radiation effects. *Planetary and Space Science, Surfaces and Atmospheres of the Outer Planets their Satellites and Ring Systems* 51, 953–961. <https://doi.org/10.1016/j.pss.2003.05.007>
- Barucci, M.A., Cruikshank, D.P., Dotto, E., Merlin, F., Poulet, F., Ore, C.D., Fornasier, S., Bergh, C. de, 2005. Is Sedna another Triton? *A&A* 439, L1–L4. <https://doi.org/10.1051/0004-6361:200500144>
- Bertrand, T., Forget, F., 2016. Observed glacier and volatile distribution on Pluto from atmosphere–topography processes. *Nature* 540, 86–89. <https://doi.org/10.1038/nature19337>
- Bertrand, T., Forget, F., 2017. 3D modeling of organic haze in Pluto's atmosphere. *Icarus, Special Issue: The Pluto System* 287, 72–86. <https://doi.org/10.1016/j.icarus.2017.01.016>
- Bertrand, T., Forget, F., White, O., Schmitt, B., Stern, S.A., Weaver, H.A., Young, L.A., Ennico, K., Olkin, C.B., Team, the N.H.S., 2020. Pluto's Beating Heart Regulates the Atmospheric Circulation: Results From High-Resolution and Multiyear Numerical Climate Simulations. *Journal of Geophysical Research: Planets* 125, e2019JE006120. <https://doi.org/10.1029/2019JE006120>
- Cheng, A.F., Summers, M.E., Gladstone, G.R., Strobel, D.F., Young, L.A., Lavvas, P., Kammer, J.A., Lisse, C.M., Parker, A.H., Young, E.F., Stern, S.A., Weaver, H.A., Olkin, C.B., Ennico, K., 2017. Haze in Pluto's atmosphere. *Icarus* 290, 112–133. <https://doi.org/10.1016/j.icarus.2017.02.024>
- Cruikshank, D.P., Hamilton Brown, R., Clark, R.N., 1984. Nitrogen on Triton. *Icarus* 58, 293–305. [https://doi.org/10.1016/0019-1035\(84\)90046-0](https://doi.org/10.1016/0019-1035(84)90046-0)
- Cruikshank, D.P., Pilcher, C.B., Morrison, D., 1976. Pluto: Evidence for Methane Frost. *Science* 194, 835–837.
- Cruikshank, D.P., Roush, T.L., Owen, T.C., Geballe, T.R., Bergh, C. de, Schmitt, B., Brown, R.H., Bartholomew, M.J., 1993. Ices on the Surface of Triton. *Science* 261, 742–745. <https://doi.org/10.1126/science.261.5122.742>
- Doressoundiram, A., 2004. Colour Properties and Trends in Trans-Neptunian Objects, in: Davies, J.K., Barrera, L.H. (Eds.), *The First Decadal Review of the Edgeworth-Kuiper Belt*. Springer Netherlands, Dordrecht, pp. 131–144. https://doi.org/10.1007/978-94-017-3321-2_12
- Dumas, C., Merlin, F., Barucci, M.A., Bergh, C. de, Hainault, O., Guilbert, A., Vernazza, P., Doressoundiram, A., 2007. Surface composition of the largest dwarf planet 136199 Eris (2003 UB). *A&A* 471, 331–334. <https://doi.org/10.1051/0004-6361:20066665>

- Gladstone, G.R., Stern, S.A., Ennico, K., Olkin, C.B., Weaver, H.A., Young, L.A., Summers, M.E., Strobel, D.F., Hinson, D.P., Kammer, J.A., Parker, A.H., Steffl, A.J., Linscott, I.R., Parker, J.W., Cheng, A.F., Slater, D.C., Versteeg, M.H., Greathouse, T.K., Retherford, K.D., Throop, H., Cunningham, N.J., Woods, W.W., Singer, K.N., Tsang, C.C.C., Schindhelm, E., Lisse, C.M., Wong, M.L., Yung, Y.L., Zhu, X., Curdt, W., Lavvas, P., Young, E.F., Tyler, G.L., Team, the N.H.S., 2016. The atmosphere of Pluto as observed by New Horizons. *Science* 351. <https://doi.org/10.1126/science.aad8866>
- Grundy, W.M., Binzel, R.P., Buratti, B.J., Cook, J.C., Cruikshank, D.P., Ore, C.M.D., Earle, A.M., Ennico, K., Howett, C.J.A., Lunsford, A.W., Olkin, C.B., Parker, A.H., Philippe, S., Protopapa, S., Quirico, E., Reuter, D.C., Schmitt, B., Singer, K.N., Verbiscer, A.J., Beyer, R.A., Buie, M.W., Cheng, A.F., Jennings, D.E., Linscott, I.R., Parker, J.W., Schenk, P.M., Spencer, J.R., Stansberry, J.A., Stern, S.A., Throop, H.B., Tsang, C.C.C., Weaver, H.A., Weigle, G.E., Young, L.A., Team, and the N.H.S., 2016. Surface compositions across Pluto and Charon. *Science* 351. <https://doi.org/10.1126/science.aad9189>
- Grundy, W.M., Fink, U., 1991. A new spectrum of Triton near the time of the Voyager encounter. *Icarus* 93, 379–385. [https://doi.org/10.1016/0019-1035\(91\)90220-N](https://doi.org/10.1016/0019-1035(91)90220-N)
- Grundy, W.M., Noll, K.S., Stephens, D.C., 2005. Diverse albedos of small trans-neptunian objects. *Icarus* 176, 184–191. <https://doi.org/10.1016/j.icarus.2005.01.007>
- Gundlach, B., Blum, J., 2013. A new method to determine the grain size of planetary regolith. *Icarus* 223, 479–492. <https://doi.org/10.1016/j.icarus.2012.11.039>
- Hansen, G.B., 2009. Calculation of single-scattering albedos: Comparison of Mie results with Hapke approximations. *Icarus* 203, 672–676. <https://doi.org/10.1016/j.icarus.2009.05.025>
- Hapke, B., 1993. *Theory of Reflectance and Emittance Spectroscopy*, Topics in Remote Sensing. Cambridge University Press, Cambridge. <https://doi.org/10.1017/CBO9780511524998>
- Ingersoll, A.P., 1990. Dynamics of Triton's atmosphere. *Nature* 344, 315–317. <https://doi.org/10.1038/344315a0>
- Johnson, R.E., Oza, A., Young, L.A., Volkov, A.N., Schmidt, C., 2015. Volatile Loss and Classification of Kuiper Belt Objects. *ApJ* 809, 43. <https://doi.org/10.1088/0004-637X/809/1/43>
- Kuiper, G.P., 1951. On the Origin of the Solar System. *Proc Natl Acad Sci U S A* 37, 1–14.
- Lellouch, E., Bergh, C. de, Sicardy, B., Ferron, S., Käufl, H.-U., 2010. Detection of CO in Triton's atmosphere and the nature of surface-atmosphere interactions. *A&A* 512, L8. <https://doi.org/10.1051/0004-6361/201014339>

- Lellouch, E., Sicardy, B., Bergh, C. de, Käufl, H.-U., Kassi, S., Campargue, A., 2009. Pluto's lower atmosphere structure and methane abundance from high-resolution spectroscopy and stellar occultations. *A&A* 495, L17–L21. <https://doi.org/10.1051/0004-6361/200911633>
- Licandro, J., Pinilla-Alonso, N., Pedani, M., Oliva, E., Tozzi, G.P., Grundy, W.M., 2006. The methane ice rich surface of large TNO 2005 FY9: a Pluto-twin in the trans-neptunian belt? *A&A* 445, L35–L38. <https://doi.org/10.1051/0004-6361:200500219>
- Lim, T.L., Stansberry, J., Müller, T.G., Mueller, M., Lellouch, E., Kiss, C., Santos-Sanz, P., Vilenius, E., Protopapa, S., Moreno, R., Delsanti, A., Duffard, R., Fornasier, S., Groussin, O., Harris, A.W., Henry, F., Horner, J., Lacerda, P., Mommert, M., Ortiz, J.L., Rengel, M., Thirouin, A., Trilling, D., Barucci, A., Crovisier, J., Doressoundiram, A., Dotto, E., Buenestado, P.J.G., Hainaut, O., Hartogh, P., Hestroffer, D., Kidger, M., Lara, L., Swinyard, B.M., Thomas, N., 2010. “TNOs are Cool”: A survey of the trans-Neptunian region - III. Thermophysical properties of 90482 Orcus and 136472 Makemake. *A&A* 518, L148. <https://doi.org/10.1051/0004-6361/201014701>
- MacKenzie, S.M., Lora, J.M., Lorenz, R.D., 2019. A Thermal Inertia Map of Titan. *Journal of Geophysical Research: Planets* 124, 1728–1742. <https://doi.org/10.1029/2019JE005930>
- McKinnon, W.B., Leith, A.C., 1995. Gas Drag and the Orbital Evolution of a Captured Triton. *Icarus* 118, 392–413. <https://doi.org/10.1006/icar.1995.1199>
- Merlin, F., 2015. New constraints on the surface of Pluto. *A&A* 582, A39. <https://doi.org/10.1051/0004-6361/201526721>
- Merlin, F., Barucci, M.A., de Bergh, C., Fornasier, S., Doressoundiram, A., Perna, D., Protopapa, S., 2010. Surface composition and physical properties of several trans-neptunian objects from the Hapke scattering theory and Shkuratov model. *Icarus* 208, 945–954. <https://doi.org/10.1016/j.icarus.2010.03.014>
- Mie, G., 1908. Beiträge zur Optik trüber Medien, speziell kolloidaler Metallösungen. *Annalen der Physik* 330, 377–445. <https://doi.org/10.1002/andp.19083300302>
- Moore, J.M., McKinnon, W.B., Spencer, J.R., Howard, A.D., Schenk, P.M., Beyer, R.A., Nimmo, F., Singer, K.N., Umurhan, O.M., White, O.L., Stern, S.A., Ennico, K., Olkin, C.B., Weaver, H.A., Young, L.A., Binzel, R.P., Buie, M.W., Buratti, B.J., Cheng, A.F., Cruikshank, D.P., Grundy, W.M., Linscott, I.R., Reitsema, H.J., Reuter, D.C., Showalter, M.R., Bray, V.J., Chavez, C.L., Howett, C.J.A., Lauer, T.R., Lisse, C.M., Parker, A.H., Porter, S.B., Robbins, S.J., Runyon, K., Stryk, T., Throop, H.B., Tsang, C.C.C., Verbiscer, A.J., Zangari, A.M., Chaikin, A.L., Wilhelms, D.E., NEW HORIZONS SCIENCE TEAM, 2016. The geology of Pluto and Charon through the eyes of New Horizons. *Science* 351, 1284–1293. <https://doi.org/10.1126/science.aad7055>
- Morbidelli, A., Brown, M.E., 2004. The kuiper belt and the primordial evolution of the solar system. *Comets II* 175–191.

- Ortiz, J.L., Sicardy, B., Braga-Ribas, F., Alvarez-Candal, A., Lellouch, E., Duffard, R., Pinilla-Alonso, N., Ivanov, V.D., Littlefair, S.P., Camargo, J.I.B., Assafin, M., Unda-Sanzana, E., Jehin, E., Morales, N., Tancredi, G., Gil-Hutton, R., de la Cueva, I., Colque, J.P., Da Silva Neto, D.N., Manfroid, J., Thirouin, A., Gutiérrez, P.J., Lecacheux, J., Gillon, M., Maury, A., Colas, F., Licandro, J., Mueller, T., Jacques, C., Weaver, D., Milone, A., Salvo, R., Bruzzone, S., Organero, F., Behrend, R., Roland, S., Vieira-Martins, R., Widemann, T., Roques, F., Santos-Sanz, P., Hestroffer, D., Dhillon, V.S., Marsh, T.R., Harlinton, C., Bagatin, A.C., Alonso, M.L., Ortiz, M., Colazo, C., Lima, H.J.F., Oliveira, A.S., Kerber, L.O., Smiljanic, R., Pimentel, E., Giacchini, B., Cacella, P., Emilio, M., 2012. Albedo and atmospheric constraints of dwarf planet Makemake from a stellar occultation. *Nature* 491, 566–569. <https://doi.org/10.1038/nature11597>
- Owen, T.C., Roush, T.L., Cruikshank, D.P., Elliot, J.L., Young, L.A., Bergh, C. de, Schmitt, B., Geballe, T.R., Brown, R.H., Bartholomew, M.J., 1993. Surface Ices and the Atmospheric Composition of Pluto. *Science* 261, 745–748. <https://doi.org/10.1126/science.261.5122.745>
- Reuter, D.C., Stern, S.A., Scherrer, J., Jennings, D.E., Baer, J.W., Hanley, J., Hardaway, L., Lunsford, A., McMuldroy, S., Moore, J., Olkin, C., Parizek, R., Reitsma, H., Sabatke, D., Spencer, J., Stone, J., Throop, H., Van Cleve, J., Weigle, G.E., Young, L.A., 2008. Ralph: A Visible/Infrared Imager for the New Horizons Pluto/Kuiper Belt Mission. *Space Sci Rev* 140, 129–154. <https://doi.org/10.1007/s11214-008-9375-7>
- Schaller, E.L., 2010. Atmospheres and surfaces of small bodies and dwarf planets in the Kuiper Belt. *EPJ Web of Conferences* 9, 267–276. <https://doi.org/10.1051/epjconf/201009021>
- Schmitt, B., Philippe, S., Grundy, W.M., Reuter, D.C., Côte, R., Quirico, E., Protopapa, S., Young, L.A., Binzel, R.P., Cook, J.C., Cruikshank, D.P., Dalle Ore, C.M., Earle, A.M., Ennico, K., Howett, C.J.A., Jennings, D.E., Linscott, I.R., Lunsford, A.W., Olkin, C.B., Parker, A.H., Parker, J.Wm., Singer, K.N., Spencer, J.R., Stansberry, J.A., Stern, S.A., Tsang, C.C.C., Verbiscer, A.J., Weaver, H.A., 2017. Physical state and distribution of materials at the surface of Pluto from New Horizons LEISA imaging spectrometer. *Icarus, Special Issue: The Pluto System* 287, 229–260. <https://doi.org/10.1016/j.icarus.2016.12.025>
- Spencer, J.R., Moore, J.M., 1992. The influence of thermal inertia on temperatures and frost stability on Triton. *Icarus* 99, 261–272. [https://doi.org/10.1016/0019-1035\(92\)90145-W](https://doi.org/10.1016/0019-1035(92)90145-W)
- Stern, S.A., Bagenal, F., Ennico, K., Gladstone, G.R., Grundy, W.M., McKinnon, W.B., Moore, J.M., Olkin, C.B., Spencer, J.R., Weaver, H.A., Young, L.A., Andert, T., Andrews, J., Banks, M., Bauer, B., Bauman, J., Barnouin, O.S., Bedini, P., Beisser, K., Beyer, R.A., Bhaskaran, S., Binzel, R.P., Birath, E., Bird, M., Bogan, D.J., Bowman, A., Bray, V.J., Brozovic, M., Bryan, C., Buckley, M.R., Buie, M.W., Buratti, B.J., Bushman, S.S., Calloway, A., Carcich, B., Cheng, A.F., Conard, S., Conrad, C.A., Cook, J.C., Cruikshank, D.P., Custodio, O.S., Ore, C.M.D., Deboy, C., Dischner, Z.J.B., Dumont, P., Earle, A.M., Elliott, H.A., Ercol, J., Ernst, C.M., Finley, T., Flanigan, S.H., Fountain, G., Freeze, M.J., Greathouse, T., Green, J.L., Guo, Y., Hahn, M., Hamilton, D.P., Hamilton, S.A., Hanley, J., Harch, A., Hart, H.M., Hersman,

- C.B., Hill, A., Hill, M.E., Hinson, D.P., Holdridge, M.E., Horanyi, M., Howard, A.D., Howett, C.J.A., Jackman, C., Jacobson, R.A., Jennings, D.E., Kammer, J.A., Kang, H.K., Kaufmann, D.E., Kollmann, P., Krimigis, S.M., Kusnierkiewicz, D., Lauer, T.R., Lee, J.E., Lindstrom, K.L., Linscott, I.R., Lisse, C.M., Lunsford, A.W., Mallder, V.A., Martin, N., McComas, D.J., McNutt, R.L., Mehoke, D., Mehoke, T., Melin, E.D., Mutchler, M., Nelson, D., Nimmo, F., Nunez, J.I., Ocampo, A., Owen, W.M., Paetzold, M., Page, B., Parker, A.H., Parker, J.W., Pelletier, F., Peterson, J., Pinkine, N., Piquette, M., Porter, S.B., Protopapa, S., Redfern, J., Reitsema, H.J., Reuter, D.C., Roberts, J.H., Robbins, S.J., Rogers, G., Rose, D., Runyon, K., Retherford, K.D., Ryschkewitsch, M.G., Schenk, P., Schindhelm, E., Sepan, B., Showalter, M.R., Singer, K.N., Soluri, M., Stanbridge, D., Steffl, A.J., Strobel, D.F., Stryk, T., Summers, M.E., Szalay, J.R., Tapley, M., Taylor, A., Taylor, H., Throop, H.B., Tsang, C.C.C., Tyler, G.L., Umurhan, O.M., Verbiscer, A.J., Versteeg, M.H., et al., 2015. The Pluto system: Initial results from its exploration by New Horizons. *Science* 350. <https://doi.org/10.1126/science.aad1815>
- Stern, S.A., Colwell, J.E., 1997. Collisional Erosion in the Primordial Edgeworth-Kuiper Belt and the Generation of the 30-50 AU Kuiper Gap. *ApJ* 490, 879. <https://doi.org/10.1086/304912>
- Stern, S.A., Trafton, L.M., 2008. On the Atmospheres of Objects in the Kuiper Belt. *The Solar System Beyond Neptune* 365–380.
- Tegler, S.C., Cornelison, D.M., Grundy, W.M., Romanishin, W., Abernathy, M.R., Bovyn, M.J., Burt, J.A., Evans, D.E., Maleszewski, C.K., Thompson, Z., Vilas, F., 2010. Methane and Nitrogen Abundances on Pluto and Eris. *ApJ* 725, 1296–1305. <https://doi.org/10.1088/0004-637X/725/1/1296>
- Trafton, L.M., Matson, D.L., Stansberry, J.A., 1998. Surface/Atmosphere Interactions and Volatile Transport (Triton, Pluto, and Io), in Schmitt, B., De Bergh, C., Festou, M. (Eds.), *Solar System Ices, Astrophysics and Space Science Library*. Springer Netherlands, Dordrecht, pp. 773–812.
- Wang, J., Bras, R.L., Sivandran, G., Knox, R.G., 2010. A simple method for the estimation of thermal inertia. *Geophysical Research Letters* 37. <https://doi.org/10.1029/2009GL041851>
- Wu, Y.-J., Wu, C.Y.R., Chou, S.-L., Lin, M.-Y., Lu, H.-C., Lo, J.-I., Cheng, B.-M., 2012. Spectra and Photolysis of Pure Nitrogen and Methane Dispersed in Solid Nitrogen with Vacuum-Ultraviolet Light. *ApJ* 746, 175. <https://doi.org/10.1088/0004-637X/746/2/175>
- Young, L.A., Braga-Ribas, F., Johnson, R.E., 2020. Chapter 6 - Volatile evolution and atmospheres of Trans-Neptunian objects, in: Prialnik, D., Barucci, M.A., Young, L.A. (Eds.), *The Trans-Neptunian Solar System*. Elsevier, pp. 127–151. <https://doi.org/10.1016/B978-0-12-816490-7.00006-0>

Chapter 2

Uncertainty in Grain Size Estimations of Volatiles on Trans-Neptunian Objects and Kuiper Belt Objects

A. Emran and V. F. Chevrier

AR Center for Space and Planetary Sciences, University of Arkansas, Fayetteville, AR 72701.

[Published in The Astronomical Journal, 163:196, 2022]

Abstract

We analyze the uncertainty in grain size estimation of pure methane (CH_4) and nitrogen saturated with methane ($\text{N}_2:\text{CH}_4$) ices, the most abundant volatile materials on trans-Neptunian objects (TNOs) and Kuiper Belt objects (KBOs). We compare the single scattering albedo, which determines the grain size estimation of outer solar system regolith (Hansen, 2009), of these ices using the Mie scattering model and two other Hapke approximations (Hapke, 1993) in radiative transfer scattering models (RTM) at near-infrared (NIR) wavelengths ($1 - 5 \mu\text{m}$). The equivalent slab (Hapke slab) approximation model predicts results much closer to Mie scattering over the NIR wavelengths at a wide range of grain sizes. In contrast, even though the internal scattering model (ISM) predicts an approximate particle diameter close to the Mie model for particles with $10 \mu\text{m}$ radii, it exhibits higher discrepancies in the predicted estimation for larger grain sizes (e.g., 100 and $1000 \mu\text{m}$ radii). Owing to the Rayleigh effect on single-scattering properties, neither Hapke approximate models could predict an accurate grain size estimation for the small

particles (radii $\leq 5\mu\text{m}$). We recommend that future studies should favor the Hapke slab approximation when employing RTMs for estimating grain sizes of the vast number of TNOs and KBOs in the outer solar system.

Unified Astronomy Thesaurus concepts: Classical Kuiper Belt objects (250); Trans-Neptunian objects (1705); Plutoids (1268); Radiative transfer (1335); Surface ices (2117)

2.1. Introduction

An abundance of methane (CH_4) and nitrogen (N_2) ices, among others, have been detected on trans-Neptunian objects (TNOs) and Kuiper Belt objects (KBOs) such as Triton (Cruikshank et al., 1984, 1993) and Pluto (Owen et al., 1993). Eris, a dwarf planet in the Kuiper Belt, also exhibits a prevalence of N_2 and CH_4 ices on its surface (Dumas et al., 2007). Of these ices, solid CH_4 ice has several strong absorption bands in near-infrared (NIR) wavelengths (Cruikshank et al., 2019). The physical and chemical properties of these ices on TNOs and KBOs have been determined from spectral observations using the radiative transfer models (RTMs; e.g., Grundy and Fink, 1991; Dumas et al., 2007; Merlin et al., 2010; Tegler et al., 2010). The RTMs enable the estimation of abundances and grain size of the constituent mixtures based on albedo or reflectance of single scattered light by an average surface grain (e.g., Mustard and Glotch, 2019). For instance, Protopapa et al. (2017) estimated the global scale spatial abundance and grain size distribution of ices (both volatile and non-volatile) on Pluto from Ralph/LEISA infrared spectrometer (Reuter et al., 2008) onboard New Horizons using Hapke modeling (1993).

Varied results have been reported in grain size estimation of water ice at outer solar system icy bodies using different scattering models (Hansen, 2009). Thus, it is reasonable to anticipate that the estimation of grain sizes of CH_4 and N_2 ices (pure and mixture) on TNOs and KBOs

surfaces will have inconsistencies owing to the different models used. Hansen (2009) argued that the differences in grain size estimation primarily arise from models used for single scattering albedo calculation rather than bidirectional reflectance models. Following the same approach, we use scattering models to NIR optical constants of CH₄ and N₂ ices (pure and mixture) at temperatures relevant to TNOs and KBOs surface conditions. Single scattering albedo can accurately be calculated using Mie theory (Mie, 1908) for simple geometric grains or can be estimated using Hapke approximation models (1981, 1993) from optical constants of materials. Accordingly, we analyze the single scattering albedo to estimate the inconsistencies in grain sizes using Mie theory and two approximation models from Hapke (1993) that have been widely used in the existing literature.

The constituent ices of TNOs and KBOs surfaces exhibit different thermodynamic phase transitions at surface conditions of the planetary bodies. For instance, the crystalline α (cubic) - β (hexagonal) solid-phase transition of N₂ occurs at 35.6K (Scott, 1976), while CH₄ I - CH₄ II solid-phase transition occurs at ~21K (Prokhvatilov and Yantsevich, 1983). On TNOs and KBOs surfaces, the CH₄ and N₂ ices form solid solutions and do not coexist as pure substances (Cruikshank et al., 2019). CH₄ and N₂ ices are completely miscible in one another and show two different solid solutions such as N₂ diluted in CH₄ (**CH₄:N₂**) and CH₄ diluted in N₂ (**N₂: CH₄**) (Trafton, 2015). In this study, we use the NIR optical constant of pure CH₄-I ice measured at 39K, as a proxy of methane saturated with nitrogen (**CH₄:N₂**), and nitrogen saturated with methane (**N₂:CH₄**) measured at two different temperatures of 35K and 38K.

The rationale of using pure CH₄ ice as the proxy **CH₄:N₂** is that at a temperature of 40K, the marginal saturation limit of N₂ in CH₄ ice is ~0.035 (e.g., Cruikshank et al., 2019). In the **CH₄:N₂** binary system, the wavelength shift of the CH₄ band is very small on the order of ~2 x

10^{-4} μm (Protopapa et al., 2015; cited in Protopapa et al., 2017). Using optical constants of pure CH_4 ice as the proxy of the $\text{CH}_4\text{:N}_2$ system is somewhat valid below 40K (Protopapa et al., 2017) since the saturation limit of N_2 in CH_4 ice is proportional to temperature changes (Prokhvatilov and Yantsevich, 1983). At the 35K temperature, the crystalline α (cubic) phase of N_2 is saturated with the $\text{CH}_4\text{-I}$, while at the 38K, the crystalline β (hexagonal) phase of N_2 is saturated with the $\text{CH}_4\text{-I}$ (Tegler et al., 2010).

2.2. Methods

2.2.1. Single scattering albedo

The single scattering albedo, w , refers to the ratio of the amount of scattered photons to the combined amount of light scattered from and absorbed by a particle:

$$w = \frac{Q_{sca}}{Q_{sca} + Q_{abs}}, \quad (1)$$

where Q_{sca} is the scattering efficiency and Q_{abs} is the absorption efficiency. The sum of Q_{sca} and Q_{abs} is termed extinction efficiency, Q_{ext} . A highly absorbing material likely exhibits a $w = 0$ whereas a transparent material is more likely to show a $w = 1$ (Shepard, 2017).

In most space science applications, the w is assumed to be the average properties, such as optical characteristics, grain size, and to some extent shape and internal structure, of particles that make up planetary regolith (Hapke 1981). The w is a function of optical constants/ indices of refraction (real, n and imaginary, k) of particles or regolith medium (e.g., Mishra et al., 2021 and references therein). A particle with a larger size and moderate to larger k tends to absorb more incident light, and therefore, exhibits a lower w (Shepard and Helfenstein, 2007). A variety of approximate models has been presented by Hapke (1993) to calculate the w from particle

refraction indices (Hansen, 2009). Of these models, the equivalent slab model (Hapke slab) and internal scattering/scatterer model (ISM) are widely used in different planetary bodies (e.g., Li and Li, 2011). Subsequent studies (Hapke, 2001, 2005, 2012) also presented versions of ISM for surface scattering function that was originally derived from Hapke (1981). We use a version of the approximate ISM and the Hapke slab models to calculate w from the optical constants of the ices found on TNOs and KBOs.

2.2.2. Optical constants

The optical constants (OC) of pure CH₄ and N₂:CH₄ were chosen based on the thermodynamic equilibrium of solid methane and nitrogen ices at different temperatures relevant to TNOs and KBOs surface conditions. As the available data permits, we use the optical constants of α -N₂:CH₄ at 35K (1- 3.97 μ m), β -N₂:CH₄ at 38K (1 - 5 μ m), and CH₄ as the proxy of CH₄:N₂ at 39K (1 - 5 μ m). The optical constants of pure CH₄ were collected from Grundy et al. (2002) and the N₂:CH₄ system from Quirico and Schmitt (1992). For detail about the optical constants used in this study see Table 2.1. Note that the α -N₂:CH₄ and β -N₂:CH₄ systems are the solid solutions with a concentration of <2% CH₄ and the absorption coefficient is normalized to a concentration of 1 for the diluted CH₄ in solutions (for detail refer to Quirico and Schmitt 1997).

Table 2.1. Optical constant used in this study.

Materials	Temperature (K)	References ^a	Wavelength range (μ m)	Notes
CH ₄	39	Grundy et al. (2002)	1 - 5	As CH ₄ :N ₂ ^b
N ₂ :CH ₄	35	Quirico et al. (1999); Quirico and Schmitt (1997)	1- 3.97	N ₂ in α phase ^c
N ₂ :CH ₄	38	Quirico et al. (1999); Quirico and Schmitt (1997)	1 - 5	N ₂ in β phase ^d

^a Optical constants are available at <https://www.sshade.eu/>

^b Filename: optcte-Vis+NIR+MIR-CH4cr-I-39K

^c Filename: optcte-NIR-CH4-lowC-alpha-N2-35K

^d Filename: optcte-NIR-CH4-lowC-beta-N2-38K-cor

2.2.3. Mie calculation

The w for particles with simple geometrics (i.e., spherical shape) can exactly be calculated from Maxwell's equations using Mie theory (Mie, 1908) if refractive indices and particle size parameters are known (Moosmüller and Sorensen, 2018). However, scattering models of highly asymmetric phase functions demand the treatment of diffraction effects from Mie w (Hansen, 2009). Thus, we use the δ -Eddington corrected Mie single scattering albedo w' as compared to the estimations of w from Hapke approximations. The δ -Eddington approximated Mie, w' can be calculated as (Wiscombe and Warren, 1980):

$$w' = \frac{(1-\epsilon^2)w}{1-\epsilon^2 w} \quad (2)$$

where ϵ is the asymmetry factor, which refers to the ratio of the forward-scattered light to the back-scattered light, calculated by Mie theory. We employ Mie w calculation following the method described in Wiscombe (1979) using `miepython` routine, a Python module licensed under the terms of the Massachusetts Institute of Technology (MIT) license. The calculated Mie w result was then adjusted to δ -Eddington corrected Mie w' following Eq. 2.

2.2.4. Hapke slab and ISM calculations

The Hapke slab approximation model (Hapke 1981, 1993) is applied if the imaginary part of the optical constant $k \ll 1$ so that w can be approximated as (Hansen, 2009):

$$w = \frac{1}{\alpha DR(n)+1} \quad (3)$$

where D is the “particle diameter” and α is the absorption coefficient, given by:

$$\alpha = \frac{4\pi k}{\lambda} \quad (4)$$

where λ is the wavelength. $R(n)$ is the reflection function of the real part (n) of the OC. The $R(n)$ can be derived as (Hansen, 2009):

$$R(n) = \frac{1-S_e}{1-S_i} \quad (5)$$

where S_e and S_i are the average Fresnel reflection coefficient for externally and internally incident light, respectively (Hapke 1993). For the case of the slab model ($k \ll l$), S_e can be approximated as (Hapke, 2001):

$$S_e = \frac{(n-1)^2}{(n+1)^2} + 0.05 \quad (6)$$

and the approximation for S_i can be written as (Lucey, 1998):

$$S_i = 1.014 - \frac{4}{n(n+1)^2} \quad (7)$$

We use the ISM (Hapke, 1981) as the second approximation method where the w can be reproduced as (Hapke, 2001):

$$w = S_e + (1 - S_e) \frac{(1-S_i)\Theta}{1-S_i\Theta} \quad (8)$$

where Θ is the internal-transmission function of the particle, given by (Hapke, 1993):

$$\Theta = \frac{r + \exp(-\sqrt{\alpha(\alpha+s)}\langle D \rangle)}{1 - r \exp(-\sqrt{\alpha(\alpha+s)}\langle D \rangle)} \quad (9)$$

where the near-surface internal scattering coefficient, $s = 0$, and the internal hemispherical (diffused) reflectance, r can be given as (Hapke, 1981):

$$r = \frac{1 - \sqrt{\alpha(\alpha+s)}}{1 + \sqrt{\alpha(\alpha+s)}} \quad (10)$$

The average distance travel by transmitted ray i.e., mean free path of photon $\langle D \rangle$ as a function of n and particle diameter, D for perfectly spherical particle can be written as (Hapke, 2005):

$$\langle D \rangle = \frac{2}{3} \left(n^2 - \frac{1}{n} (n^2 - 1)^{\frac{3}{2}} \right) D \quad (11)$$

In the ISM model, S_i is derived from Eq. (7) while S_e is a function of both n and k , as given by:

$$S_e = \frac{(n-1)^2 + k^2}{(n+1)^2 + k^2} + 0.05 \quad (12)$$

2.3. Results

2.3.1. Calculated single scattering albedo

To evaluate how the Mie and Hapke models produce different w at a specific particle diameter, we compare w of a 10 μm radius particle for pure CH_4 at 39K, $\alpha\text{-N}_2\text{:CH}_4$ at 35K, and $\beta\text{-N}_2\text{:CH}_4$ at 38K (Fig. 2.1). The calculated w exhibits small spikes over the wavelengths, and therefore we smoothen our calculated w curves by applying the *Savitzky-Golay* filters (Savitzky and Golay, 1964), an algorithm typically used for signal processing, with a 3rd order of the polynomial fit.

The result of w from the Hapke slab and ISM calculated for pure CH_4 ice shows a varying degree of closeness to the result of Mie calculation at different NIR wavelengths (Fig 2.1a).

More specifically, at shorter wavelengths up to 2 μm , both ISM and slab model exactly follow and mimic the results of Mie calculation. However, at wavelengths of 2.13 and 2.37 μm , the slab model results show slightly higher w than the Mie calculation. This indicates that the Hapke slab model predicts a slightly smaller pure CH_4 grain size compared to the Mie model at these wavelengths (Hansen, 2009). The ISM w is closer to the Mie result at longer wavelengths at 3.3 and 3.5 μm -- implying that the grain-size prediction by ISM at these wavelengths is similar to that of Mie's prediction. In contrast, the Hapke slab predicts a smaller and larger pure CH_4 ice grain compared to the Mie results at 3.3 and 3.5 μm , respectively. At 3.82 μm , both approximation models predicate a slightly higher grain size than the Mie results.

The $\text{N}_2:\text{CH}_4$ system results (Fig. 2.1b and 2.1c) show that the Hapke slab model, overall, produces w values much closer to the Mie model than ISM at both 35 and 38K temperatures, except at $\sim 3.3\mu\text{m}$ wavelength for 38K where the ISM's w gets closer to Mie. In the $\alpha\text{-N}_2:\text{CH}_4$ ice (Fig. 2.1b), the w calculated from the Hapke slab model is much closer to the Mie model while ISM predicted a much higher w than Mie calculations over the entire NIR wavelengths. This indicates a much smaller $\alpha\text{-N}_2:\text{CH}_4$ ice grain-size prediction by ISM. Likewise, in the case of the $\beta\text{-N}_2:\text{CH}_4$ system (Fig. 2.1c), the slab model result follows much closer to the Mie result over the wavelengths, except for the 3.3 μm where ISM gets closer to Mie than the slab result. This implies that the Hapke slab model produces a slightly smaller grain size around 2.3, 3.3, and 3.5 μm at 35K and 2.3 and 3.5 μm at 38K than the Mie model. Around the wavelength of 3.3 μm at 38K, the ISM predicts a slightly smaller grain size than the Mie compared to the Hapke slab to Mie. Overall, for the $\text{N}_2:\text{CH}_4$ systems, ISM predicts a much smaller grain size than the Mie compared to the slab model to Mie over the NIR wavelengths for the particles with 10 μm radii.

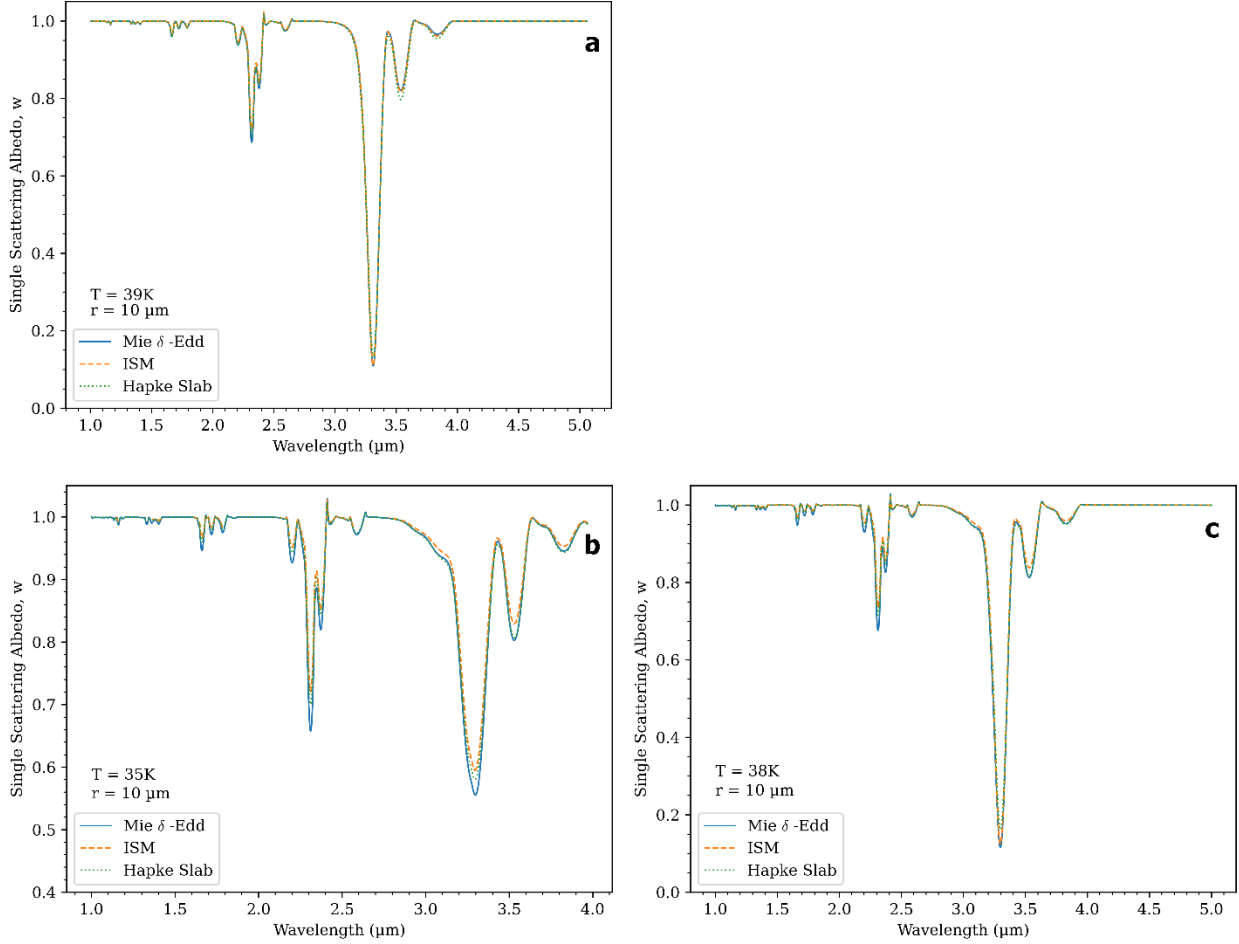


Fig. 2.1: Plots for single scattering albedo of pure CH_4 at 39K (a), $\alpha\text{-N}_2:\text{CH}_4$ at 35K (b), and $\beta\text{-N}_2:\text{CH}_4$ at 38K (c) for a grain $10\ \mu\text{m}$ radius. The dashed solid line presents δ -Eddington corrected Mie, the dashed yellow represents ISM, and the dotted green represents Hapke slab results. The plots were smoothed using the *Savitzky-Golay* filter (Savitzky and Golay, 1964).

2.3.2. Discrepancies in grain size estimation

We compare the relative grain size predicted by the approximated Hapke models to the Mie model over the NIR wavelengths. To end that, we first estimate the δ -Eddington corrected Mie w' at grain radii of 1, 10, 100, and 1000 μm . Then we estimate the grain sizes corresponding to these Mie w' values by applying the inverse ISM and Hapke slab models. The w is a non-linear function of diameter (D) in both Hapke approximation models (Eq. 3 and 8). We solve the non-linear equations of the Hapke slab and ISM for D using Powell's hybrid (dogleg) method

(Powell, 1970; Chen and Stadtherr, 1981). Lastly, we estimate the relative discrepancies in grain size determination by normalizing the estimated grain sizes from the Hapke slab and ISM models to the Mie grain size for pure CH₄, α -N₂:CH₄, and β -N₂:CH₄ (Fig. 2.2). In summary, we calculate the single scattering albedos at fixed grain sizes for NIR wavelengths using Mie theory and then determine the corresponding grain sizes from the approximation models to fit the Mie spectra.

For pure CH₄ ice, the Hapke slab model (Fig. 2.2a) better predicts the grain sizes than the ISM model (Fig. 2.2b). Overall, the predicted grain sizes by the Hapke slab model are within ~20% of the grain size of Mie, whereas the discrepancies in the predicted grain sizes by the ISM model are much higher. However, around the 3.3 μ m region, neither model did predict grain sizes very well to Mie's results. Even though the slab model can predict twice as much as the Mie results at some wavelengths, for instance, at around 2.3~2.4 μ m region for larger grain sizes (e.g., 1000 μ m radii), the ISM predicated results still show much more discrepancies than slab model results at these wavelengths. The continuous rise of the 1 μ m curve is due to largely the Rayleigh effect (Hansen, 2009) from the Mie model that the Hapke slab method does not model. Likewise, the Rayleigh effect on single-scattering properties is not modeled by the ISM. Both Hake slab and ISM provide a better prediction at 10 μ m grain size, within ~30% of the grain size of Mie. However, larger grain-sized were not modeled very well by the ISM and predicted the grain sizes that are many times the grain size of Mie (Fig. 2.2b).

The N₂:CH₄ system results (Fig. 2.2c, d for 35K and Fig. 2.2e, f for 38K) show that, overall, the Hapke slab model has better a prediction, and thus lower discrepancies in grain size estimation to the Mie model than the ISM model. Owing to the Rayleigh effect on single-scattering properties modeled by Mie theory (Hansen, 2009) but not by either of the approximation models for smaller grain sizes (e.g., 1 μ m), there is a trend of continuously

increasing discrepancies in grain sizes estimation by both Hapke slab and ISM. Similar to the case of CH₄ ice, both Hapke slab and ISM models fit best at 10 μm, where it is within ~30% of the Mie result, for the α-N₂:CH₄ and β-N₂:CH₄ ices. For larger grain radii (e.g., 100 and 1000 μm) the Hapke slab exhibits comparatively lower discrepancies than ISM results and predicted grain sizes within the twice of the Mie over most of the NIR wavelengths, except at 3.3μm for both temperatures. In contrast, though ISM models a good fit at 10 μm, the larger particles (e.g., 100 and 1000 μm) exhibit higher degrees of discrepancies compared to the Hapke slab results to Mie. This characteristic result from the N₂:CH₄ system is also consistent with the result for water ice grain sizes of Enceladus (Hansen, 2009).

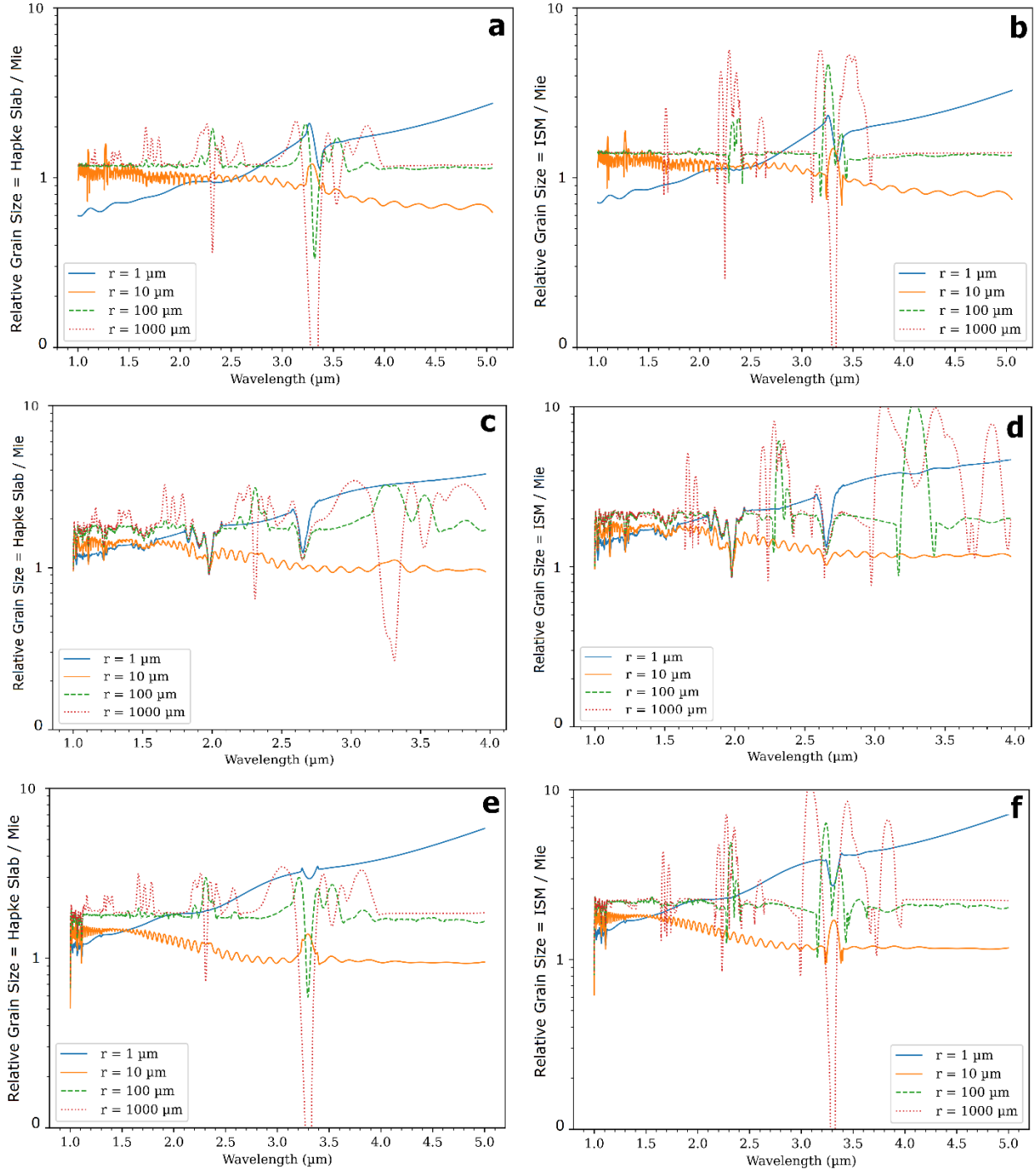


Fig. 2.2: Grain sizes determined from the Hapke slab (left column) and ISM (right column) using spectra calculated using the Mie model at different particle radii of 1, 10, 100, 1000 μm for pure CH_4 ice at 39K (top row), $\alpha\text{-N}_2\text{:CH}_4$ at 35K (middle row), and $\beta\text{-N}_2\text{:CH}_4$ at 38K (bottom row). The resulting grain sizes are normalized to the input grain sizes. The plots were smoothed using the *Savitzky-Golay* filter (Savitzky and Golay, 1964).

2.3.3. Effect of the absorption coefficient

The distribution of absorption coefficients (α) of pure CH₄ and CH₄ saturated with N₂ ices over the NIR wavelength region is given in Fig. 2.3. Absorption coefficients of pure CH₄ show a peak around the 3.3 μm wavelength (Fig. 2.3a). Though absorption coefficients are quite similar for N₂:CH₄ systems both 35 and 38K, at the latter temperature (Fig. 2.3c), absorption coefficients at around 3.3 μm wavelength are much higher than the former temperature (Fig. 2.3b). Pure CH₄ and β -N₂:CH₄ ice show a similar higher absorption coefficient at 3.3 μm wavelength. The anomalies in grain size prediction of larger particles by the Hapke slab method for pure CH₄ and β -N₂:CH₄ at 3.3 μm are, perhaps, due to the larger k value at this NIR wavelength region.

The absorption coefficient peaks at 3.3 μm at 38K and 39K are consistent with the fact of lower single scattering albedo or higher absorption. This is also evident in the relative grain-size curve for 10 μm , the best grain-size prediction by the Hapke approximated models. The grain-size curves at 38K (Fig. 2.2a, b) and 39K (Fig. 2.2e, f) follow a continuum over the NIR wavelengths except for a “dome” in the 3.3 μm region – indicating a predicted larger grain size corresponding to higher absorption. We compare α from our result to that of water (H₂O) ices in outer solar system bodies as given in Fig. 4 of Hansen (2009). Water ice has a higher absorption coefficient in most NIR wavelength regions compared to both pure CH₄ and N₂:CH₄ systems. This implies that pure CH₄ and N₂:CH₄ ice grains have higher reflectance and lower absorption compared to water ice grains over the NIR wavelengths. One possible interpretation of this comparison is that grain size estimation of H₂O ice using the Hapke approximation models may predict relatively larger grains (particularly at the wavelengths with higher α values) compared to pure CH₄ and N₂:CH₄ ices grains at the outer solar systems bodies. However, this interpretation

is based on the distribution of absorption coefficient over NIR wavelengths, while other factors are involved, different interpretations are also plausible.

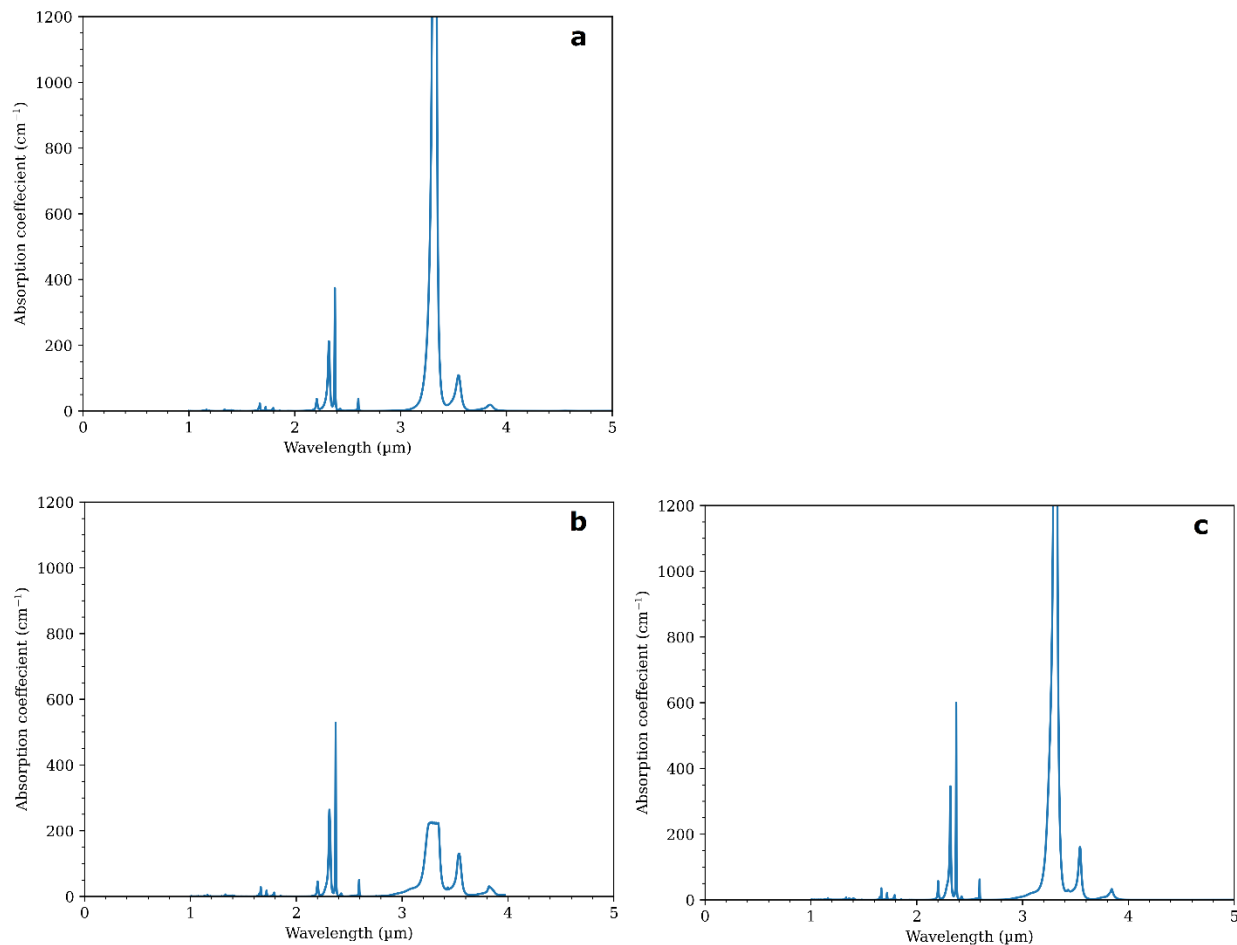


Fig. 2.3: Absorption coefficient of pure CH₄ ice at 39K (a), CH₄ saturated with α-N₂ ice at 35K (b), and CH₄ saturated with β-N₂ ice at 38K (c). Pure CH₄ has an absorption coefficient peak at 3.3 μm. The absorption coefficient is much higher over the wavelength around 3.3 μm at 38K compared to 35K for CH₄ saturated with N₂ ices.

2.3.4. The interplay between albedo, absorption coefficient, and grain size

We analyze characteristic distribution w as a function of α for Mie, ISM, and Hapke slab models. The w verses α for pure CH₄ (left column), α -N₂:CH₄ (middle column), and β -N₂:CH₄ (right column), ices at different grain radii (in rows) are given in Fig. 2.4. In 1 μ m gain size graphs (upper row of Fig. 2.4), the Mie calculation follows two different paths, and their separation is largely due to the Rayleigh scattering effect at smaller grain-sized particles (Hansen, 2009). At all temperatures, each approximation model follows a relatively linear path while one of the Mie paths shows a slightly exponential fall of albedo for pure CH₄ and β -N₂:CH₄ ices plots. In the N₂:CH₄ systems, the Hapke slab and ISM models follow a relatively similar path. However, one of the routes of Mie plots follows closely to the Hapke slab and ISM plots for pure CH₄. Most of the weakly absorbing points with higher single-scattering albedos are located below the absorption coefficient of $\sim 0.07\mu\text{m}^{-1}$ in pure CH₄ and β -N₂:CH₄ ices, whereas below $0.03\mu\text{m}^{-1}$ in α -N₂:CH₄ ice.

There is an exponential drop in the single scattering plots for 10 μ m graphs at all temperatures and thermodynamics ice phases of methane and nitrogen (2nd row of Fig. 2.4). The Rayleigh scattering effect (i.e., two separate routes of Mie plots) is also evident here, but in the weakly separated routes. The plots of the Hapke slab and ISM approximate models follow along (similar trend) one of the Mie paths for all thermodynamic pure and mixture ice phases – indicating a close fit of these approximates models to Mie result at this grain size. There are few points beyond the absorption coefficient of $0.07\mu\text{m}^{-1}$, that we consider roughly the exponential breakpoint, for pure CH₄ and β -N₂:CH₄, whereas this breakpoint is $\sim 0.03\mu\text{m}^{-1}$ for α -N₂:CH₄.

For the 100 μ m plots (3rd row of Fig. 2.4), there is a steep decline of the plots for all phases. Neither of the approximation models consistently follows the Mie route; at some absorption

coefficient values, ISM gets closer to Mie while at other points Hapke slab model closely follows the Mie path. The breakpoint of the steeply declined plots is roughly around $0.01 \mu\text{m}^{-1}$ and most of the absorption points reside below this threshold where single scattering albedo value varies in a wide range (e.g., $w = 0.1 - 1.0$). In the $1000 \mu\text{m}$ plots (lower row of Fig. 2.4), the single scattering albedo plots more steeply decline at all thermodynamics ice phases of methane and nitrogen. However, the breakpoint of the albedo plots is $< 0.01 \mu\text{m}^{-1}$, meaning the single scattering albedo steeply falls at a lower absorption coefficient for larger grain sizes. Similar to the $100 \mu\text{m}$ plots, in $1000 \mu\text{m}$ plots neither of the approximation models consistently follows the Mie route.

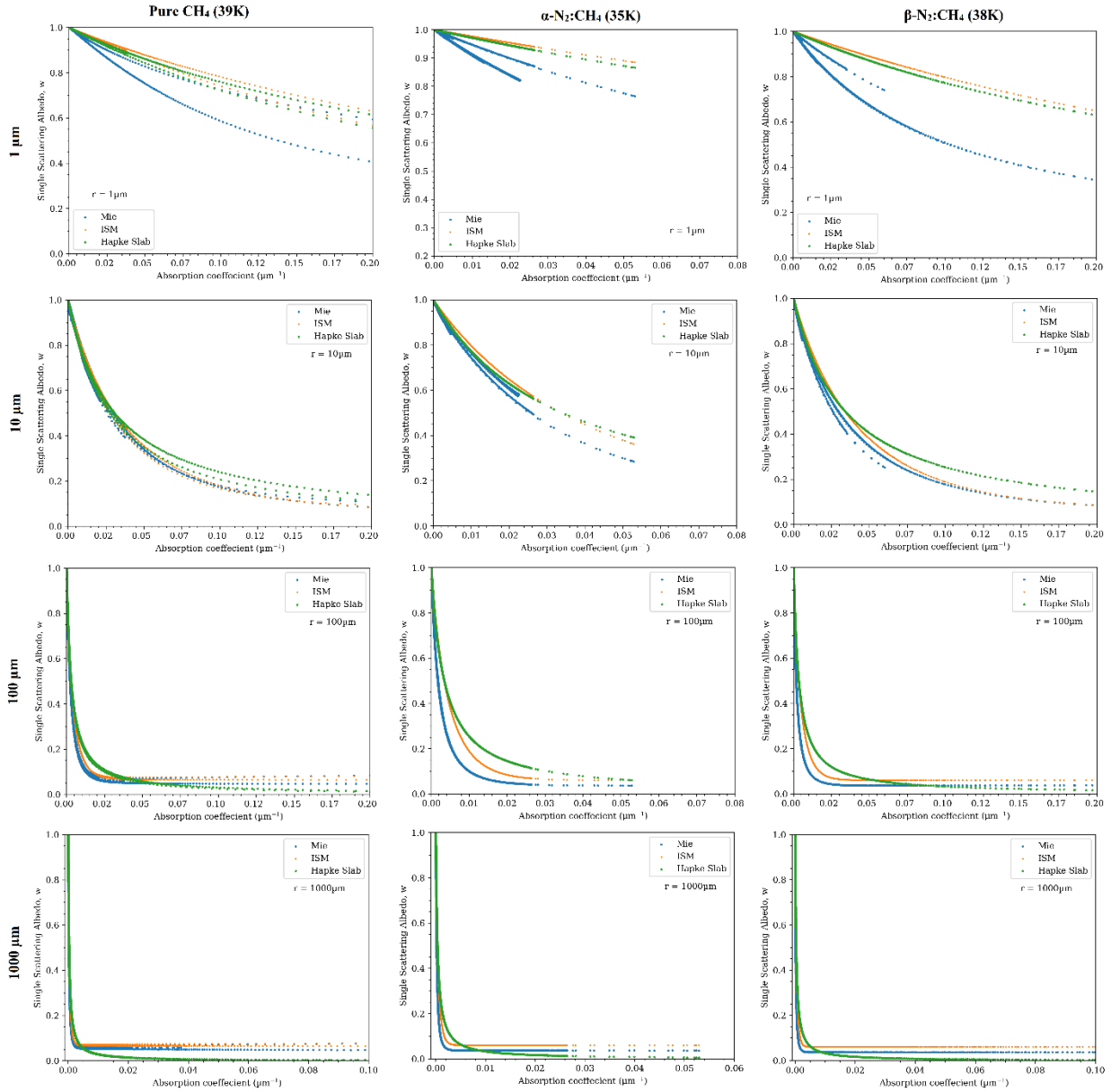


Fig. 2.4: Plot of the single scattering albedo against absorption coefficient for pure CH₄ ice particle at 39K (left column), α-N₂:CH₄ particle at 35K (middle column), and β-N₂:CH₄ particle at 38K (right column). The subplots show the distribution of w at grain radii at 1 μm (upper row), 10 μm (2nd row), 100 μm (3rd row), and 1000 μm (bottom row). In all subplots, the scattering albedo from the Mie calculation (blue), ISM (yellow), and Hapke slab (green). The Mie calculation follows two different paths due to the Rayleigh scattering effect at lower grain-size particles.

2.4. Discussion and conclusion

Amidst inconsistent results in the grain size estimation of water ice on outer solar system bodies (Hansen, 2009), we analyze the relative differences of grain size estimation for pure CH₄ and N₂:CH₄ ices relevant to TNOs and KBOs. We calculate the single scattering albedo using Mie and two other Hapke approximations models for these ices at NIR wavelengths (1 - 5 μm). Accordingly, we assess the discrepancies in the relative grain sizes predictions by the Hapke approximation models to the Mie theory over a finely spaced range of grain sizes (1, 10, 100, 1000 μm). This range (micron to millimeter) covers a wide variety of grain sizes on TNOs. For instance, on Triton, the model reported a lower limit of mean grain sizes of methane ices to be 20 μm while the CH₄ grain sizes were expected to be much larger to an order of 100 μm (Grundy and Fink, 1991; Quirico et al., 1999). Moreover, the use of a 1 μm grain size facilitates in evaluating Rayleigh's effects on single scattering albedo that happens at grains that have sizes close to wavelengths.

Compared to ISM, the Hapke slab approximation model predicts much closer results to Mie scattering results. In pure CH₄ ice, the overall estimated grain size differences between the Hapke slab and ISM are about 10% for the particles with different grain radii, except in the case of larger particles and longer wavelengths where the imaginary part of the refractive index is much larger. Similarly, in N₂:CH₄ systems, the average differences between the estimated grain sizes from Hapke slab and ISM are around ~20% for wide ranges of grain size. Both Hapke slab and ISM were found to be appropriate models for a grain size radius of 10 μm. For smaller grain-sized particles (radii of ≤5μm), neither approximate model predicts an accurate grain size due to the Rayleigh effect. For larger grains at longer wavelengths, particularly at wavelengths with higher absorption coefficient values, the ISM predicted grain sizes exhibit larger anomalies

compared to the Mie result. Overall, the results estimated prediction at different grain sizes indicate that the Hapke slab model is the more well-predicted model to the Mie result over the NIR optical constants of pure CH₄ and N₂:CH₄ systems while ISM's predictions show higher discrepancies. Existing literature indicates that the discrepancy in grain-size determination for larger particles at longer wavelengths using the ISM can be mitigated by fine-tuning the value of free parameters. For instance, Roush et al. (2007) used an increased value of s in their Eq. (2) and (3) from 10^{-17} to 1.25 cm^{-1} to fit the modeled spectrum of gypsum power to the measured spectrum (Hansen, 2009).

The particle diameter in the Hapke slab model is associated with a scaling factor that varies from $3/4$ to $4/3$ (Hansen, 2009). In ISM, similar uncertainty in selecting the mean free path of photon ($\langle D \rangle$) by using different scale factors to effective grain size D . For instance, for spherical particles, $\langle D \rangle$ can be approximated to $\cong 0.9D$ (Hapke, 2012), $2D/3$ (Melamed, 1963), etc., while for irregular particles $\langle D \rangle = 0.2D$ (Shkuratov and Grynko, 2005). This study uses a scale factor of 1 in the Hapke slab model. We use the mean free path of photon ($\langle D \rangle$) calculated from effective grain size (D) and the real part (n) of the refractive index using Eq. (12). The Hapke slab and IMS can, therefore, be improved by fine-tuning the scale factors to the approximate models. The slab model accounts for only n while the ISM considers both the n and k parts of the refractive indices in the calculation of the average Fresnel reflection coefficients. If the internal scattering coefficient, s is set to 0, the internal hemispherical (diffused) reflectance, r equals 0. However, the relationship between the internal scattering coefficient (s) and effective particle diameter (D) has also been expressed as $s = 1/D$ (Sharkey et al., 2019). This relationship also defines that the number of scattering events within a single grain is set to 1. Consequently, this relationship indicates that the value of s cannot be 0.

The application of the scattering (and absorption) properties of Mie spheres has been shown to be satisfactory for varied non-spherical particle shapes (e.g., Grenfell and Warren, 1999; Neshyba et al., 2003; Grenfell et al., 2005). The Mie formulation accurately predicts the scattering properties of equivalent spheres of particles, even it can produce satisfactory scattering results for irregular particles (e.g., Neshyba et al., 2003). Thus, the size of spherical particles from the Mie model can somewhat be analogous to non-spherical particles (Hansen, 2009). Moreover, the Mie scattering formulation properly accounts for the Rayleigh effects of scattering properties for smaller particle sizes that are ignored by the Hapke approximation models. Therefore, based on our results, we recommend using the Mie calculation for radiative transfer modeling to unknown spectra of TNOs and KBOs. Our results show that the Hapke slab approximation model, overall, well predicts the grain size to the Mie model over the NIR wavelengths. Thus, if the Hapke approximation models are to choose, we suggest using the equivalent slab model over the internal scattering model in estimating the pure CH₄ and N₂:CH₄ ice grain sizes on trans-Neptunian objects and Kuiper Belt objects. Note that the information of single scattering albedo may not readily be available in orbital measurements. Radiance or reflectance is the typically available measurement in orbital spacecraft data. However, radiance and/or reflectance measured by orbital instruments can easily be converted to a single scattering albedo using the radiative transfer model of Hapke (1993). Our study provides a guideline for the future application of RTM in estimating ice grain sizes at TNOs and KBOs.

2.5. APPENDIX

A. Notation

List of notations and symbols used in this paper

$\langle D \rangle$	mean free path of a photon
D	particle diameter
ξ	asymmetry parameters of Mie theory
k	imaginary part of the refractive index
n	real part of the refractive index
r	internal diffused reflectance
$R(n)$	reflection function
s	internal scattering coefficient
S_e	Fresnel reflection coefficient for externally incident light,
S_i	Fresnel reflection coefficient for internally incident light,
w	single scattering albedo
w'	δ -Eddington Mie single scattering albedo
α	absorption coefficient
λ	wavelength
Θ	internal transmission coefficient

2.6. Acknowledgments

The authors would like to thank anonymous reviewers for their useful comments.

2.7. References

- Chen, H.-S., Stadtherr, M.A., 1981. A modification of Powell's dogleg method for solving systems of nonlinear equations. *Computers & Chemical Engineering* 5, 143–150. [https://doi.org/10.1016/0098-1354\(81\)85003-X](https://doi.org/10.1016/0098-1354(81)85003-X)
- Cruikshank, D.P., Grundy, W.M., Jennings, D.E., Olkin, C.B., Protopapa, S., Reuter, D.C., Schmitt, B., Stern, S.A., 2019. Spectroscopy of Pluto and Its Satellites, in: Bell III, J.F., Bishop, J.L., Moersch, J.E. (Eds.), *Remote Compositional Analysis: Techniques for Understanding Spectroscopy, Mineralogy, and Geochemistry of Planetary Surfaces*, Cambridge Planetary Science. Cambridge University Press, Cambridge, pp. 442–452. <https://doi.org/10.1017/9781316888872.024>
- Cruikshank, D.P., Hamilton Brown, R., Clark, R.N., 1984. Nitrogen on Triton. *Icarus* 58, 293–305. [https://doi.org/10.1016/0019-1035\(84\)90046-0](https://doi.org/10.1016/0019-1035(84)90046-0)
- Cruikshank, D.P., Roush, T.L., Owen, T.C., Geballe, T.R., Bergh, C. de, Schmitt, B., Brown, R.H., Bartholomew, M.J., 1993. Ices on the Surface of Triton. *Science* 261, 742–745. <https://doi.org/10.1126/science.261.5122.742>
- Dumas, C., Merlin, F., Barucci, M.A., Bergh, C. de, Hainault, O., Guilbert, A., Vernazza, P., Doressoundiram, A., 2007. Surface composition of the largest dwarf planet 136199 Eris (2003 UB). *A&A* 471, 331–334. <https://doi.org/10.1051/0004-6361:20066665>
- Grenfell, T.C., Neshyba, S.P., Warren, S.G., 2005. Representation of a nonspherical ice particle by a collection of independent spheres for scattering and absorption of radiation: 3. Hollow columns and plates. *Journal of Geophysical Research: Atmospheres* 110. <https://doi.org/10.1029/2005JD005811>
- Grenfell, T.C., Warren, S.G., 1999. Representation of a nonspherical ice particle by a collection of independent spheres for scattering and absorption of radiation. *Journal of Geophysical Research: Atmospheres* 104, 31697–31709. <https://doi.org/10.1029/1999JD900496>
- Grundy, W.M., Fink, U., 1991. A new spectrum of Triton near the time of the Voyager encounter. *Icarus* 93, 379–385. [https://doi.org/10.1016/0019-1035\(91\)90220-N](https://doi.org/10.1016/0019-1035(91)90220-N)
- Grundy, W.M., Schmitt, B., Quirico, E., 2002. The Temperature-Dependent Spectrum of Methane Ice I between 0.7 and 5 μm and Opportunities for Near-Infrared Remote Thermometry. *Icarus* 155, 486–496. <https://doi.org/10.1006/icar.2001.6726>
- Hansen, G.B., 2009. Calculation of single-scattering albedos: Comparison of Mie results with Hapke approximations. *Icarus* 203, 672–676. <https://doi.org/10.1016/j.icarus.2009.05.025>
- Hapke, B., 1981. Bidirectional reflectance spectroscopy: 1. Theory. *Journal of Geophysical Research: Solid Earth* 86, 3039–3054. <https://doi.org/10.1029/JB086iB04p03039>

- Hapke, B., 1993. *Theory of Reflectance and Emittance Spectroscopy*, Topics in Remote Sensing. Cambridge University Press, Cambridge. <https://doi.org/10.1017/CBO9780511524998>
- Hapke, B., 2001. Space weathering from Mercury to the asteroid belt. *Journal of Geophysical Research: Planets* 106, 10039–10073. <https://doi.org/10.1029/2000JE001338>
- Hapke, B., 2005. *Theory of Reflectance and Emittance Spectroscopy*, Cambridge University Press, Cambridge.
- Hapke, B., 2012. *Theory of Reflectance and Emittance Spectroscopy*, 2nd ed. Cambridge University Press, Cambridge. <https://doi.org/10.1017/CBO9781139025683>
- Li, S., Li, L., 2011. Radiative transfer modeling for quantifying lunar surface minerals, particle size, and submicroscopic metallic Fe. *Journal of Geophysical Research: Planets* 116. <https://doi.org/10.1029/2011JE003837>
- Lucey, P.G., 1998. Model near-infrared optical constants of olivine and pyroxene as a function of iron content. *Journal of Geophysical Research: Planets* 103, 1703–1713. <https://doi.org/10.1029/97JE03145>
- Melamed, N.T., 1963. Optical Properties of Powders. Part I. Optical Absorption Coefficients and the Absolute Value of the Diffuse Reflectance. Part II. Properties of Luminescent Powders. *Journal of Applied Physics* 34, 560–570. <https://doi.org/10.1063/1.1729309>
- Merlin, F., Barucci, M.A., de Bergh, C., Fornasier, S., Doressoundiram, A., Perna, D., Protopapa, S., 2010. Surface composition and physical properties of several trans-neptunian objects from the Hapke scattering theory and Shkuratov model. *Icarus* 208, 945–954. <https://doi.org/10.1016/j.icarus.2010.03.014>
- Mie, G., 1908. Beiträge zur Optik trüber Medien, speziell kolloidaler Metallösungen. *Annalen der Physik* 330, 377–445. <https://doi.org/10.1002/andp.19083300302>
- Mishra, I., Lewis, N., Lunine, J., Helfenstein, P., MacDonald, R.J., Filacchione, G., Ciarniello, M., 2021. Bayesian analysis of Juno/JIRAM's NIR observations of Europa. *Icarus* 357, 114215. <https://doi.org/10.1016/j.icarus.2020.114215>
- Moosmüller, H., Sorensen, C.M., 2018. Single scattering albedo of homogeneous, spherical particles in the transition regime. *Journal of Quantitative Spectroscopy and Radiative Transfer* 219, 333–338. <https://doi.org/10.1016/j.jqsrt.2018.08.015>
- Mustard, J.F., Glotch, T.D., 2019. *Theory of Reflectance and Emittance Spectroscopy of Geologic Materials in the Visible and Infrared Regions*, in: Bell III, J.F., Bishop, J.L., Moersch, J.E. (Eds.), *Remote Compositional Analysis: Techniques for Understanding Spectroscopy, Mineralogy, and Geochemistry of Planetary Surfaces*, Cambridge Planetary Science. Cambridge University Press, Cambridge, pp. 21–41. <https://doi.org/10.1017/9781316888872.004>

- Neshyba, S.P., Grenfell, T.C., Warren, S.G., 2003. Representation of a nonspherical ice particle by a collection of independent spheres for scattering and absorption of radiation: 2. Hexagonal columns and plates. *Journal of Geophysical Research: Atmospheres* 108. <https://doi.org/10.1029/2002JD003302>
- Owen, T.C., Roush, T.L., Cruikshank, D.P., Elliot, J.L., Young, L.A., Bergh, C. de, Schmitt, B., Geballe, T.R., Brown, R.H., Bartholomew, M.J., 1993. Surface Ices and the Atmospheric Composition of Pluto. *Science* 261, 745–748. <https://doi.org/10.1126/science.261.5122.745>
- Powell, M.J.D., 1970. A hybrid method for nonlinear equations. *Numerical Methods for Nonlinear Algebraic Equations* p 87-114
- Prokhvatilov, A.I., Yantsevich, L.D., 1983. X-ray investigation of the equilibrium phase diagram of CH₄-N₂ solid mixtures. *Sov. J. Low Temp. Phys.* 9, 94–98.
- Protopapa, S., Grundy, W.M., Reuter, D.C., Hamilton, D.P., Dalle Ore, C.M., Cook, J.C., Cruikshank, D.P., Schmitt, B., Philippe, S., Quirico, E., Binzel, R.P., Earle, A.M., Ennico, K., Howett, C.J.A., Lunsford, A.W., Olkin, C.B., Parker, A., Singer, K.N., Stern, A., Verbiscer, A.J., Weaver, H.A., Young, L.A., 2017. Pluto's global surface composition through pixel-by-pixel Hapke modeling of New Horizons Ralph/LEISA data. *Icarus, Special Issue: The Pluto System* 287, 218–228. <https://doi.org/10.1016/j.icarus.2016.11.028>
- Protopapa, S., Grundy, W.M., Tegler, S.C., Bergonio, J.M., 2015. Absorption coefficients of the methane–nitrogen binary ice system: Implications for Pluto. *Icarus* 253, 179–188. <https://doi.org/10.1016/j.icarus.2015.02.027>
- Quirico, E., Douté, S., Schmitt, B., de Bergh, C., Cruikshank, D.P., Owen, T.C., Geballe, T.R., Roush, T.L., 1999. Composition, Physical State, and Distribution of Ices at the Surface of Triton. *Icarus* 139, 159–178. <https://doi.org/10.1006/icar.1999.6111>
- Quirico, E., Schmitt, B., 1992. NIR optical constant spectra of CH₄ in solid solution in alpha and beta-N₂ phases at 5 different temperatures (35K - 43K). SSHADE/GhoSST (OSUG Data Center). Dataset/Spectral Data. https://doi.org/10.26302/SSHADE/EXPERIMENT_BS_20130103_003
- Quirico, E., Schmitt, B., 1997. Near-Infrared Spectroscopy of Simple Hydrocarbons and Carbon Oxides Diluted in Solid N₂ and as Pure Ices: Implications for Triton and Pluto. *Icarus* 127, 354–378. <https://doi.org/10.1006/icar.1996.5663>
- Reuter, D.C., Stern, S.A., Scherrer, J., Jennings, D.E., Baer, J.W., Hanley, J., Hardaway, L., Lunsford, A., McMuldroch, S., Moore, J., Olkin, C., Parizek, R., Reitsma, H., Sabatke, D., Spencer, J., Stone, J., Throop, H., Van Cleve, J., Weigle, G.E., Young, L.A., 2008. Ralph: A Visible/Infrared Imager for the New Horizons Pluto/Kuiper Belt Mission. *Space Sci Rev* 140, 129–154. <https://doi.org/10.1007/s11214-008-9375-7>

- Roush, T.L., Esposito, F., Rossman, G.R., Colangeli, L., 2007. Estimated optical constants of gypsum in the regions of weak absorptions: Application of scattering theories and comparisons to independent measurements. *Journal of Geophysical Research: Planets* 112. <https://doi.org/10.1029/2007JE002920>
- Savitzky, Abraham., Golay, M.J.E., 1964. Smoothing and Differentiation of Data by Simplified Least Squares Procedures. *Anal. Chem.* 36, 1627–1639. <https://doi.org/10.1021/ac60214a047>
- Scott, T.A., 1976. Solid and liquid nitrogen. *Physics Reports* 27, 89–157. [https://doi.org/10.1016/0370-1573\(76\)90032-6](https://doi.org/10.1016/0370-1573(76)90032-6)
- Sharkey, B.N.L., Reddy, V., Sanchez, J.A., Izawa, M.R.M., Emery, J.P., 2019. Compositional Constraints for Lucy Mission Trojan Asteroids via Near-infrared Spectroscopy. *AJ* 158, 204. <https://doi.org/10.3847/1538-3881/ab46c0>
- Shepard, M.K. (Ed.), 2017. The Physical Basis of Photometric Scattering Models, in: *Introduction to Planetary Photometry*. Cambridge University Press, Cambridge, pp. 95–130. <https://doi.org/10.1017/9781316443545.005>
- Shepard, M.K., Helfenstein, P., 2007. A test of the Hapke photometric model. *Journal of Geophysical Research: Planets* 112. <https://doi.org/10.1029/2005JE002625>
- Shkuratov, Y.G., Grynko, Y.S., 2005. Light scattering by media composed of semitransparent particles of different shapes in ray optics approximation: consequences for spectroscopy, photometry, and polarimetry of planetary regoliths. *Icarus, Hapke Symposium* 173, 16–28. <https://doi.org/10.1016/j.icarus.2003.12.022>
- Tegler, S.C., Cornelison, D.M., Grundy, W.M., Romanishin, W., Abernathy, M.R., Bovyn, M.J., Burt, J.A., Evans, D.E., Maleszewski, C.K., Thompson, Z., Vilas, F., 2010. Methane and Nitrogen Abundances on Pluto and Eris. *ApJ* 725, 1296–1305. <https://doi.org/10.1088/0004-637X/725/1/1296>
- Trafton, L.M., 2015. On the state of methane and nitrogen ice on Pluto and Triton: Implications of the binary phase diagram. *Icarus, Special Issue: The Pluto System* 246, 197–205. <https://doi.org/10.1016/j.icarus.2014.05.022>
- Wiscombe, W.J., 1979. Mie scattering calculations: Advances in technique and fast, vector-speed computer codes. Atmospheric Analysis and Prediction Division, National Center for Atmospheric Research.
- Wiscombe, W.J., 1980. Improved Mie scattering algorithms. *Appl. Opt.*, AO 19, 1505–1509. <https://doi.org/10.1364/AO.19.001505>
- Wiscombe, W.J., Warren, S.G., 1980. A Model for the Spectral Albedo of Snow. I: Pure Snow. *Journal of the Atmospheric Sciences* 37, 2712–2733. [https://doi.org/10.1175/1520-0469\(1980\)037<2712:AMFTSA>2.0.CO;2](https://doi.org/10.1175/1520-0469(1980)037<2712:AMFTSA>2.0.CO;2)

Chapter 3

Discrepancy in Grain Size Estimation of H₂O Ice in the Outer Solar System

A. Emran and V. F. Chevrier

Space and Planetary Sciences, University of Arkansas, Fayetteville, AR 72701, USA

[Under review in Res. in Astronomy and Astrophysics]

Abstract

Detection of amorphous and crystalline water (H₂O) ice in the outer solar system bodies has been confirmed over the past decades. Radiative transfer models (RTMs) have been used to estimate the grain sizes of H₂O ice from near-infrared (NIR) wavelengths. However, wide discrepancies in the estimation of grain size have been reported for H₂O ice on Saturnian moons. We assess the discrepancy in grain size estimation of H₂O ice, both amorphous and crystalline phases, in the outer solar system bodies including the trans-Neptunian objects (TNOs) and Kuiper Belt objects (KBOs) using RTMs. Radiative scattering models were implemented to predict the H₂O ice grain sizes at temperatures of 15, 40, 60, and 80 K (amorphous) and 20, 40, 60, and 80 K (crystalline). We compare the single scattering albedos of H₂O ice phases using the Mie theory and two Hapke approximation models – Hapke slab and internal scattering model (ISM) – from the optical constants at NIR wavelengths (1 – 5 μm). This study reveals that the Hapke approximation models predict grain size of the crystalline phase, overall, much better than the amorphous phase at temperatures of 15 – 80 K. However, the Hapke slab model predicts, in general, grain sizes

much closer to that of the Mie model's estimations while ISM predicted grain sizes exhibit a higher uncertainty. We recommend using the Mie model for unknown spectra of outer solar system bodies to estimate H₂O ice grain sizes. When using approximation model for RTMs, we recommend using a Hapke slab approximation model over the internal scattering model. Thus, this study provides a guideline for future research in choosing the appropriate scattering models for estimating H₂O ice grain sizes in the outer solar system using RTMs at NIR wavelengths.

Keywords: Outer Solar System; Classical Kuiper Belt objects; Trans-Neptunian objects; Radiative transfer; Surface ices

3.1. Introduction

Detection of water (H₂O) ice has previously been established on outer solar system bodies (giant planets' rings and their icy moons and dwarf planets), cometary bodies (originates from the Kuiper Belt and Oort cloud), and interstellar medium (see Kofman et al., 2019 for an exhaustive list of references). Solid H₂O ice in the solar system may appear as crystalline, amorphous, or both based on temperature, radiation history, and formation temperature and pressure conditions (Schmitt et al., 1998; Cruikshank et al., 1998; Mastrapa et al., 2008). Though amorphous water ice (microporous amorphous phase) is considered the most abundant form of H₂O in the universe (Baragiola, 2003), the crystalline phase has also been spotted in many outer solar system bodies.

Phases of amorphous and crystalline H₂O ice were investigated on the Galilean moons of Jupiter using data from the NIMS instrument onboard the Galileo spacecraft (Hansen and McCord, 2004). Neptune's moon Triton, a trans-Neptunian object (TNO), is also assumed to host amorphous and crystalline water ice (Cruikshank et al., 2000). Although the presence of

crystalline H₂O ice has been reported on Pluto's surface (Cook et al., 2019), its largest satellite Charon hosts both amorphous and crystalline H₂O phases (Dalle Ore et al., 2018). Molecules of amorphous H₂O ice have been detected on icy dust grains in dense interstellar clouds (e.g., Herbst, 2001). Due to the formation of cometary icy grains in very low temperatures, the water ice within cometesimals is thought to be in an amorphous phase (Raponi et al., 2016).

Observations from different spectral wavelengths are used to study the outer reach of the solar system. Among the wavelengths, the near infrared (NIR, typically 0.8 to 5 μm wavelength) has the most diagnostic bands and therefore has been extensively used for characterizing ices and volatiles on outer solar system bodies (Barucci and Merlin, 2020). The interaction between infrared photons and H₂O ices and their resultant absorption bands and positions are dependent on its crystalline vs amorphous phases and the temperature of the ice (Mastrapa et al., 2009). Thus, the shapes and position of the infrared absorption bands and their variations in response to temperature are considered diagnosing for astronomical ices (Schmitt et al., 1998). At NIR wavelengths, amorphous water ice exhibits different spectral characteristics (i.e., the shape of the absorption bands) above and below the temperature of 70 K (Mastrapa et al., 2008).

Radiative transfer models (RTMs) have been used to characterize the composition of outer solar system bodies such as Kuiper Belt objects (KBOs) and TNOs (e.g., Grundy and Fink, 1991; Dumas et al., 2007; Merlin et al., 2010; Tegler et al., 2010). However, wide discrepancies in the estimation of grain size have been reported for H₂O ice on Saturnian moons such as Enceladus (Hansen, 2009), as well as nitrogen (N₂) and methane (CH₄) ices on TNOs and KBOs using different scattering models (Emran and Chevrier, 2022). These uncertainties are believed to arise due to the use of different single scattering albedo (w) calculations rather than a choice of using bidirectional scattering models (Hansen, 2009). Accordingly, Hansen (2009) compared the single

scattering albedos using the optical constant data of crystalline H₂O ice at 110 K – relevant to Saturnian moons and other icy bodies. However, temperatures at the far reach of the solar system at the trans-Neptunian objects and the Kuiper Belt are much lower, and amorphous ice should dominate these environments. For instance, Pluto has a maximum global temperature of 37.7 K in its current epoch (Earle et al., 2017).

Furthermore, while employing RTMs in the outer solar system bodies, there has been extensive use of optical constants of crystalline and/or amorphous phases of H₂O ice and a variety of scattering models. For instance, Protopapa et al. (2017) used the optical constant of crystalline H₂O ice and employed the equivalent slab model of Hapke (1993) for mapping the spatial distribution and grain size of water ice (along with other ices) on Pluto. For the same planetary body, Cook et al. (2019) used the optical constant of both amorphous and crystalline ices while their scattering model was following the formulations of Roush (1994) and Cruikshank et al. (1998) with some modifications. Because w is the primary cause of discrepancies in the grain size estimation of ices (Hansen, 2009; Emran and Chevrier, 2022), the uncertainty of the grain size estimation of amorphous and crystalline H₂O ice, at temperatures analogous to the outer solar system (i.e., 15 K – 80 K), using different scattering models is warranted.

We assess the uncertainty in predicting the H₂O ice grain sizes at a temperature of 15, 40, 60, and 80 K (amorphous) and 20, 40, 60, and 80 K (crystalline) analogous to the outer solar system bodies including the TNOs and KBOs. The theory of Mie (1908) and approximation models of Hapke (1993) are commonly used methods for calculating the w of a material from its optical constants. Accordingly, we calculate the w of water (amorphous and crystalline) ices by implementing Mie theory and the widely used Hapke approximation models from the optical

constants over the wavelengths between 1 – 5 μm . We follow that up by comparing the relative grain sizes of amorphous and crystalline H_2O ice predicted by the approximation models to the Mie model.

3.2. Methods

3.2.1. Optical constants

We use the NIR optical constants of H_2O ice at a temperature of 15 – 80 K (amorphous phase) and 20 – 80 K (crystalline phase). The optical constants of amorphous and crystalline ice at NIR wavelengths between 1.1 – 2.6 μm were prepared by Mastrapa et al. (2008) and NIR to mid-infrared wavelengths between 2.5 – 22 μm by Mastrapa et al. (2009). A compiled optical constant data for both ice phases over the entire NIR wavelengths (1 – 5 μm) – used in this study – can be found in Mastrapa et al. (2009). Note that the crystalline phase used in this study is assumed to be the cubic ice form – a meta-stable H_2O ice phase (Mastrapa et al., 2009). The cubic and hexagonal crystalline ices exhibit nearly identical spectra at infrared wavelengths (Bertie and Whalley, 1967). Thus, in this study, we do not distinguish cubic vs hexagonal ice, but rather we treat the crystalline phases as a unified entity. We use the cubic ice as the representative of the crystalline ice, and hereafter, we denote the crystalline ice as Ic and amorphous ice as Ia.

We use the optical constant data from Mastrapa et al. (2008, 2009) to maintain consistency across the entire wavelength range since the samples used to determine the parameters were prepared using the same instrumental setup, although there are other sources of optical constants of water ice. For instance, Grundy and Schmitt (1998) prepared the optical constants for monocrystalline (hexagonal) H_2O ice samples between the wavelengths of 0.97 – 2.73 μm at

temperatures of 20 to 270 K. On the other hand, Hudgins et al. (1993) prepared the optical constants of ice Ia between the wavelengths of 2.5 – 20 μm at temperatures of 10 - 120 K.

3.2.2. Single scattering albedo

Photon interaction with a material grain happens at the atomic-molecular level through the process of selective absorption, emission, and scattering (e.g., Shepard, 2017). The sum of scattering and absorption efficiencies of a particle, at a given wavelength, by its physical cross-section is called extinction efficiency, $Q_{ext} = Q_{sc} + Q_{ab}$. The w is the ratio of scattering efficiency and extinction efficiency, $w = Q_{sc} / Q_{ext}$.

For planetary regolith, w is a representative of characteristic surface properties including grain size, optical properties, internal structure, and partly shapes (Hapke, 1981). Consequently, the grain size estimation of the regolith primarily depends on the characteristic value of w by the surface particles (Hansen, 2009). A material's w is a function of optical properties (indices of refraction) of its single grain (e.g., Hapke, 1993; Mustard and Glotch, 2019). Thus, w can be calculated if optical constants – both real (n) and imaginary (k) parts – of the regolith medium are known. Larger particles with moderate to larger k values result in higher absorption of incident light and therefore, are associated with a lower w value (Shepard and Helfenstein, 2007).

Mie scattering theory can accurately estimate the w for a particle with a spherical shape (Mie, 1908). On the other hand, Hapke (1993) formulates a variety of approximation models for the estimation of w from material optical constants. We employ two of these approximation models – the “*espat*” slab (hereafter the Hapke slab or simply slab model; Hapke 1981, 1993) and a

version of the internal scattering model (ISM; Hapke, 1993) – which have widely been used in the RTMs of the outer solar system bodies. Note that the version of the scattering model by Roush (1994) uses, indeed, a formulation of the ISM in the original paper by Hapke (1981) and devised the versions of surface scattering functions (Hansen, 2009).

3.2.3. Mie calculation

The scattering properties of a particle with the simplest three-dimensional geometrics (spheres) can accurately be calculated using the Mie theory by employing Maxwell’s equations (Mie, 1908; Wiscombe 1980). The formulation of the Mie theory accounts for optical constants ($n + ik$) of the particle and the fraction of the particle's size to wavelengths under investigation (Hapke, 1993). However, the treatment of diffraction effects in Mie’s w is required for a scattering model with highly asymmetric phase functions (Hansen, 2009). Thus, in this study we use δ -Eddington corrected (Joseph et al., 1976) Mie single scattering albedo, w' , calculated as (Wiscombe and Warren, 1980):

$$w' = \frac{(1-\xi^2)w}{1-\xi^2 w} \quad (1)$$

where ξ is the asymmetry factor calculated by Mie theory. Following the approach of Emran and Chevrier (2022), the Mie w was calculated by utilizing the method of Wiscombe (1979) using the `miepython` routine (an open-source Python module). The δ -Eddington corrected Mie w' was then adjusted from Mie’s w following Eq. 1.

3.2.4. Hapke approximation models

Using the “*espat*” function or the slab model of Hapke (1981, 1993), the approximate w of an equant particle can be simplified as:

$$w = \frac{1}{\alpha D_e + 1} \quad (2)$$

where α is the absorption coefficient and D_e is the “effective particle size”.

The absorption coefficient is given by:

$$\alpha = \frac{4\pi k}{\lambda} \quad (3)$$

where k is the imaginary part of the optical constant and λ is the wavelength under consideration. The Hapke slab model should be applied for materials with $k \ll 1$ and D_e can be approximated as (Hapke, 1993):

$$D_e = \hat{g} \frac{1-S_e}{1-S_i} D \quad (4)$$

where D is the particle diameter, \hat{g} is a constant (scaling parameter of diameter) which is roughly $\simeq 1$, and S_e and S_i are the average Fresnel reflection coefficient for externally and internally incident light, respectively. The derivations of the approximate equations for the calculation of S_e and S_i are given in Hapke (1993) where k is set to be zero, therefore is not considered, for the slab model. These approximate equations (S_e and S_i) can also be found elsewhere in the literature that uses the Hapke models including the study of Emran and Chevrier (2022). The calculation of w using the ISM can be approximated as (Hapke, 1993):

$$w = S_e + (1 - S_e) \frac{(1-S_i)\Theta}{1-S_i\Theta} \quad (5)$$

where particles’ internal-transmission function, Θ , given by (Hapke, 1993):

$$\Theta = \frac{r + \exp(-\sqrt{\alpha(\alpha+s)}\langle D \rangle)}{1 - r \exp(-\sqrt{\alpha(\alpha+s)}\langle D \rangle)} \quad (6)$$

where s is the near-surface internal scattering coefficient. The mean free path of the photon, $\langle D \rangle$ for a perfectly spherical particle can be approximated as (Hapke, 1993):

$$\langle D \rangle = \frac{2}{3} \left(n^2 - \frac{1}{n} (n^2 - 1)^{\frac{3}{2}} \right) D \quad (7)$$

The internal diffused reflectance inside the particle, r , can be written as (Hapke, 1981):

$$r = \frac{1 - \sqrt{\alpha(\alpha+s)}}{1 + \sqrt{\alpha(\alpha+s)}} \quad (8)$$

If s is set to zero (Lucey, 199), then $r = 0$ and $\Theta = e^{-\alpha\langle D \rangle}$ (e.g., Lawrence and Lucey, 2007; Hansen, 2009; Li and Li, 2011). The list of notations used in this study is given in Appendix (B).

3.3. Results

3.3.1. Calculated single scattering albedo

We compare the w spectra of 10 μm radii Ia and Ic particles to assess the difference in calculated single scattering albedo at that specific diameter using the Mie and Hapke approximation models over the NIR range (Fig. 3.1). Following the approach of Emran and Chevrier (2022), we apply the *Savitzky-Golay* filter (Savitzky and Golay, 1964) to smoothen the small spikes in calculated w curves over the wavelength range. We implement the filter algorithm with a 3rd order polynomial fit. Note that all plots used in this study were smoothened using the *Savitzky-Golay* filter, if not mentioned otherwise.

The w plots from the Hapke approximation models follow the spectra generated by the Mie model with varying degrees of closeness at different NIR wavelengths. In the case of Ia at every investigated temperature (left column in Fig. 3.1), the Hapke slab model provides a much better approximation of the Mie model spectra compared to the ISM spectra, except around the broader 3.0 μm region. At shorter wavelengths up to 2.5 μm , the slab model produces slightly higher w values than the Mie model, notably around the weak overtones at 1.5 and 2.0 μm at every investigated temperature. This represents a prediction of a slightly smaller H₂O grain size by the slab model compared to the Mie model (Hansen, 2009) over the shorter wavelengths.

The w spectra of Ia at the broader 4.5 μm absorption band show that the slab model either exactly reproduces the Mie spectra (at 15K) or renders slightly higher w values than the Mie spectra (at 40, 60, and 80K). This indicates that the slab model predicts identical or slightly smaller grain sizes than Mie's prediction. In contrast, at every temperature, the ISM renders much lower w than the Mie spectra at the 4.5 μm band – indicating a larger grain size prediction by the ISM. At the wavelengths around 3.5 and 5 μm , both approximation models show smaller w values than the Mie model – meaning a larger grain size prediction by the approximation models at these bands. However, the grain size prediction by the approximation models is much larger at 5 μm than the 3.5 μm .

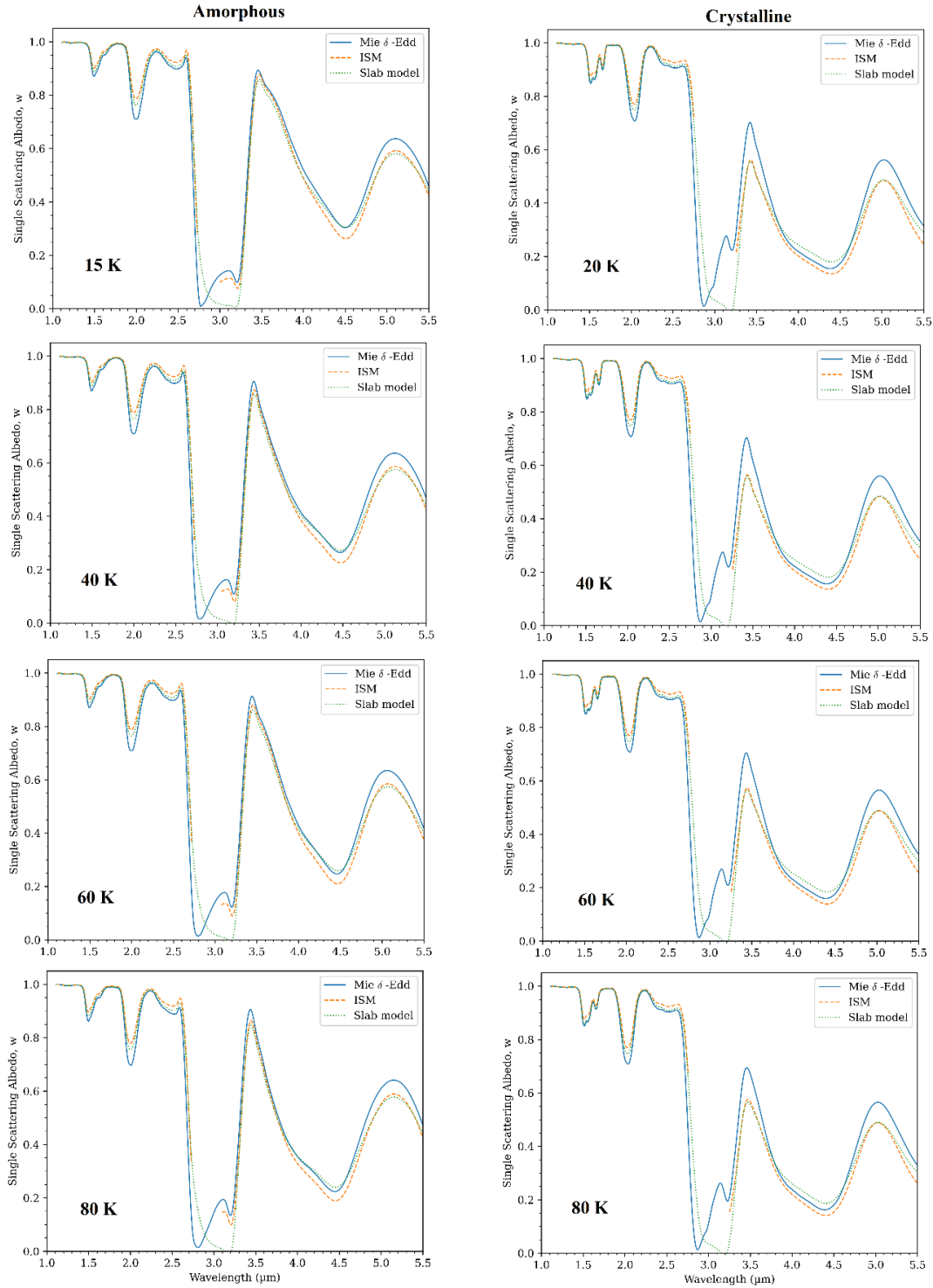


Fig. 3.1: Calculated single scattering albedo plots for 10 μm radii particles of amorphous (left column) and crystalline (right column) H_2O ice at the NIR wavelengths. The subplots in the rows are the measurements at different temperatures where blue solid lines are δ -Eddington corrected Mie, green dotted lines are Hapke slab, and yellow dashed lines are ISM spectra.

In the instance of Ic at every investigated temperature (right column in Fig. 3.1), the slab model almost accurately reproduces the Mie model for the weak overtone at 1.5 μm while it shows slightly higher w values for the weak overtone at 2.0 μm . This represents an accurate grain size prediction at 1.5 μm and a slightly smaller grain size prediction at 2.0 μm by the slab model. The ISM, on the other hand, predicts much smaller grain sizes than the Mie model at both 1.5 and 2.0 μm . At the broader 4.4 μm absorption band of Ic, the slab model predicts smaller grain sizes while the ISM model predicts larger grain sizes compared to Mie's prediction – because the calculated w values by the slab model and ISM at the wavelength region are higher and lower, respectively than the Mie model. Both the approximation models follow the same path and show much smaller w values at the 3.5 and 5 μm bands – indicating a much larger grain size prediction by the approximation models at these bands. However, the differences between spectra of the Hapke approximations and Mie models at 3.5 μm are much higher for Ic compared to Ia at every investigated temperature (see the left and right columns of Fig. 3.1).

Though the ISM spectra can reproduce the 3.1 μm reflection peak of Ia at lower temperatures (e.g., 15 and 40 K), it partially reproduces the reflection peak at higher temperatures (e.g., 80 K). Whereas the slab model fails to reproduce the 3.1 μm reflection peak of Ia at every temperature. The 3.1 μm reflection peak of Ic is much sharper and slightly red-shifted than ice Ia. Neither of the approximation models reproduces the 3.1 μm reflection peak of Ic at any investigated temperatures. The inability of the slab model in predicting the 3.1 μm reflection peak of H₂O is likely due to having higher k values at these wavelengths (Hansen, 2009).

3.3.2. Relative grain size estimation

We assess the uncertainty in the predictions of grain sizes by the Hapke approximation models for the ice phases at the investigated temperatures. A finely spaced range of grain sizes at radii of 1, 10, 100, and 1000 μm (hereafter we denote as reference grain radii) was used to show the relative discrepancies of grain size prediction at NIR wavelengths. We chose this range because it covers the grain sizes, expected to be found in the outer solar system bodies. For instance, fine-grain H_2O ice with a diameter of $< 1 \mu\text{m}$ has been predicted on Pluto (Cook et al., 2019). Much larger grain sizes are also believed to be present in outer solar system bodies such as icy moons and rings of Saturn (e.g., Filacchione et al., 2012) and Pluto (Cook et al., 2019).

Accordingly, we first compute the δ -Eddington corrected Mie w' at these reference grain radii over the NIR wavelengths. Once the Mie w' is calculated, we determine the grain sizes from each of the Hapke approximation models that provide the best fit to the Mie spectra over the selected wavelengths. To this end, we solve the inverse of the ISM and Hapke slab model for D to fit the corresponding Mie w' values. We use the modified Powell's hybrid method (Powell, 1970; Chen and Stadtherr, 1981) to solve the non-linear function of the Hapke slab and ISM (Eq. 2 and 5) in finding the solution for D . The relative grain size prediction is then determined by normalizing the predicted grain sizes by the approximation models to the reference grain radii input in the Mie model.

We estimate the medians and their 16% quantile as a lower 1σ error bar and 84% quantile as an upper 1σ error bar of predicted grain sizes using the approximation models for Ia (Table 3.1a) and Ic (Table 3.1b) at the investigated temperatures. As additional supporting information, we

also list the mean $\pm 1\sigma$ standard deviation in predicted grain sizes in the Appendix (Table 3A.1). The statistics were derived from the normalized values of the estimated grain sizes predicted by the slab model and ISM to the Mie model. A value of 1 represents exact prediction while the higher or lower values imply an over or underestimation, respectively, of the grain sizes by the respective approximation models to the Mie model. Thus, the values in Table 3.1 (and Table 3A.1) indicate the magnitude of the discrepancies in grain size prediction by the approximation models.

To facilitate visual comparisons of our result over the NIR wavelengths, we plot the normalized predicted grain size for Ia (Fig. 3.2) and Ic (Fig. 3.3) by approximation models at different reference grain radii and temperatures. Similar to Table 3.1, the y-axis value of 1 in each subplot of Fig. 3.2 and 3.3 represents an exact prediction while the higher or lower values imply an over or underestimation, respectively, of the grain sizes by the approximation models to the Mie model. Thus, the y-axis values in the subplots of Fig. 3.2 and 3.3 indicate the magnitude of discrepancies in predicted grain sizes at NIR wavelengths.

Table 3.1: Medians and their 16% quantile as a lower 1σ error bar and 84% quantile as an upper 1σ error bar of relative discrepancies in predicted grain sizes using the Hapke slab and ISM calculated at particle radii of 1, 10, 100, and 1000 μm for amorphous (a) and crystalline (b) H_2O ice at different temperatures.

a).

Grain radii (μm)	Amorphous H_2O ice*							
	15 K		40 K		60 K		80 K	
	Slab	ISM	Slab	ISM	Slab	ISM	Slab	ISM
1	$1.07^{+1.04}_{-0.25}$	$1.28^{+1.08}_{-0.29}$	$1.07^{+0.97}_{-0.25}$	$1.28^{+1.02}_{-0.29}$	$1.07^{+0.96}_{-0.25}$	$1.29^{+1.04}_{-0.30}$	$1.08^{+0.92}_{-0.26}$	$1.29^{+1.03}_{-0.30}$
10	$1.19^{+0.06}_{-0.34}$	$1.44^{+0.05}_{-0.56}$	$1.20^{+0.07}_{-0.29}$	$1.45^{+0.05}_{-0.57}$	$1.21^{+0.06}_{-0.31}$	$1.46^{+0.05}_{-0.58}$	$1.21^{+0.06}_{-0.26}$	$1.46^{+0.05}_{-0.58}$
100	$1.46^{+0.58}_{-0.12}$	$1.66^{+0.35}_{-0.10}$	$1.46^{+0.58}_{-0.26}$	$1.66^{+0.48}_{-0.09}$	$1.47^{+0.62}_{-0.26}$	$1.67^{+0.45}_{-0.09}$	$1.47^{+0.60}_{-0.35}$	$1.67^{+0.51}_{-0.09}$
1000	$1.54^{+1.08}_{-1.37}$	$1.67^{+4.34}_{-1.08}$	$1.54^{+1.09}_{-1.38}$	$1.67^{+4.34}_{-1.19}$	$1.55^{+1.11}_{-1.37}$	$1.68^{+4.35}_{-1.23}$	$1.55^{+1.10}_{-1.40}$	$1.68^{+3.87}_{-1.26}$

b).

Grain radii μm	Crystalline H_2O ice*							
	20 K		40 K		60 K		80 K	
	Slab	ISM	Slab	ISM	Slab	ISM	Slab	ISM
1	$0.88^{+0.67}_{-0.19}$	$1.03^{+0.76}_{-0.22}$	$0.87^{+0.67}_{-0.19}$	$1.03^{+0.76}_{-0.22}$	$0.88^{+0.67}_{-0.19}$	$1.03^{+0.75}_{-0.22}$	$0.87^{+0.67}_{-0.19}$	$1.03^{+0.75}_{-0.22}$
10	$1.10^{+0.08}_{-0.07}$	$1.30^{+0.07}_{-0.44}$	$1.09^{+0.07}_{-0.06}$	$1.30^{+0.07}_{-0.44}$	$1.09^{+0.07}_{-0.07}$	$1.30^{+0.07}_{-0.44}$	$1.09^{+0.07}_{-0.07}$	$1.30^{+0.07}_{-0.44}$
100	$1.24^{+0.65}_{-0.54}$	$1.46^{+0.40}_{-0.03}$	$1.24^{+0.65}_{-0.54}$	$1.46^{+0.40}_{-0.03}$	$1.25^{+0.64}_{-0.51}$	$1.46^{+0.41}_{-0.03}$	$1.24^{+0.64}_{-0.51}$	$1.46^{+0.41}_{-0.03}$
1000	$1.34^{+0.80}_{-1.27}$	$1.47^{+3.57}_{-1.25}$	$1.34^{+0.81}_{-1.27}$	$1.47^{+3.64}_{-1.25}$	$1.34^{+0.81}_{-1.26}$	$1.47^{+3.78}_{-1.24}$	$1.34^{+0.81}_{-1.26}$	$1.47^{+3.78}_{-1.24}$

*Note: The statistics were computed by normalizing the estimated grain sizes from the Hapke slab and ISM to the Mie grain size. The number values are the medians and their 16% quantile as a lower 1σ error bar and 84% quantile as an upper 1σ error bar.

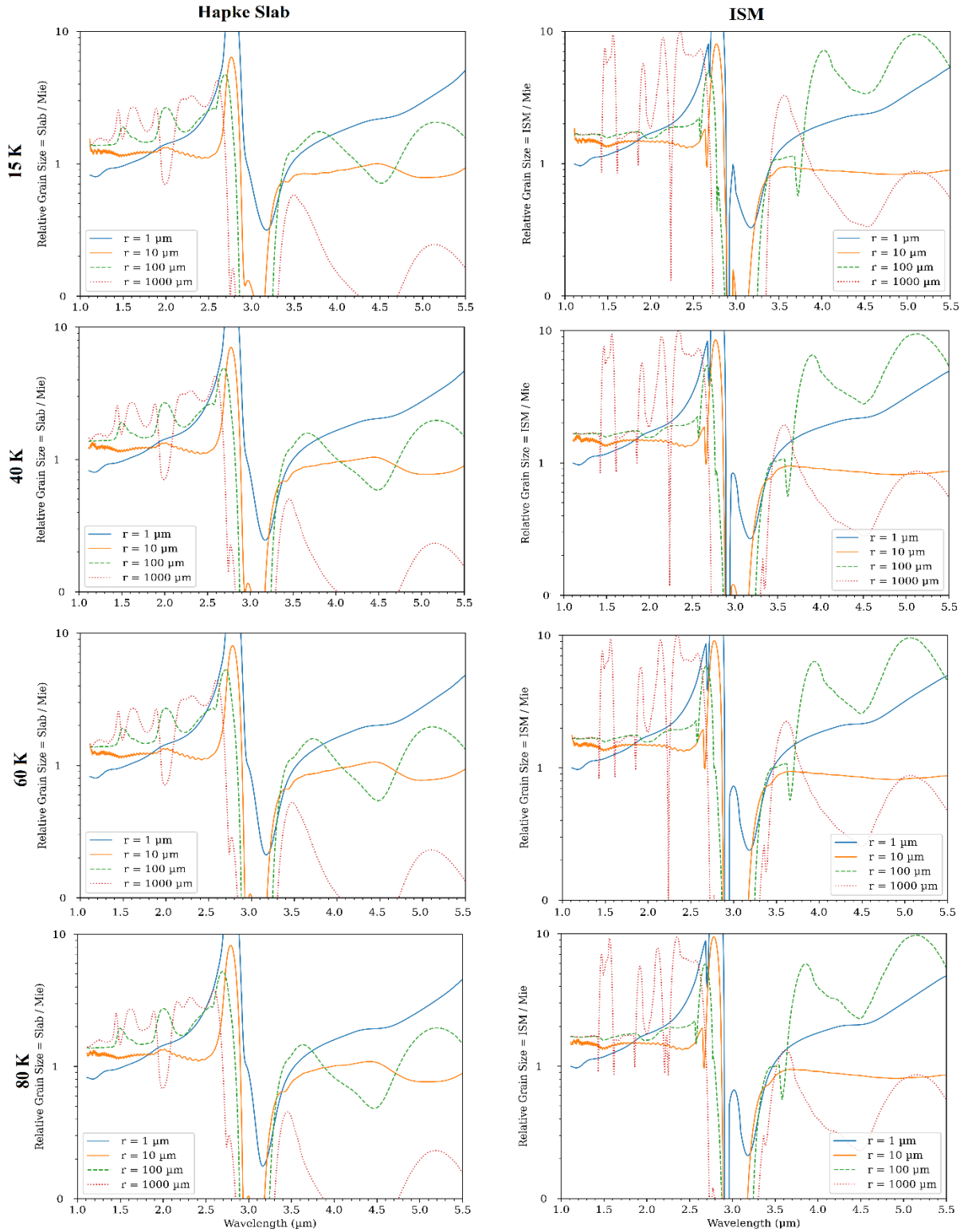


Fig. 3.2: Predicted relative gain sizes (normalized to the Mie prediction) using the Hapke slab (left column) and ISM (right column) calculated at particle radii of 1, 10, 100, and 1000 μm for amorphous H_2O ice, for temperatures ranging between 15 and 80 K.

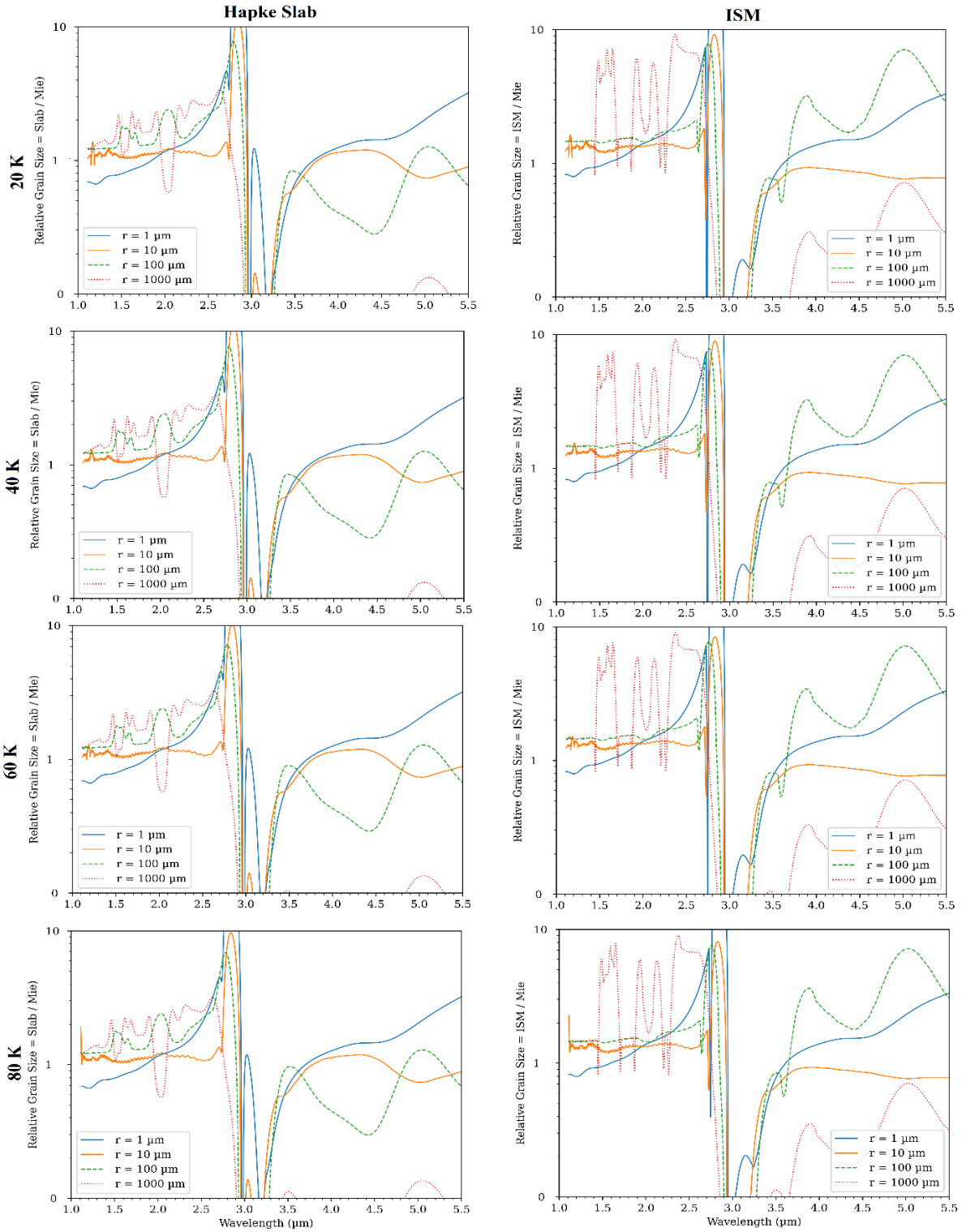


Fig. 3.3: Predicted relative gain sizes (normalized to the Mie prediction) using the Hapke slab (left column) and ISM (right column) calculated at particle radii of 1, 10, 100, and 1000 μm for crystalline H_2O ice, for temperatures ranging between 20 and 80 K.

The discrepancies in the estimated grain sizes combining all parameters (i.e., ice phases, grain radii, temperatures, and scattering models) simultaneously are complicated, and, consequently, interpreting the result accommodating all parameters together is difficult. Thus, we analyze our result by comparing the discrepancies in predicted grain sizes within a particular parameter while keeping the rest of the other parameters constant/fixed. For instance, we first start by comparing the discrepancies in estimated grain sizes between ice phases (Ia vs Ic) predicted by the approximation models at corresponding temperature and reference grain radii.

Overall, the predicted grain sizes are much better for Ic than Ia by both approximation models. Because the median values are much closer to 1 for Ic compared to Ia at the corresponding temperature and grain radii (see Table 3.1). In other words, between the ice phases at most of the corresponding temperatures and grain radii, both approximation models produce median values that are much better for Ic compared to Ia. As an example, for 10 μm radii at 40 K, the Ic and Ia show a median value of 1.09 vs 1.20 by the slab model, respectively, and 1.30 vs 1.45 by the ISM, respectively (Table 3.1). One exception in this instance is that the slab model's prediction of 1 μm radii is slightly better for Ia than Ic, such as a median value of 1.07 vs 0.88 at 60 K, respectively (Table 3.1). However, the corresponding 16 and 84% quantiles error bars for the 1 μm grain are higher for Ia than Ic. The mean values (Table 3A.1) between the ice phases are also mostly consistent with the median values, except for smaller grains ($\leq 10 \mu\text{m}$ radii) at lower temperatures ($\leq 40 \text{ K}$). Therefore, we conclude that the Hapke approximation models predict much better, in general, grain sizes for Ic than for the Ia phase. Quantitatively, the predicted grain sizes by the approximation models are roughly 10 – 20% higher (on average) for Ia than Ic.

While comparing discrepancies between the approximation models for a particular ice phase, temperature, and reference grain radii, the slab model shows a better approximation (i.e., median values much closer to 1) than the ISM. This is evident from the median (except for Ic at 1 μm radii) and means $\pm 1\sigma$ values (except Ia for 10 μm radii at 40K) at every temperature, grain radii, and ice phase. As an example, for 10 μm radii Ia particle at 40 K, the medians are 1.20 and 1.45 for the slab model and ISM, respectively (Table 3.1a). Likewise, for 10 μm radii Ic particle at 40 K, the median value is 1.09 vs 1.30 for the slab model and ISM, respectively (Table 3.1b). Even though the median of ISM is slightly better than the slab model for 1 μm radii Ic grain (for instance, a median value of 1.03 vs 0.88 at 20 K, respectively), the 16 and 84% quantiles error bars are lower for the slab model than the ISM. The mean values (Table 3A.1) between the approximation models for both ice phases are also consistent (with only one exception) with the median values. Quantitatively, the ISM predicted grain sizes are around 10 – 25 % higher than the slab model's prediction for both ice phases (ignoring the exceptions). The subplots in the left and right columns of Fig. 3.2 and 3.3 also support that the slab model's predictions are much better (qualitatively) than ISM at a particular ice phase, temperature, and grain radii. For instance, the 1000 μm radii curve of ISM shows much more fluctuations on the y-axis than the slab model's curve for similar grain radii at every temperature of ice phases. The higher discrepancies in grain size estimation by ISM are consistent with the result of Hansen (2009).

The discrepancies in response to temperature changes (from ~15 to 80 K) indicate that the median values of both ice phases for particular grain radii by the approximate models do not substantially change in response to temperature variations (Table 3.1). This implies that the

temperature changes within an ice phase may not have a major impact on predicting H₂O grain size using the Hapke approximation models. Unlike median values, the mean values of Ia particles by the approximation models slightly change in response to temperature. However, the change does not follow a particular pattern for most of the grain radii (Table 3A.1). In contrast, the mean values for Ic by the slab model slightly decrease in response to temperature increase while for ISM the change does not show a particular pattern for grain radii (Table 3A.1). Overall, the discrepancies in predicted H₂O ice grain sizes by the approximation models due to the temperature variations roughly vary $\sim 1 - 5 \%$. This is further supported by the row-wise subplots in Fig. 3.2 and 3.3 which clearly show that the shapes of the different radii curves do not substantially change due to temperature changes.

The grain size prediction of the Ia phase at every temperature indicates that both approximation models produce higher median values (higher uncertainty) for larger grain radii (Table 3.1a). As an example, for an Ia particle at 60 K, the slab model predicts a median value of 1.07 and 1.55 for the 1 and 1000 μm radii, respectively, while for ISM it is 1.29 and 1.68, respectively. A similar trend is also evident for Ic particles at every temperature such that the prediction of the larger grain sizes has higher uncertainty by both approximation models (Table 3.1b). Note that the slab model's prediction of 1 μm radii Ic particle is slightly smaller than the Mie models – the median values are all less than 1. Quantitatively, the discrepancies in predicting larger grain radii by the approximation models can be up to 40 – 50 % of the Mie model's prediction. This effectively means that both approximation models' performances substantially deteriorate in predicting larger H₂O ice grains irrespective of ice phase.

We visually compare and, subsequently, qualitatively interpret the discrepancies in predicting different grain sizes over the NIR wavelengths (Fig. 3.2 and 3.3). The 1 μm radii curves (for both the ice phase and each temperature) rise continuously at shorter wavelengths up to $\sim 2.8 \mu\text{m}$ (Fig. 3.2 and 3.3). This continuous rise at shorter wavelengths is largely due to the Rayleigh effect on w from the Mie model that happens at wavelengths close to or smaller than the grain size (Hansen, 2009). The Hapke approximation models do not account for the Rayleigh effect. Thus, even though the median values of the 1 μm radii show a good prediction (Table 3.1), the mean $\pm 1\sigma$ standard deviation shows one of the highest discrepancies (Table 3A.1). The 10 μm radii curves (for each ice phase and temperature) show a better prediction than other radii curves over the NIR wavelengths. The median values are also in agreement with the above conclusion since the medians are close to 1 (except for 1 μm radii). This is further supported by mean values for 10 μm radii which are closest to 1 (lowest discrepancy) compared to other grain radii.

Though the 100 μm radii curves by the ISM show relatively less fluctuation around the value 1 on the y-axis at shorter wavelengths than the slab model, at longer wavelengths ($>3 \mu\text{m}$) this behavior is the opposite. Consequently, the 100 μm radii curves by the slab model overall exhibit much better than the ISM's prediction for both ice phases at each temperature. The 1000 μm radii curves by the slab model for both ice phases show much larger fluctuations on the y-axis amongst the other radii curves in Fig. 3.2 and 3.3 – which explains why they have the highest median values among the grain radii. However, the corresponding 1000 μm curve by ISM produces much higher discrepancies.

For larger particles ($\geq 100 \mu\text{m}$ radii) at each ice phase and temperatures, the approximation models predict much smaller grain sizes at longer wavelengths (above $3.5 \mu\text{m}$) than Mie's prediction (Fig. 3.2 and 3.3). A possible reason for smaller grain size prediction is that the approximation models do not reproduce the characteristic higher saturation level of the Mie model (Hansen, 2009). For both ice phases, the fluctuation of the $1000 \mu\text{m}$ radii curves by ISM at shorter wavelengths is even much higher than the $1 \mu\text{m}$ radii curve, where there is a continuous rise of the curves due to the Rayleigh effect (see the right columns in Fig. 3.2 and 3.3). In both ice phases, the mean and median values by the ISM for the $1000 \mu\text{m}$ radii are the largest among all corresponding values (Tables 3.1 and Table 3A.1).

3.3.3. Characteristic absorption coefficient

To explain the effect of absorption coefficient in grain size prediction, we plot the dependency of the α on wavelength (following Eq. 3) for both ice phases and temperatures (Fig. 3.4). At each temperature, both phases exhibit a maximum value of α at the wavelengths close to $3.0 \mu\text{m}$, although with a slight shift toward shorter wavelengths for ice Ia compared to ice Ic. The higher absorption peak at $3.0 \mu\text{m}$ (orders of magnitude higher α values than at other wavelengths) is due to the higher k values (the imaginary part of the optical constant) at these bands. This renders grain size prediction impossible by the approximation models – also evident at $3 \mu\text{m}$ wavelengths in Fig. 3.2 and 3.3. This result supports the assumption that the slab model should be used if $k \ll 1$ (Hapke, 1981). A blue shift in α spectra of Ia compared to the Ic phase is also evident at the weak $2 \mu\text{m}$ band, which coincides with the fact that Ic has much stronger, sharper, and red-shifted at infrared bands than Ia (Schmitt et al., 1998).

Higher values of α are also seen at the longer wavelengths for both ice phases. However, a peak of α happens at around 4.5 μm for Ia while this peak shifts toward shorter wavelengths at 4.4 for Ic – in agreement with Mastrapa et al. (2009). The effects of these α peaks are evident in the characteristic shapes (i.e., a dip) in grain radii curves at these wavelengths for larger particles (i.e., 100 and 1000 μm ; Fig. 3.2 and 3.3). The relatively higher α value at 4.5 μm for Ic compared to Ia is apparent in the curve of the 1000 μm particle (Fig. 3.2 and 3.3) where the Ic reveals a higher discrepancy in grain size prediction than the Ia for both approximation models at the wavelength.

The α of pure CH_4 and $\text{N}_2:\text{CH}_4$ (N_2 saturated with CH_4) systems, the other abundant volatile ices found on KBOs and TNOs surfaces, at NIR wavelengths (see Fig. 3 of Emran and Chevrier, 2022) have a much lower α than water ice phases. A simple interpretation of this fact is that may be the H_2O ice may have higher absorption and lower reflectance compared to the pure CH_4 and $\text{N}_2:\text{CH}_4$ ices on the TNOs (e.g., Triton) and KBOs (e.g., Pluto, Eris, and Sedna). However, this interpretation may not be true amid different other parameters/ factors involved with spectral signatures of the ices. The results above show that the higher discrepancies in predicated grain sizes for larger particles are largely aligned to the wavelengths with higher α values. Accordingly, the estimation of H_2O ice grain size using the Hapke approximation models for larger particles may be susceptible to higher uncertainty than that of CH_4 and $\text{N}_2:\text{CH}_4$ ices at the Kuiper Belt (Emran and Chevrier, 2022).

The α of Ia at the 4.5 μm absorption band (and slightly at 1.5 and 2 μm bands) increases with changes in temperature from 15 to 80 K (Fig. 3.4). This α vs temperature characteristic of Ia may

likely be the cause of the slightly higher discrepancy in grain size prediction than the Mie model's prediction with the higher temperatures at these bands (Fig. 3.2). In contrast, Ic does not show any substantial variation in α values with the temperature at the 4.4 μm absorption band, although α slightly decreases with temperature increase. Therefore, in the case of Ic, there are no substantial differences in grain size estimations at this wavelength between each temperature (Fig. 3.3).

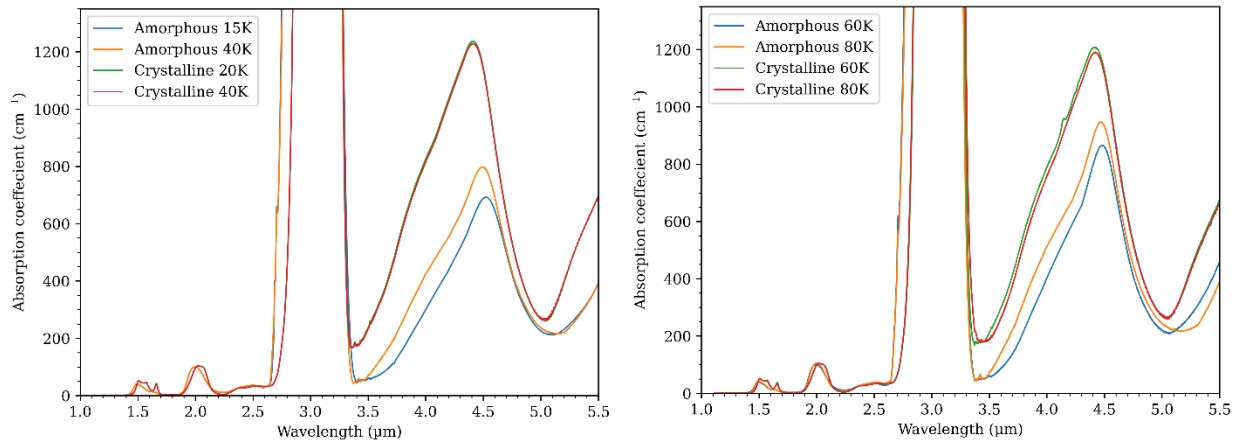


Fig. 3.4: Absorption coefficient of amorphous and crystalline H₂O ice at different temperatures over NIR wavelengths. Both phases of H₂O have a broad absorption coefficient peak of around 3.0 μm with a little shift toward shorter wavelengths by the Ia. Another absorption peak is seen at 4.5 μm for Ia while this peak shifts toward shorter wavelengths at 4.4 for Ic with much higher α values. The higher absorption peak for Ic compared to Ia at longer wavelengths is associated with the higher k values at these wavelengths.

3.4. Discussion

We use the Hapke models for predicting grain sizes of 1 μm radii even though the approximation model assumes that the particle size should be much larger than the wavelengths (Hapke, 1981). This study uses wavelengths close to or even larger than grain radii of 1 μm . Alternatively, we also test a more conventional scenario with a wide range of grain sizes much larger than the considered wavelengths. The rationale for using 1 μm radii is based on reports of

the presence of H₂O ice with similar sizes on the surface of outer solar system bodies like KBOs (e.g., Cook et al., 2019). Moreover, the use of a 1 μm grain size emphasizes the Rayleigh effect that happens at grains that have sizes close to NIR wavelengths often used to study the composition of outer solar system planetary surfaces (e.g., Hansen, 2009; Emran and Chevrier, 2022). And by taking smaller particle sizes, we evaluate the grain size prediction discrepancies at wavelengths close to or even larger than the grain size of 1 μm radii. On top of that our result shows how deviant, as is expected, grain size prediction the approximation models can produce (Fig. 3.2 and 3.3) when the wavelengths are close to or even larger than the grain size.

The predicted grain sizes by the Hapke approximation models vary over the investigated wavelengths due to the optical constants (and, therefore, different absorption coefficient values) at different NIR bands and the formulation of the approximation models used (see Eq. 2 and 5). In simple words, the approximation models predict different grain sizes based on optical constant values ($n + ik$) at different wavelengths. Accordingly, assessing the predictions of these varying grain sizes at different wavelengths by the approximation models was the motivation of the study and thus, we evaluate the discrepancies in predicting varying grain sizes by the scattering models. As mentioned above, we only consider the optical constant of cubic crystalline ice as a generalization of crystalline ice. However, there are only subtle differences in spectra between the cubic and hexagonal phases (Bertie and Whalley, 1967), and thus, we emphasize that the crystalline phases are substitutable (Mastrapa et al., 2009) and the use of Ic for generalization of the crystalline ice is reasonable.

Between the ice phases, the grain size estimation for Ic using the Hapke approximation models results in a much closer, in general, estimate to Mie's prediction. Conversely, the Hapke approximation models show higher discrepancies in grain size estimation for Ia. The variation in temperature within a phase does not influence much on average grain size estimation at NIR wavelengths. However, grain size estimation for larger Ia particles at longer wavelengths reveals a pattern such that the discrepancy in grain sizes increases with temperatures from 15 to 80 K. In contrast, the discrepancies in grain size estimation of larger Ic particles at longer wavelengths are negligible between the temperature range. Interestingly, grain size estimation for larger particles at the broad 4.4 - 4.5 μm absorption band leads to a higher discrepancy for Ic compared to the Ia. Overall, the relative discrepancies of the grain size estimation are better for the Hapke slab model than ISM at the investigated cryogenic temperatures. This indicates Hapke slab is a better approximation model for deriving the water ice grain sizes in the icy bodies in the far reach of the Solar System. Our result is consistent with the results previously analyzed by Hansen (2009) using the optical constant of Ic at a temperature of 110 K.

Owing to the Rayleigh effects on single scattering albedo, neither of the approximation models predicts accurate grain size estimation results for the particles with diameters less than or close to the wavelengths ($\leq 5 \mu\text{m}$). For both Ia and Ic, grain size estimations for 10 μm radii H₂O ice are best predicted by both Hapke approximation models. Though grain size prediction by the approximation models for larger radii shows higher discrepancies largely at the wavelengths with higher absorption coefficient values, the uncertainty in the instance of ISM is much higher than in the Hapke slab model. The higher discrepancies of grain size estimation for larger particles by ISM can be compromised by adjusting the free parameters used in calculating single scattering

albedo, for instance, the study of Roush et al. (2007) used a higher value of s to fit modeled spectra.

While formulating the “*espat*” function for the slab model, Hapke (1981) used a scaling factor of $\hat{g} = 2/3$ for particle diameter. However, the scaling factor of diameter in the Hapke slab model varies between $3/4 - 4/3$ which can, in principle, result in a difference in grain size estimation by the slab model (Hansen, 2009). Likewise, the difference in grain size estimation by ISM can also be produced by scaling factor to the particle diameter by calculating the mean free path of the photon $\langle D \rangle$ as seen in Eq. 7. There have been different approximate expressions for the relationship between D and $\langle D \rangle$. This relationship is approximated as $\langle D \rangle \cong 0.9D$ or $2D/3$ (e.g., Hapke, 2012; Melamed, 1963) for spherical particles while it's $\langle D \rangle = 0.2D$ for irregular particles (Shkuratov and Grynko, 2005). Hence, the grain sizes estimation by the approximations models can be improved by carefully adjusting the scale factor for particle diameters. We use a scale factor of 1 for the slab model while the mean free path of a photon in ISM was calculated as a function of the diameter and real part of the refraction index.

An obvious difference between the ISM and the slab models is the calculation of average Fresnel reflection coefficients – the former model employs data from both n and k parts while the latter uses only n part of the refractive indices (e.g., Emran and Chevrier, 2022). Since the slab model can be applied when k is very small (Hapke, 1981, 1993) and therefore, wavelengths with a substantially higher k value can lead to a higher difference in calculated results between the models. Note that if the approximation model assumes the internal scattering coefficient, $s = 0$ (as used by many existing studies, for example, Lucey, 1998; Lawrence and Lucey, 2007) then

the internal diffused reflectance, r equals to be zero as well. However, Sharkey et al. (2019) expressed the relationships between the s and D (“effective diameter”) as $s = 1/D$ and the number of scattering events $(sD) = 1$ within a single grain. Thus, this relationship indicates that s cannot be zero (Emran and Chevrier, 2022).

As has previously been mentioned that Mie’s theory (Mie, 1908) can accurately calculate the scattering properties of uniform (shapes) particles. Further, besides application to scattering properties for the equant particles of Mie spheres, the Mie scattering model has been devised to be satisfactorily employed for particles with varied “equivalent” non-spherical shapes if each non-spherical particle can be represented by assembles of spheres with the same volume-to-surface-area ratio as the non-spherical particle (Grenfell and Warren, 1999; Grenfell et al., 2005). In other words, roughly similar scattering properties have been reported by irregular particles to that of the scattering properties calculated by the similar-sized spherical particles using Mie’s theory (Hapke, 1981). This implies that the scattering properties of Mie theory for spherical particles can be mimicked to irregular particles (Neshyba et al., 2003), and thus application to Mie theory in the grain size estimation of a Mie’s equant particle is somewhat analogous to non-spherical/ irregular grains (e.g., Hapke, 1981; Hansen, 2009).

While both Hapke approximation models do not account for the Rayleigh effect on the single scattering albedo that happens to grain size close to the wavelengths ($\leq 5 \mu\text{m}$), the Mie theory appropriately accounts for this shortcoming. Though the rough average difference between the predicted grain sizes by the ISM and slab model is about $\sim 10 - 25\%$ (based on the median values in Table 3.1) for a wide range of particles, we emphasize that it’s still an

over/underestimation by one approximation model to another. And our study shows which approximation model predicts much better results than others in estimating the grains sizes of Ia and Ic found in the vast region of the outer solar system.

A better estimation of H₂O ice grain sizes by the slab model than ISM is also in agreement with the grain size estimation of the abundant surface volatile of N₂ and CH₄ ices on TNOs and KBOs surfaces (Emran and Chevrier, 2022). Thus, the Hapke slab model is better equipped for the implementation of RTMs in the approximate grain size estimation for a range of surface ices (H₂O, N₂, and CH₄) in the outer solar system bodies. We recommend using the Mie formulation of the single scattering albedo for estimation of H₂O ice (Ia and Ic) grain sizes for unknown spectra of outer solar system bodies. When choosing the approximation models, we recommend using the Hapke slab model over ISM since our result presumes that the slab model better approximates the H₂O grain size prediction, overall, than the internal scattering model at 1 – 5 μm wavelengths.

The single scattering albedo may not be readily available from the measurements of spacecraft observations. However, the reflectance (or radiance coefficient) measurements by spacecraft observation are converted to single scattering albedo using the radiative transfer model such as Hapke (1993). Conversion of reflectance (r_c) measurement from remote sensing observation to single scattering albedo (w) using the Hapke model (1993) requires other parameters of the RTM to be known or calculated. Of these the important parameters are observation geometry (i.e., incident (i), emission (e), and phase (g) angles), single scattering phase function ($P(g)$), and backscattering function ($B(g)$), and multiple scattering functions (H ,

for both up-welling and down-welling radiance; e.g., Lawrence and Lucey, 2007; Mustard and Glotch, 2019). The parameters related to observation geometry (i , e , and g) come directly with remote sensing reflectance (or radiance) measurements while other parameters can be approximated using the appropriate equations given in Hapke (1981, 1993, 2012).

Conversion of remote sensing reflectance to single scattering albedo is crucial for deriving the material abundance and grain size of planetary regolith using RTMs. Because it is predicated that a linear mixing of regolith components for an intimate mixing systematic is only reasonable if a single scattering albedo is converted from reflectance (e.g., Mustard and Glotch, 2019). Thus, the implementation of RTMs to estimate grain size involves first the conversion of remote sensing reflectance (r_c) measurements to single scattering albedo (w), followed by the implementation of a linear fitting (least squares or other minimizations routine) algorithm to estimate the abundance and grain size of surface components. The linear fitting algorithm assumes that the average w of a planetary regolith is a linear combination of the w of a plausible set of endmembers present in the mixture systematic weighted by each endmember's relative geometric cross-section (e.g., Mustard and Glotch, 2019). The w spectra of the endmembers are calculated from their optical constants data such as, in this instance, amorphous and crystalline H₂O ice for the outer solar system.

Ultimately, therefore, an estimation of the grain size of the surface components in the outer solar system bodies through the implementation of the RTMs feeds on single scattering albedos spectra – both from remote sensing observations and plausible endmembers. Hence, the predicted grain sizes of planetary surface components (e.g., H₂O ice) using RTMs ought to be

affected by the differences in the estimated single scattering albedo spectra (i.e., remote sensing observation and endmembers) and, inherently, the methods used to derive endmembers' single scattering albedo from their optical constants. This is further supported by Hansen (2009) who argued and showed that the variations in the estimation of H₂O grain sizes at Saturnian moons are attributed due to the differences in single scattering albedo calculation rather than the bidirectional scattering model. Accordingly, we assess the discrepancies in grain size estimation of H₂O ice in the outer solar system owing to the implementation of a variety of widely used scattering models (Mie and Hapke approximations) in the existing literature.

Despite having concerns related to the validity of the models and uncertainty in the parameters involved (e.g., Mustard and Glotch, 2019), the RTMs have been widely utilized and have successfully been implemented in estimating the grain size of a wide range of planetary regolith in the solar system including terrestrial and icy surfaces (e.g., planets, asteroids, moons, etc.). Note that in remote sensing observations, the single scattering albedos are the calculated properties of a planetary surface using the radiative transfer model rather than directly measured. In Hapke's formulation of RTM, the single scattering phase function ($P(g)$) and single scattering albedo (w) are closely associated such that if $P(g)$ is smaller in the direction of the observer remote sensing instrument, a larger w can compensate, and vice versa (Hapke, 1993). Thus, a variation in $P(g)$ estimation can influence the calculation of w and, consequently, can influence the prediction of grain size. However, the discrepancies in the estimation of grain size of H₂O ice due to variation in different single scattering phase function ($P(g)$) is beyond the scope of the present study. In this study, our focus was rather to assess how the implementation of a variety of the widely used scattering models can render in the variation of w calculations and resultant

discrepancies in H₂O grain sizes, how much are the variations, and based on the results of these variations what is the most appropriate method at what situation.

3.5. Conclusion

The mechanical strengths and thermal properties of planetary surfaces are directly influenced by the grain size of planetary regolith (e.g., Gundlach and Blum, 2013). Thus, an accurate grain size estimation of the outer solar system bodies is very important for an improved understanding of the surface volatile transport and thermophysical modeling of the planetary bodies. The icy bodies in the outer solar system host a widespread presence of water ice on their surfaces. Understanding the grain sizes of planetary regolith supports both landing or sample return missions (Gundlach and Blum, 2013), and thus accurate information about the water ice grains sizes is crucial for future missions to the outer reach of the solar system.

We assess the discrepancies in the grain size estimation of amorphous and crystalline H₂O ice at cryogenic temperatures from 15 – 80 K at a ~20 K interval. The relative grain size prediction by the Hapke approximation models was assessed, both quantitatively and qualitatively, concerning ice phases, grain sizes, and temperatures analogous to the icy zones of the solar system. Having a satisfactory application of Mie theory to an equant as well as “equivalent” non-spherical particles, we recommend using Mie formulation for unknown spectra of the outer solar system bodies. However, if approximation models are preferred, our study suggests using the slab model rather than the internal scattering model.

We demonstrate which model works better for the approximate grain size estimation of phases of water ice found in the outer solar system. Incorporating the results from Emran and Chevrier (2022), we conclude which approximate model is better in predicting the grain sizes of a variety of surface ices found in the outer solar system bodies, specifically on trans-Neptunian objects and Kuiper Belt objects. Thus, this study put forward a guideline for future studies in choosing scattering models in estimating the water ice grain sizes in the outer solar system using the radiative transfer models at near-infrared bands.

3.6. Acknowledgments

The authors would like to thank Samuel Cano, Abhilash Ramachandran, and anonymous reviewers for the useful comments.

3.7. Software

NumPy (Harris et al., 2020), SciPy (Virtanen et al., 2020), Matplotlib (Hunter, 2007), MiePython (<https://pypi.org/project/miepython/>)

3.8. APPENDIX

A. The mean and $\pm 1\sigma$ standard deviation of relative discrepancies in grain sizes are predicated by the approximation models.

Table 3A.1: The mean and $\pm 1\sigma$ standard deviation of relative discrepancies in predicted grain sizes using the Hapke slab and ISM calculated at different particle radii of 1, 10, 100, and 1000 μm for amorphous (a) and crystalline (b) H_2O ice at different temperatures.

a).

Grain radii (μm)	Amorphous H_2O ice*							
	15 K		40 K		60 K		80 K	
	Slab	ISM	Slab	ISM	Slab	ISM	Slab	ISM
1	1.89 \pm 3.06	2.07 \pm 2.96	1.96 \pm 3.42	2.25 \pm 4.13	2.08 \pm 3.97	2.43 \pm 5.14	2.11 \pm 4.10	2.44 \pm 5.22
10	1.21 \pm 0.74	1.40 \pm 0.92	1.23 \pm 0.82	1.14 \pm 0.98	1.26 \pm 0.95	1.42 \pm 1.06	1.27 \pm 0.98	1.43 \pm 1.10
100	1.58 \pm 0.72	2.05 \pm 1.62	1.57 \pm 0.75	2.06 \pm 1.59	1.59 \pm 0.80	2.04 \pm 1.57	1.59 \pm 0.81	2.06 \pm 1.59
1000	1.51 \pm 1.00	2.62 \pm 2.44	1.51 \pm 1.02	2.57 \pm 2.47	1.52 \pm 1.03	2.58 \pm 2.48	1.50 \pm 0.99	2.41 \pm 2.29

b).

Grain radii μm	Crystalline H_2O ice*							
	20 K		40 K		60 K		80 K	
	Slab	ISM	Slab	ISM	Slab	ISM	Slab	ISM
1	2.07 \pm 5.76	2.19 \pm 5.99	2.05 \pm 5.64	2.17 \pm 5.89	1.97 \pm 5.15	2.13 \pm 5.62	1.97 \pm 5.15	2.13 \pm 5.62
10	1.24 \pm 1.35	1.32 \pm 1.08	1.24 \pm 1.3	1.31 \pm 1.05	1.22 \pm 1.20	1.30 \pm 0.99	1.22 \pm 1.20	1.30 \pm 0.99
100	1.44 \pm 1.05	1.74 \pm 1.25	1.44 \pm 1.04	1.74 \pm 1.24	1.43 \pm 0.99	1.75 \pm 1.26	1.43 \pm 0.99	1.75 \pm 1.26
1000	1.28 \pm 0.86	2.30 \pm 2.21	1.27 \pm 0.85	2.31 \pm 2.21	1.27 \pm 0.84	2.31 \pm 2.22	1.22 \pm 0.84	2.31 \pm 2.22

*Note: The statistics were estimated by normalizing the predicted grain sizes from the Hapke slab and ISM to the Mie grain size. The number values are the mean $\pm 1\sigma$ standard deviation of predicted grain sizes by slab and ISM models to the Mie grain size H_2O ice phases at different temperatures. A value of 1 represents exact prediction by the approximation models while the higher or lower values indicate over or underestimation, respectively, of the grain sizes by the respective approximation models.

B. Notations

List of notations used in this paper

$B(g)$	backscattering function
$\langle D \rangle$	mean free path of a photon
D	particle diameter
D_e	effective particle sizes
e	emission angle
ζ	asymmetry parameters of Mie theory
g	phase angle
\hat{g}	a constant, roughly ≈ 1
H	multiple scattering function
i	incident angle
k	imaginary part of the refractive index
n	real part of the refractive index
$P(g)$	phase function
r	internal diffused reflectance
r_c	reflectance or radiance coefficient
s	internal scattering coefficient
S_e	Fresnel reflection coefficient for externally incident light,
S_i	Fresnel reflection coefficient for internally incident light,
w	single scattering albedo
w'	δ -Eddington Mie single scattering albedo
α	absorption coefficient
λ	wavelength
Θ	internal transmission coefficient

3.9. References

- Baragiola, R.A., 2003. Water ice on outer solar system surfaces: Basic properties and radiation effects. *Planetary and Space Science, Surfaces and Atmospheres of the Outer Planets their Satellites and Ring Systems* 51, 953–961. <https://doi.org/10.1016/j.pss.2003.05.007>
- Barucci, M.A., Merlin, F., 2020. Surface composition of Trans-Neptunian objects, The Trans-Neptunian Solar System. <https://doi.org/10.1016/B978-0-12-816490-7.00005-9>
- Bertie, J.E., Whalley, E., 1967. Optical Spectra of Orientationally Disordered Crystals. II. Infrared Spectrum of Ice Ih and Ice Ic from 360 to 50 cm⁻¹. *J. Chem. Phys.* 46, 1271–1284. <https://doi.org/10.1063/1.1840845>
- Chen, H.-S., Stadtherr, M.A., 1981. A modification of Powell's dogleg method for solving systems of nonlinear equations. *Computers & Chemical Engineering* 5, 143–150. [https://doi.org/10.1016/0098-1354\(81\)85003-X](https://doi.org/10.1016/0098-1354(81)85003-X)
- Cook, J.C., Dalle Ore, C.M., Protopapa, S., Binzel, R.P., Cruikshank, D.P., Earle, A., Grundy, W.M., Ennico, K., Howett, C., Jennings, D.E., Lunsford, A.W., Olkin, C.B., Parker, A.H., Philippe, S., Reuter, D., Schmitt, B., Singer, K., Stansberry, J.A., Stern, S.A., Verbiscer, A., Weaver, H.A., Young, L.A., Hanley, J., Alketbi, F., Thompson, G.L., Pearce, L.A., Lindberg, G.E., Tegler, S.C., 2019. The distribution of H₂O, CH₃OH, and hydrocarbon-ices on Pluto: Analysis of New Horizons spectral images. *Icarus* 331, 148–169. <https://doi.org/10.1016/j.icarus.2018.09.012>
- Cruikshank, D.P., Roush, T.L., Owen, T.C., Quirico, E., Bergh, C.D., 1998. The Surface Compositions of Triton, Pluto, and Charon, in: Schmitt, B., De Bergh, C., Festou, M. (Eds.), *Solar System Ices: Based on Reviews Presented at the International Symposium "Solar System Ices" Held in Toulouse, France, on March 27–30, 1995*, Astrophysics and Space Science Library. Springer Netherlands, Dordrecht, pp. 655–684. https://doi.org/10.1007/978-94-011-5252-5_27
- Cruikshank, D.P., Schmitt, B., Roush, T.L., Owen, T.C., Quirico, E., Geballe, T.R., de Bergh, C., Bartholomew, M.J., Dalle Ore, C.M., Douté, S., Meier, R., 2000. Water Ice on Triton. *Icarus* 147, 309–316. <https://doi.org/10.1006/icar.2000.6451>
- Dalle Ore, C.M., Protopapa, S., Cook, J.C., Grundy, W.M., Cruikshank, D.P., Verbiscer, A.J., Ennico, K., Olkin, C.B., Stern, S.A., Weaver, H.A., Young, L.A., 2018. Ices on Charon: Distribution of H₂O and NH₃ from New Horizons LEISA observations. *Icarus* 300, 21–32. <https://doi.org/10.1016/j.icarus.2017.08.026>
- Dumas, C., Merlin, F., Barucci, M.A., Bergh, C. de, Hainault, O., Guilbert, A., Vernazza, P., Doressoundiram, A., 2007. Surface composition of the largest dwarf planet 136199 Eris (2003 UB). *A&A* 471, 331–334. <https://doi.org/10.1051/0004-6361:20066665>

- Earle, A.M., Binzel, R.P., Young, L.A., Stern, S.A., Ennico, K., Grundy, W., Olkin, C.B., Weaver, H.A., 2017. Long-term surface temperature modeling of Pluto. *Icarus, Special Issue: The Pluto System* 287, 37–46. <https://doi.org/10.1016/j.icarus.2016.09.036>
- Emran, A., Chevrier, V.F., 2022. Uncertainty in Grain Size Estimations of Volatiles on Trans-Neptunian Objects and Kuiper Belt Objects. *AJ* 163, 196. <https://doi.org/10.3847/1538-3881/ac559f>
- Filacchione, G., Capaccioni, F., Ciarniello, M., Clark, R.N., Cuzzi, J.N., Nicholson, P.D., Cruikshank, D.P., Hedman, M.M., Buratti, B.J., Lunine, J.I., Soderblom, L.A., Tosi, F., Cerroni, P., Brown, R.H., McCord, T.B., Jaumann, R., Stephan, K., Baines, K.H., Flamini, E., 2012. Saturn's icy satellites and rings investigated by Cassini–VIMS: III – Radial compositional variability. *Icarus* 220, 1064–1096. <https://doi.org/10.1016/j.icarus.2012.06.040>
- Grenfell, T.C., Neshyba, S.P., Warren, S.G., 2005. Representation of a nonspherical ice particle by a collection of independent spheres for scattering and absorption of radiation: 3. Hollow columns and plates. *Journal of Geophysical Research: Atmospheres* 110. <https://doi.org/10.1029/2005JD005811>
- Grenfell, T.C., Warren, S.G., 1999. Representation of a nonspherical ice particle by a collection of independent spheres for scattering and absorption of radiation. *Journal of Geophysical Research: Atmospheres* 104, 31697–31709. <https://doi.org/10.1029/1999JD900496>
- Grundy, W.M., Fink, U., 1991. A new spectrum of Triton near the time of the Voyager encounter. *Icarus* 93, 379–385. [https://doi.org/10.1016/0019-1035\(91\)90220-N](https://doi.org/10.1016/0019-1035(91)90220-N)
- Grundy, W.M., Schmitt, B., 1998. The temperature-dependent near-infrared absorption spectrum of hexagonal H₂O ice. *Journal of Geophysical Research: Planets* 103, 25809–25822. <https://doi.org/10.1029/98JE00738>
- Gundlach, B., Blum, J., 2013. A new method to determine the grain size of planetary regolith. *Icarus* 223, 479–492. <https://doi.org/10.1016/j.icarus.2012.11.039>
- Hansen, G.B., 2009. Calculation of single-scattering albedos: Comparison of Mie results with Hapke approximations. *Icarus* 203, 672–676. <https://doi.org/10.1016/j.icarus.2009.05.025>
- Hansen, G.B., McCord, T.B., 2004. Amorphous and crystalline ice on the Galilean satellites: A balance between thermal and radiolytic processes. *Journal of Geophysical Research: Planets* 109. <https://doi.org/10.1029/2003JE002149>
- Hapke, B., 1981. Bidirectional reflectance spectroscopy: 1. Theory. *Journal of Geophysical Research: Solid Earth* 86, 3039–3054. <https://doi.org/10.1029/JB086iB04p03039>
- Hapke, B., 1993. *Theory of Reflectance and Emittance Spectroscopy*, Topics in Remote Sensing. Cambridge University Press, Cambridge. <https://doi.org/10.1017/CBO9780511524998>

- Hapke, B., 2012. *Theory of Reflectance and Emittance Spectroscopy*, 2nd ed. Cambridge University Press, Cambridge. <https://doi.org/10.1017/CBO9781139025683>
- Harris, C.R., Millman, K.J., van der Walt, S.J., Gommers, R., Virtanen, P., Cournapeau, D., Wieser, E., Taylor, J., Berg, S., Smith, N.J., Kern, R., Picus, M., Hoyer, S., van Kerkwijk, M.H., Brett, M., Haldane, A., del Río, J.F., Wiebe, M., Peterson, P., Gérard-Marchant, P., Sheppard, K., Reddy, T., Weckesser, W., Abbasi, H., Gohlke, C., Oliphant, T.E., 2020. Array programming with NumPy. *Nature* 585, 357–362. <https://doi.org/10.1038/s41586-020-2649-2>
- Herbst, E., 2001. The chemistry of interstellar space. *Chem. Soc. Rev.* 30, 168–176. <https://doi.org/10.1039/A909040A>
- Hudgins, D.M., Sandford, S.A., Allamandola, L.J., Tielens, A.G.G.M., 1993. Mid- and Far-Infrared Spectroscopy of Ices: Optical Constants and Integrated Absorbances. *The Astrophysical Journal Supplement Series* 86, 713. <https://doi.org/10.1086/191796>
- Hunter, J.D., 2007. Matplotlib: A 2D Graphics Environment. *Computing in Science & Engineering* 9, 90–95. <https://doi.org/10.1109/MCSE.2007.55>
- Joseph, J.H., Wiscombe, W.J., Weinman, J.A., 1976. The Delta-Eddington Approximation for Radiative Flux Transfer. *Journal of the Atmospheric Sciences* 33, 2452–2459. [https://doi.org/10.1175/1520-0469\(1976\)033<2452:TDEAFR>2.0.CO;2](https://doi.org/10.1175/1520-0469(1976)033<2452:TDEAFR>2.0.CO;2)
- Kofman, V., He, J., Kate, I.L. ten, Linnartz, H., 2019. The Refractive Index of Amorphous and Crystalline Water Ice in the UV–vis. *ApJ* 875, 131. <https://doi.org/10.3847/1538-4357/ab0d89>
- Lawrence, S.J., Lucey, P.G., 2007. Radiative transfer mixing models of meteoritic assemblages. *Journal of Geophysical Research: Planets* 112. <https://doi.org/10.1029/2006JE002765>
- Li, S., Li, L., 2011. Radiative transfer modeling for quantifying lunar surface minerals, particle size, and submicroscopic metallic Fe. *Journal of Geophysical Research: Planets* 116. <https://doi.org/10.1029/2011JE003837>
- Lucey, P.G., 1998. Model near-infrared optical constants of olivine and pyroxene as a function of iron content. *Journal of Geophysical Research: Planets* 103, 1703–1713. <https://doi.org/10.1029/97JE03145>
- Mastrapa, R.M., Bernstein, M.P., Sandford, S.A., Roush, T.L., Cruikshank, D.P., Ore, C.M.D., 2008. Optical constants of amorphous and crystalline H₂O-ice in the near infrared from 1.1 to 2.6 μm . *Icarus* 197, 307–320. <https://doi.org/10.1016/j.icarus.2008.04.008>

- Mastrapa, R.M., Sandford, S.A., Roush, T.L., Cruikshank, D.P., Dalle Ore, C.M., 2009. Optical Constants of Amorphous and Crystalline H₂O-ice: 2.5-22 μm (4000-455 cm^{-1}) Optical Constants of H₂O-ice. *The Astrophysical Journal* 701, 1347–1356. <https://doi.org/10.1088/0004-637X/701/2/1347>
- Melamed, N.T., 1963. Optical Properties of Powders. Part I. Optical Absorption Coefficients and the Absolute Value of the Diffuse Reflectance. Part II. Properties of Luminescent Powders. *Journal of Applied Physics* 34, 560–570. <https://doi.org/10.1063/1.1729309>
- Merlin, F., Barucci, M.A., de Bergh, C., Fornasier, S., Doressoundiram, A., Perna, D., Protopapa, S., 2010. Surface composition and physical properties of several trans-neptunian objects from the Hapke scattering theory and Shkuratov model. *Icarus* 208, 945–954. <https://doi.org/10.1016/j.icarus.2010.03.014>
- Mie, G., 1908. Beiträge zur Optik trüber Medien, speziell kolloidaler Metallösungen. *Annalen der Physik* 330, 377–445. <https://doi.org/10.1002/andp.19083300302>
- Mustard, J.F., Glotch, T.D., 2019. Theory of Reflectance and Emittance Spectroscopy of Geologic Materials in the Visible and Infrared Regions, in: Bell III, J.F., Bishop, J.L., Moersch, J.E. (Eds.), *Remote Compositional Analysis: Techniques for Understanding Spectroscopy, Mineralogy, and Geochemistry of Planetary Surfaces*, Cambridge Planetary Science. Cambridge University Press, Cambridge, pp. 21–41. <https://doi.org/10.1017/9781316888872.004>
- Neshyba, S.P., Grenfell, T.C., Warren, S.G., 2003. Representation of a nonspherical ice particle by a collection of independent spheres for scattering and absorption of radiation: 2. Hexagonal columns and plates. *Journal of Geophysical Research: Atmospheres* 108. <https://doi.org/10.1029/2002JD003302>
- Powell, M.J.D., 1970. A hybrid method for nonlinear equations. *Numerical Methods for Nonlinear Algebraic Equations* p 87-114
- Protopapa, S., Grundy, W.M., Reuter, D.C., Hamilton, D.P., Dalle Ore, C.M., Cook, J.C., Cruikshank, D.P., Schmitt, B., Philippe, S., Quirico, E., Binzel, R.P., Earle, A.M., Ennico, K., Howett, C.J.A., Lunsford, A.W., Olkin, C.B., Parker, A., Singer, K.N., Stern, A., Verbiscer, A.J., Weaver, H.A., Young, L.A., 2017. Pluto's global surface composition through pixel-by-pixel Hapke modeling of New Horizons Ralph/LEISA data. *Icarus, Special Issue: The Pluto System* 287, 218–228. <https://doi.org/10.1016/j.icarus.2016.11.028>
- Raponi, A., Ciarniello, M., Capaccioni, F., Filacchione, G., Tosi, F., De Sanctis, M.C., Capria, M.T., Barucci, M.A., Longobardo, A., Palomba, E., Kappel, D., Arnold, G., Mottola, S., Rousseau, B., Quirico, E., Rinaldi, G., Erard, S., Bockelee-Morvan, D., Leyrat, C., 2016. The temporal evolution of exposed water ice-rich areas on the surface of 67P/Churyumov–Gerasimenko: spectral analysis. *Monthly Notices of the Royal Astronomical Society* 462, S476–S490. <https://doi.org/10.1093/mnras/stw3281>

- Roush, T.L., 1994. Charon: More than Water Ice? *Icarus* 108, 243–254. <https://doi.org/10.1006/icar.1994.1059>
- Roush, T.L., Esposito, F., Rossman, G.R., Colangeli, L., 2007. Estimated optical constants of gypsum in the regions of weak absorptions: Application of scattering theories and comparisons to independent measurements. *Journal of Geophysical Research: Planets* 112. <https://doi.org/10.1029/2007JE002920>
- Savitzky, Abraham., Golay, M.J.E., 1964. Smoothing and Differentiation of Data by Simplified Least Squares Procedures. *Anal. Chem.* 36, 1627–1639. <https://doi.org/10.1021/ac60214a047>
- Schmitt, B., Quirico, E., Trotta, F., Grundy, W.M., 1998. Optical Properties of Ices From UV to Infrared, in: Schmitt, B., De Bergh, C., Festou, M. (Eds.), *Solar System Ices: Based on Reviews Presented at the International Symposium “Solar System Ices” Held in Toulouse, France, on March 27–30, 1995*, Astrophysics and Space Science Library. Springer Netherlands, Dordrecht, pp. 199–240. https://doi.org/10.1007/978-94-011-5252-5_9
- Sharkey, B.N.L., Reddy, V., Sanchez, J.A., Izawa, M.R.M., Emery, J.P., 2019. Compositional Constraints for Lucy Mission Trojan Asteroids via Near-infrared Spectroscopy. *AJ* 158, 204. <https://doi.org/10.3847/1538-3881/ab46c0>
- Shepard, M.K. (Ed.), 2017. *The Physical Basis of Photometric Scattering Models*, in: *Introduction to Planetary Photometry*. Cambridge University Press, Cambridge, pp. 95–130. <https://doi.org/10.1017/9781316443545.005>
- Shepard, M.K., Helfenstein, P., 2007. A test of the Hapke photometric model. *Journal of Geophysical Research: Planets* 112. <https://doi.org/10.1029/2005JE002625>
- Shkuratov, Y.G., Grynko, Y.S., 2005. Light scattering by media composed of semitransparent particles of different shapes in ray optics approximation: consequences for spectroscopy, photometry, and polarimetry of planetary regoliths. *Icarus, Hapke Symposium* 173, 16–28. <https://doi.org/10.1016/j.icarus.2003.12.022>
- Tegler, S.C., Cornelison, D.M., Grundy, W.M., Romanishin, W., Abernathy, M.R., Bovyn, M.J., Burt, J.A., Evans, D.E., Maleszewski, C.K., Thompson, Z., Vilas, F., 2010. Methane and Nitrogen Abundances on Pluto and Eris. *ApJ* 725, 1296–1305. <https://doi.org/10.1088/0004-637X/725/1/1296>
- Virtanen, P., Gommers, R., Oliphant, T.E., Haberland, M., Reddy, T., Cournapeau, D., Burovski, E., Peterson, P., Weckesser, W., Bright, J., van der Walt, S.J., Brett, M., Wilson, J., Millman, K.J., Mayorov, N., Nelson, A.R.J., Jones, E., Kern, R., Larson, E., Carey, C.J., Polat, İ., Feng, Y., Moore, E.W., VanderPlas, J., Laxalde, D., Perktold, J., Cimrman, R., Henriksen, I., Quintero, E.A., Harris, C.R., Archibald, A.M., Ribeiro, A.H., Pedregosa, F., van Mulbregt, P., 2020. SciPy 1.0: fundamental algorithms for scientific computing in Python. *Nat Methods* 17, 261–272. <https://doi.org/10.1038/s41592-019-0686-2>

Wiscombe, W.J., 1979. Mie scattering calculations: Advances in technique and fast, vector-speed computer codes. Atmospheric Analysis and Prediction Division, National Center for Atmospheric Research.

Wiscombe, W.J., Warren, S.G., 1980. A Model for the Spectral Albedo of Snow. I: Pure Snow. *Journal of the Atmospheric Sciences* 37, 2712–2733. [https://doi.org/10.1175/1520-0469\(1980\)037<2712:AMFTSA>2.0.CO;2](https://doi.org/10.1175/1520-0469(1980)037<2712:AMFTSA>2.0.CO;2)

Chapter 4

Pluto's Surface Mapping using Unsupervised Learning from Near-Infrared Observations of LEISA/Ralph

A. Emran¹, C. M. Dalle Ore², C. J. Ahrens³, M. K. H. Khan⁴, V. F. Chevrier¹, and D. P. Cruikshank⁵

¹ Space and Planetary Sciences, University of Arkansas, Fayetteville, AR 72701, USA.

² Carl Sagan Center at the SETI Institute, Mountain View, CA 94043, USA.

³ NASA Goddard Space Flight Center, Greenbelt, MD 20771, USA.

⁴ Department of Mathematical Sciences, University of Arkansas, Fayetteville, AR 72701, USA.

⁵ Department of Physics, University of Central Florida, Orlando, FL 32816, USA.

[Under Revision in The Planetary Science Journal]

Abstract

We map the surface of Pluto using an unsupervised machine learning technique from the near-infrared observations of the LEISA/Ralph instrument onboard NASA's New Horizons spacecraft. The principal component reduced Gaussian mixture model was implemented to investigate the geographic distribution of the surface units across the dwarf planet. We also present the likelihood of each surface unit at the image pixel level. Average I/F spectra of each unit were analyzed – in terms of the position and strengths of absorption bands of abundant volatiles such as N₂, CH₄, and CO and nonvolatile H₂O – to connect the unit to surface composition, geology, and geographic location. The distribution of surface units shows a latitudinal pattern with distinct surface compositions of volatiles – consistent with the existing literature. However, previous mapping

efforts were based primarily on compositional analysis using spectral indices (indicators) or implementation of complex radiative transfer models, which need (prior) expert knowledge, label data, or optical constants of representative endmembers. We prove that an application of unsupervised learning in this instance renders a satisfactory result in mapping the spatial distribution of ice compositions without any prior information or label data. Thus, such an application is specifically advantageous for a planetary surface mapping when label data are poorly constrained or completely unknown, because an understanding of surface material distribution is vital for volatile transport modeling at the planetary scale. We emphasize that the unsupervised learning used in this study has wide applicability and can be expanded to other planetary bodies of the solar system for mapping surface material distribution.

Unified Astronomy Thesaurus concepts: Pluto (7777); Surface ices (2117); Astronomy data analysis (1858); Astrostatistics techniques (1886); Astroinformatics (78)

4.1. Introduction

Pluto, a dwarf planet and largest trans-Neptunian object (TNO), is one of the fascinating outer solar system bodies in the Kuiper Belt. The dwarf planet exhibits abundances of volatile and nonvolatile ices on its surface with different spatial abundance and geographic distributions (Stern et al., 2015; Moore et al., 2016; Grundy et al., 2016). The presence and distribution of these various ice compositions are associated with some form of surface geological processes and seasonal interaction with the tenuous atmosphere, driven by the climate cycle of the dwarf planet (Moore et al., 2016; Schmitt et al., 2017; Binzel et al., 2017). Thus, mapping the spatial distribution of the ices and their relationship with surface geology and atmospheres is vital for a better understanding of the volatile transport models on the dwarf planet (Bertrand and Forget 2016). Accordingly, over

the past decades, the spatial distribution of surface materials has been observed from the spectra at visible (VIS) and near-infrared (NIR) wavelengths from both ground-based telescopes and New Horizons fly-by to analyze the geographic distribution of ices on Pluto (see Cruikshank et al., 2015, 2019, and 2021 for a comprehensive review).

In the conditions on Pluto's surface, nitrogen (N_2), methane (CH_4), and carbon monoxide (CO) ices are the most abundant volatile materials (Stern et al., 2018). Among these volatiles, CH_4 ice has several strong absorptions bands at NIR wavelengths, such as 1.30 – 1.43 μm (region 1), 1.59 – 1.83 μm (region 2), 1.90 – 2.0 μm (region 3), and 2.09 – 2.48 μm (region 4) which have been utilized to characterize CH_4 ice on Pluto by previous studies (see Schmitt et al., 2017 and Scipioni et al., 2021). These characteristic absorption bands of CH_4 are also covered by the near-infrared spectrometer instruments onboard NASA's New Horizons spacecraft. N_2 ice can be detected by the presence of a 2.15 μm absorption band and CO by the 2.35 and 1.58 μm absorption bands, which have also been observed by ground-based facilities (Owen et al., 1993). Besides the volatile materials of CH_4 , N_2 , and CO , Pluto's surface hosts photochemically formed organic hydrocarbon called tholins and a trace amount of ethane (C_2H_6) and water (H_2O) ice (Merlin, 2015; Cook et al., 2019). H_2O ice acts as nonvolatile ice on Pluto's surface and the geology of rugged terrain and undulating morphology of the dwarf planet indicate that H_2O ice forms the supporting bedrock for the surface volatiles (Stern et al., 2015; Spencer et al., 2020). The equatorial-colored area of Pluto represents the residue of deposited tholins which are assumed to form due to the ultra-violet (UV) or charged-particle irradiation and energetic processing of (both likely atmospheric or surface processes) methane and nitrogen (Cruikshank et al., 2005).

Before NASA's New Horizons spacecraft's flyby in 2015, Pluto was studied from ground-based observation or space telescope such as Hubble Space Telescope (HST). For instance, methane was first identified on the surface of Pluto from ground-based observations (Cruikshank et al., 1976), followed by the identification of nitrogen and carbon monoxide ice (Owen et al., 1993). However, owing to the lack of the resolution needed, a detailed disk resolved surface mapping was not possible with these ground and space-based observations. Thus, constraining the latitudinal distribution of surface ices was not possible due to the dearth of resolution needed to resolve the surface. NASA's New Horizons spacecraft returned an unprecedented amount of data to Earth for analysis that paved the way to study the surface of Pluto (and its satellites) in finer detail. The initial results of the flyby mission can be found in Stern et al. (2015) and Grundy et al. (2016), and a comprehensive review can also be found in Stern et al. (2018) and Stern et al. (2021).

Efforts have been put forward to map the surface composition and materials on Pluto from the NIR hyperspectral spectra from the Lisa Hardaway Infrared Mapping Spectrometer (LEISA) instrument, a part of the Ralph instrument package (Reuter et al. 2008) onboard New Horizons. For instance, Grundy et al. (2016) used band depths measurement to map the surface distribution of CH₄, N₂, and CO on Pluto's encounter hemisphere. Schmitt et al (2017) used principal component analysis (PCA), spectral indicators, and correlation plots to study the distribution and physical state of ices, both volatile and nonvolatile, on Pluto's illuminated disk. Protopapa et al. (2017) used radiative transfer modeling (Hapke, 1993) on LEISA spectra to derive the spatial distribution and grain sizes of volatile and nonvolatile ices on Pluto's surface. Recently, Gabasova et al. (2021) used the intensity-based registration technique to the lower resolution data to make a global qualitative compositional map for surface ices. However, existing mapping efforts on the

spatial distribution of ices are mostly accomplished from the compositional analysis using spectral indices (e.g., band depth) or an application of complex radiative transfer modeling (RTMs). An implication of these techniques requires reliable label data, spectral endmembers, or prior knowledge about the spectral characteristics of the representative surface composition.

The convenience of a machine learning technique lies in the potential to analyze large dimensional datasets more efficiently and effectively. Unsupervised learning, such as a clustering analysis (Marzo et al., 2006, 2008, 2009), is one of the widely used methods adopted to map the surface of planetary bodies. The unique advantage of unsupervised learning is that it does not need any label data or prior information. The unsupervised method utilizes the inherent characteristics of the data itself to recognize unseen but meaningful information in the data. Unsupervised spectral K-means clustering has successfully been used to characterize the surface of Mars (Marzo et al., 2006), asteroids Bennu (Rizos et al., 2019) and Ceres (Rizos et al., 2021), Saturn's moon Iapetus (Pinilla-Alonso et al., 2011), Pluto (Dalle Ore et al., 2019) and its largest satellite Charon (Dalle Ore et al., 2018). However, even though having the merit of fast computation and satisfactory results in many instances, the K-means clustering has its inherent limitations. The K-means clustering uses a rigid segmentation algorithm which may not effectively be used with many real-world datasets. Moreover, the K-means algorithm may not capture the inherent heterogeneity of the datasets and does not work well if the data has a complex non-linear pattern (see Patel and Kushwaha (2020) for an assessment of the performance of K-means clustering).

As an alternative unsupervised clustering and classification scheme, the Gaussian mixture model (GMM; Berge and Schistad Solberg, 2006; Li et al., 2014) has been used for hyperspectral images

like the LEISA data. GMM uses a probabilistic approach which assumes each data point comes from a mixture of a finite normal distribution with unknown parameters (Patel and Kushwaha, 2020). GMM can uncover complex patterns, trace inherent heterogeneity, and group the data into cohesive components such that the clusters are a very close representation of the real world (Patel and Kushwaha, 2020). Moreover, for overlapping clusters, GMM performs considerably better than the K-means algorithm because K-means split the data into k non-overlapping groups while the GMM can infer probabilities for the overlapping clusters.

However, the implementation of GMM to higher dimensionality (i.e., hyperspectral) data constrains its wide applicability due to the impractically large size of the parameter space (Li et al., 2014) and to the component distribution, formalized as a probability density function in a mixture model (Alqahtani and Kalantan, 2020). Moreover, working with big and higher-dimensional data is challenging, computationally expensive, and time-consuming. Thus, efficient dimensional reduction methods such as Principal component analysis (PCA; Pearson, 1901) are widely used to reduce data dimension, keeping much of the possible variance in the original data, which can further be used for classification or clustering schemes. Of late, similar implementation of principal component reduced Gaussian mixture models (hereafter we refer to as PC-GMM), an unsupervised machine learning approach, has demonstrated to be satisfactory in many scientific fields (Alqahtani and Kalantan, 2020; Hertrich et al., 2022).

This study implements the PC reduced GMM to map the surface distribution of ices. The basic framework of PC-GMM used in this study is that we first apply PCA to reduce the higher dimension LEISA data to a lower dimension and then implement the GMM to that principal

component reduced data. We provide the likelihood of the surface units at pixel scales, which gives an insight into a deeper understanding of the distribution of ices on Pluto's surface. We then extract I/F spectra of the surface units and analyze them in terms of the position and strengths of absorption bands of abundant volatiles such as N₂, CH₄, and CO and nonvolatile H₂O. An interpretation of the connection of the clusters to surface composition, geology, and location (latitudes and longitudes) is provided subsequently. We also compare the result of surface mapping from the PC-GMM to the existing surface compositional mapping results.

4.2. Observations

We use spatially resolved hyperspectral scenes from the LEISA instrument (Reuter et al., 2008) that cover the entire disk of Pluto. LEISA is a wedged etalon infrared spectral imager with a 256 x 256-pixel detector array, scans at 0.9° × 0.9° FOV, and operates in a push-broom mode. The instrument filter has two segments: one with wavelengths range of 1.25 - 2.5 μm and another is 2.1 - 2.25 μm at the spectral resolving power (wavelength / Δ wavelength) $\lambda/\Delta \lambda = 240$ and 560, respectively. We use the lower resolution wavelength segment (1.25 - 2.5 μm with the $\lambda/\Delta \lambda = 240$) which has been used to map the distribution of ices of CH₄, N₂, CO, and H₂O over the surface of the dwarf planet and H₂O frost on Pluto's largest satellite Charon. The two LEISA scenes, originally at a spatial resolution of 6 and 7 km/pixels, used in this study were taken at ~100,000 km from the surface during the New Horizon's Pluto encounter period in July 2015. The details of the datasets used are given in Table 4.1.

Table 4.1. Details of the two LEISA scenes used in this study.

MET	Scan name	UT date and time	Range (km)	Sub S/C Lon (°)	Sub S/C Lat (°)
0299172014	P_LEISA_Alice_2a	2015-07-14 09:33:05	112742	158.62	38.52
0299172889	P_LEISA_Alice_2b	2015-07-14 09:48:16	100297	158.81	37.91

The two image scenes were processed and calibrated with the mission data pipeline processing routine including bad pixel masking, background noise cleaning, flat fielding, and conversion of DN to radiance factor (*RADF*; commonly known as I/F). The images were then projected to a common orthographic viewing geometry appropriate to the mid-time between them using the United States Geological Survey's (USGS) Integrated Software for Imagers and Spectrometers (ISISv3) software package. For details on the LEISA data processing and reduction, please see Schmitt et al. (2017), Protopapa et al. (2017), and Cook et al. (2019).

We use the derived LEISA data (I/F) products generated by the New Horizons Pluto encounter surface compositional science theme team (Stern, 2018) available at NASA PDS: Small Bodies Node¹. The dataset consists of the spatial-spectral I/F cubes at the spatial dimension of 800 x 800 pixels and the spectral dimension of 256 wavelength bands. Note that the derived data products were reprojected at a higher spatial resolution (using the nearest neighbor resampling algorithm) than the native LEISA data to minimize the loss of spatial information during projecting the scenes in orthographic viewing geometry (Schmitt et al., 2017). Thus, the derived product we used in this study has about 2 – 3 times greater spatial resolution than the original. The lower spectral resolution of the 1.25 - 2.5 μm wavelength segment used in the study consists of 0 - 196 channels

¹<https://pds-smallbodies.astro.umd.edu/>

(# 200 – 255 channels cover wavelengths between 2.10 and 2.25 μm at higher spectral resolution). Note that some of the spectral channels (e.g., # 1, 2, 198) were excluded from the original I/F cube because of a strong photometric calibration caveat at these spectral bands (Schmitt et al., 2017). The two LEISA scenes used in this study overlap and cross through Sputnik Planitia (SP) and we cut the image cubes and joined them together (Fig. 4.1) in a similar fashion to that by Schmitt et al. (2017).

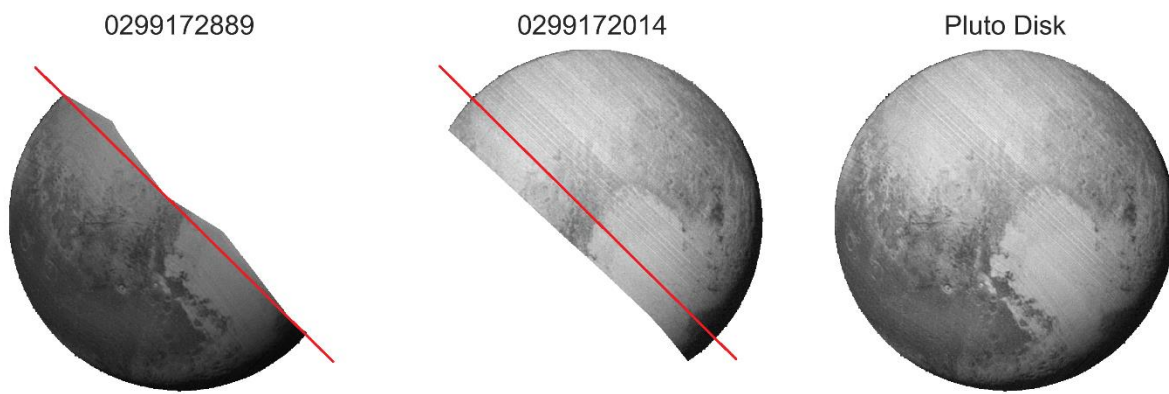


Fig. 4.1: Images of two LEISA cubes at a band at 2 μm and mosaics covering the entire Pluto disk, adopted from Schmitt et al. (2017). The image cubes are projected to a common orthographic viewing geometry appropriate to mid-time between scenes. The red line represents the overlapping line where the image cubes were cut and joined together side by side.

4.3. Methodology

The radiance I/F data were converted to reflectance factor (*REFF*) by dividing the I/F cube by the cosine of the incident angle as defined by Hapke (2012) following the equation for Lambertian photometry (isotropic scattering from the surface). This correction minimizes the effect of solar irradiation on the reflected radiance and represents the intrinsic photometric properties of surface materials and has been successfully implemented on Pluto for the same LEISA image datasets (Schmitt et al., 2017). The I/F data cubes were further calibrated by the scaling factor of LEISA radiometric calibration of 0.74 ± 0.05 (Protopapa et al., 2020). We also excluded the pixels that

correspond to an incident angle of greater than 85° (and belong to a strongly shadowed area; see the Pluto disk in Fig. 4.1) since such weakly illuminated areas result in a noisier reflected signal and strongly affect the photometric properties of *REFF* (Schmitt et al., 2017). Very few scattered pixels at some spectral bands ($\sim 0.03\%$ of the entire observations) show no data values inside Pluto’s illuminated disk and they were filled in using the linear interpolation technique for each pixel location. Note that no data values were found in some spectral bands not all the bands at a particular pixel. Thus, we did not need to interpolate values for all spectral bands at a pixel based on the values of the nearest pixels rather we fill the missing spectral band values based on the values of other spectral bands at that pixel. We emphasize that this gap-filling of a few scattered pixels does not change the original data characteristics.

4.3.1. Principal component reduced Gaussian mixture model (PC-GMM)

With the implementation of PC-GMM, we reduce the higher dimension LESIA data to a lower dimensionality dataset (of an order of tens) using a principal component analysis. For convenience, we present the conceptual frameworks of the mathematical formulation of the PCA. The original input dataset is considered to be a matrix of Y . In what follows, $Y \in \mathbb{R}^{n \times m}$ where $Y_i = (Y_{i1}, Y_{i2}, \dots, Y_{id})^T$ for $i = 1, 2, \dots, n$, and m is the data dimension. If the rank of the matrix is r where $r \leq \min(n, m)$, then the principal components (Abdi and Williams, 2010) of Y can be computed using the singular value decomposition given by:

$$Y = U\Sigma W^T \quad (1)$$

where Σ is the $r \times r$ diagonal matrix whose diagonal entries are the nonzero singular values $\{\sigma_l: l = 1, 2, \dots, r\}$ with $\sigma_1 \geq \sigma_2 \geq \dots \geq \sigma_r$, U is the $n \times r$ matrix of left singular vectors, and W is the $m \times r$ matrix of right singular vectors. Thus, the full principal components decomposition of Y can be written as:

$$P = YW = U\Sigma W^T W = U\Sigma \quad (2)$$

We use the scikit-learn (Pedregosa et al., 2011) python module to implement the PCA on the LEISA cube data. To this end, we first standardize the *REFF* data since standardization is recommended before the implementation of PCA (e.g., Jolliffe and Cadima, 2016; Gewers et al., 2021). The standardization approach used here involves removing the mean and scaling the data to unit variance. We find that the axes of principal components (PC) up to the first four pc-axes encompass substantial surface information of the Pluto disk (Fig. 4.2). The pc-axes look largely similar to that of Schmitt et al. (2017). From pc#5 onward the pc-axes contain noisy data and, therefore, were not considered in the further analysis because their inclusion may mislead the further statistical analysis. The assignment of “noisy” data was accomplished subjectively by visually analyzing (qualitative) if the resultant pc-axes can represent the appearance of the underlying geomorphology of Pluto (visible structure/feature) seen in the basemap. We plot the variance for the pc-axes showing that with the first four pc-axes it covers 92.93% of the total variance of the data and incorporate a scree plot in determining the optimum number of pc-axes (see Fig. 4A1 in Appendix). Moreover, from pc#4 onward the cumulative explained variance shows a fairly gentle increase – no substantial information will be gained if a higher number of components is included in the analysis. We consider the report of cumulative explained variance

as a function of pc-axes, scree plot, and visual inspection of the pc-axis in choosing the number of pc-axes to use in this study.

Once the principal components are calculated, we implement the multivariate Gaussian mixture model to the first four pc-axes. For convenience, we present the conceptual framework for the mathematical formulation of multivariate GMM. The pc-axes are considered as a matrix of X . For what follows, $X \in \mathbb{R}^{n \times d}$ and $X_i = (X_{i1}, X_{i2}, \dots, X_{id})^T$ for $i = 1, 2, \dots, n$. The multivariate Gaussian mixture distribution of n independent observations can be written as:

$$X_i | z_i = j \sim N_d(X_i | \mu_j, \Sigma_j) \quad (3)$$

where $z_i \in \{1, 2, \dots, k\}$ is the latent variable representing the mixture component for X_i , k is the total number of mixture components, $p(z_i = j) = \pi_j$ with $\sum_{j=1}^k \pi_j = 1$, μ_j and Σ_j are the mean vector of length d and the $d \times d$ covariance matrix of the j -th component, respectively, and N_d is the d -dimensional Gaussian distribution. The marginal distribution of X_i integrating out of z_i can be written as:

$$p(X_i) = \sum_{j=1}^k p(X_i, z_i = j) = \sum_{j=1}^k p(z_i = j) p(X_i | z_i = j) = \sum_{j=1}^k \pi_j N_d(X_i | \mu_j, \Sigma_j) \quad (4)$$

which is the k -component multivariate Gaussian mixture model (e.g., Bishop and Nasrabadi 2006) with the mixture weights $\{\pi_j\}_{j=1}^k$.

If the parameter to estimate is $\theta = \{\mu_1, \mu_2, \dots, \mu_k, \Sigma_1, \Sigma_2, \dots, \Sigma_k, \pi_1, \pi_2, \dots, \pi_k\}$, then the log-likelihood function can be written as:

$$l(\theta) = \sum_{i=1}^n \log \left(\sum_{j=1}^k \pi_j N_d(X_i | \mu_j, \Sigma_j) \right) \quad (5)$$

We use the expectation-maximization (EM; Dempster et al., 1977) algorithm to calculate the maximum likelihood estimator of the parameter θ . For convenience, we present the detailed EM algorithm in Appendix (Section 4A.2.).

We implement the *Gaussian Mixture Model* python module available in the scikit-learn (Pedregosa et al., 2011). The selection of the optimal number of gaussian components (GC) or clusters is one of the critical considerations for the implementation of GMM. Choosing the optimal number of clusters can be accomplished by evaluating the Akaike information criterion (AIC) and Bayesian information criterion (BIC) values for the applied models. In machine learning, BIC and AIC diagnoses are also treated as internal cluster validation measures/ indicators in evaluating the quality of the modeled clustering structure. Internal cluster validation measures (e.g., BIC) have been instigated in astrophysical data problems for the implementation of a probabilistic gaussian mixture model (e.g., de Souza et al., 2017). In this study, we utilize both BIC and AIC measures in determining the optimal number of clusters to use for GMM on the pc-axes (and as an indicator of internal cluster validation).

The AIC provides an estimation of the prediction error by an implemented model and thus indicates the relative goodness of the model in fitting the data upon which the model was built. The calculation of AIC is based on maximum likelihood criteria (Akaike, 1974) given as:

$$AIC = -2\log(\hat{L}) + 2d \quad (10)$$

where \hat{L} is the maximized value of the likelihood function and d is the total number of (independently adjusted) parameters. The concept of BIC is closely aligned to AIC since the BIC is also based on the maximum likelihood function and calculated as (Schwarz, 1978):

$$BIC = -2\log(\hat{L}) + \log(N)d \quad (11)$$

where N is the total number of observations.

Both AIC and BIC penalize the model if it incorporates overfitting. However, the penalty is more extreme for BIC as it heavily penalizes the model complexity (Bishop and Nasrabadi, 2006). Typically, the best model minimizes AIC values; a lower AIC value corresponds to a better fit (Liddle, 2007). Conversely, the first local minima of BIC value is considered the optimal number of clusters (Dasgupta and Raftery, 1998; Fraley and Raftery, 1998). Note that BIC values are also presented with an opposite sign by different studies (Fraley and Raftery, 1998), in which case the optimal number of clusters will be at the first local maxima. We choose the optimal number of clusters considering the AIC and BIC values – a lower AIC value and first local minima, respectively. Accordingly, the optimal number of the cluster in this instance was set at 8 (which agrees with both the AIC and BIC criteria). A plot of AIC and BIC values at different numbers of clusters is given in Appendix (Fig. 4A2).

In unsupervised learning, a goodness-of-fit diagnostic is required to validate the model further in simulating the original data. We provide an assessment of the model fit for the observed data in hand and its capabilities in predicting future datasets. To that end, we first simulate the input data (synthetically reproduces the original data structure) based on our implemented GMM model parameters for different gaussian component solutions i.e., numbers of clusters. In this instance,

we have observed data from the first 4 pc-axes used as the input data for GMM, and the predicted data were simulated from the resulting GMM model parameters. Then, we calculate the density for both observed and predicted data from multivariate kernel density estimates using the *kde* module of R in a python environment. Finally, we compare the estimated kernel densities for observed data against the predicted data by utilizing a linear fit for different GC solutions (see Fig. 4A3 in Appendix). A similar goodness-of-fit diagnostics for the probabilistic GMM has successfully been implemented in an astronomical problem (de Souza et al., 2017). We calculate the coefficient of determination (R^2) between the observed and predicted kernel density for 5 – 12 GC solutions (Fig. 4A3). The R^2 values for different GC solutions suggest that 8 GC solution renders the highest value of 0.96 – which suggests a good fit for the model.

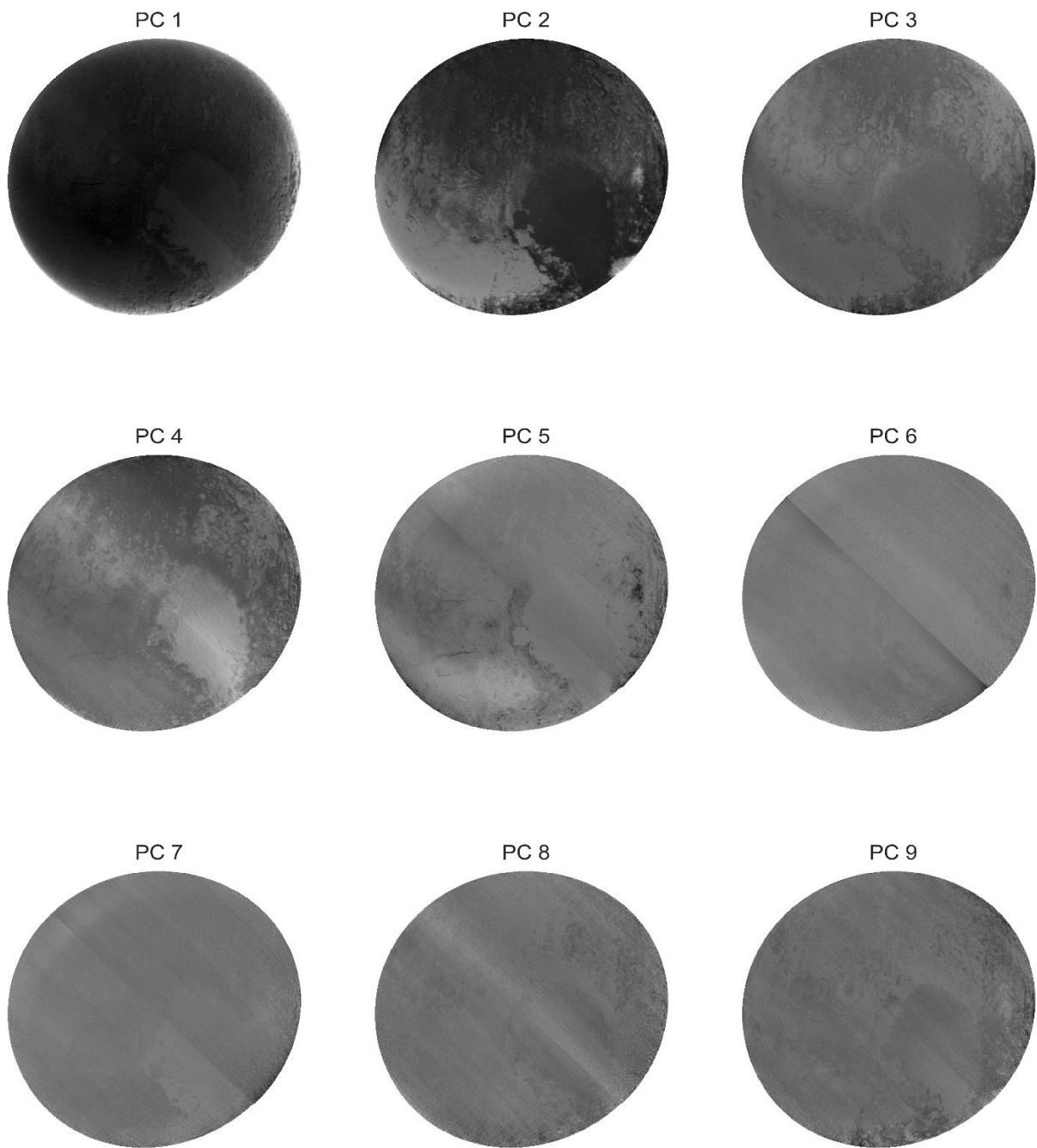


Fig. 4.2: The first nine principal components from LEISA *REFF* data cubes. Up to four pc-axes, the disks show substantial surface information (covers 92.93% total variance of the data). The pc#5 and onward components show noisy data therefore the pc-axes #5 and higher were not considered in the analysis. Note: the assignment of “noisy” data was accomplished subjectively by visually analyzing if pc-axes can represent the underlying geomorphology of Pluto.

4.4. Results

As suggested by the AIC and BIC values, we classify the entire Pluto's surface into eight representative surface units (Fig. 4.3). For the convenience of interpretation of the surface unit distribution, we hereafter call the surface unit by # followed by the assigned surface unit number. The surface units are distributed in different geographic regions (with different latitudinal and longitudinal extent) across the dwarf planet. Moreover, the distribution of the surface units coincides with the major geologic features e.g., basin, crater, montes, terra, etc. Note that some of the names of features and regions on Pluto used in this study are informal, while other names have been formally adopted by the Nomenclature Committee of the International Astronomical Union. We label the major geological features on the reference map in Fig. 4.3, however, to reference local scale geologic features, a basemap showing the names of all geologic provinces and features on Pluto was added in Appendix (Fig. 4A4).

The north polar region around Lowell Regio is a distinct surface unit (#2) that extends up to Voyager Terra to the south. Roughly, the north polar unit runs from the pole to $\sim 60^\circ$ N. Likewise, the equatorial Cthulhu Macula (or simply Cthulhu) – located in the western part of SP and spans between $\sim 15^\circ$ S to 12° N – exhibits a separate surface unit (#7). The surface unit #6 covers a large part of Sputnik Planitia and a portion of the northern mid-latitudes at Venera Terra (between $\sim 45^\circ$ to 60° N). However, the surface unit in the northern mid-latitudes at Pioneer Terra (below the Lowell Regio) belongs to #8 – extending at the latitudes of ~ 30 to 70° N with varying widths at different longitudes. Tombaugh Regio – located in the south and eastern part of SP (between $\sim 15^\circ$ S to 30° N latitudes) – indicates a distinct surface unit (#5). The eastern and southern limbs of the Pluto disk, including the Tartarus Dorsa region, belong to surface unit #1. This unit follows a narrow strip along the limb of Pluto's illuminated disk during the New Horizon flyby in 2015.

The broader region between the Cthulhu Macula (stretching from the latitude of Elliot crater and Virgil Fossae) and the latitude of the Burney crater shows a distinct surface unit (#4). This unit follows a latitudinal pattern and stretches between ~ 10 to 35° N. The mountains at the western fringe of the SP such as Baret Montes, Al-Idrisi Montes, Hillary Montes, etc belong to #4. Note that a narrow strip of #8 is placed (also seen in the base of the Burney crater) in between the surface units of #4 and #6. Kiladze crater, Krun Macula, inner rims of Oort crater, and the parallel stripe region following the south of the Cthulhu Macula belong to surface unit #3. The mountains (e.g., Pigafetta Montes) and small depressions (probably small craters) in the Cthulhu Macula and some patchy spots in Tombaugh Regio (smaller fraction) are also part of #3.

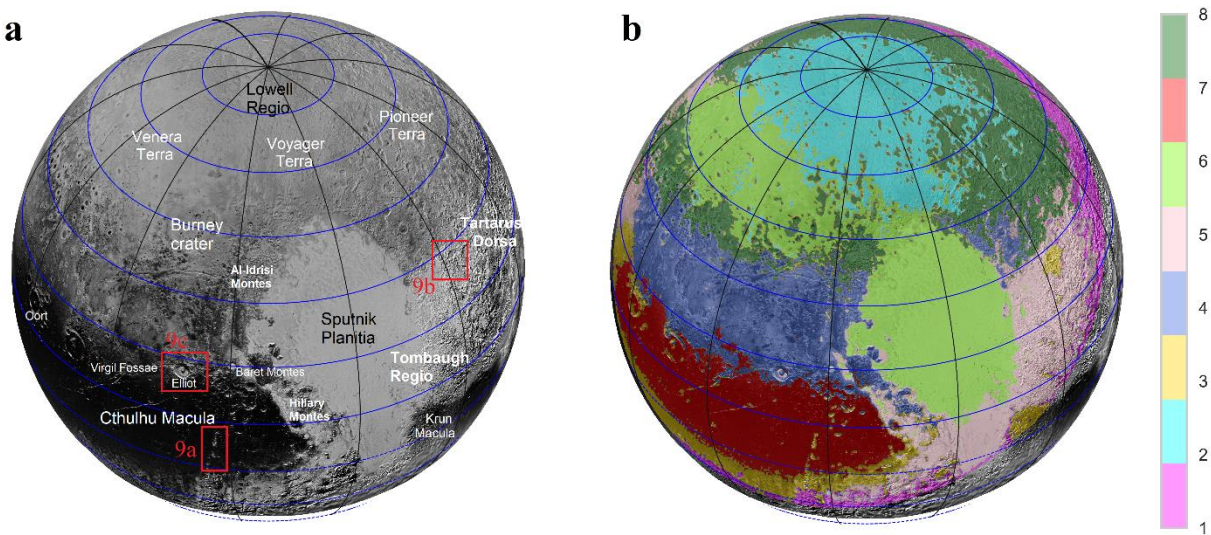


Fig. 4.3: Long Range Reconnaissance Imager (LORRI) higher resolution (panchromatic) basemap projected to LEISA scenes (a). The LORRI base map is labeled with latitude (blue) & longitude (black) grid and formal & informal names of major geomorphic features. The red rectangles represent the reference locations in Fig. 4.9. Eight surface units were found on Pluto using PC-GMM (b). The surface units follow the latitudinal pattern and are consistent with broad geographic regions and geologic features. The north pole at Lowell Regio, Cthulhu Macula, Tombaugh Regio, Sputnik Planitia and Venera Terra, and Pioneer Terra region show distinct surface units. The values in the legend indicate the assigned surface unit number. Note: the lower right region belongs to strongly shadowed areas and, thus, the pixels at these locations were excluded from the map (see the text for a detailed explanation).

Because the GMM employs probability distribution, we provide the likelihood of each surface unit at the LEISA pixel level (Fig. 4.4). While predicting the probability, the GMM algorithm treats each surface unit as a Gaussian component and infers the likelihood based on the estimated component density for every pixel. The probability subplots indicate that most of the surface units are distributed in a spatially distinct location – not much disjointed or scattered around different locations, with some exceptions.

The probability scale ranges from 0 to 1, where higher values indicate a higher probability for the corresponding surface unit. For pixels that are close to multiple cluster centroids, the GMM algorithm infers the probabilities of the pixels for these multiple clusters. Thus, the probability subplots in Fig. 4.4 indicate whether a pixel does purely belong to a particular surface unit or shares characteristics of multiple units. Most of the surface units are dominated by pixels with higher probability values (close to 1) – indicating the dominance of mostly pure pixels at each unit. This is further supported by the boxplot of the probability distributions extracted from the pixels corresponding to each class (Fig. 4A5 in Appendix). As seen in the probability boxplot, the median probability of every class is more than 0.95 – confirming that each class host pixels with higher probability values.

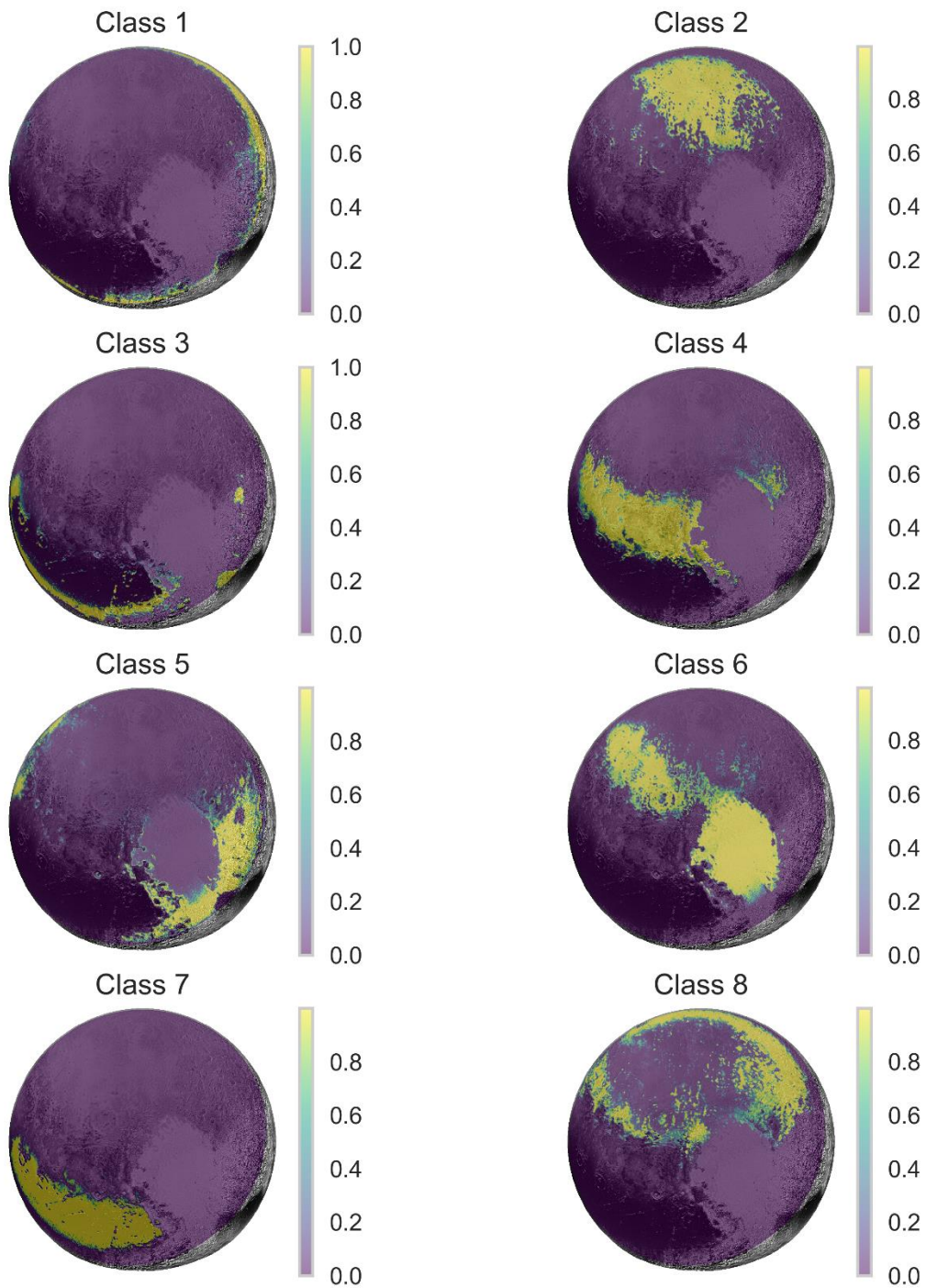


Fig. 4.4: The probability plot of each surface unit at LESIA image pixel level using PC-GMM. The subplots are superposed on the LORRI base map. The probability scale ranges from 0 to 1, where higher values indicate a higher probability of the corresponding unit. We also refer the readers to Fig. 4A5 in Appendix which shows that most of the surface units are dominated by pixels with higher probability values (close to 1).

Note that the resultant surface units using unsupervised learning are agnostic of the physical and geological meaning of the different terrains. Thus, a connection of the surface units to the chemical composition of the corresponding unit is necessary for the geologic explanation of the classification. Accordingly, we retrieve the mean and 1σ standard deviation of the I/F spectra from all the pixels that fall into each surface unit (Fig. 4.5). For the convenience of interpretation, the spectral subplot for the corresponding surface unit is labeled as C followed by the assigned unit number. For instance, the I/F spectra of surface unit #6 is labeled as C6. Note that these signs (C and #) are used interchangeably to denote the surface unit and corresponding spectra later in the paper for simplicity.

The standard deviation (gray shade) of the I/F spectra shows varying degrees of closeness to the mean spectra (red) at different wavelengths (see Fig. 4.5). The mean I/F spectra indicate the presence or absence of absorption bands of the abundant volatiles of CH₄, N₂, and CO. However, compared to N₂ and CO ices, CH₄ has very strong absorption bands at the wavelengths (1.2 to 2.5 μm) covered by the LEISA instrument. Thus, CH₄ absorption bands are much more readily identifiable than the other volatile ices from the mean I/F spectra of the surface unit (see Table 4.3 which lists important bands for different ice). All the classes, except the Cthulhu Macula (C7), exhibit a clear presence of CH₄ ice absorption bands with varying degrees of strength in the absorption bands. This is evidence of the widespread CH₄ ice distribution on Pluto's surface. The north polar unit (around Lowell Regio) – stretching from $\sim 60^\circ$ N to the north pole – shows a zone with a higher concentration of CH₄ ice (Grundy et al., 2016; Earle et al., 2018) as evidenced by the strong absorption features in the I/F spectra. More details of the spectral interpretations of all surface units are given in the later section of the paper.

The I/F spectra for the broad surface unit of Sputnik Planitia and Venera Terra (#6) exhibit the presence of N₂ and CO absorption bands at 2.15 μm and 1.58 μm, respectively (see C6 in Fig. 4.5). These bands are subtle at the scale shown, but are statistically reliable (because the absorption bands plotted in the figure accompany with 1-σ error bar). We did not see the sharp 2.35-μm absorption band for CO at the LEISA spectral resolution since the absorption band is blended between two broad CH₄ absorption bands (Schmitt et al., 2017). Since both N₂ and CO absorption bands are much weaker compared to the CH₄ bands, a finer difference in the spatial distribution of N₂ and CO abundance may not be sharply evident when applying an unsupervised classification scheme to the entire Pluto disk data. Thus, we re-classify the N₂ and CO-rich surface unit (#6) into multiple subunits to probe the finer difference in the distribution of N₂ and CO ices using a post-classification scheme. During re-classification, we treat the surface unit (#6) independently i.e., did not increase the original gaussian components.

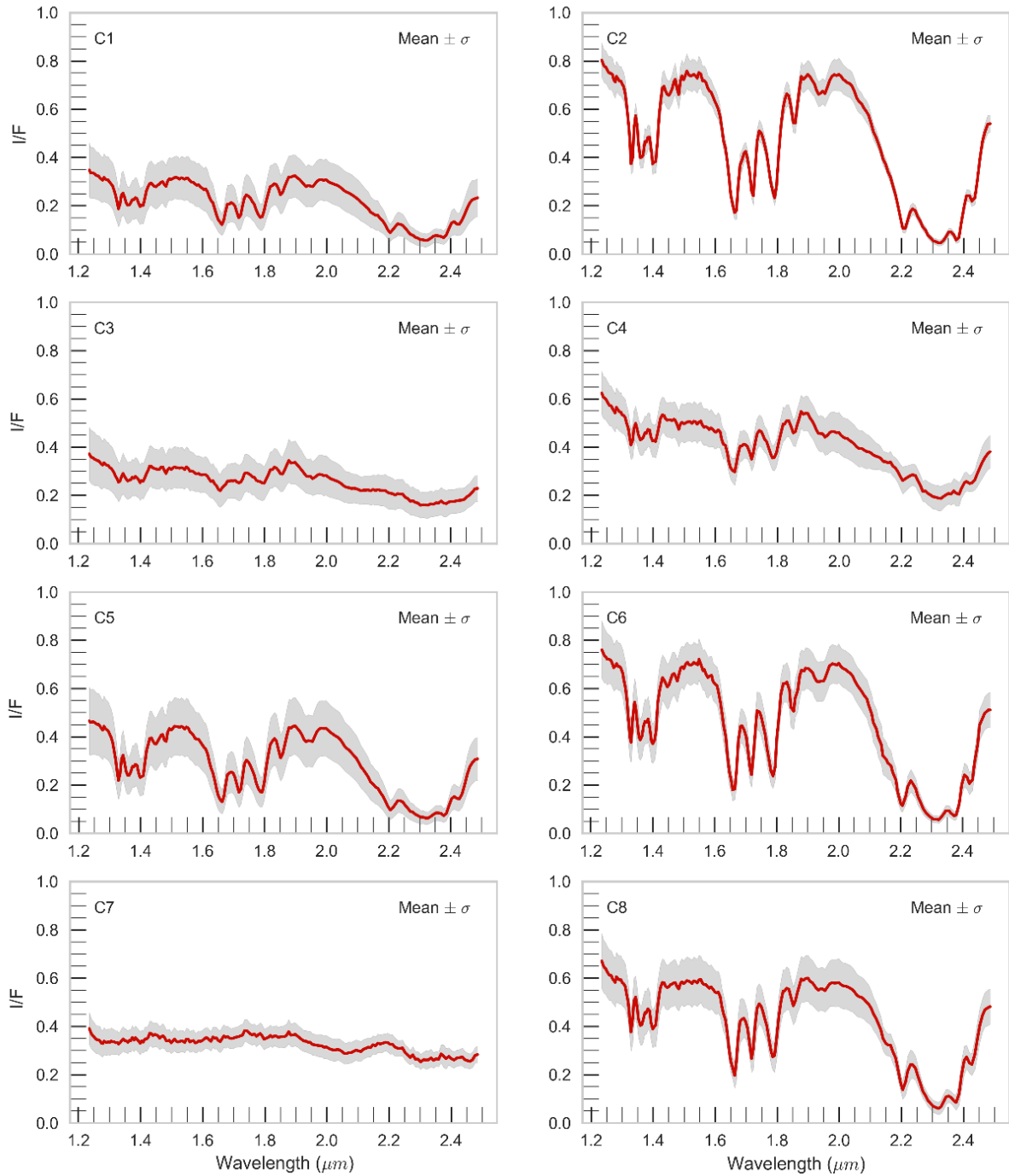


Fig. 4.5: The mean (red line) $\pm 1\sigma$ standard deviation (gray shade) I/F spectra of each surface unit on Pluto using PC-GMM. The spectra of the surface units in the subplots are labeled as C followed by the corresponding assigned surface unit number. The standard deviation of the I/F spectra shows varying degrees of closeness to the mean spectra at different wavelengths. All the classes (except the C7) exhibit a clear presence of CH_4 ice absorption bands with varying degrees of strength.

H₂O ice on the dwarf planet can be detected using the absorption bands at 1.65 and 2.0 μm which are an indicator of the crystalline ice phase (Cook et al., 2019). On Pluto's surface, the volatile ices of N₂, CO, and CH₄ mostly hide the H₂O ice bedrock from being identified in the LEISA wavelengths (Cruikshank et al., 2021). Moreover, the spectral signature of H₂O on Pluto is indiscernible because the broad spectral bands of H₂O are much shallower and overlain by strong CH₄ bands (Cruikshank et al., 2021). However, a relatively higher abundance of H₂O ice has been identified in different isolated areas (in smaller areal fractions) including the Kiladze crater and Krun Macula (Cook et al., 2019). These water-ice-abundant areas correspond to our surface unit #3 –which shows the presence of an absorption band at 1.65 μm in the I/F spectra (Fig. 4.5).

Though the spectra for C3 (see Fig. 4.5) do not show a very strong 2.0- μm absorption band, the broad absorption feature of CH₄ around the 2.3 μm region is less intense (also the shoulder of 2.0 μm is much lower compared to the 1.9- μm shoulder). Moreover, the CH₄ absorption band is absent at 2.2 μm . Thus, we consider these characteristics to be an indicator of H₂O ice abundance. The spatial distribution of #3 indicates that the H₂O ice-dominated areas are distributed at different geographic locations and associated with a variety of geologic features. Here, we are interested to probe if there are any differences in H₂O ice distribution due to geographic locations or if differences are more aligned to geology. To this end, we apply a post-classification scheme to distinctly separate possible H₂O ice-abundant subunits.

We employ the same GMM algorithm for the post-classification of the surface units (# 3 and 6) into two subunits. The probabilities of subunits for #6 are shown in the upper row and the subunits for #3 are shown in the bottom row of Fig. 4.6. For reference, the mean $\pm 1\sigma$ standard

deviation of the I/F spectra from all the pixels that fall into each subunit of #3 and #6 is also included in the Appendix (Fig. 4A6). The post-classification result of #6 indicates that the central part of Sputnik Planitia consists of a distinct subunit while the northern part of the SP and Venera Terra share common characteristics. The Venera Terra is in the northern mid-latitudes above 50° N while Sputnik Planitia barely exceeds 45° N. The geology of the central part of SP is different from its northern part and they show different albedos (White et al. 2017). Thus, the probability plots of subunits for #6 implies that differences between N₂ and CO-rich areas may be controlled by latitude, geology, and/or volatile transport mechanism within the SP basin (further interpretation are given in the later section). The histogram of the probabilities extracted from the pixels of each corresponding post-class of C6 is provided in the Appendix (see Fig. 4A7). The histogram plot indicates that each sub-unit is dominated by pixels with higher probability values (mostly pure pixels).

Likewise, the post-classification of #3 shows that the composition (H₂O mixed with other ices) at Kiladze crater is different from that of Krun Macula. The mean spectral plot (see Fig. 4A6 in Appendix) also indicates that there are differences in the spectral signature in those two regions most likely because the fractions of water on these units are different. The mountains and depressions (in small areal extend) in the Cthulhu Macula, Oort crater, and patchy spots in Tombaugh Regio belong to the same subunit of the Kiladze crater. However, the geographic locations of this subunit are distributed at different latitudes on Pluto's surface. Thus, the probability plot of subunits for #6 indicates that the compositional difference in H₂O-rich areas does not closely correlate with latitude, but rather is perhaps aligned to surface geology or other factors. We provide a histogram of the probabilities extracted from the pixels of each

corresponding post class of C3 in the Appendix (see Fig. 4A7). The histogram plots show that the post-classified surface units are dominated by pixels with higher probability values (close to 1). This indicates dominance of mostly pure pixels at each post-class for the C3 unit.

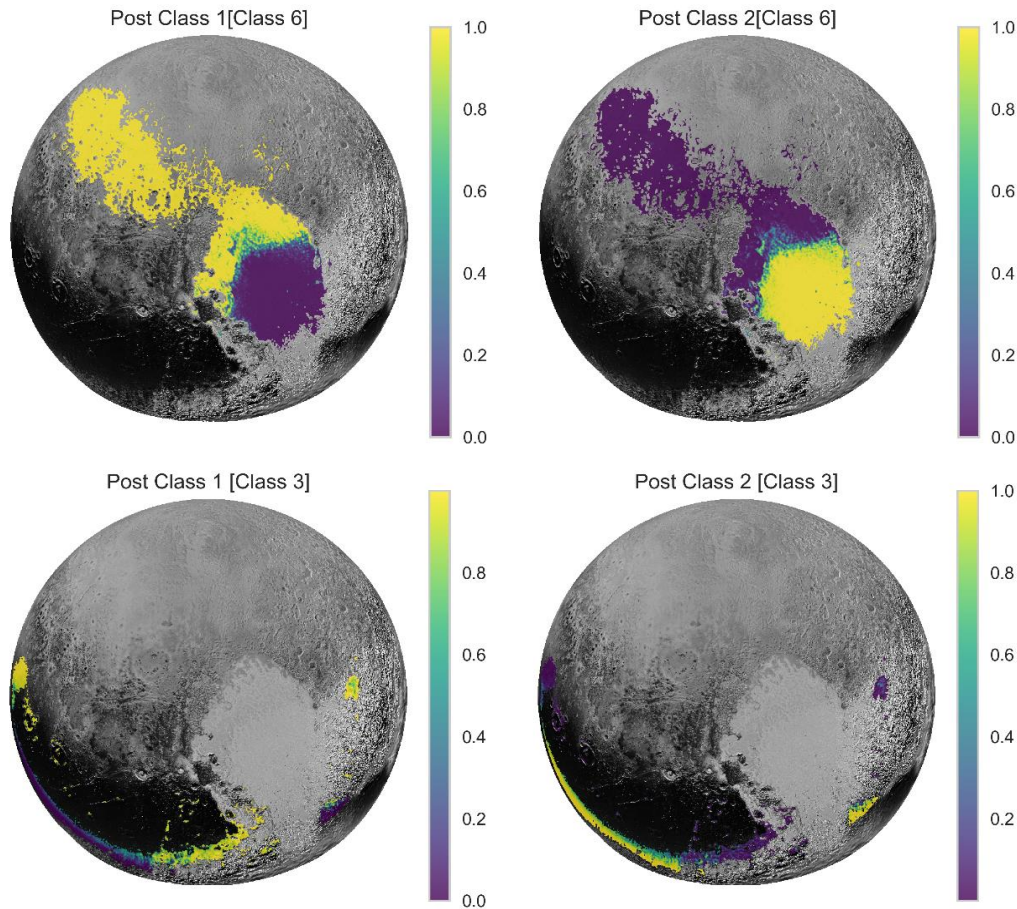


Fig. 4.6: Post-classification probabilities of subunits for the region enriched with N_2 and CO region (#6; upper row) and the subunits for the H_2O -rich areas (#3; bottom row). The central part of Sputnik Planitia shows a distinct subunit while the southern SP and Venera Terra share common characteristics. H_2O ice at the Kiladze crater shows a difference from that of at Krun Macula. Refer to the histogram plot in Fig. 4A7 in Appendix which shows that the post-class surface units of C3 and C6 are dominated by pixels with higher probability values.

Finally, we integrate all post-classification subunits into the original surface units shown in Fig. 4.4 to make a composite surface unit map encompassing a total of ten surface units (Fig. 4.7). In the composite surface unit map, the subunits forming the central part of Sputnik Planitia were reassigned the surface unit #9 while the subunit of Krun Macula was reassigned the surface unit #10. The compositional information of each surface unit is also labeled on the final surface unit map. Thus, we hereafter alternatively call the composite surface unit map as the generalized global compositional map. A summary of the characteristics and bulk compositions (qualitative) of the surface units is given in Table 4.2.

To facilitate the compositional comparison between the surface units, the average I/F spectra for ten composite surface units from the generalized global compositional map are given in Fig. 4.8. The colors in the average I/F spectra plot are the same as the corresponding surface unit colors in the generalized global compositional map. The characteristic absorption bands for N_2 at 2.15 μm and CO at 1.58 μm are labeled as the vertical lines in the plot. We also label the 1.65- and 2.0- μm absorption bands of H_2O . As noted above, the broad absorption bands of H_2O ice are indiscernible due to overlaid strong CH_4 absorption bands at NIR wavelengths. Thus, the relative comparison between the shoulders at 1.9 and 2.0 μm is also considered for interpreting H_2O abundance. Moreover, we utilize the shape of the characteristic absorption band of CH_4 at 2.2 μm for the interpretation of the presence of water ice.

On the outer solar system bodies, the surface volatiles are often found in different combinations or mixtures rather than in a pure state. The abundant volatile methane and nitrogen ices, at Pluto's average surface temperature of 40 K, are partly soluble and can form two binary mixing phases –

CH₄-rich ices diluted with N₂ (CH₄:N₂) and N₂-rich ice diluted with CH₄ (N₂:CH₄) (e.g., Prokhvatilov and Yantsevich, 1983; Trafton, 2015). CH₄ absorption bands shifts towards shorter wavelengths when a small amount of CH₄ is dissolved within N₂ such that with the increase of CH₄ concentration the absorption band shifts decrease (e.g., Protopapa et al. 2015). That means that higher concentrations of CH₄ correspond to smaller observed band shift (e.g., Scipioni et al., 2021). Thus, we use the shift of the peak at 1.69 μm as an indicator of N₂:CH₄ such that a shift toward shorter wavelengths represents the presence of CH₄ in the N₂ ice matrix while a shift toward longer wavelengths may be an indicator of CH₄-rich (with larger grains) materials.

Some of the surface units also show the dilution of N₂ in CH₄ as evident in the average spectra of the surface classes. We assess the dilution of N₂ in CH₄ ice (CH₄:N₂) by examining the absorption band at 1.69 μm. On Pluto, the absorption band at 1.69 μm has been historically attributed to the presence of pure CH₄ because the band only occurs in pure methane spectra and has not been observed in an ice mixture of CH₄ diluted with a smaller concentration of either α or β phases of N₂ ice at any temperature (Cruikshank et al., 2021). However, the recent laboratory study by Protopapa et al. (2015) demonstrated that the 1.69 μm absorption feature can no longer exclusively be attributed to the presence of pure CH₄ ice on Pluto's surface since the absorption feature has also been observed in CH₄:N₂ samples.

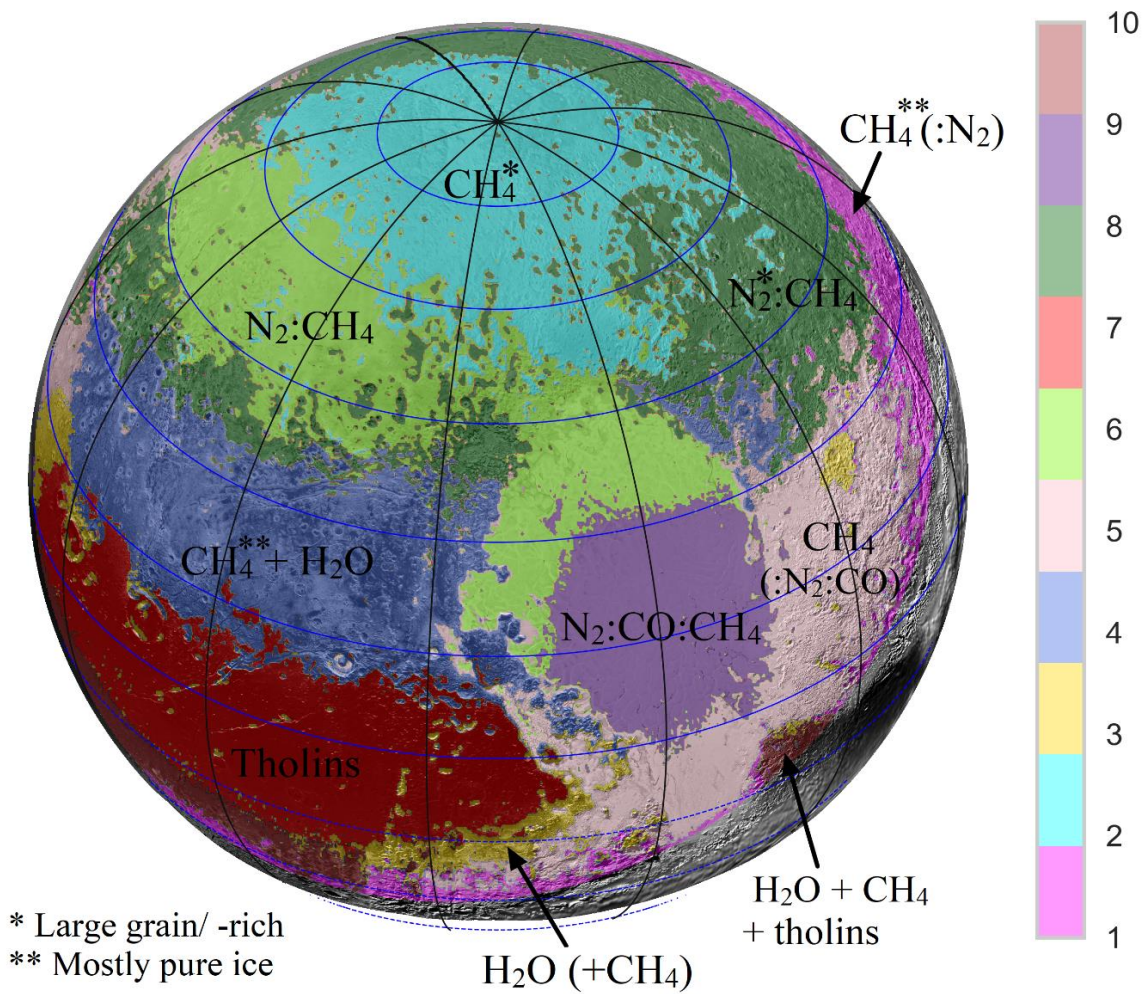


Fig. 4.7: The generalized global compositional map of Pluto superposed on a higher resolution LORRI basemap. The compositions of the surface units are labeled to the corresponding unit. The asterisk (*) superscript appended to a component refers only to that component where * = larger grain/-rich material and ** = pure ice. The latitude and longitude are labeled as the blue and black grid, respectively. The values in the legend indicate the assigned surface unit number.

Table 4.2: Summary of the characteristics and composition of the surface units.

# Unit	Major geographic province	Composition
1	Tartarus Dorsa	CH ₄ is diluted in a smaller amount of N ₂ ; CH ₄ (: N ₂); CH ₄ ice is mostly pure
2	Lowell Regio up to Voyager Terra to the south	Pure or larger grain of CH ₄ ; perhaps no or very little N ₂
3	Kiladze crater, Oort crater, and Pigafetta Montes	An abundance of H ₂ O + CH ₄ ice; CH ₄ snow-capped mountains supported by H ₂ O
4	Al-Idrisi Montes, Baret Montes, Hillary Montes, Viking Terra	CH ₄ and H ₂ O; CH ₄ ice is mostly pure; perhaps a very little amount of N ₂
5	South of Sputnik Planitia and Tombaugh Regio	CH ₄ ice might be slightly diluted with N ₂ and CO; CH ₄ (: N ₂ :CO)
6	Northern lobe of Sputnik Planitia and Venera Terra	N ₂ ice diluted with CH ₄ (N ₂ :CH ₄); perhaps a very little amount of CO
7	Cthulhu Macula	Red materials, tholins, refractory organics [inferred from colors and not spectral bands]
8	Pioneer Terra and the base of Burney crater	N ₂ ice diluted with CH ₄ (N ₂ :CH ₄); coarser N ₂ ice grains
9	Central Sputnik Planitia; the heart of SP	N ₂ :CO:CH ₄ ; the highest abundance of N ₂ and CO; the cold trap
10	Krun Macula and a belt follow south of Cthulhu Macula	A mixture of H ₂ O + tholins + CH ₄ ; absorption bands are not stronger

Using the global compositional maps, we focus on the broad generalized regions on Pluto's surface that show particularly interesting comparisons between their spectral composition with respect to geologic structures and topographic maps. Previous studies using MVIC (Multispectral Visible Imaging Camera) also noticed a latitudinal pattern to some of Pluto's ices (see Earle et al., 2018). We highlight these interesting features on Pluto where different volatile interactions are occurring and demonstrate the level of detail between spectral and geological study at Pluto. Note

the surface unit we refer to hereafter in our discussion corresponds to the surface units in generalized global compositional maps in Fig. 4.7 and corresponding average I/F spectra in Fig. 4.8. A list of the spectral components used to characterize surface compositions and surface units that exhibit the spectral components is also provided in Table 4.3. We also incorporate an interpretation of the geology of the surface units based on existing literature.

Area 1: Sputnik Planitia (SP)

SP is an N₂-dominated, volatile-filled basin that is currently undergoing solid-state convection, creating large (10 – 40 km across) polygonal cells across the basin (Stern et al., 2015; Protopapa et al., 2017). SP has also been observed from MVIC (Equivalent Width) data to have minor concentrations of methane, with weaker absorptions between the MVIC equivalent width of 2 – 4 nm (Earle et al., 2018). The composite surface unit map shows that Sputnik Planitia exhibits multiple classes with different surface compositions. Notably, the central part has spectral signatures of a higher concentration of N₂ and the presence of CO ices while the northern portion has a lower concentration of the N₂. Overall, the SP basin appears to have three main spectral regions – corresponding to I/F spectra indicated as C5, C6, and C9 (see Fig. 4.8).

The northwestern-most lobe of SP is darker in albedo (White et al. 2017). This portion of SP is indicated as spectra C6, which has a small N₂ signature and no discernible (or very weak) CO feature. The peak of the 1.69 μm slightly shifts towards shorter wavelengths – representing a surface composition of N₂ ice diluted with CH₄ (N₂:CH₄). As previously discussed, when CH₄ is diluted in N₂, there is a shift of the CH₄ bands to slightly shorter wavelengths (Quirico and Schmitt, 1997). The unit may host a very low concentration of CO since there is no discernible (or very weak) absorption at 1.58 μm. From the geologic mapping of SP (White et al., 2017), this part of

SP has dark-cellular plains (*dcp*) and dark-trough-bounding plains (*tbp*). The *dcp* unit is deficient in N₂ relative to the innermost (central) portion of SP, also displaying a higher content of entrained tholins, along with the *tbp* unit (Scipioni et al., 2021). The *tbp* unit also represents entrained tholins at the edges of the convective cells and bounding troughs.

The central lobe of SP has the spectral indicator C9, which is observed to have a more prominent signature of CO and N₂ compared to the other spectra. Having the presence of N₂ and CO in this central portion of SP gives more evidence into SP being a cold trap of such volatiles (Bertrand & Forget 2016; Keane et al. 2016). Moreover, the peak at 1.69 μm shows its highest shift towards shorter wavelengths compared to other spectra – representing the presence of the highest concentration of N₂ ice at the central part of SP compared to all other units. The CO absorption at 1.58 μm also shows a sharp feature. This represents a surface unit of the highest amount of N₂ and CO deposition. The geologic unit corresponding to this part of SP is bright-cellular-plains (*bcp*). The *bcp* unit is inferred to be resurfaced (relatively fresh, bright) N₂ ice (also inferred from the lack of impact craters in this region; see Singer et al. 2021). The cellular patterns indicate active solid-state convection (McKinnon et al. 2016). The higher albedo could be the condensation of N₂ from the atmosphere (White et al., 2017).

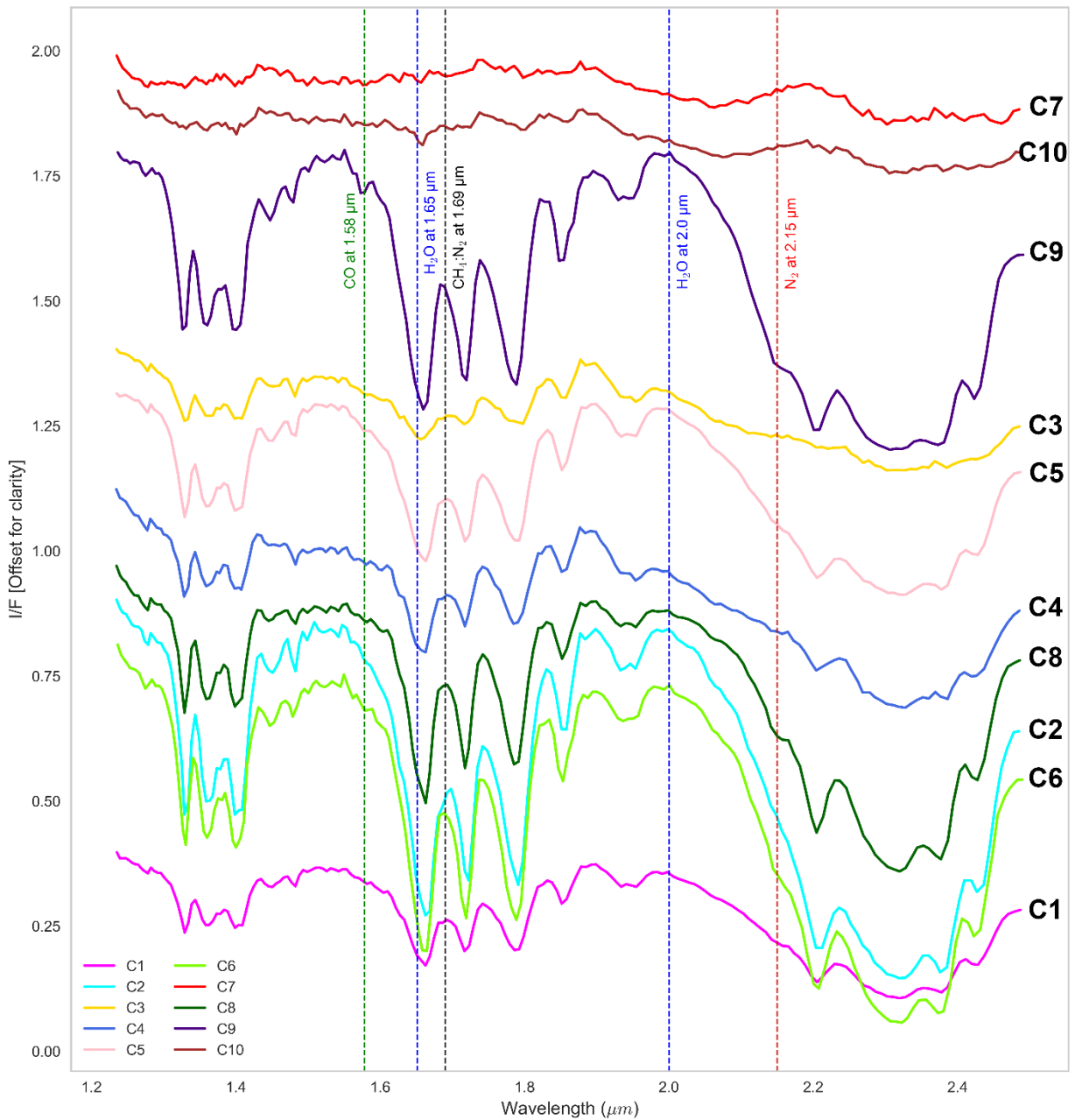


Fig. 4.8: The average I/F spectra of the ten composite surface units. The colors of the spectra correspond to the colors of the surface unit in Fig. 4.7. The dashed vertical lines indicate N_2 absorption at 2.15 μm (red), CO absorption at 1.58 μm (green), $CH_4:N_2$ absorption at 1.69 μm (black), and H_2O absorption at 1.65 and 2.0 μm (blue). Note that the I/F values in the y-axis have offsets for clarity. For a higher resolution colored version of the figure, the readers are referred to the online version of the paper².

² The wavelengths and average I/F data behind the figure are available in the publicly available repository at <https://github.com/alemran042/Pluto-PC-GMM-Data>

The southern-most unit within the SP basin (along with Tombaugh Regio) is spectral unit C5, which is observed to have a smaller spectral signature of N₂ and CO. The N₂ observed in this surface unit could be from the lightly pitted plains (*lpp*), in which N₂ is sublimating from the pits (White et al., 2017). This region also has patchy, pitted, marginal plains (*pmp*), which have shallow N₂ ice, and sparsely pitted plains (*spp*), which also N₂ ice-dominate, either from resurfacing or atmospheric condensation (White et al., 2017).

Table 4.3: List of the spectral components used to characterize compositions and their surface units.

Composition	Spectral component (μm)	Surface units (#)
N ₂	2.15 μm	C8, C9 (strong) C1, C5, C6 (weak)
CH ₄	1.30 – 1.43 μm, 1.59 – 1.83 μm, 1.90 – 2.0 μm, and 2.09 – 2.48 μm	All units with different strengths, except C7
CO	1.58 μm 2.35 μm (indiscernible)	C9 (strong) C5, C6 (weak)
H ₂ O*	1.65 μm, 2.0 μm (shoulder)	C3, C4, C10
N ₂ :CH ₄	peak shift at 1.69 μm (blue or red shift)	C6, C9 (blue shift) C2 (redshift)
CH ₄ :N ₂	absorption at 1.69 μm	C1, C4 (strong) C3 (weak/ indiscernible)

***Note:** We also consider the shape of the characteristic absorption band of CH₄ at 2.2 μm for the interpretation of the presence of H₂O ice. Please see the text for detail description of the approach.

Area 2: Al-Idrisi Montes and western SP glaciers

The Al-Idrisi Montes and the western shores of SP show an amalgamation of chaotic blocky terrain and mountainous glaciers, such as the Baret Montes and Hillary Montes glacier chain to the southwestern shores, rising several kilometers over SP (Moore et al., 2016). These mountains and glaciers are reddish in nature, while the chaos blocks to the northwestern portion of SP are more neutral in coloring. The glaciers and chaotic terrain floating on the western shores of SP are mainly water ice blocks (Howard et al. 2017; Cook et al. 2019; White et al. 2021). This spectral region (indicated as C4) from our global maps also extends in a latitudinal band into Viking Terra [$\sim 13^\circ$ - $\sim 40^\circ\text{N}$], tracing the northern boundary of Cthulhu Macula.

From the spectra, the CH_4 signature is not as deep comparatively, probably indicating some dilution in N_2 ice (Schmitt et al., 2017). However, interestingly, a slight $1.69 \mu\text{m}$ absorption band is seen in the spectra (C4). However, we do not see any discernible N_2 absorption band at $2.15 \mu\text{m}$. As has been noted above, the $1.69 \mu\text{m}$ absorption band is attributed to the presence of both pure CH_4 and $\text{CH}_4:\text{N}_2$ ice (Protopapa et al., 2015; Cruikshank et al., 2021). Thus, based on spectral characteristics we presume the composition of the surface unit #4 to be the presence of pure CH_4 ice. The H_2O correlation map by Cook et al. (2019) also reported the presence of water ice throughout this surface unit. Though the average spectra (C4) do not clearly show a strong absorption band at $1.65 \mu\text{m}$, the shoulder peak at $1.9 \mu\text{m}$ is much higher compared to $2.0 \mu\text{m}$. Thus, the possible composition for this surface unit is $\text{CH}_4 + \text{H}_2\text{O}$. We note that this latitudinal band does not extend to the eastern close-encounter hemisphere (except for a very small area on the northeastern shores of Sputnik Planitia).

Area 3: Northern Terrae and Polar Cap

The northern plains of Pluto are sectioned into different major regions plus the polar cap. The polar unit (officially known as Lowell Regio) is predominantly our spectral unit C2, which is a sampling of CH₄-rich components with little or no detection of CO and N₂. Notably, the peak of 1.69 μm shows a shift toward longer wavelengths among other spectra, indicating the presence of a CH₄-rich component. This pure CH₄ ice was also confirmed by observations from Schmitt et al. (2017). Venera Terra [Lat 38° – 74.9°N; Lon 99.8° – 135°E] is dominantly the spectral unit C6, which consists of CH₄ absorption bands and with a weak spectral signature of N₂. Like the northern portion of SP, this region has a surface composition of N₂:CH₄ (N₂ ice diluted with CH₄). Venera Terra geology involves the large (585-km long) Djanggawul Fossae and Piri Rupes structure (549-km long).

Pioneer Terra [Lat 43.5° - 69°N; 170° – 214°E] is dominated by unit C8, which is mostly CH₄ and N₂ mixtures (N₂:CH₄). However, compared to the Venera Terra unit (C6), this unit has a much broader 2.15-μm absorption band which is probably indicative of the presence of coarse grain N₂ ice. The Hayabusa Terra [Lat 28° – 62°N; 196° – 264°E], the easternmost region in the close-encounter hemisphere, is also dominated by the C8 spectral unit. Within these icy compounds, N₂-rich ices are very coarse-grained (few to 10s of centimeters), whereas CH₄-rich ices are typically < 1 mm in size (Protopapa et al. 2017). Most of the region is speckled with large, flat-floored pits and uplands (Howard et al. 2017). Water ice forms the base layer bedrock but is extensively mantled by other icy constituents. These erosional regions may reflect bulk composition, though the mantles may be of deeper, varied depths that may reflect seasonal volatile interactions and migrations (Earle et al. 2017; Protopapa et al. 2017). While CH₄ tends to accumulate at higher

elevations, N₂ collects in depressions (Bertrand and Forget 2016). N₂ ice detected in the spectral unit C8 is compatible with the origin of N₂ by atmospheric condensation condensing in these low-lying depressions.

The northwestern-most close-encounter hemisphere region is Vega Terra [Lat 10.5°–57°N; Lon 42.9° – 128°E]. There are two main spectral units from our global maps observed in this region: C6 and C8. C6 is in the northern portion of Vega Terra, which is observed to have a small amount of N₂, like the northern portion of SP. The southern part of Vega Terra is a mixture of CH₄ and N₂ (C8) in a much narrower latitudinal band. The geology in this portion of Pluto is mostly CH₄-haloed impact craters (Villaça et al. 2021).

Voyager Terra [Lat 36° – 77°N; Lon 129° – 176.5°E] consists of blotches of the spectral units C6, C2, and C8. We note that the C8 unit also corresponds to the relatively higher elevations of Hunahpu Valles, which has also been verified with observations of CH₄ concentrations at higher elevations in the MVIC data (Earle et al. 2017). These concentrations of CH₄ and N₂ could correspond to the condensation of atmospheric volatiles, like the CH₄-capped mountains observed in Cthulhu Macula (Bertrand et al. 2020).

Area 4: Cthulhu Macula and Southern Tombaugh Regio

Cthulhu Macula is a large, dark, reddish region in Pluto's western close-encounter hemisphere. The reddish coloring is possibly mostly the result of atmospheric tholins deposition (see Grundy et al. 2018). However, the reddish-colored component at Virgil Fossae has been hypothesized to originate from the recent cryovolcanic activities at the fossae (Cruikshank et al., 2019). This region

shows little to no methane absorption, as also confirmed by previous MVIC studies (Earle et al. 2018). To the southeast of Cthulhu Macula (southern portion of Tombaugh Regio) lies the putative cryovolcanic structures, Wright Mons and Piccard Mons (Singer et al., 2022). While most of the region consists of spectral units C3 and C5, it is curious to note that the spectral unit C1 intersects the summit pit depression of Wright Mons, which may imply some atmospheric deposition, and continues at an angle through Krun Macula and Tartarus Dorsa in the close-encounter eastern hemisphere.

The C1 unit is very similar to the C5 spectra, though the C1 may have a small detectable amount of N₂ that the C5 unit doesn't exhibit. Interestingly, C1 shows the presence of a 1.69 - μ m absorption band coupled with the N₂ absorption at 2.15 μ m. The 1.69 - μ m absorption has indeed been attributed to pure CH₄ or CH₄:N₂ (Protopapa et al., 2015) which the C1 spectrum corroborates. Thus, the likely composition at C1 is that CH₄ ice might be slightly diluted with N₂ [CH₄(: N₂)]. The detection of CH₄ at Wright Mons most likely represents a thin surficial layer deposited out of the atmosphere (Singer et al., 2022). N₂ and CH₄ have been previously observed at Tartarus Dorsa as the main drivers of the sublimation processes of the penitents (Moores et al., 2017).

Area 5: Water ice areas

The spectra for the Kiladze crater unit (C3) show evidence of abundant water ice. There is a clear presence of the H₂O absorption band at 1.65 μ m. Though the 2.0- μ m absorption band is not strongly evident in the spectra, the shoulder at 2.0 μ m is much lower than 1.9 μ m. We label this surface unit as the crystalline water ice abundant area, consistent with the previous study by Cook et al. (2019). We do not see the presence of a characteristic CH₄ absorption band at 2.2 μ m, though

other absorption bands of CH₄ are weakly present. Thus, the H₂O ice in the Kiladze crater area likely coexists with CH₄ ice (H₂O + CH₄ ice). The unit is also evident in the mountains and small depression in Cthulhu Macula. In the case of Krun Macula, neither CH₄ nor H₂O has strong absorption bands. The spectra show a similar shape to the spectra of Cthuhulu Macula – an indication of the presence of red materials or tholins. We note that the presence of tholins and other red materials is inferred on the basis of spectral slope (color), both in the spectral region covered by LEISA and analyzed here, and by MVIC at shorter wavelengths, and not on discrete, assignable spectral bands. Thus, on the basis of spectral shape, we infer that the surface unit at Krun Macula is likely to host a mixture of H₂O, CH₄, and tholins.

4.5. Discussion

The PC-GMM method implemented in this study not only mapped the geographic distribution of surface units on Pluto but also distinguish the differences in composition (both mixing and physical states of volatiles) from the average I/F spectra of the corresponding surface units. The generalized compositional map shows the presence of different surface units at different geologic features. The mountains such as Pigafetta and Elcano Montes in the Cthulhu Macula region (Fig. 4.9a) belong to a surface unit comparable to the Kiladze crater area and their spectra show the presence of an H₂O absorption band mixed with CH₄ ice. The top of these mountains hosts a high concentration of methane while the lower altitudes are mostly CH₄ depleted (Earle et al., 2018; Bertrand et al., 2020). The undulating mountainous terrains on Pluto suggest that H₂O ice forms the supporting bedrock for the surface volatiles and holds the base of the mountains (Stern et al., 2015; Spencer et al., 2020). Thus, our result bolsters the hypothesis that they are CH₄-capped H₂O-

supported mountains. The presence of an H₂O-rich surface unit on one side of the Kiladze crater (Fig. 4.9b) may be indicative of the spatial span of the crater ejecta.

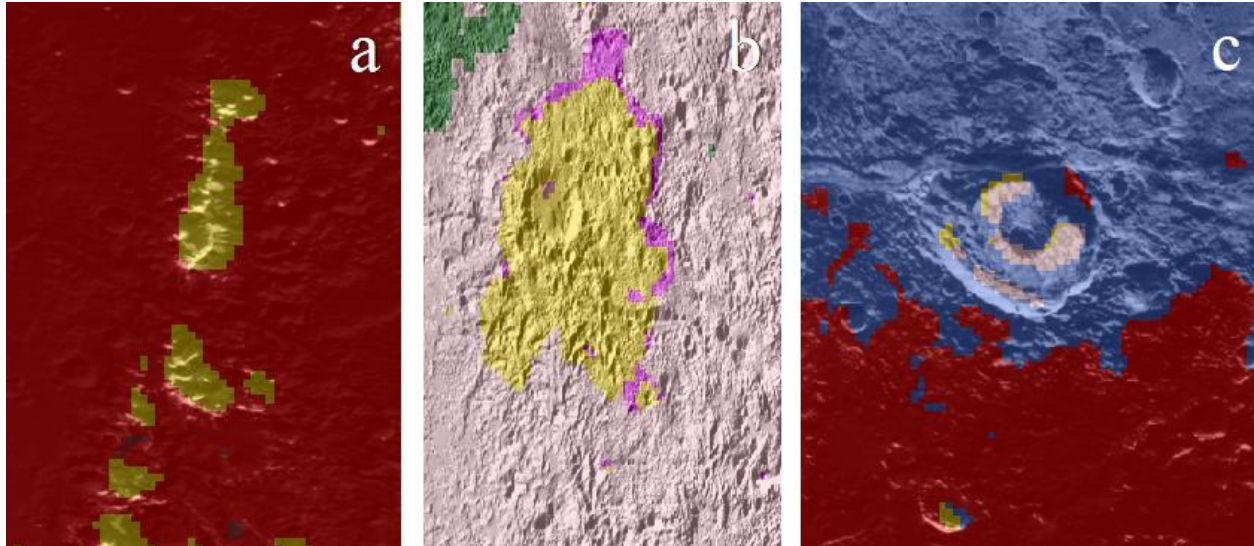


Fig. 4.9: The subset of the generalized surface map at mountains in the Cthulhu Macula (a), Kiladze crater (b), and Elliot crater (c). For the reference location, please see Fig. 4.1a.

The PC-GMM method also performed well in distinguishing the local scale difference in surface composition. The base of the Elliot crater (Fig. 4.9c) shows the presence of multiple surface units. The bottom floor indicates that surface unit #5 follows the central peak of the crater (except the north-eastern part of the crater floor). This unit corresponds to a surface composition rich in CH₄ ice which might be slightly diluted with N₂ and CO. It is notable that this surface unit (#5) shows no H₂O ice. The local scale compositional study at Elliot crater also confirmed the presence of non-H₂O materials at these locations (Dalle Ore et al. 2019). A few pixels on the floor of the crater show # 3 – presence of crystalline H₂O ice mixed with CH₄. The presence of the H₂O ice at these isolated spots on the floor of the crater is also consistent with Dalle Ore et al. (2019).

The **areas with H₂O ice** (i.e., #3, #4, and #10) show an interesting distribution across Pluto since these surface units are limited below ~45°N. We did not find any water ice-containing surface unit from ~45°N to the north pole. The absence of exposed H₂O in the higher northern latitude can be explained by the thick coverage of the volatile deposits at these latitudes (Cruikshank et al., 2019). This hypothesis is consistent with the results of our study such that of the distribution of the CH₄-rich unit (#2) on the north pole surrounded by the N₂:CH₄ units (#6 and #8) on the Venera Terra, Voyager Terra, and Pioneer Terra. We found H₂O-rich areas in some small craters (depressions) at Cthulu Macula or associated with specific geologic features. For instance, the presence of the H₂O ice-rich surface unit (#3) was seen along the Virgil Fossae, Beatrice Fossae, Edgeworth crater, and Oort crater areas. This suggests that the exposed H₂O distribution on Pluto's surface is likely controlled by geologic features.

On a global scale (Pluto encounter hemisphere during New Horizons fly-by), the output of the study helps in achieving a better understanding of the volatile transport modeling on the dwarf planet. The map of the global compositional distribution of surface ices is largely consistent with the compositional mapping by previous studies by Schmitt et al. (2017) and Protopapa et al. (2017). On top of that, the current study provides a quantitative aspect of the surface units thanks to the ability to estimate the areas of the different segments in the Sputnik Planitia basin. The central part of SP – considered as the cold trap for N₂ and CO ices – has an estimated area of ~284,000 sq. km which is more than one-third (1/3) of the total area of the basin. Based on our global-scale compositional distribution result we can infer volatile transport directions across the dwarf planet (Fig. 4.10) confirming and refining the results from the study of Protopapa et al. (2017) as mentioned in Cruikshank et al. (2021).

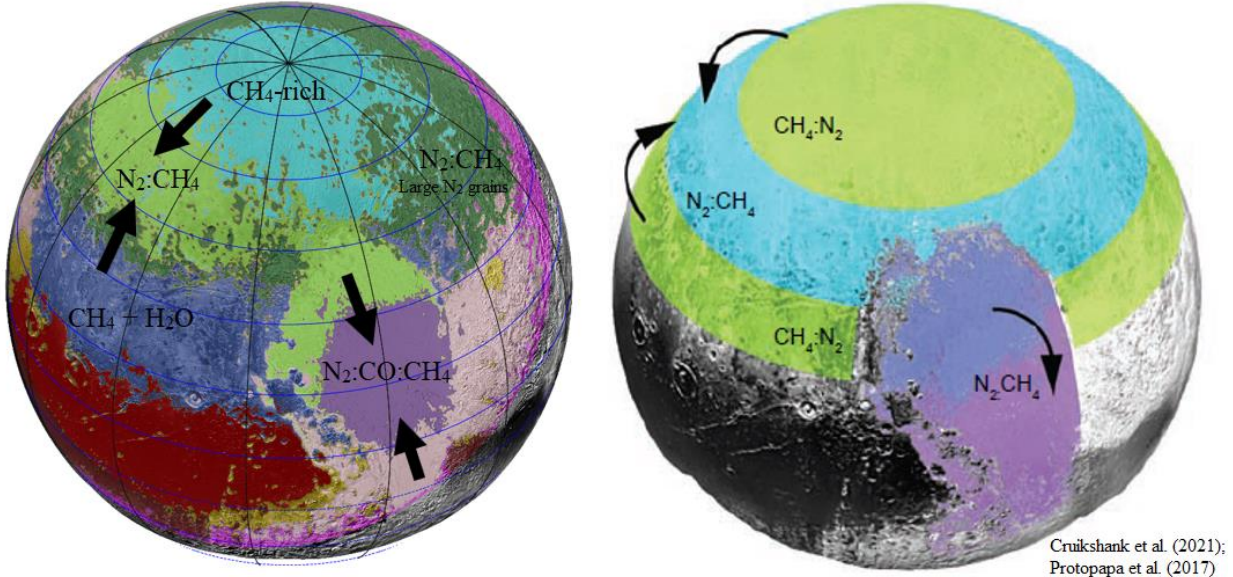


Fig. 4.10: Global-scale surface compositional distribution and inferred volatile transport directions (indicated by arrows) proposed in this study (a) and schematic view of the major ice distribution and direction of nitrogen sublimation transport (b) explained by Protopapa et al. (2017). Figure (b) was adopted from Cruikshank et al. (2021) and Protopapa et al. (2017).

Non-volatile H₂O ice should be exposed on the surface unless it's covered by the seasonal deposits and substantial reservoirs of the CH₄ and N₂ ices (Schaller and Brown, 2007). Exposed H₂O ice has not been detected across all the latitudes except in small patchy areas. The latitudinal patterns in the volatile N₂, CH₄, and CO distribution across Pluto's surface might suggest that insolation is the major controlling parameter for volatile distribution (Protopapa et al., 2017). However, the distribution of surface compositional units also corresponds to larger geological provinces (e.g., Venera Terra and Pioneer Terra) and local scale topography (e.g., Pigafetta Montes, Baret Montes, Elliot crater). Thus, we presume that besides being influenced by insolation, the distribution of volatile ices on Pluto's surface is controlled by geological structure and topography – consistent with Protopapa et al. (2017) and Bertrand et al. 2016.

Among the N_2 , CH_4 , and CO ices, N_2 is the most volatile component; it has the highest vapor pressure and sublimates first when heated by solar irradiation. Thus, the spatial abundance and distribution of nitrogen on Pluto's surface highlight the direction of nitrogen sublimation transport or volatile transport. A volatile transport (nitrogen sublimation and deposition) mechanism is interpreted for the northern hemisphere since the compositional surface units follow latitudinal patterns. The vigorous spring sublimation after a long polar winter over the past 20 years may lead to the illuminated north pole being devoid of N_2 ice by sublimation and redeposition at latitudes southward (Protopapa et al., 2017). However, between the years 1975 to 1995, the region covering surface unit #4 (i.e., northern lower latitudes) received more solar heating than the north (Protopapa et al., 2017). The intense solar heating at this latitude resulted in the sublimation of N_2 from these areas, which was then atmospherically transported and eventually deposited in the north (Protopapa et al., 2017). Consequently, sublimated N_2 ice from the north pole and northern lower latitudes found its resort in the regions between these surface units. Notably, the strength of the N_2 absorption band at $2.15 \mu m$ increases from the north pole (#2) southward (#8). This indicates the decreasing relative abundance of CH_4 -to- N_2 -rich ices with decreasing latitudes from the north pole southward (Cruikshank et al., 2021).

The Sputnik Planitia basin exhibits a distinct pattern of volatile transport by itself which, in fact interrupts the latitudinal patterns of volatile distribution and N_2 sublimation transport described above. The central part of the Sputnik Planitia hosts a higher abundance of the N_2 (and CO) ice compared to the northern and southern lobes of the basin. Thousands of elongated dark-floored pits structures are seen in higher resolution LORRI images at the southern lobe of the SP.

Evidence of mass loss and sublimation erosion of the dark-floored pits structures in the southern lobe of SP has been observed (Stern et al., 2021). This mass loss by these pits has been hypothesized to be deposited elsewhere on Pluto's surface through a volatile transport mechanism (atmospheric transport). Since this missing mass cannot reside in the atmosphere it has to be transported and re-condensed elsewhere (Stern et al., 2021). Our results support that the sublimation mass losses of these pits are deposited on the central part of SP (indicated by the black arrow shown in Fig. 4.10). However, this postulation of volatile migration at SP is inferred from the simple interpretation based on geological evidence (Stern et al., 2021) and correlation between the adjacent compositional units and does not account for the effects of insolation and winds.

The northern lobe of SP has a shallower 2.15- μm absorption band of N_2 compared to the central part. This suggests that the northern lobe has a lower abundance of $\text{N}_2\text{:CH}_4$ while the central part of SP has a much smaller concentration of CH_4 in N_2 (Cruikshank et al., 2021). Protopapa et al. (2017) interpreted these characteristic differences to be the transport of N_2 from the northwestern lobe southward. Loss of ices in northwestern SP (on both annual and seasonal timescale) and redeposition of the ices below 25° N have also been described by Bertrand et al. (2018). The sublimation of N_2 at northwestern SP leaves behind CH_4 as a lag deposit (Cruikshank et al., 2021). Thus, we conclude that the northern and southern lobes of SP may host active N_2 sublimation, whose sublimated mass is then atmospherically transported and ultimately deposited in the central part of SP. In recapitulation, we illustrate the source and sink of the N_2 ice sublimation transport (volatile transport mechanism) across the Sputnik Planitia basin.

We applied the PC-GMM technique to the LEISA data on Pluto's encounter disk of the 2015 New Horizons' fly-by. The results showed a latitudinal pattern in the volatile ices' distribution and showcase the nitrogen transport sublimation patterns at Pluto's global and local scale in the case of Sputnik Planitia. We emphasize that a similar method can be applied to other planetary bodies to characterize their surface compositions on a global scale. However, the results from our unsupervised clustering (GMM) are also consistent with the results of local scale applications of different other clustering techniques (i.e., K-means, Dalle Ore et al., 2018). Thus, we don't rule out the fact that an application of other unsupervised learning such as K-means or spectral clustering may render a satisfactory result in mapping the surface composition of planetary bodies.

4.6. Conclusions

Mapping spatial abundance and geographic distribution of ices and their relationship with the geological features are crucial for an in-depth understanding of volatile transport on Pluto (Bertrand and Forget, 2016). Thus, the surface compositional abundance and geographic distribution of volatile (N_2 , CH_4 , and CO) and non-volatiles (H_2O , tholins, etc.) have been thoroughly reported in the existing studies from near-infrared spectral observations from the instruments onboard New Horizons. However, existing studies in mapping surface ices on Pluto were mostly accomplished using band depth measurements of known ices, spectral indices or indicators, or implementation of radiative transfer models. The execution of these methods requires prior knowledge of representative surface ices or needs the reflectance or optical constants data of the end members (label data). Thanks to the development of sophisticated machine learning algorithms, unsupervised learning methods have gained popularity due to their agnostic wide applicability and rendering of satisfactory results.

We use the Gaussian mixture model, an unsupervised machine learning technique, to map the geographic distribution of ices on Pluto's surface. The input hyper-dimensional data were reduced to the lower dimension without compromising a substantial variation of the original data, followed by an implementation of GMM. The average I/F spectra from each surface unit have been extracted and analyzed – in terms of position and depth of the major absorption bands of CH₄, N₂, CO, and H₂O – to connect the surface units with latitudes and geologic features. The geographic distribution of the surface units demonstrates a correlation with latitudinal patterns and geologic features. The method was able to recognize local-scale variations (interpreted as indicative of surface composition and the physical states of ice) of the geological features. The mapped distribution of surface units and their compositions are consistent with the existing literature and help in an improved understanding of the volatile transport mechanism on Pluto, both on global (encounter hemisphere of Pluto during New Horizons flyby in 2015) and local scales.

We implement the unsupervised method without any label data or optical constants and showed a satisfactory result. Thus, an application of this unsupervised learning technique can specifically be beneficial for mapping the distribution of surface constituents of a planetary body when label data are poorly constrained or completely unknown. An improved understanding of the surface volatile transport mechanism at planetary scale can be attained through mapping of the geographic distribution of surface material. Thus, we emphasize that the unsupervised learning (PC-GMM) used in this study has wide applicability and can be expanded to other planetary bodies of the solar system for mapping surface material distribution and achieving a complete understating of volatile transport modeling in particular and physical processes in general on the icy bodies at the outer solar system.

4.7. Acknowledgment

The authors would like to thank The National Aeronautics and Space Administration (NASA)'s New Horizons mission team for collecting and processing LEISA/RALPH instrument data. We use the derived data (I/F) products of LEISA scenes generated by the New Horizons Pluto encounter surface compositional science theme team available at NASA Planetary Data System: Small Bodies Node (<https://pds-smallbodies.astro.umd.edu/>). The authors would like to thank Will Grundy, Leslie Young, Richard Binzel, Jason Cook, Francesca Scipioni, Silvia Protopapa, and anonymous reviewers for their useful comments.

4.8. Appendix

Section 4A.1. Cumulative explained variance and scree plot of PC axes.

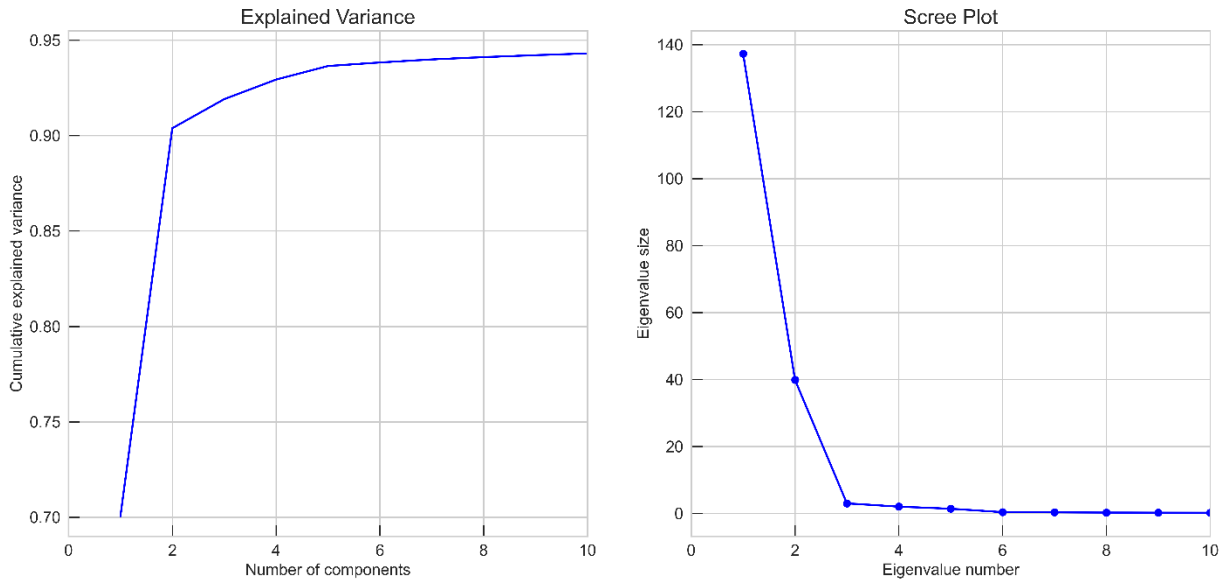


Fig. 4A1: The cumulative explained variance (left panel) and scree plot (right panel) of the PC axes. At four pc-axes, the plot shows 92.93% total variance of the data. The pc#5 and onward the plot shows a very gentle increase in the cumulative explained variance.

Section 4A.2. EM Algorithm for Multivariate Gaussian Mixture Model.

Algorithm: EM Algorithm for Multivariate Gaussian Mixture Model

Initialize: $\pi_j^{(0)}, \mu_j^{(0)}$ and $\Sigma_j^{(0)}$ for $j = 1, 2, \dots, k$.

for $m = 1, 2, \dots$ **do**

E-step: Let $\theta^{(m)} = \{\mu_1^{(m)}, \mu_2^{(m)}, \dots, \mu_k^{(m)}, \Sigma_1^{(m)}, \Sigma_2^{(m)}, \dots, \Sigma_k^{(m)}, \pi_1^{(m)}, \pi_2^{(m)}, \dots, \pi_k^{(m)}\}$ is the set of θ at m -th iteration. For $i = 1, 2, \dots, n$ and $j = 1, 2, \dots, k$ compute

$$\gamma_{ij}^{(m)} = p(z_i = j | X_i, \theta^{(m-1)}) = \frac{\pi_j^{(m-1)} N_d(X_i | \mu_j^{(m-1)}, \Sigma_j^{(m-1)})}{\sum_{j=1}^k \pi_j^{(m-1)} N_d(X_i | \mu_j^{(m-1)}, \Sigma_j^{(m-1)})} \quad (6)$$

$\gamma_{ij}^{(m)}$ is the posterior probability that $z_i = j$ given X_i and $\theta^{(m-1)}$ at m -th iteration.

M-step: For $j = 1, 2, \dots, k$ compute

$$\mu_j^{(m)} = \frac{1}{n_j^{(m)}} \sum_{i=1}^n \gamma_{ij}^{(m)} X_i \quad (7)$$

$$\Sigma_j^{(m)} = \frac{1}{n_j^{(m)}} \sum_{i=1}^n \gamma_{ij}^{(m)} (X_i - \mu_j^{(m)})^T (X_i - \mu_j^{(m)}) \quad (8)$$

$$\pi_j^{(m)} = \frac{n_j^{(m)}}{n} \quad (9)$$

where $n_j^{(m)} = \sum_{i=1}^n \gamma_{ij}^{(m)}$

end for.

Section 4A.3. Scaled AIC and BIC values at the different # of clusters.

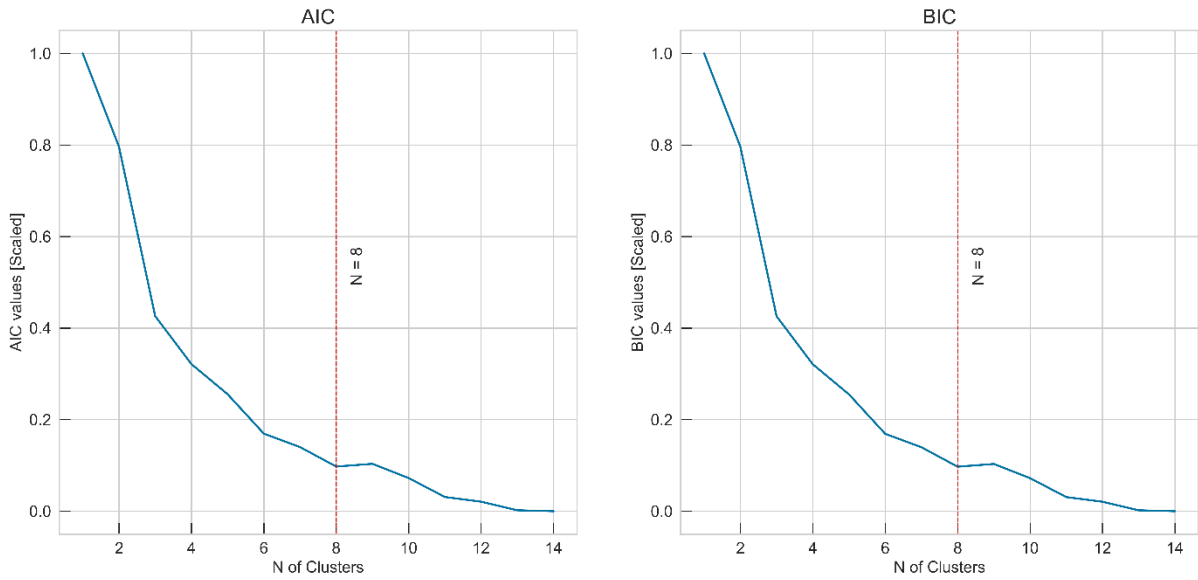


Fig. 4A2: Scaled AIC and BIC values at the different number of clusters. Both AIC and BIC show a similar trend as a function of the number of clusters. The plot shows the first local minima BIC (and AIC) value to be 8 and therefore was considered the optimal # of clusters in this study.

Section 4A.4. Linear fits between the observed and predicted density estimates.

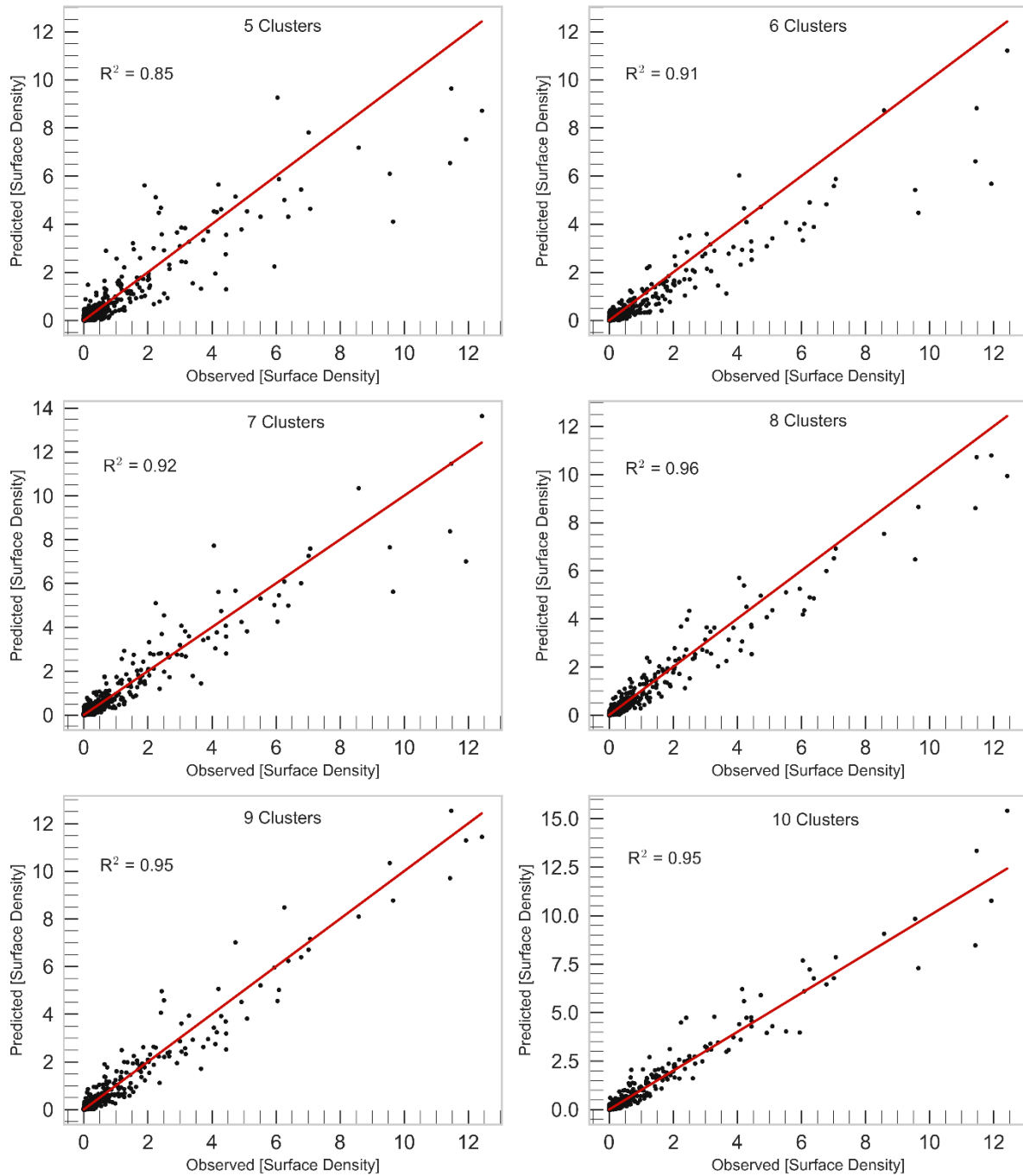


Fig. 4A3: Observed and predicted density plot for different numbers of clusters using the PC-GMM algorithm. The observed data were the first 4 pc-axes used as the input data for GMM while the predicted data were simulated from the resulting GMM model parameter. The density for both observed and predicted data was calculated from multivariate kernel density estimates. The coefficient of the determination (R^2) for linear fit between the observed and predicted density for 8 GC solution is 0.96 – suggesting a good fit of the model.

Section 4A.6. The boxplot of the probability of each corresponding 8 gaussian components.

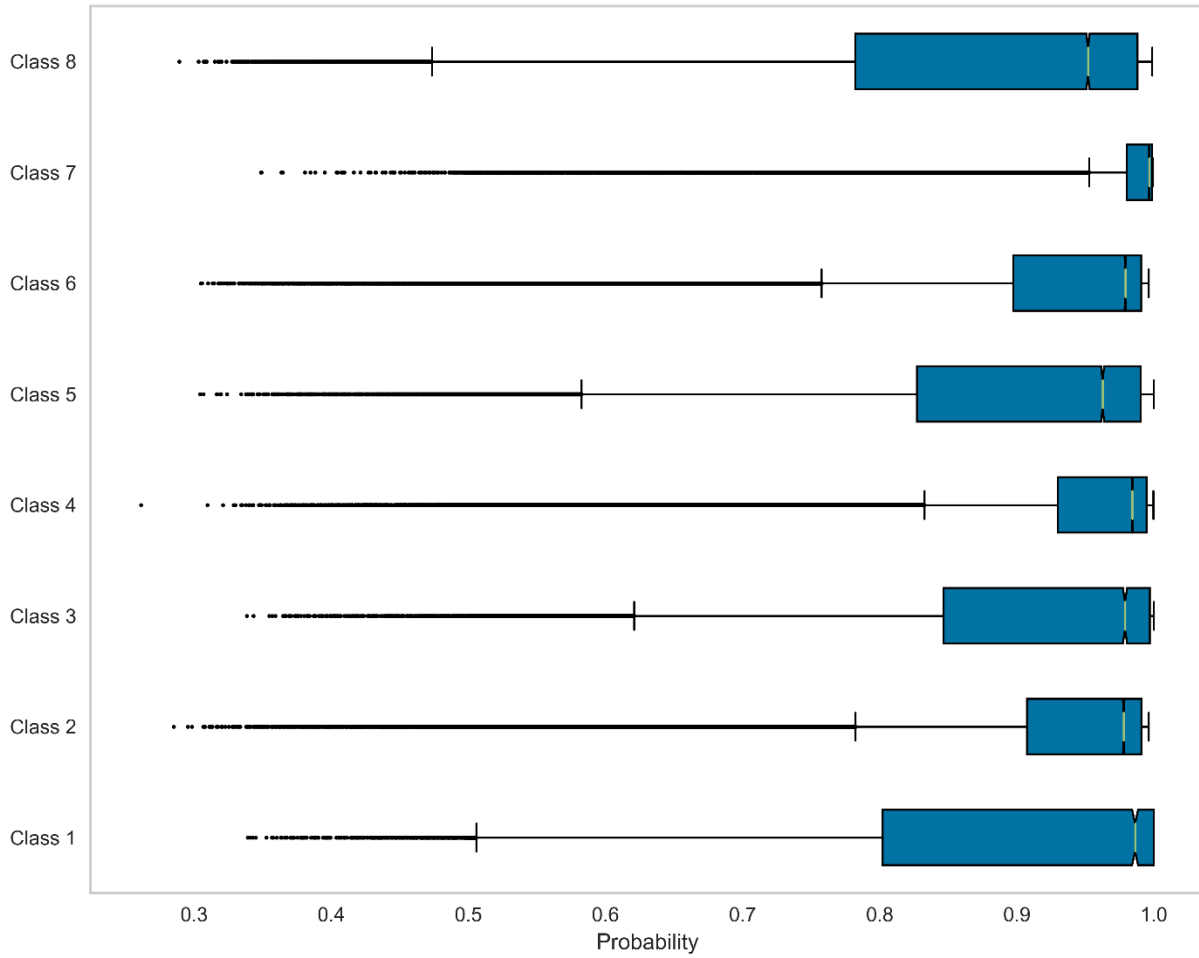


Fig. 4A5: The boxplot of the probabilities extracted from the pixels of corresponding classes (gaussian components). The median is shown by the line that divides the box into two parts while the left and right lines of the box represent the lower quartile (25%) and upper quartile (75%), respectively. The plot shows that most of the surface units are dominated by pixels with higher probability values (close to 1) – indicating the dominance of mostly pure pixels at each unit.

Section 4A.7. The mean $\pm 1\sigma$ standard deviation I/F spectra of subunits for #6 and #3

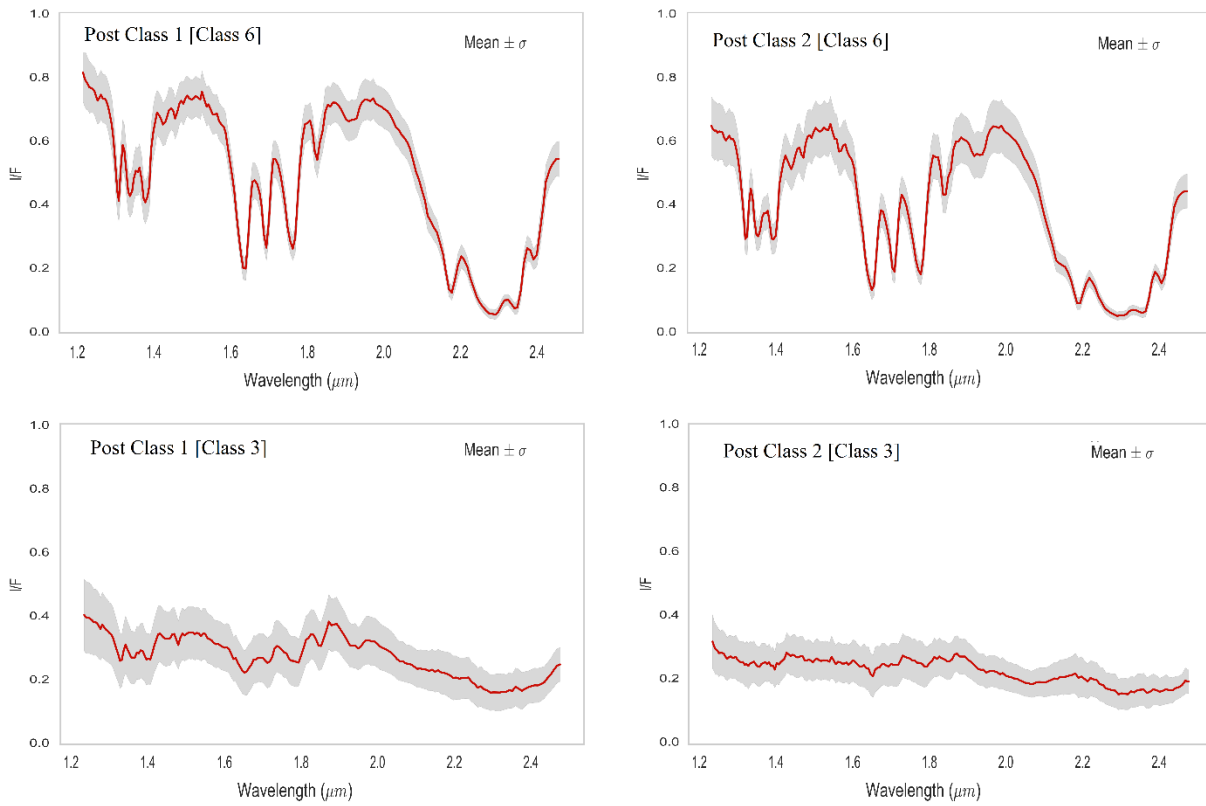


Fig. 4A6: The mean (red line) $\pm 1\sigma$ standard deviation (gray shade) I/F spectra of each subunit for #6 (upper row) and #3 (lower row). The standard deviation of the I/F spectra shows varying degrees of closeness to the mean spectra at different wavelengths.

Section 4A.8. The histogram of the probabilities of corresponding post-classes of C3 and C6.

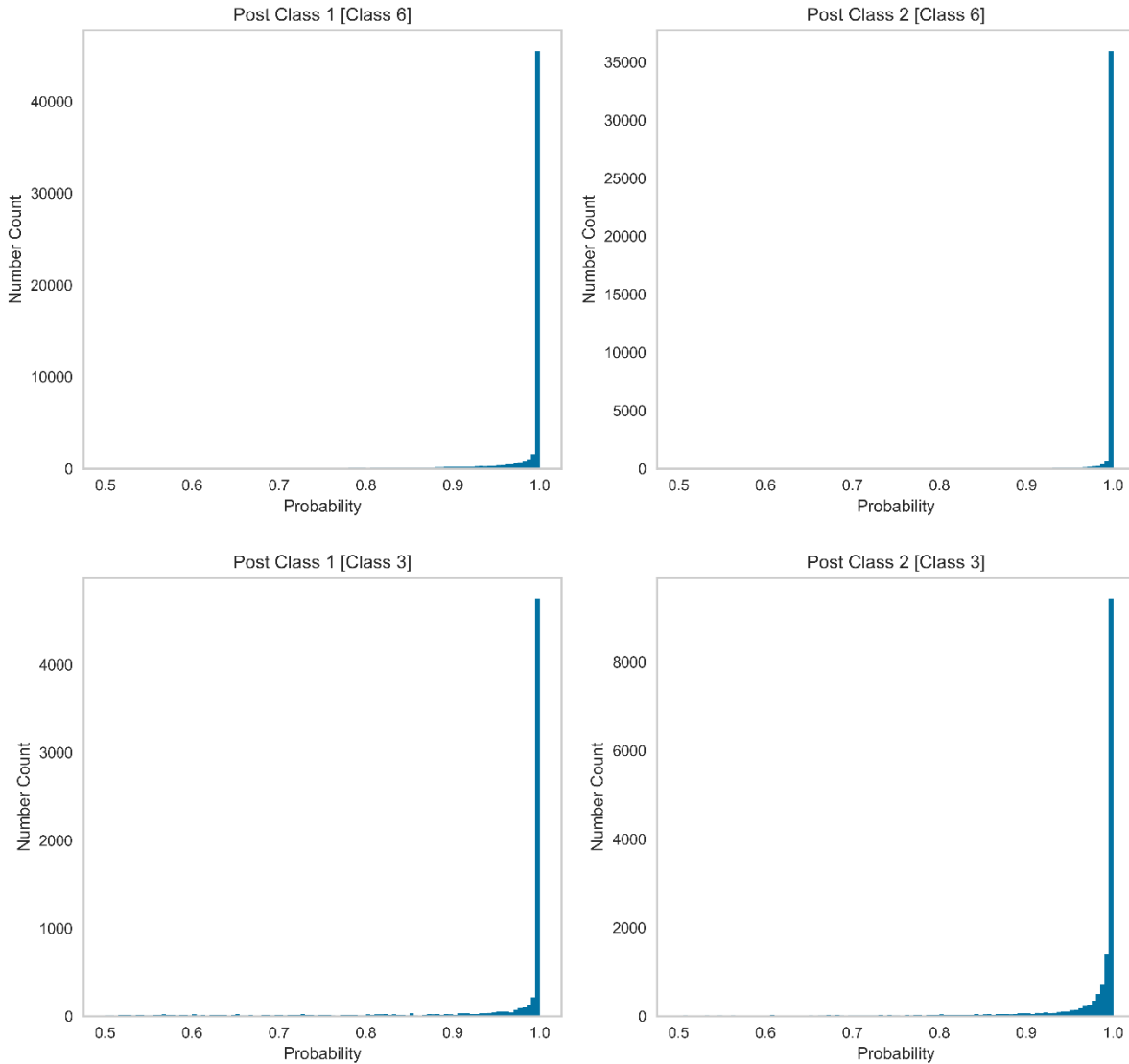


Fig. 4A7: The histogram of the probabilities extracted from the pixels corresponding to each post class of C3 and C6 unit. The plot shows that the surface units are dominated by pixels with higher probability values (close to 1) – indicating the dominance of mostly pure pixels at each unit.

4.9. References

- Abdi, H., Williams, L.J., 2010. Principal component analysis. *WIREs Computational Statistics* 2, 433–459. <https://doi.org/10.1002/wics.101>
- Akaike, H., 1974. A new look at the statistical model identification. *IEEE Transactions on Automatic Control* 19, 716–723. <https://doi.org/10.1109/TAC.1974.1100705>
- Alqahtani, N.A., Kalantan, Z.I., 2020. Gaussian Mixture Models Based on Principal Components and Applications. *Mathematical Problems in Engineering* 2020, e1202307. <https://doi.org/10.1155/2020/1202307>
- Berge, A., Schistad Solberg, A.H., 2006. Structured Gaussian Components for Hyperspectral Image Classification. *IEEE Transactions on Geoscience and Remote Sensing* 44, 3386–3396. <https://doi.org/10.1109/TGRS.2006.880626>
- Bertrand, T., Forget, F., 2016. Observed glacier and volatile distribution on Pluto from atmosphere–topography processes. *Nature* 540, 86–89. <https://doi.org/10.1038/nature19337>
- Bertrand, T., Forget, F., Schmitt, B., White, O.L., Grundy, W.M., 2020. Equatorial mountains on Pluto are covered by methane frosts resulting from a unique atmospheric process. *Nat Commun* 11, 5056. <https://doi.org/10.1038/s41467-020-18845-3>
- Binzel, R.P., Earle, A.M., Buie, M.W., Young, L.A., Stern, S.A., Olkin, C.B., Ennico, K., Moore, J.M., Grundy, W., Weaver, H.A., Lisse, C.M., Lauer, T.R., 2017. Climate zones on Pluto and Charon. *Icarus*, Special Issue: The Pluto System 287, 30–36. <https://doi.org/10.1016/j.icarus.2016.07.023>
- Bishop, C.M. and Nasrabadi, N.M., 2006. *Pattern recognition and machine learning* . Vol. 4, No. 4, p. 738. New York: springer.
- Cherkassky, V., Ma, Y., 2003. Comparison of Model Selection for Regression. *Neural Computation* 15, 1691–1714. <https://doi.org/10.1162/089976603321891864>
- Cook, J.C., Dalle Ore, C.M., Protopapa, S., Binzel, R.P., Cruikshank, D.P., Earle, A., Grundy, W.M., Ennico, K., Howett, C., Jennings, D.E., Lunsford, A.W., Olkin, C.B., Parker, A.H., Philippe, S., Reuter, D., Schmitt, B., Singer, K., Stansberry, J.A., Stern, S.A., Verbiscer, A., Weaver, H.A., Young, L.A., Hanley, J., Alketbi, F., Thompson, G.L., Pearce, L.A., Lindberg, G.E., Tegler, S.C., 2019. The distribution of H₂O, CH₃OH, and hydrocarbon-ices on Pluto: Analysis of New Horizons spectral images. *Icarus* 331, 148–169. <https://doi.org/10.1016/j.icarus.2018.09.012>
- Cruikshank D. P., Grundy W. M., Protopapa S., Schmitt B., and Linscott I. R., 2021. Surface composition of Pluto. In S. A. Stern, J. M. Moore, W. M. Grundy, L. A. Young, and R. P. Binzel (Eds.), *The Pluto System After New Horizons*. pp. 165–193. Univ. of Arizona, Tucson.

- Cruikshank, D.P., Grundy, W.M., Jennings, D.E., Olkin, C.B., Protopapa, S., Reuter, D.C., Schmitt, B., Stern, S.A., 2019. Spectroscopy of Pluto and Its Satellites, in: Bell III, J.F., Bishop, J.L., Moersch, J.E. (Eds.), *Remote Compositional Analysis: Techniques for Understanding Spectroscopy, Mineralogy, and Geochemistry of Planetary Surfaces*, Cambridge Planetary Science. Cambridge University Press, Cambridge, pp. 442–452. <https://doi.org/10.1017/9781316888872.024>
- Cruikshank, D.P., Grundy, W.M., DeMeo, F.E., Buie, M.W., Binzel, R.P., Jennings, D.E., Olkin, C.B., Parker, J.W., Reuter, D.C., Spencer, J.R., Stern, S.A., Young, L.A., Weaver, H.A., 2015. The surface compositions of Pluto and Charon. *Icarus*, Special Issue: The Pluto System 246, 82–92. <https://doi.org/10.1016/j.icarus.2014.05.023>
- Cruikshank, D.P., Imanaka, H., Dalle Ore, C.M., 2005. Tholins as coloring agents on outer Solar System bodies. *Advances in Space Research, Space Life Sciences: Astrobiology: Steps toward Origin of Life and Titan before Cassini* 36, 178–183. <https://doi.org/10.1016/j.asr.2005.07.026>
- Cruikshank, D.P., Pilcher, C.B., Morrison, D., 1976. Pluto: Evidence for Methane Frost. *Science* 194, 835–837. <https://doi.org/10.1126/science.194.4267.835>
- Cruikshank, D.P., Umurhan, O.M., Beyer, R.A., Schmitt, B., Keane, J.T., Runyon, K.D., Atri, D., White, O.L., Matsuyama, I., Moore, J.M., McKinnon, W.B., Sandford, S.A., Singer, K.N., Grundy, W.M., Dalle Ore, C.M., Cook, J.C., Bertrand, T., Stern, S.A., Olkin, C.B., Weaver, H.A., Young, L.A., Spencer, J.R., Lisse, C.M., Binzel, R.P., Earle, A.M., Robbins, S.J., Gladstone, G.R., Cartwright, R.J., Ennico, K., 2019. Recent cryovolcanism in Virgil Fossae on Pluto. *Icarus* 330, 155–168. <https://doi.org/10.1016/j.icarus.2019.04.023>
- Dalle Ore, C.M., Cruikshank, D.P., Protopapa, S., Scipioni, F., McKinnon, W.B., Cook, J.C., Grundy, W.M., Schmitt, B., Stern, S.A., Moore, J.M., Verbiscer, A., Parker, A.H., Singer, K.N., Umurhan, O.M., Weaver, H.A., Olkin, C.B., Young, L.A., Ennico, K., NEW HORIZONS SURFACE COMPOSITION SCIENCE THEME TEAM, 2019. Detection of ammonia on Pluto's surface in a region of geologically recent tectonism. *Science Advances* 5, eaav5731. <https://doi.org/10.1126/sciadv.aav5731>
- Dalle Ore, C.M., Protopapa, S., Cook, J.C., Grundy, W.M., Cruikshank, D.P., Verbiscer, A.J., Ennico, K., Olkin, C.B., Stern, S.A., Weaver, H.A., Young, L.A., 2018. Ices on Charon: Distribution of H₂O and NH₃ from New Horizons LEISA observations. *Icarus* 300, 21–32. <https://doi.org/10.1016/j.icarus.2017.08.026>
- Dasgupta, A., Raftery, A.E., 1998. Detecting Features in Spatial Point Processes with Clutter via Model-Based Clustering. *Journal of the American Statistical Association* 93, 294–302. <https://doi.org/10.2307/2669625>
- de Souza, R.S., Dantas, M.L.L., Costa-Duarte, M.V., Feigelson, E.D., Killedar, M., Lablanche, P.-Y., Vilalta, R., Krone-Martins, A., Beck, R., Gieseke, F., 2017. A probabilistic approach

- to emission-line galaxy classification. *Monthly Notices of the Royal Astronomical Society* 472, 2808–2822. <https://doi.org/10.1093/mnras/stx2156>
- Dempster, A.P., Laird, N.M., Rubin, D.B., 1977. Maximum Likelihood from Incomplete Data via the EM Algorithm. *Journal of the Royal Statistical Society. Series B (Methodological)* 39, 1–38.
- Earle, A.M., Binzel, R.P., Young, L.A., Stern, S.A., Ennico, K., Grundy, W., Olkin, C.B., Weaver, H.A., 2017. Long-term surface temperature modeling of Pluto. *Icarus*, Special Issue: The Pluto System 287, 37–46. <https://doi.org/10.1016/j.icarus.2016.09.036>
- Earle, A.M., Grundy, W., Howett, C.J.A., Olkin, C.B., Parker, A.H., Scipioni, F., Binzel, R.P., Beyer, R.A., Cook, J.C., Cruikshank, D.P., Dalle Ore, C.M., Ennico, K., Protopapa, S., Reuter, D.C., Schenk, P.M., Schmitt, B., Stern, S.A., Weaver, H.A., Young, L.A., 2018. Methane distribution on Pluto as mapped by the New Horizons Ralph/MVIC instrument. *Icarus* 314, 195–209. <https://doi.org/10.1016/j.icarus.2018.06.005>
- Fraley, C., Raftery, A.E., 1998. How Many Clusters? Which Clustering Method? Answers Via Model-Based Cluster Analysis. *The Computer Journal* 41, 578–588. <https://doi.org/10.1093/comjnl/41.8.578>
- Gabasova, L.R., Schmitt, B., Grundy, W., Bertrand, T., Olkin, C.B., Spencer, J.R., Young, L.A., Ennico, K., Weaver, H.A., Stern, S.A., 2021. Global compositional cartography of Pluto from intensity-based registration of LEISA data. *Icarus*, Pluto System, Kuiper Belt, and Kuiper Belt Objects 356, 113833. <https://doi.org/10.1016/j.icarus.2020.113833>
- Gewers, F.L., Ferreira, G.R., Arruda, H.F.D., Silva, F.N., Comin, C.H., Amancio, D.R., Costa, L.D.F., 2021. Principal Component Analysis: A Natural Approach to Data Exploration. *ACM Comput. Surv.* 54, 70:1-70:34. <https://doi.org/10.1145/3447755>
- Grundy, W.M., Bertrand, T., Binzel, R.P., Buie, M.W., Buratti, B.J., Cheng, A.F., Cook, J.C., Cruikshank, D.P., Devins, S.L., Dalle Ore, C.M., Earle, A.M., Ennico, K., Forget, F., Gao, P., Gladstone, G.R., Howett, C.J.A., Jennings, D.E., Kammer, J.A., Lauer, T.R., Linscott, I.R., Lisse, C.M., Lunsford, A.W., McKinnon, W.B., Olkin, C.B., Parker, A.H., Protopapa, S., Quirico, E., Reuter, D.C., Schmitt, B., Singer, K.N., Spencer, J.A., Stern, S.A., Strobil, D.F., Summers, M.E., Weaver, H.A., Weigle, G.E., Wong, M.L., Young, E.F., Young, L.A., Zhang, X., 2018. Pluto’s haze as a surface material. *Icarus* 314, 232–245. <https://doi.org/10.1016/j.icarus.2018.05.019>
- Grundy, W.M., Binzel, R.P., Buratti, B.J., Cook, J.C., Cruikshank, D.P., Dalle Ore, C.M., Earle, A.M., Ennico, K., Howett, C.J.A., Lunsford, A.W., Olkin, C.B., Parker, A.H., Philippe, S., Protopapa, S., Quirico, E., Reuter, D.C., Schmitt, B., Singer, K.N., Verbiscer, A.J., Beyer, R.A., Buie, M.W., Cheng, A.F., Jennings, D.E., Linscott, I.R., Parker, J.Wm., Schenk, P.M., Spencer, J.R., Stansberry, J.A., Stern, S.A., Throop, H.B., Tsang, C.C.C., Weaver, H.A., Weigle, G.E., Young, L.A., AND THE NEW HORIZONS SCIENCE TEAM, 2016.

- Surface compositions across Pluto and Charon. *Science* 351, aad9189. <https://doi.org/10.1126/science.aad9189>
- Hapke, B., 1993. *Theory of Reflectance and Emittance Spectroscopy*, Topics in Remote Sensing. Cambridge University Press, Cambridge. <https://doi.org/10.1017/CBO9780511524998>
- Hapke, B., 2012. *Theory of Reflectance and Emittance Spectroscopy*, 2nd ed. Cambridge University Press, Cambridge. <https://doi.org/10.1017/CBO9781139025683>
- Hertrich, J., Nguyen, D.-P.-L., Aujol, J.-F., Bernard, D., Berthoumieu, Y., Saadaldin, A., Steidl, G., 2022. PCA reduced Gaussian mixture models with applications in superresolution. *Inverse Problems and Imaging* 16, 341. <https://doi.org/10.3934/ipi.2021053>
- Howard, A.D., Moore, J.M., Umurhan, O.M., White, O.L., Anderson, R.S., McKinnon, W.B., Spencer, J.R., Schenk, P.M., Beyer, R.A., Stern, S.A., Ennico, K., Olkin, C.B., Weaver, H.A., Young, L.A., 2017. Present and past glaciation on Pluto. *Icarus*, Special Issue: The Pluto System 287, 287–300. <https://doi.org/10.1016/j.icarus.2016.07.006>
- Jolliffe, I.T., Cadima, J., 2016. Principal component analysis: a review and recent developments. *Philosophical Transactions of the Royal Society A: Mathematical, Physical and Engineering Sciences* 374, 20150202. <https://doi.org/10.1098/rsta.2015.0202>
- Keane, J.T., Matsuyama, I., Kamata, S., Steckloff, J.K., 2016. Reorientation and faulting of Pluto due to volatile loading within Sputnik Planitia. *Nature* 540, 90–93. <https://doi.org/10.1038/nature20120>
- Li, W., Prasad, S., Fowler, J.E., 2014. Hyperspectral Image Classification Using Gaussian Mixture Models and Markov Random Fields. *IEEE Geoscience and Remote Sensing Letters* 11, 153–157. <https://doi.org/10.1109/LGRS.2013.2250905>
- Liddle, A.R., 2007. Information criteria for astrophysical model selection. *Monthly Notices of the Royal Astronomical Society: Letters* 377, L74–L78. <https://doi.org/10.1111/j.1745-3933.2007.00306.x>
- Marzo, G.A., Roush, T.L., Blanco, A., Fonti, S., Orofino, V., 2006. Cluster analysis of planetary remote sensing spectral data. *Journal of Geophysical Research: Planets* 111. <https://doi.org/10.1029/2005JE002532>
- Marzo, G.A., Roush, T.L., Blanco, A., Fonti, S., Orofino, V., 2008. Statistical exploration and volume reduction of planetary remote sensing spectral data. *Journal of Geophysical Research: Planets* 113. <https://doi.org/10.1029/2008JE003219>
- Marzo, G.A., Roush, T.L., Hogan, R.C., 2009. Automated classification of visible and infrared spectra using cluster analysis. *Journal of Geophysical Research: Planets* 114. <https://doi.org/10.1029/2008JE003250>

- McKinnon, W.B., Nimmo, F., Wong, T., Schenk, P.M., White, O.L., Roberts, J.H., Moore, J.M., Spencer, J.R., Howard, A.D., Umurhan, O.M., Stern, S.A., Weaver, H.A., Olkin, C.B., Young, L.A., Smith, K.E., 2016. Convection in a volatile nitrogen-ice-rich layer drives Pluto's geological vigour. *Nature* 534, 82–85. <https://doi.org/10.1038/nature18289>
- Merlin, F., 2015. New constraints on the surface of Pluto. *A&A* 582, A39. <https://doi.org/10.1051/0004-6361/201526721>
- Moore, J.M., McKinnon, W.B., Spencer, J.R., Howard, A.D., Schenk, P.M., Beyer, R.A., Nimmo, F., Singer, K.N., Umurhan, O.M., White, O.L., Stern, S.A., Ennico, K., Olkin, C.B., Weaver, H.A., Young, L.A., Binzel, R.P., Buie, M.W., Buratti, B.J., Cheng, A.F., Cruikshank, D.P., Grundy, W.M., Linscott, I.R., Reitsema, H.J., Reuter, D.C., Showalter, M.R., Bray, V.J., Chavez, C.L., Howett, C.J.A., Lauer, T.R., Lisse, C.M., Parker, A.H., Porter, S.B., Robbins, S.J., Runyon, K., Stryk, T., Throop, H.B., Tsang, C.C.C., Verbiscer, A.J., Zangari, A.M., Chaikin, A.L., Wilhelms, D.E., NEW HORIZONS SCIENCE TEAM, 2016. The geology of Pluto and Charon through the eyes of New Horizons. *Science* 351, 1284–1293. <https://doi.org/10.1126/science.aad7055>
- Moores, J.E., Smith, C.L., Toigo, A.D., Guzewich, S.D., 2017. Penitentes as the origin of the bladed terrain of Tartarus Dorsa on Pluto. *Nature* 541, 188–190. <https://doi.org/10.1038/nature20779>
- O'Hara, S.T., Dombard, A.J., 2021. Downhill sledding at 40 AU: Mobilizing Pluto's chaotic mountain blocks. *Icarus, Pluto System, Kuiper Belt, and Kuiper Belt Objects* 356, 113829. <https://doi.org/10.1016/j.icarus.2020.113829>
- Owen, T.C., Roush, T.L., Cruikshank, D.P., Elliot, J.L., Young, L.A., de Bergh, C., Schmitt, B., Geballe, T.R., Brown, R.H., Bartholomew, M.J., 1993. Surface Ices and the Atmospheric Composition of Pluto. *Science* 261, 745–748. <https://doi.org/10.1126/science.261.5122.745>
- Patel, E., Kushwaha, D.S., 2020. Clustering Cloud Workloads: K-Means vs Gaussian Mixture Model. *Procedia Computer Science, Third International Conference on Computing and Network Communications (CoCoNet'19)* 171, 158–167. <https://doi.org/10.1016/j.procs.2020.04.017>
- Pearson, K., 1901. LIII. On lines and planes of closest fit to systems of points in space. *The London, Edinburgh, and Dublin Philosophical Magazine and Journal of Science* 2, 559–572. <https://doi.org/10.1080/14786440109462720>
- Pedregosa, F., Varoquaux, G., Gramfort, A., Michel, V., Thirion, B., Grisel, O., Blondel, M., Prettenhofer, P., Weiss, R., Dubourg, V., Vanderplas, J., Passos, A., Cournapeau, D., Brucher, M., Perrot, M., Duchesnay, É., 2011. Scikit-learn: Machine Learning in Python. *Journal of Machine Learning Research* 12, 2825–2830.

- Pinilla-Alonso, N., Roush, T.L., Marzo, G.A., Cruikshank, D.P., Dalle Ore, C.M., 2011. Iapetus surface variability revealed from statistical clustering of a VIMS mosaic: The distribution of CO₂. *Icarus* 215, 75–82. <https://doi.org/10.1016/j.icarus.2011.07.004>
- Prokhvatilov, A.I., Yantsevich, L.D., 1983. X-ray investigation of the equilibrium phase diagram of CH₄-N₂ solid mixtures. *Sov. J. Low Temp. Phys.*, vol. 9, p. 94-98 (1983). 9, 94–98.
- Protopapa, S., Grundy, W.M., Reuter, D.C., Hamilton, D.P., Dalle Ore, C.M., Cook, J.C., Cruikshank, D.P., Schmitt, B., Philippe, S., Quirico, E., Binzel, R.P., Earle, A.M., Ennico, K., Howett, C.J.A., Lunsford, A.W., Olkin, C.B., Parker, A., Singer, K.N., Stern, A., Verbiscer, A.J., Weaver, H.A., Young, L.A., 2017. Pluto's global surface composition through pixel-by-pixel Hapke modeling of New Horizons Ralph/LEISA data. *Icarus*, Special Issue: The Pluto System 287, 218–228. <https://doi.org/10.1016/j.icarus.2016.11.028>
- Protopapa, S., Grundy, W.M., Tegler, S.C., Bergonio, J.M., 2015. Absorption coefficients of the methane–nitrogen binary ice system: Implications for Pluto. *Icarus* 253, 179–188. <https://doi.org/10.1016/j.icarus.2015.02.027>
- Protopapa, S., Olkin, C.B., Grundy, W.M., Li, J.-Y., Verbiscer, A., Cruikshank, D.P., Gautier, T., Quirico, E., Cook, J.C., Reuter, D., Howett, C.J.A., Stern, A., Beyer, R.A., Porter, S., Young, L.A., Weaver, H.A., Ennico, K., Ore, C.M.D., Scipioni, F., Singer, K., 2020. Disk-resolved Photometric Properties of Pluto and the Coloring Materials across its Surface. *AJ* 159, 74. <https://doi.org/10.3847/1538-3881/ab5e82>
- Quirico, E., Schmitt, B., 1997. Near-Infrared Spectroscopy of Simple Hydrocarbons and Carbon Oxides Diluted in Solid N₂ and as Pure Ices: Implications for Triton and Pluto. *Icarus* 127, 354–378. <https://doi.org/10.1006/icar.1996.5663>
- Reuter, D.C., Stern, S.A., Scherrer, J., Jennings, D.E., Baer, J.W., Hanley, J., Hardaway, L., Lunsford, A., McMuldroy, S., Moore, J., Olkin, C., Parizek, R., Reitsma, H., Sabatke, D., Spencer, J., Stone, J., Throop, H., Van Cleve, J., Weigle, G.E., Young, L.A., 2008. Ralph: A Visible/Infrared Imager for the New Horizons Pluto/Kuiper Belt Mission. *Space Sci Rev* 140, 129–154. <https://doi.org/10.1007/s11214-008-9375-7>
- Rizos, J.L., de León, J., Licandro, J., Campins, H., Popescu, M., Pinilla-Alonso, N., Golish, D., de Prá, M., Lauretta, D., 2019. Spectral clustering tools applied to Ceres in preparation for OSIRIS-REx color imaging of asteroid (101955) Bennu. *Icarus* 328, 69–81. <https://doi.org/10.1016/j.icarus.2019.03.007>
- Rizos, J.L., de León, J., Licandro, J., Golish, D.R., Campins, H., Tatsumi, E., Popescu, M., DellaGiustina, D.N., Pajola, M., Li, J.-Y., Becker, K.J., Lauretta, D.S., 2021. Bennu's global surface and two candidate sample sites characterized by spectral clustering of OSIRIS-REx multispectral images. *Icarus* 364, 114467. <https://doi.org/10.1016/j.icarus.2021.114467>

- Schaller, E.L., Brown, M.E., 2007. Volatile Loss and Retention on Kuiper Belt Objects. *ApJ* 659, L61. <https://doi.org/10.1086/516709>
- Schmitt, B., Philippe, S., Grundy, W.M., Reuter, D.C., Côte, R., Quirico, E., Protopapa, S., Young, L.A., Binzel, R.P., Cook, J.C., Cruikshank, D.P., Dalle Ore, C.M., Earle, A.M., Ennico, K., Howett, C.J.A., Jennings, D.E., Linscott, I.R., Lunsford, A.W., Olkin, C.B., Parker, A.H., Parker, J.Wm., Singer, K.N., Spencer, J.R., Stansberry, J.A., Stern, S.A., Tsang, C.C.C., Verbiscer, A.J., Weaver, H.A., New Horizons Science Team, 2017. Physical state and distribution of materials at the surface of Pluto from New Horizons LEISA imaging spectrometer. *Icarus* 287, 229–260. <https://doi.org/10.1016/j.icarus.2016.12.025>
- Scipioni, F., White, O., Cook, J.C., Bertrand, T., Cruikshank, D.P., Grundy, W.M., Beddingfield-Cartwright, C., Binzel, R.P., Dalle Ore, C.M., Jennings, D., Moore, J.M., Olkin, C.B., Protopapa, S., Reuter, D.C., Schmitt, B., Singer, K.N., Spencer, J.R., Stern, S.A., Weaver, H.A., Verbiscer, A.J., Young, L.A., 2021. Pluto’s Sputnik Planitia: Composition of geological units from infrared spectroscopy. *Icarus* 359, 114303. <https://doi.org/10.1016/j.icarus.2021.114303>
- Singer, K. N., Greenstreet, S., Schenk, P. M., Robbins, S. J., & Bray, V. J., 2021. Impact craters on Pluto and Charon and terrain age estimates. In S. A. Stern, J. M. Moore, W. M. Grundy, L. A. Young, and R. P. Binzel (Eds.), *The Pluto System After New Horizons*, 121.
- Singer, K.N., White, O.L., Schmitt, B., Rader, E.L., Protopapa, S., Grundy, W.M., Cruikshank, D.P., Bertrand, T., Schenk, P.M., McKinnon, W.B., Stern, S.A., Dhingra, R.D., Runyon, K.D., Beyer, R.A., Bray, V.J., Ore, C.D., Spencer, J.R., Moore, J.M., Nimmo, F., Keane, J.T., Young, L.A., Olkin, C.B., Lauer, T.R., Weaver, H.A., Ennico-Smith, K., 2022. Large-scale cryovolcanic resurfacing on Pluto. *Nat Commun* 13, 1542. <https://doi.org/10.1038/s41467-022-29056-3>
- Spencer, J.R., Grundy, W.M., Nimmo, F., Young, L.A., 2020. Chapter 12 - The Pluto system after New Horizons, in: Prialnik, D., Barucci, M.A., Young, L.A. (Eds.), *The Trans-Neptunian Solar System*. Elsevier, pp. 271–288. <https://doi.org/10.1016/B978-0-12-816490-7.00012-6>
- Stern, A., 2018. New Horizons Pluto Encounter Surface Composition Data Archive, NH-P/PSA-LEISA/MVIC-5-COMP-V1.0, NASA Planetary Data System.
- Stern, S. A. , J. M. Moore, W. M. Grundy, L. A. Young, and R. P. Binzel, 2021. *The Pluto System After New Horizons*, Illustrated edition. ed. University of Arizona Press, Tucson Houston.
- Stern, S.A., Bagenal, F., Ennico, K., Gladstone, G.R., Grundy, W.M., McKinnon, W.B., Moore, J.M., Olkin, C.B., Spencer, J.R., Weaver, H.A., Young, L.A., Andert, T., Andrews, J., Banks, M., Bauer, B., Bauman, J., Barnouin, O.S., Bedini, P., Beisser, K., Beyer, R.A., Bhaskaran, S., Binzel, R.P., Birath, E., Bird, M., Bogan, D.J., Bowman, A., Bray, V.J., Brozovic, M., Bryan, C., Buckley, M.R., Buie, M.W., Buratti, B.J., Bushman, S.S., Calloway, A., Carcich, B., Cheng, A.F., Conard, S., Conrad, C.A., Cook, J.C., Cruikshank,

- D.P., Custodio, O.S., Dalle Ore, C.M., Deboy, C., Dischner, Z.J.B., Dumont, P., Earle, A.M., Elliott, H.A., Ercol, J., Ernst, C.M., Finley, T., Flanigan, S.H., Fountain, G., Freeze, M.J., Greathouse, T., Green, J.L., Guo, Y., Hahn, M., Hamilton, D.P., Hamilton, S.A., Hanley, J., Harch, A., Hart, H.M., Hersman, C.B., Hill, A., Hill, M.E., Hinson, D.P., Holdridge, M.E., Horanyi, M., Howard, A.D., Howett, C.J.A., Jackman, C., Jacobson, R.A., Jennings, D.E., Kammer, J.A., Kang, H.K., Kaufmann, D.E., Kollmann, P., Krimigis, S.M., Kusnierkiewicz, D., Lauer, T.R., Lee, J.E., Lindstrom, K.L., Linscott, I.R., Lisse, C.M., Lunsford, A.W., Mallder, V.A., Martin, N., McComas, D.J., McNutt, R.L., Mehoke, D., Mehoke, T., Melin, E.D., Mutchler, M., Nelson, D., Nimmo, F., Nunez, J.I., Ocampo, A., Owen, W.M., Paetzold, M., Page, B., Parker, A.H., Parker, J.W., Pelletier, F., Peterson, J., Pinkine, N., Piquette, M., Porter, S.B., Protopapa, S., Redfern, J., Reitsema, H.J., Reuter, D.C., Roberts, J.H., Robbins, S.J., Rogers, G., Rose, D., Runyon, K., Retherford, K.D., Ryschkewitsch, M.G., Schenk, P., Schindhelm, E., Sepan, B., Showalter, M.R., Singer, K.N., Soluri, M., Stanbridge, D., Steffl, A.J., Strobel, D.F., Stryk, T., Summers, M.E., Szalay, J.R., Tapley, M., Taylor, A., Taylor, H., Throop, H.B., Tsang, C.C.C., Tyler, G.L., Umurhan, O.M., Verbiscer, A.J., Versteeg, M.H., Vincent, M., Webbert, R., Weidner, S., Weigle, G.E., White, O.L., Whittenburg, K., Williams, B.G., Williams, K., Williams, S., Woods, W.W., Zangari, A.M., Zirnstein, E., 2015. The Pluto system: Initial results from its exploration by New Horizons. *Science* 350, aad1815. <https://doi.org/10.1126/science.aad1815>
- Stern, S.A., Grundy, W.M., McKinnon, W.B., Weaver, H.A., Young, L.A., 2018. The Pluto System After New Horizons. *Annual Review of Astronomy and Astrophysics* 56, 357–392. <https://doi.org/10.1146/annurev-astro-081817-051935>
- Trafton, L.M., 2015. On the state of methane and nitrogen ice on Pluto and Triton: Implications of the binary phase diagram. *Icarus, Special Issue: The Pluto System* 246, 197–205. <https://doi.org/10.1016/j.icarus.2014.05.022>
- Villaça, C.V.N., Crósta, A.P., Grohmann, C.H., 2021. Morphometric Analysis of Pluto's Impact Craters. *Remote Sensing* 13, 377. <https://doi.org/10.3390/rs13030377>
- White, O.L., Moore, J.M., McKinnon, W.B., Spencer, J.R., Howard, A.D., Schenk, P.M., Beyer, R.A., Nimmo, F., Singer, K.N., Umurhan, O.M., Stern, S.A., Ennico, K., Olkin, C.B., Weaver, H.A., Young, L.A., Cheng, A.F., Bertrand, T., Binzel, R.P., Earle, A.M., Grundy, W.M., Lauer, T.R., Protopapa, S., Robbins, S.J., Schmitt, B., 2017. Geological mapping of Sputnik Planitia on Pluto. *Icarus, Special Issue: The Pluto System* 287, 261–286. <https://doi.org/10.1016/j.icarus.2017.01.011>

Chapter 5

The Outer Solar System Astrophysics Lab: A New Experimental Facility for Spectral and Thermal Investigations of Ices at Cryogenic Temperatures

A. Emran and V. F. Chevrier

Space and Planetary Sciences, University of Arkansas, Fayetteville, AR 72701, USA

[To be submitted in Journal of Astronomical Instrumentation]

Abstract

Ices of nitrogen (N_2), methane (CH_4), and carbon monoxide (CO), both in pure form and different combinations of mixtures, have been spotted on trans-Neptunian objects (TNOs) and Kuiper Belt objects (KBOs). The characteristics of these ices and their spatial distributions on the planetary bodies are directly associated with geological activities, volatile transport, and their seasonal surface-atmospheric activities. Thus, an accurate estimation of the spectral and thermal properties of the ices is incredibly important for an in-depth understanding of surface-atmospheric mechanisms on TNOs and KBOs. Nevertheless, the estimation of spectral and thermal properties of ice needs an experimental facility to investigate the intrinsic characteristics of volatiles at cryogenic temperatures. While laboratory experimental data on spectral properties are, to some extent, available and known, the data on thermal properties are not widely available, or poorly constrained. In this paper, we propose a method to estimate thermal conductivity, volumetric heat capacity, thermal diffusivity, and thermal inertia of N_2 , CH_4 , and CO ices, and mixtures thereof in

a simulated laboratory setting at temperatures of 20 to 60 K – relevant to TNOs and KBOs. To implement the method, we built a new experimental facility – named the *Outer Solar System Astrophysics Lab* – housed at the University of Arkansas. The laboratory has the capability to experiment with the thermal and spectral (reflectance spectroscopy) properties of ices found in the outer solar system. We provide detailed technical specifications of the laboratory in this paper with the objective that it can be used as a guideline for building similar cryogenic facilities in the future. We expect that the laboratory will provide a wealth of thermal (as well as spectral) data on ices that will pave the way to an improved understanding of the surface-subsurface heat flow, volatile transport mechanisms, and surface-atmospheric interactions at the outer solar system bodies.

Unified Astronomy Thesaurus concepts: Surface ices (2117); Laboratory Astrophysics (2004); Experimental techniques (2078); Thermal Properties (Ice) (2278); Classical Kuiper Belt objects (250); Trans-Neptunian objects (1705)

5.1. Introduction

Ices of nitrogen (N_2), methane (CH_4), and carbon monoxide (CO), both in pure form and different combinations of mixtures, have been discovered to be present abundantly on trans-Neptunian objects (TNOs) and Kuiper Belt objects (KBOs). For instance, N_2 and CH_4 ices have been spotted on Triton, the largest moon of Neptune and a captured KBO (Agnor and Hamilton, 2006), from ground-based observations (Cruikshank et al., 1984, 1993). Spectral signatures of N_2 , CO , and CH_4 ices have been detected on Pluto from both ground-based observations (Cruikshank et al., 1976; Owen et al., 1993) and instruments onboard the New Horizons spacecraft (Stern et al., 2015; Grundy et al., 2016). The observations of Eris, a dwarf planet in the Kuiper Belt, suggest that it hosts ices of N_2 and CH_4 (Dumas et al., 2007). Visible (VIS) and near-infrared (NIR) spectra of

Sedna exhibit the presence of ices that resemble Triton – believed to host N₂ and CH₄ ices (Barucci et al., 2005). Heterogeneous ice mixtures of N₂ and CH₄, along with ethane (C₂H₆), have been reported on the surface of Makemake (Ortiz et al., 2012; Lim et al., 2010).

Owing to the temperature and pressure conditions, N₂, CH₄, and CO ices act as volatile components on the surfaces of TNOs and KBOs. Even though water (H₂O) ice is most prevalent in the outer solar system and interstellar medium (Baragiola, 2003), it acts as non-volatile ice in the surface conditions of many outer solar system bodies. A widespread presence of volatiles on these planetary bodies implies that vapor pressure supports a permanent or seasonal atmosphere around the larger bodies beyond or at the orbit of Neptune (Johnson et al., 2015). For instance, Pluto has a tenuous atmosphere composed mainly of N₂ and trace amounts of CH₄ and CO (Stern et al., 2015; Gladstone et al., 2016). Triton also possesses a thin tenuous molecular N₂-rich atmosphere with a surface pressure of 1.5 – 1.9 Pa (15 – 19 μ bar) as evident from the Voyager 2 encounter data (Ingersoll, 1990), with a trace amount of CH₄ (Lellouch et al., 2010).

Over the past decades, the identifications and characterizations of ices on KBOs and TNOs have been accomplished by the observations at VIS and NIR wavelengths from the ground and space-based facilities. Previous studies confirm that ices on these planetary bodies are distributed in different spatial abundances and geographic locations on their surfaces. For example, the distribution of ices on Pluto’s surface shows a latitudinal pattern with distinct surface compositions of volatiles as characterized by observations from instruments onboard NASA’s New Horizons spacecraft (Schmitt et al., 2017; Protopapa et al., 2017; Emran et al., 2022). The distributions of ices on Pluto are associated with surface geological processes, global volatile transport, and seasonal interactions with the atmosphere driven by its climate dynamics (Bertrand and Forget, 2016). Importantly, surface-atmospheric interactions and volatile transport on a planetary body are

regulated by the thermal properties of surface components. For instance, the characteristic thermal inertia of surface constituents on an icy body of the solar system governs global volatile transport and its seasonal interactions with the atmosphere, such as Triton (Spencer and Moore, 1992).

Thermal inertia (TI) is a measure of how efficiently surface materials can store and release thermal energy or respond to a thermal perturbation. The diurnal and seasonal temperatures of planetary surfaces are directly controlled by the thermal inertia of surface materials (Wang et al., 2010). Thus, surface volatile transport, both short and long-term, on icy planetary bodies in the outer solar system, such as TNOs and KBOs, are influenced by the characteristic thermal inertia of surface regolith. Accordingly, an in-depth understanding of volatile transport on icy bodies necessitates an accurate estimation of the thermal inertia of surface constituents. Furthermore, seasonal variations in the surface temperature of a planetary body are influenced by the subsurface heat conduction and release during the summer and winter seasons, respectively (Spencer and Moore, 1992).

Heat conduction through a material (or conductivity) is directly associated with its thermal inertia and, therefore, determining thermal inertia would provide a clue for the seasonal temperature variation of planetary surfaces. Likewise, characteristic thermal inertia correlates with the ability of seasonal surface-subsurface heat transfer and heat storage of a planetary body. This seasonal heat storage is crucial for icy bodies with very low surface temperatures because they lose less thermal energy by radiation transfer during the winter and store more heat energy that was retained from the previous summer in their subsurface (Spencer and Moore, 1992). Moreover, the stored heat energy and surface thermal inertia influence the temperature and frost (volatiles) stability on icy bodies such as Triton (Spencer and Moore, 1992).

Surface thermal inertia, together with topography and albedo, regulates the surface-atmospheric energy exchange and, thus, influences the climate of a planetary body (MacKenzie et al., 2019). Thus, knowing large-scale variations in surface thermal inertia is important for better simulation of the global circulation models (GCM) at a planetary body. Thermal inertia of the planetary body has also been successfully used for estimating the thickness of dark materials on icy satellites, for instance, Iapetus (Rivera-Valentin et al., 2011). With thermal inertia being a function of heat conduction, a material with lower thermal inertia conducts heat energy (both heating up and cooling down) at a much faster rate compared to a material with higher thermal inertia (MacKenzie et al., 2019). The surface thermal inertia of a planetary body is influenced by the characteristics of the surface constituents and is calculated as:

$$TI = \sqrt{k \rho c} \quad (1)$$

where TI represents the thermal inertia ($\text{J m}^{-2} \text{K}^{-1} \text{s}^{-1/2}$), k is the thermal conductivity ($\text{W m}^{-1} \text{K}^{-1}$), ρ is the density (kg m^{-3}), and c is the specific heat ($\text{J kg}^{-1} \text{K}^{-1}$).

On planetary bodies, thermal inertia is influenced by the physical nature of surface regolith such as grain size, material abundance, porosity, compaction, and so on (see Kieffer et al., 1977; Jakosky, 1986; Putzig et al., 2005; Fergason et al., 2006). Direct global measurements of these surface physical characteristics are unrealistic and impossible for celestial objects (Wang et al., 2010). Hence, thermal inertia for planetary bodies has been estimated from orbital observations or estimated using laboratory simulants. For instance, the thermal inertia of the martian surface was computed by fitting a model of multiple parameters to the brightness temperature measurement from thermal infrared (TIR) observations onboard orbital spacecraft (Jakosky et al., 2000; Fergason et al., 2006).

Using the thermal infrared measurements from Cassini's Composite Infrared Spectrometer (CIRS) instrument, the thermal inertia of the Saturnian moons was estimated (Howett et al., 2010; Rivera-Valentin et al., 2011). Recently, MacKenzie et al. (2019) prepared a global thermal inertia map of Titan's surface based on terrain types using the Cassini RADAR and the Visible and Infrared Mapping Spectrometer (VIMS) data. Likewise, thermal inertia was estimated for other planetary bodies in the solar system such as the lunar regolith (Feng et al., 2020), near-Earth asteroids (Delbo' et al., 2007), and the main-belt asteroid Ceres (Rognini et al., 2020).

Though the constituent volatiles and their spatial abundances on TNO and KBO surfaces are known, to some extent, their thermal properties have not been hitherto measured for all possible compounds and mixtures thereof. This is unfortunate, since they are important to understanding seasonal volatile transport modeling and atmosphere-climate dynamics. Albeit estimated for terrestrial planets, moons, and asteroids, no attempt has been put forward in determining the thermal properties of TNOs and KBOs surface ice, at large, yet. Having a paucity of orbital spacecraft's thermal observations permits a potential avenue for utilizing laboratory experiments for estimating the thermal properties of N_2 , CH_4 , and CO ices (pure and mixture) relevant to KBOs and TNOs. Thus, the laboratory estimation of thermal properties (conductivity, diffusivity, volumetric heat capacity, and thermal inertia) certainly uncovers a new avenue for an improved understanding of a vast number of planetary objects in the outer solar system.

The volatiles on TNO and KBO surfaces show a wide variety of thermodynamic solid phase transitions. For instance, CH_4 ice shows an I-II solid phase transition at around ~ 21 K (Prokhvatilov and Yantsevich, 1983) whereas the α (cubic) - β (hexagonal) phase transition of N_2 appears at ~ 35.6 K (Scott, 1976), and the α - β phase transition of CO occurs at 61 K (e.g., Vetter et al., 2007). These solid phases are important because the phase transitions of crystalline ices are

associated with the slow seasonal surface volatile movements and evolution of the thin atmosphere present on TNOs and KBOs, specifically the thin N₂-rich atmospheres of the Pluto and Triton (Cruikshank and Silvaggio, 1980; Hubbard et al., 1988; Lellouch et al., 2009). Existing data shows that the thermal properties of cryogenic N₂ ice are dependent on its thermodynamic solid phases – see Sagmiller and Hartwig (2020) for a comprehensive review. The volumetric heat capacity and, thus, the thermal inertia of N₂ ice changes at the α - β phase boundary at 35.6 K (Fig. 5.1). Thus, it is reasonable to hypothesize that the thermal properties of other surface volatiles on TNOs and KBOs are also dependent on the thermodynamic phases of their constituent ices.

N₂, CH₄, and CO ices in KBOs and TNOs surface conditions are often observed to appear in different mixtures (binary and ternary) rather than in pure forms. For instance, at 40 K temperature (Pluto's average surface), N₂ and CH₄ ices are partly soluble and form two different binary mixtures; N₂-rich ice diluted with CH₄ (N₂:CH₄) and CH₄-rich ice diluted with N₂ (CH₄:N₂; Prokhvatilov and Yantsevich, 1983; Trafton, 2015). Likewise, ice mixtures of CO and N₂ are fully miscible and the binary undergoes an α - β transition at a range of temperatures, depending on the N₂ molar ratio (Angwin and Wasserman, 1966). The ices can also form the ternary mixtures as N₂ + CH₄ + CO, though the phase diagram for the mixture of the ternary mixture is not available to date (currently under development). Unfortunately, the thermal properties of these different ices (pure and mixtures) on TNOs and KBOs are not available or poorly constrained. Thus, an estimation of the thermal properties of N₂, CH₄, and CO ices, and mixtures thereof at temperatures range of 20 - 60 K using laboratory simulation is warranted.

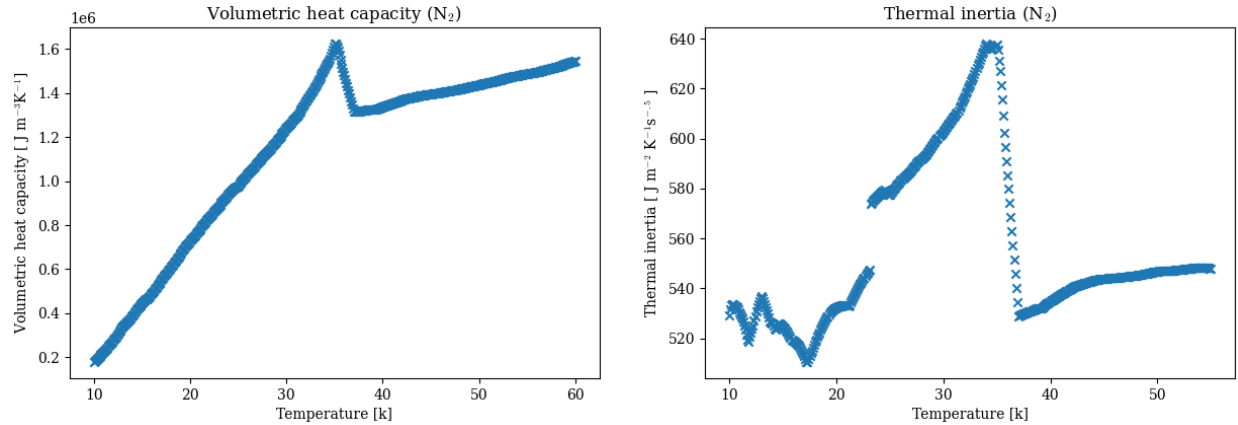


Fig. 5.1: The volumetric heat capacity and thermal inertia of solid N_2 ice at temperatures of 10 to 60 K (compiled data from Sagmiller and Hartwig, 2020) – relevant to TNO and KBO surfaces. The subplots exhibit an abrupt change in the volumetric heat capacity and thermal inertia trends at the α (cubic) - β (hexagonal) phase transition of N_2 ice at ~ 35.6 K.

In this paper, we propose a method to estimate thermal conductivity, volumetric heat capacity, thermal diffusivity, and thermal inertia of N_2 , CH_4 , and CO ices, and mixtures thereof in a simulated laboratory setting. We describe a detailed methodology, including the theory of the proposed method, which can be used to estimate the thermal properties of ices at cryogenic temperatures. To implement the method, we built a new experimental facility at the University of Arkansas – named the *Outer Solar System Astrophysics Lab (OSSAL)*. The laboratory has facilities to experiment with spectral and thermal properties of volatile ices found on the surfaces of outer solar system bodies. We provide detailed technical specifications of the new experimental facility so that it can help as a guideline for building a similar cryogenic chamber in the future for scientific experiments on the characteristics of ices.

We also include the proposed experimental protocol to estimate the thermal properties of the ices in that laboratory setting. The parameters to be estimated are thermal conductivity, volumetric heat capacity, and thermal diffusivity of N_2 , CH_4 , and CO ices, and mixtures thereof at cryogenic conditions (20 - 60 K). As the key thermal properties are intended to be measured, the experimental

facility will help in estimating the thermal inertia of ice mixtures at different thermodynamic phases present in TNOs and KBOs surface environments. Accordingly, the results from the laboratory experiments will help in an improved understanding of the volatile transport mechanisms and the diurnal and seasonal variations of the surface temperature and other associated processes on TNOs and KBOs. As this has not been fully tested yet in the lab to date of publication of this paper, we also include potential limitations of the proposed methods and explain potential mitigations for these shortcomings.

5.2. Method

We use the dual-probe heat-pulse (DPHP) method (Bristow et al., 1994) to estimate the thermal properties of the ices. The method is based on radial heat conduction theory and has successfully been used for estimating the thermal properties of snow (Liu and Si, 2008). The same generic method has also been applied in measuring the thermal properties of icy Mars regolith simulants (Siegler et al., 2012). A DPHP device hosts two parallel needles as probes, though more needles are also used to estimate the thermal properties of materials using a similar theory. One needle probe contains a heater (heat probe) to produce a heat pulse for a short duration while another contains a temperature sensor (sensor probe). Both probes are separated by a certain distance. The DPHP method measures the temperature changes over time at the sensor probe liberated from the heater probe (Campbell et al., 1991). A heat pulse is propagated into the sample of interest by introducing an electric current through the heater probe. The temporal changes in temperature rise are recorded by a thermal sensor (thermistor/ silicon-diode/ thermocouple) at the sensor probe. Thermal properties including thermal conductivity, volumetric heat capacity, and thermal diffusivity are estimated from the data of amplitude and time of maximum temperature rise at the sensor probe.

5.2.1. Theory

We consider the radial heat conduction from an infinite line source through a homogenous isotropic sample. Moreover, the sample is also considered to have an initial temperature that is uniform. The heat conduction equation for radial coordinates can be written as (Bristow et al., 1994):

$$\frac{\partial T}{\partial t} = \lambda \left\{ \frac{\partial^2 T}{\partial r^2} + r^{-1} \frac{\partial T}{\partial r} \right\} \quad (2)$$

where T is the temperature (K), t is time (s), λ is the thermal diffusivity ($\text{m}^2 \text{s}^{-1}$), and r is the radial distance (m). If a heat pulse of a short-duration t_0 (s) at a constant rate per unit length q ($\text{J m}^{-1} \text{s}^{-1}$) is applied to an infinite solid, then an analytic solution of the rise of temperature ΔT at a distance r can be derived as (De Vries, 1952; Kluitenberg et al., 1995):

$$\Delta T(t, r) = -\frac{q}{4\pi k} Ei \left[-\frac{r^2}{4\lambda t} \right]; 0 < t \leq t_0 \quad (3)$$

$$\Delta T(t, r) = \frac{q}{4\pi k} \left\{ Ei \left[\frac{-r^2}{4\lambda(t-t_0)} \right] - Ei \left[\frac{-r^2}{4\lambda t} \right] \right\}; t > t_0 \quad (4)$$

here, $-Ei(-x)$ is the exponential integral of the argument and k is the thermal conductivity ($\text{W m}^{-1} \text{K}^{-1}$). From the time derivatives of equations (3) and (4) we estimate the thermal diffusivity, λ and volumetric heat capacity, ρc ($\text{J m}^{-3} \text{K}^{-1}$) as (Bristow et al., 1994):

$$\lambda = \frac{r^2}{4} \left\{ \frac{\frac{1}{(t_m-t_0)} \frac{1}{t_m}}{\ln \left[\frac{t_m}{t_m-t_0} \right]} \right\} \quad (5)$$

$$\rho c = \frac{q}{4\pi\lambda\Delta T_m} \left\{ Ei \left(\frac{-r^2}{4\lambda(t_m-t_0)} \right) - Ei \left(\frac{-r^2}{4\lambda t_m} \right) \right\} \quad (6)$$

where ΔT_m is the maximum temperature rise and t_m is the time at which ΔT_m occurs. Once λ and ρc are known, the thermal conductivity, k can be computed from the following relation:

$$\lambda = \frac{k}{\rho c} \quad (7)$$

Alternatively, k can also be derived as (Noborio et al., 1996):

$$k = \frac{q}{4\pi\lambda \Delta T_m} \left[Ei \left\{ -\frac{\ln\left[\frac{t_m}{t_m-t_0}\right]}{\frac{t_0}{t_m}} \right\} - Ei \left\{ -\frac{\ln\left[\frac{t_m}{t_m-t_0}\right]}{\frac{t_0}{t_m}} \right\} \right] \quad (8)$$

The parameters (r , q , t_0 , t_m , and ΔT_m) present in equations (5) to (8) are known or directly measured. From those, we can estimate the thermal conductivity, volumetric heat capacity, thermal diffusivity, and thermal inertia of samples.

5.2.2. *Samples*

The laboratory experiment starts by making sample mixtures (pure, binary, and ternary) of N₂, CH₄, and CO ices. Binary samples (N₂-CH₄, N₂-CO, and CH₄-CO) are prepared in a range of 10 mol% - 90 mol% in 10 mol% increments. Consequently, each binary adds up to 9 different ratios every 10 K in the range of 20-60 K, totaling 45 thermal inertia measurements. Likewise, ternary samples (N₂-CH₄-CO) are prepared at different mol% combinations at a minimum of 5 mol% to a maximum of 90 mol% of each constituent which adds to 12 mixture samples to be tested at different temperatures.

Each ice sample is prepared initially at an experimental minimum of 20 K. Once the sample is at an initial uniform temperature, a short-duration radiating heat pulse is liberated from the heater probe of a DPHP device. The temperature histories (rise) of the samples are recorded at the sensor

probe. This procedure is repeated for each sample by ramping up the temperature at 10 K increments up to an experimental maximum of 60 K. For each temperature point, the parameter values of r , q , t_0 , t_m , and ΔT_m are recorded from the DPHP device. Lastly, the thermal properties of the samples are calculated by plugging in the parameters' values in equations (5) to (8), and finally (1) to derive thermal inertia.

5.3. Outer Solar System Astrophysics Lab

We built a brand-new planetary simulation chamber – named the *Outer Solar System Astrophysics Lab (OSSAL)* – which is the latest addition to the W.M. Keck Laboratory for Planetary Simulations at the University of Arkansas, Fayetteville. The chamber has been built to investigate spectral and thermal properties of ices under tantamount TNOs and KBOs surface conditions. The basic configuration of the chamber was designed following the similar facility available at the *Astrophysical Materials Laboratory* located in the Department of Astronomy and Planetary Science at Northern Arizona University (Tegler et al., 2010). We employ expertise and previous experiences in building our existing *Pluto Simulation Chamber*, which is currently being used for spectral characterization of outer solar system ices. However, the existing *Pluto Simulation Chamber* is, unfortunately, not designed to prepare large volumes (cm-sized cubes) of ice requires for the investigation of the thermal properties.

The OSSAL is a custom-designed chamber made of 304L stainless steel in a cylindrical shape. The main chamber is analogous to a vacuum-evacuated body and was built keeping in mind that it maintains proper thermal insulation and does not allow contaminants to condense inside it. The chamber is 20" (50.8 cm) long by 12" (30.48 cm) in diameter in the outer dimension (see Fig. 5.2 for the schematic of the chamber). The top and bottom of the cylindrical chamber hold 14" ConFlat

(CF) flanges (1-fixed feed-thru, 1-rotating feed-thru) such that the lid of the chamber holds the fixed feed-thru. The bottom flange adapter is the rotating feed-thru with a machined profile to mate with a CH-110LT 40K Cryocooler Series helium refrigerator system. The chamber has eight 2.75" CF ports, of which 4 are fixed feed-thru and the rest 4 are rotating feed-thru (see Fig. 5.3 for the pictures of the chamber).

The port enables access to facilities for inserting sample gas, thermocouples, fiber optics feed port for Raman and NIR spectroscopic investigations, optical camera, LED light, and electric supply inside the chamber from outside. Furthermore, there is a 6" CF port (rotating feed-thru) for connecting vacuum pumps with the chamber. The main body of the chamber was built by Kurt J. Lesker at Jefferson, PA. Vacuum pumps are used to achieve a simulant pressure ($\sim 14 \mu\text{bar}$) and the cryocooler is used to obtain cryogenic temperatures (down to 15 K) inside the chamber. These temperature and pressure conditions are relevant to the outer solar system bodies. Note that the chamber was designed in such a way that it can accommodate both roughing and turbo pumps to achieve high to ultra-vacuum conditions inside the chamber.

We use an enclosed ice sample cell with a cubic volume inside (edge of $\sim 15 \text{ mm}$) made of aluminum alloy. The cell device was machined by the electronic shop in the Department of Physics at the University of Arkansas. The DPHP device was built and tested by the East 30 Sensor in Pullman, WA. The cell is mounted/ placed onto the upward-pointing cold tip of the helium cryocooler within the chamber cylinder (see Fig. 5.4 for the schematic of the cell). For visual investigation of samples, there is a glass window on one side of the cell sealed in place with indium gaskets. Furthermore, for reflectance spectroscopy such as Raman and Fourier-transform infrared spectroscopy (FTIR) of samples, there is a sapphire/quartz window on another side of the cell sealed in place also with indium gaskets.

To monitor the temperature of the cell, we use a pair of silicon diode thermometers attached to the body of the cell. One silicon diode is placed in the upper part (T2) and another in the lower part (T1) of the cell. We wrap a pair of heater wires (nickel-chromium) around the cell to tweak the temperature gradient in different parts of the cell. To maintain good thermal contact, the heater wires are cemented with an epoxy glue that has higher thermal conductivity. Like the silicon diodes, one heater wire is warped around the upper part (H2) and another in the lower part (H1) of the cell. To monitor and control the temperature of the cell, we use a high-performance temperature controller. This control of cell temperature is accomplished via proportional, integral, and derivative (PID) closed-loop control of both heater wires. The temperature controller is regulated by a program written in the LabView programming environment developed by the Department of Physics at the University of Arkansas.

The DPHP probes are inserted into the cell from above in such a way that the heater probe is placed in the center of the cell volume (see Fig. 5.4). In this instance, the DPHP device consists of two needle probes each 12-mm length mounted in a sensor body. The probes are placed parallel with a 6 mm spacing between them. The sensor probe contains a temperature sensor (silicon diode thermometer) placed in the needle's center, and the other probe contains a heater wire with a known resistance. The probes are fabricated from thin stainless-steel tubing filled with thermally conductive epoxy glue to reduce radial heat gradient across the probe and provide liquid resistance and electric insulation. We use a LabView controller program to make our lab protocol facility automatic, such that it generates a heat pulse of short duration at the heater probe, and then records the temperature rise at the sensor probe as the time elapses.

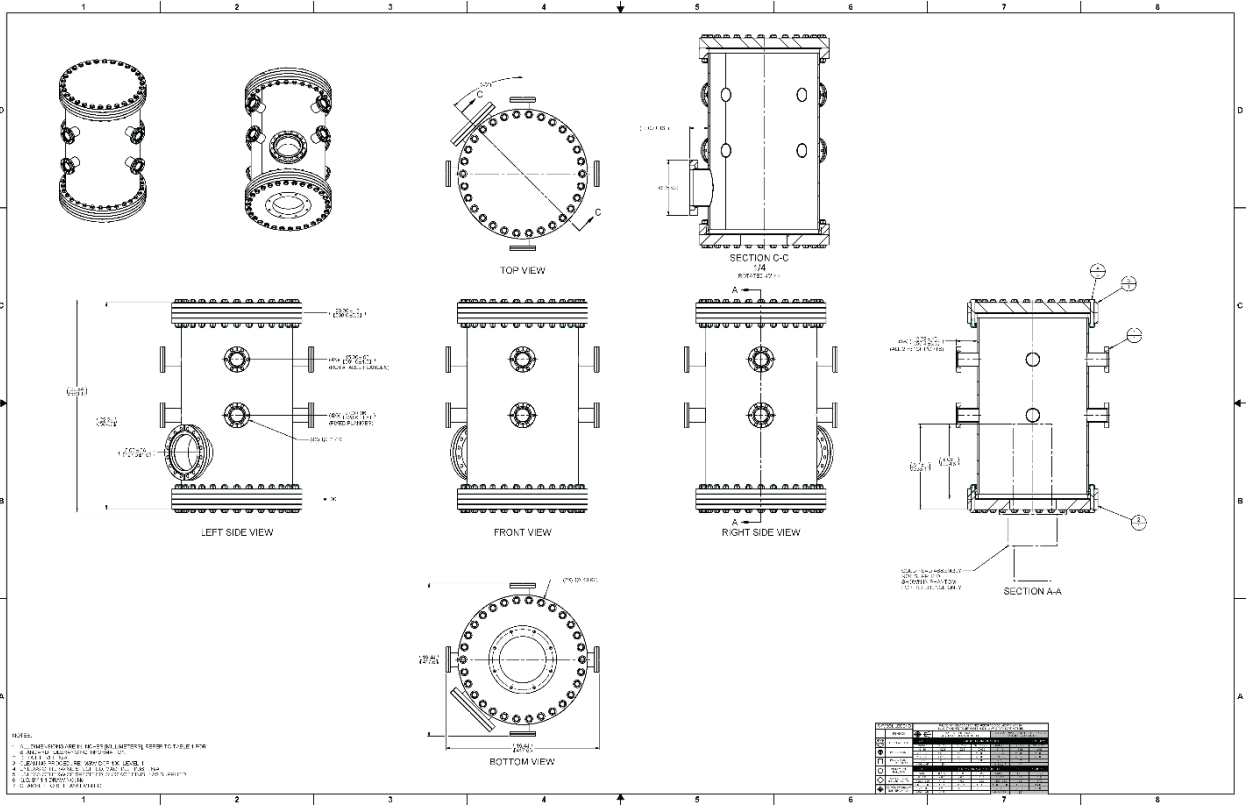


Fig. 5.2: Schematic diagram of the *Outer Solar System Astrophysics Lab* at the University of Arkansas. The chamber is 20" (50.8 cm) long by 12" (30.48 cm) in diameter in the outer dimension. The top and bottom of the cylindrical chamber hold 14" ConFlat (CF) flanges (1-fixed feed-thru, 1-rotating feed-thru) such that the lid of the chamber is the fixed feed-thru. The bottom flange adapter is the rotating feed-thru with a machined profile to mate with a CH-110LT 40K Cryocooler Series helium refrigerator system. The chamber has eight 2.75" CF ports, of which 4 are fixed feed-thru and the rest 4 are rotating feed-thru. The chamber drawing was adopted and subsequently modified from the official manufacture order at Kurt J. Lesker in Jefferson, PA. For a higher resolution version of the diagram, the readers are referred to the online version of the figure.



Fig. 5.3: Pictures of the *Outer Solar System Astrophysics Lab* at the Keck Laboratory for Planetary Simulations at the University of Arkansas. A CH-110LT 40K Cryocooler Series helium refrigerator system is attached to the chamber with the bottom flange adapter. The chamber has eight CF ports, of which 4 are fixed feed-thru and the rest 4 are rotating feed-thru. A pressure gauge is connected to the chamber with a feed-thru (see Super Bee pressure gauge attached on the left side of the chamber). For measurement of temperature inside the chamber, a thermocouple feed-thru is also connected to the chamber. For a higher resolution version of the diagram, the readers are referred to the online version of the figure.

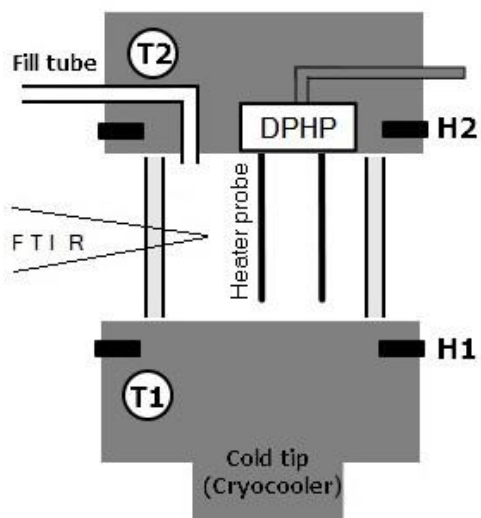


Fig. 5.4: The schematic diagram of the cell (mounted upon the cold tip of the cryocooler) in cross-section as seen from the side. Gas enters the cell via a fill tube. Glass windows for visual inspections of ice and the sapphire window for Raman and FTIR (reflectance spectroscopic) investigations. Thermometer T1 and T2 and heating wires H1 and H2 are used to monitor and control temperature, respectively. The DPHP sensor probe enters the cell from above.

5.4. Experimental procedure

The chamber has access points for instrumentation probe purposes. Amid a similar laboratory configuration, we adopt the basic experimental procedure followed by Tegler et al. (2010) and Protopapa et al. (2015), with some modifications based on our intended objectives and chamber uniqueness. Binary and ternary mixtures of N_2 - CH_4 - CO ice are prepared in a pre-mixing chamber using partial pressures and ideal gas law to control molar ratios. A purging process is carried out several times before the experiment starts. Upon purge, we fill the pre-mixing chamber with a gas mixture of a particular molar ratio, depending on the experiment, at around 1 bar and room temperature. Next, the cell is pumped down to $\sim 5 \times 10^{-8}$ torr and starts cooling down. Initially, we cool down the cell at a temperature that is slightly higher than the melting point of the sample ice. For instance, a temperature of ~ 65 K is kept at the bottom of the cell. However, this temperature is subject to change depending on the gas mixing ratio. An analogous procedure has been shown to be successful in making ice in a similar laboratory setting (Tegler et al., 2010).

The mixture of gases is then transferred through a flexible fill tube (made of stainless steel) into the simulation chamber and bled into the cell where it immediately condenses into liquid and starts filling in the cell volume. Once the cell volume is filled with the liquid sample, we immediately stop the transfer of gas. Upon filling the cell with a liquid sample, we slowly decrease the cell temperature (at a rate of ~ 0.1 K/minute) to below the sample's melting point based on existing phase diagrams, such as the CH₄-N₂ binary system (Prokhvatilov and Yantsevich, 1983) or visual inspection of the sample. A thermal gradient (~ 2 K) is maintained across the cell during the freezing of the ice using heater wires (Fig. 5.4) so that the sample freezes from bottom to top.

Once the entire sample inside the cell is condensed, the thermal gradient is removed, and the cell temperature is further dropped down to an experiment minimum of 20 K. Once the sample achieves a uniform temperature within the cell, a heat pulse is introduced by applying a known voltage from a direct-current (DC) source to the heater needle probe (q). Note that the heat pulse is produced for a fixed short period of time (t_0). We plan to initially apply a heat pulse for ~ 8 s for most of the experiments (subject to change based on experimental results). The LabView controller controls the heat pulse, monitors the current through the heater, and measures the resulting temperature rise as the time elapses using the sensor probe at a particular distance (r). Next, the values of t_m and ΔT_m are obtained from temperature histories recorded by the DPHP device.

While the values of t_m and ΔT_m along with r , q , and t_0 are determined, we calculate the thermal conductivity, volumetric heat capacity, thermal diffusivity, and eventually thermal inertia of ice mixtures using the equations (5) to (8) and (1). To maximize accuracy, we repeat this measurement 5 times at each temperature point for each sample ratio. Once done with the experiment at 20 K, we increase the temperature of the sample by 10 K increments up to the experimental maximum of 60 K to constrain the temperature phase transition of mixtures, and particularly the α - β

transitions of nitrogen and methane at ~35 and 21 K, respectively. Thus, the above DPHP procedure is repeated at temperatures of 30, 40, 50, and 60 K.

5.5. Uncertainty and mitigation of risk

The generic DPHP technique is a well-established method and has successfully been applied to terrestrial materials (Bristow et al., 1994), planetary icy regolith simulants (Siegler et al., 2012), and snow (Liu and Si, 2008). Thus, we are confident that the method works successfully in estimating the thermal properties of N₂, CH₄, and CO ices at cryogenic temperatures. Thermal conductivity measurement may slightly be influenced by the contact resistance between the probe and sample (Siegler et al., 2012). Consequently, a portion of the pulse-generated heat may flow to the body of the DPHP device. To limit this issue, the body of the device is glued with epoxy of low thermal conductivity in a Teflon spin, for instance (Siegler et al., 2012).

The studied ices are highly volatile even at the surface temperatures of TNOs and KBOs and, thus, liberating a short-duration heat pulse may cause some sublimation of the sample. To mitigate this possible setback, we generate a small amount of heat pulse, determined by trial-and-error and experimental results, so that radial heat conduction happens through the sample without sublimation of ices. Moreover, all experiments run below the melting points of ice mixtures in an enclosed cell and the sample is heated in the center of the ice cube - leaving a negligible chance of sample sublimation due to introducing a short-duration heat pulse.

As thermodynamics dictates, at lower temperatures in the outer solar system, such as the temperature on Pluto, the N₂, CH₄, and CO ices condense and form van der Waals bonded crystalline ices (e.g., Cruickshank et al., 2021). Accordingly, we make crystallized solid ices from

liquid and the quality of crystalline samples is primarily dependent on the cooling rates, more specifically during $\beta \rightarrow \alpha$ phase transition (Stachowiak et al., 1994). We cool down the sample at a rate slow enough (initially 0.1 K/min) so that the sample does not have any visually observable defects – the samples are transparent without cracks. We repeat each experiment multiple times to confirm the good quality of the samples and adapt the cooling rate to minimize defects (e.g., inhomogeneity) in the sample.

Because of how the ices are grown and mixed from the liquid phase, the method doesn't account for porosity, a parameter that can affect the thermal properties of ices (Ferrari and Lucas, 2016). However, the thermal properties of a porous sample can be computed if the thermal properties of the solid/particle sample – measured in this project – are known. For instance, the effective thermal conductivity of a porous solid can be derived from the Maxwell–Eucken relation (Woodside and Messmer, 1961) or equivalently the Hashin–Shtrikman upper bound (Smith et al., 2013). Note that the porous regolith of TNOs and KBOs is filled with $\text{N}_2\text{-CH}_4\text{-CO}$ gas mixtures. The thermal conductivity of the $\text{N}_2\text{-CH}_4\text{-CO}$ gas mixture is known $k_g = k_0 T^\alpha$; where T is the temperature; $\alpha = 1.12$; $k_0 = 5.63 \text{ erg cm}^{-1}\text{s}^{-1} \text{ K}^{-2}$ (Zhang et al., 2017). Thus, the net effective thermal conductivity of the icy porous regolith can be computed once the thermal conductivities of the solid ices are known and modified to account for porosity.

The experimental results, here measurement of thermal properties e.g., thermal conductivity and specific heat, may have errors due to instrumental glitches. We estimate and subsequently calibrate these errors by comparing the result of thermal conductivity (and thermal inertia) of pure N_2 , CH_4 , and CO ices at a range of temperatures from our experiments to existing literature listed in table II by Spencer et al. (1997) and other references found in Sagmiller and Hartwig (2020). Comparison with the existing data also provides an understanding of the sensitivity of the implemented

technique (DPHP) in deriving the thermal properties of ices at cryogenic temperatures in a laboratory setting.

5.6. Conclusions

The surface-atmospheric interactions at TNOs and KBOs involve the exchange of matter and energy, which are associated with the constituent materials involved and their thermal states. Thermal inertia influences surface volatile transport on icy bodies such as Pluto, Triton, and Titan by controlling the subsurface heat conduction, diurnal and seasonal temperature variation, and subsurface heat storage (Spencer and Moore, 1992). On Triton, thermal inertia determines the thickness and extent of seasonal N₂ frosts (Spencer and Moore, 1992), which is a major surface constituent of TNOs and KBOs. Surface thermal inertia, together with topography and albedo, controls energy exchange between the surface and atmosphere and, thus, influences the weather and climate of a planetary body (MacKenzie et al., 2019). In this way, the determination of variation in thermal inertia, at a large scale, is essential for better simulation of global circulation models (GCM) for planetary bodies in the outer solar system.

Though estimated for other planetary bodies (terrestrial and icy surfaces) of the solar system, no attempt has been put forward in determining the thermal properties of the vast amount of TNOs and KBOs. Thus, determining thermal inertia will certainly uncover a new avenue for a better understanding of a large number of planetary objects on the outer edge of the solar system. In this paper, we propose a method to estimate the thermal properties of N₂, CH₄, and CO ices, and mixtures thereof in a simulated laboratory setting at temperatures of 20 – 60 K. To implement the method, we built a new experimental facility at the University of Arkansas, which has facilities to experiment with spectral and thermal properties of ices found on KBOs and TNOs. We provide

detailed technical specifications of the chamber in this paper so that it can be utilized as a guideline for building similar laboratory facilities in the future. The resulting thermal data, estimated from the implementation of the proposed method using the new laboratory facility, will provide a wealth of information about the thermal properties of ices at cryogenic temperatures. Since N₂, CH₄, and CO ices are abundant volatiles on the planetary bodies of the outer solar system, therefore, the output from this paper will help with the interpretation of the mysteries of KBOs and TNOs.

5.7. Acknowledgments

We are grateful to Kevin Lyon, Stephen Tegler, Will Grundy, Walter Graupner Jr., Gregory Talley, Matt Siegler, Caitlin Ahrens, Jill McDonald, William (Lin) Oliver, Pradeep Kumar, Hugh Churchill, and Hasan Doha for their support during the design and building of the cryogenic chamber and formulating method for thermal properties measurement. We are also grateful to Kurt J. Lesker company for custom building the vacuum chamber and supplying the other laboratory accessories and to East 30 company for building the custom-designed dual-probe thermal conductivity sensor. The authors would also like to thank anonymous reviewers for their useful comments.

5.8. Appendix

List of notations used in this paper

c	Specific heat
Ei	Exponential of integral
k	Thermal conductivity
q	Heat pulse
r	Radial distance
T	Temperature
t	Time
TI	Thermal inertia
T_m	Time at maximum temperature
t_o	Short duration
ΔT	Temperature rise
λ	Thermal diffusivity
ρ	Density
ρc	Volumetric heat capacity

5.9. References

- Agnor, C.B., Hamilton, D.P., 2006. Neptune's capture of its moon Triton in a binary–planet gravitational encounter. *Nature* 441, 192–194. <https://doi.org/10.1038/nature04792>
- Angwin, M.J., Wasserman, J., 1966. Nitrogen—Carbon Monoxide Phase Diagram. *Journal of Chemical Physics* 44, 417–418. <https://doi.org/10.1063/1.1726486>
- Baragiola, R.A., 2003. Water ice on outer solar system surfaces: Basic properties and radiation effects. *Planetary and Space Science, Surfaces and Atmospheres of the Outer Planets their Satellites and Ring Systems* 51, 953–961. <https://doi.org/10.1016/j.pss.2003.05.007>
- Barucci, M.A., Cruikshank, D.P., Dotto, E., Merlin, F., Poulet, F., Ore, C.D., Fornasier, S., Bergh, C. de., 2005. Is Sedna another Triton? *A&A* 439, L1–L4. <https://doi.org/10.1051/0004-6361:200500144>
- Bertrand, T., Forget, F., 2016. Observed glacier and volatile distribution on Pluto from atmosphere–topography processes. *Nature* 540, 86–89. <https://doi.org/10.1038/nature19337>
- Bristow, K.L., Kluitenberg, G.J., Horton, R., 1994. Measurement of Soil Thermal Properties with a Dual-Probe Heat-Pulse Technique. *Soil Science Society of America Journal* 58, 1288–1294. <https://doi.org/10.2136/sssaj1994.03615995005800050002x>
- Campbell, G.S., Calissendorff, C., Williams, J.H., 1991. Probe for Measuring Soil Specific Heat Using A Heat-Pulse Method. *Soil Science Society of America Journal* 55, 291–293. <https://doi.org/10.2136/sssaj1991.03615995005500010052x>
- Cruikshank D. P., Grundy W. M., Protopapa S., Schmitt B., and Linscott I. R., 2021. Surface composition of Pluto. In S. A. Stern, J. M. Moore, W. M. Grundy, L. A. Young, and R. P. Binzel (Eds.), *The Pluto System After New Horizons*. pp. 165–193. Univ. of Arizona, Tucson.
- Cruikshank, D.P., Hamilton Brown, R., Clark, R.N., 1984. Nitrogen on Triton. *Icarus* 58, 293–305. [https://doi.org/10.1016/0019-1035\(84\)90046-0](https://doi.org/10.1016/0019-1035(84)90046-0)
- Cruikshank, D.P., Pilcher, C.B., Morrison, D., 1976. Pluto: Evidence for Methane Frost. *Science* 194, 835–837.
- Cruikshank, D.P., Roush, T.L., Owen, T.C., Geballe, T.R., Bergh, C. de, Schmitt, B., Brown, R.H., Bartholomew, M.J., 1993. Ices on the Surface of Triton. *Science* 261, 742–745. <https://doi.org/10.1126/science.261.5122.742>
- Cruikshank, D.P., Silvaggio, P.M., 1980. The surface and atmosphere of Pluto. *Icarus* 41, 96–102. [https://doi.org/10.1016/0019-1035\(80\)90162-1](https://doi.org/10.1016/0019-1035(80)90162-1)
- De Vries, A. D., 1952. A nonstationary method for determining thermal conductivity of soil in situ. *Soil Science* 73, 83–90.

- Delbo', M., dell'Oro, A., Harris, A.W., Mottola, S., Mueller, M., 2007. Thermal inertia of near-Earth asteroids and implications for the magnitude of the Yarkovsky effect. *Icarus* 190, 236–249. <https://doi.org/10.1016/j.icarus.2007.03.007>
- Dumas, C., Merlin, F., Barucci, M.A., Bergh, C. de, Hainault, O., Guilbert, A., Vernazza, P., Doressoundiram, A., 2007. Surface composition of the largest dwarf planet 136199 Eris (2003 UB). *A&A* 471, 331–334. <https://doi.org/10.1051/0004-6361:20066665>
- Emran, A., Dalle Ore, C.M, Ahrens, C. J., Khan, M.K.H., Chevrier, V.F., and Cruickshank, D. P. Pluto's surface mapping using unsupervised learning from LEISA/Ralph. *The Planet. Sci. Journal* (under review)
- Feng, J., Siegler, M.A., Hayne, P.O., 2020. New Constraints on Thermal and Dielectric Properties of Lunar Regolith from LRO Diviner and CE-2 Microwave Radiometer. *Journal of Geophysical Research: Planets* 125, e2019JE006130. <https://doi.org/10.1029/2019JE006130>
- Ferguson, R.L., Christensen, P.R., Kieffer, H.H., 2006. High-resolution thermal inertia derived from the Thermal Emission Imaging System (THEMIS): Thermal model and applications. *Journal of Geophysical Research: Planets* 111. <https://doi.org/10.1029/2006JE002735>
- Ferrari, C., Lucas, A., 2016. Low thermal inertias of icy planetary surfaces - Evidence for amorphous ice? *A&A* 588, A133. <https://doi.org/10.1051/0004-6361/201527625>
- Gladstone, G.R., Stern, S.A., Ennico, K., Olkin, C.B., Weaver, H.A., Young, L.A., Summers, M.E., Strobel, D.F., Hinson, D.P., Kammer, J.A., Parker, A.H., Steffl, A.J., Linscott, I.R., Parker, J.W., Cheng, A.F., Slater, D.C., Versteeg, M.H., Greathouse, T.K., Retherford, K.D., Throop, H., Cunningham, N.J., Woods, W.W., Singer, K.N., Tsang, C.C.C., Schindhelm, E., Lisse, C.M., Wong, M.L., Yung, Y.L., Zhu, X., Curdt, W., Lavvas, P., Young, E.F., Tyler, G.L., Team, the N.H.S., 2016. The atmosphere of Pluto as observed by New Horizons. *Science* 351. <https://doi.org/10.1126/science.aad8866>
- Grundy, W.M., Binzel, R.P., Buratti, B.J., Cook, J.C., Cruickshank, D.P., Ore, C.M.D., Earle, A.M., Ennico, K., Howett, C.J.A., Lunsford, A.W., Olkin, C.B., Parker, A.H., Philippe, S., Protopapa, S., Quirico, E., Reuter, D.C., Schmitt, B., Singer, K.N., Verbiscer, A.J., Beyer, R.A., Buie, M.W., Cheng, A.F., Jennings, D.E., Linscott, I.R., Parker, J.W., Schenk, P.M., Spencer, J.R., Stansberry, J.A., Stern, S.A., Throop, H.B., Tsang, C.C.C., Weaver, H.A., Weigle, G.E., Young, L.A., Team, and the N.H.S., 2016. Surface compositions across Pluto and Charon. *Science* 351. <https://doi.org/10.1126/science.aad9189>
- Howett, C.J.A., Spencer, J.R., Pearl, J., Segura, M., 2010. Thermal inertia and bolometric Bond albedo values for Mimas, Enceladus, Tethys, Dione, Rhea and Iapetus as derived from Cassini/CIRS measurements. *Icarus, Cassini at Saturn* 206, 573–593. <https://doi.org/10.1016/j.icarus.2009.07.016>
- Hubbard, W.B., Hunten, D.M., Dieters, S.W., Hill, K.M., Watson, R.D., 1988. Occultation evidence for an atmosphere on Pluto. *Nature* 336, 452–454. <https://doi.org/10.1038/336452a0>

- Ingersoll, A.P., 1990. Dynamics of Triton's atmosphere. *Nature* 344, 315–317. <https://doi.org/10.1038/344315a0>
- Jakosky, B.M., Mellon, M.T., Kieffer, H.H., Christensen, P.R., Varnes, E.S., Lee, S.W., 2000. The thermal inertia of Mars from the Mars Global Surveyor Thermal Emission Spectrometer. *Journal of Geophysical Research: Planets* 105, 9643–9652. <https://doi.org/10.1029/1999JE001088>
- Johnson, R.E., Oza, A., Young, L.A., Volkov, A.N., Schmidt, C., 2015. Volatile loss and classification of Kuiper Belt Objects. *ApJ* 809, 43. <https://doi.org/10.1088/0004-637X/809/1/43>
- Kieffer, H.H., Martin, T.Z., Peterfreund, A.R., Jakosky, B.M., Miner, E.D., Palluconi, F.D., 1977. Thermal and albedo mapping of Mars during the Viking primary mission. *Journal of Geophysical Research (1896-1977)* 82, 4249–4291. <https://doi.org/10.1029/JS082i028p04249>
- Kluitenberg, G.J., Bristow, K.L., Das, B.S., 1995. Error Analysis of Heat Pulse Method for Measuring Soil Heat Capacity, Diffusivity, and Conductivity. *Soil Science Society of America Journal* 59, 719–726. <https://doi.org/10.2136/sssaj1995.03615995005900030013x>
- Lellouch, E., Bergh, C. de, Sicardy, B., Ferron, S., Käufl, H.-U., 2010. Detection of CO in Triton's atmosphere and the nature of surface-atmosphere interactions. *A&A* 512, L8. <https://doi.org/10.1051/0004-6361/201014339>
- Lellouch, E., Sicardy, B., Bergh, C. de, Käufl, H.-U., Kassi, S., Campargue, A., 2009. Pluto's lower atmosphere structure and methane abundance from high-resolution spectroscopy and stellar occultations. *A&A* 495, L17–L21. <https://doi.org/10.1051/0004-6361/200911633>
- Lim, T.L., Stansberry, J., Müller, T.G., Mueller, M., Lellouch, E., Kiss, C., Santos-Sanz, P., Vilenius, E., Protopapa, S., Moreno, R., Delsanti, A., Duffard, R., Fornasier, S., Groussin, O., Harris, A.W., Henry, F., Horner, J., Lacerda, P., Mommert, M., Ortiz, J.L., Rengel, M., Thirouin, A., Trilling, D., Barucci, A., Crovisier, J., Doressoundiram, A., Dotto, E., Buenestado, P.J.G., Hainaut, O., Hartogh, P., Hestroffer, D., Kidger, M., Lara, L., Swinyard, B.M., Thomas, N., 2010. “TNOs are Cool”: A survey of the trans-Neptunian region - III. Thermophysical properties of 90482 Orcus and 136472 Makemake. *A&A* 518, L148. <https://doi.org/10.1051/0004-6361/201014701>
- Liu, G., Si, B.C., 2008. Dual-probe heat pulse method for snow density and thermal properties measurement. *Geophysical Research Letters* 35. <https://doi.org/10.1029/2008GL034897>
- MacKenzie, S.M., Lora, J.M., Lorenz, R.D., 2019. A Thermal Inertia Map of Titan. *Journal of Geophysical Research: Planets* 124, 1728–1742. <https://doi.org/10.1029/2019JE005930>
- Noborio, K., McInnes, K.J., Heilman, J.L., 1996. Measurements of soil water content, heat capacity, and thermal conductivity with a single TDR probe. *Soil Science* 161, 22–28.

- Ortiz, J.L., Sicardy, B., Braga-Ribas, F., Alvarez-Candal, A., Lellouch, E., Duffard, R., Pinilla-Alonso, N., Ivanov, V.D., Littlefair, S.P., Camargo, J.I.B., Assafin, M., Unda-Sanzana, E., Jehin, E., Morales, N., Tancredi, G., Gil-Hutton, R., de la Cueva, I., Colque, J.P., Da Silva Neto, D.N., Manfroid, J., Thirouin, A., Gutiérrez, P.J., Lecacheux, J., Gillon, M., Maury, A., Colas, F., Licandro, J., Mueller, T., Jacques, C., Weaver, D., Milone, A., Salvo, R., Bruzzone, S., Organero, F., Behrend, R., Roland, S., Vieira-Martins, R., Widemann, T., Roques, F., Santos-Sanz, P., Hestroffer, D., Dhillon, V.S., Marsh, T.R., Harlinton, C., Bagatin, A.C., Alonso, M.L., Ortiz, M., Colazo, C., Lima, H.J.F., Oliveira, A.S., Kerber, L.O., Smiljanic, R., Pimentel, E., Giacchini, B., Cacella, P., Emilio, M., 2012. Albedo and atmospheric constraints of dwarf planet Makemake from a stellar occultation. *Nature* 491, 566–569. <https://doi.org/10.1038/nature11597>
- Owen, T.C., Roush, T.L., Cruikshank, D.P., Elliot, J.L., Young, L.A., Bergh, C. de, Schmitt, B., Geballe, T.R., Brown, R.H., Bartholomew, M.J., 1993. Surface Ices and the Atmospheric Composition of Pluto. *Science* 261, 745–748. <https://doi.org/10.1126/science.261.5122.745>
- Prokhorov, A., Yantsevich, L., 1983. X-ray investigation of the equilibrium phase diagram of CH₄-N₂ solid mixtures. *Sov. J. Low Temp. Phys.* 9(2), 94-98.
- Protopapa, S., Grundy, W.M., Reuter, D.C., Hamilton, D.P., Dalle Ore, C.M., Cook, J.C., Cruikshank, D.P., Schmitt, B., Philippe, S., Quirico, E., Binzel, R.P., Earle, A.M., Ennico, K., Howett, C.J.A., Lunsford, A.W., Olkin, C.B., Parker, A., Singer, K.N., Stern, A., Verbiscer, A.J., Weaver, H.A., Young, L.A., 2017. Pluto's global surface composition through pixel-by-pixel Hapke modeling of New Horizons Ralph/LEISA data. *Icarus*, Special Issue: The Pluto System 287, 218–228. <https://doi.org/10.1016/j.icarus.2016.11.028>
- Protopapa, S., Grundy, W.M., Tegler, S.C., Bergonio, J.M., 2015. Absorption coefficients of the methane–nitrogen binary ice system: Implications for Pluto. *Icarus* 253, 179–188. <https://doi.org/10.1016/j.icarus.2015.02.027>
- Putzig, N.E., Mellon, M.T., Kretke, K.A., Arvidson, R.E., 2005. Global thermal inertia and surface properties of Mars from the MGS mapping mission. *Icarus* 173, 325–341. <https://doi.org/10.1016/j.icarus.2004.08.017>
- Rivera-Valentin, E.G., Blackburn, D.G., Ulrich, R., 2011. Revisiting the thermal inertia of Iapetus: Clues to the thickness of the dark material. *Icarus* 216, 347–358. <https://doi.org/10.1016/j.icarus.2011.09.006>
- Rognini, E., Capria, M.T., Tosi, F., Sanctis, M.C.D., Ciarniello, M., Longobardo, A., Carrozzo, F.G., Raponi, A., Frigeri, A., Palomba, E., Fonte, S., Giardino, M., Ammannito, E., Raymond, C.A., Russell, C.T., 2020. High Thermal Inertia Zones on Ceres From Dawn Data. *Journal of Geophysical Research: Planets* 125, e2018JE005733. <https://doi.org/10.1029/2018JE005733>
- Sagmiller, D., Hartwig, J., 2020. Survey of Cryogenic Nitrogen Thermomechanical Property Data Relevant to Outer Solar System Bodies. *Earth and Space Science* 7, e2019EA000640. <https://doi.org/10.1029/2019EA000640>

- Schmitt, B., Philippe, S., Grundy, W.M., Reuter, D.C., Côte, R., Quirico, E., Protopapa, S., Young, L.A., Binzel, R.P., Cook, J.C., Cruikshank, D.P., Dalle Ore, C.M., Earle, A.M., Ennico, K., Howett, C.J.A., Jennings, D.E., Linscott, I.R., Lunsford, A.W., Olkin, C.B., Parker, A.H., Parker, J.Wm., Singer, K.N., Spencer, J.R., Stansberry, J.A., Stern, S.A., Tsang, C.C.C., Verbiscer, A.J., Weaver, H.A., 2017. Physical state and distribution of materials at the surface of Pluto from New Horizons LEISA imaging spectrometer. *Icarus*, Special Issue: The Pluto System 287, 229–260. <https://doi.org/10.1016/j.icarus.2016.12.025>
- Scott, T.A., 1976. Solid and liquid nitrogen. *Physics Reports* 27, 89–157. [https://doi.org/10.1016/0370-1573\(76\)90032-6](https://doi.org/10.1016/0370-1573(76)90032-6)
- Siegler, M., Aharonson, O., Carey, E., Choukroun, M., Hudson, T., Schorghofer, N., Xu, S., 2012. Measurements of thermal properties of icy Mars regolith analogs. *Journal of Geophysical Research: Planets* 117. <https://doi.org/10.1029/2011JE003938>
- Smith, D.S., Alzina, A., Bourret, J., Nait-Ali, B., Pennec, F., Tessier-Doyen, N., Otsu, K., Matsubara, H., Elser, P., Gonzenbach, U.T., 2013. Thermal conductivity of porous materials. *Journal of Materials Research* 28, 2260–2272. <https://doi.org/10.1557/jmr.2013.179>
- Spencer, J.R., Moore, J.M., 1992. The influence of thermal inertia on temperatures and frost stability on Triton. *Icarus* 99, 261–272. [https://doi.org/10.1016/0019-1035\(92\)90145-W](https://doi.org/10.1016/0019-1035(92)90145-W)
- Spencer, J.R., Stansberry, J.A., Trafton, L.M., Young, E.F., Binzel, R.P., Croft, S.K., 1997. Volatile transport, seasonal cycles, and atmospheric dynamics on Pluto, in *Pluto and Charon*, ed. by S. Stern, D. Tholen, University of Arizona Press, Tucson, pp. 435–473.
- Stachowiak, P., Sumarokov, V.V., Mucha, J., Jeżowski, A., 1994. Thermal conductivity of solid nitrogen. *Phys. Rev. B* 50, 543–546. <https://doi.org/10.1103/PhysRevB.50.543>
- Stern, S.A., Bagenal, F., Ennico, K., Gladstone, G.R., Grundy, W.M., McKinnon, W.B., Moore, J.M., Olkin, C.B., Spencer, J.R., Weaver, H.A., Young, L.A., Andert, T., Andrews, J., Banks, M., Bauer, B., Bauman, J., Barnouin, O.S., Bedini, P., Beisser, K., Beyer, R.A., Bhaskaran, S., Binzel, R.P., Birath, E., Bird, M., Bogan, D.J., Bowman, A., Bray, V.J., Brozovic, M., Bryan, C., Buckley, M.R., Buie, M.W., Buratti, B.J., Bushman, S.S., Calloway, A., Carcich, B., Cheng, A.F., Conard, S., Conrad, C.A., Cook, J.C., Cruikshank, D.P., Custodio, O.S., Ore, C.M.D., Deboy, C., Dischner, Z.J.B., Dumont, P., Earle, A.M., Elliott, H.A., Ercol, J., Ernst, C.M., Finley, T., Flanigan, S.H., Fountain, G., Freeze, M.J., Greathouse, T., Green, J.L., Guo, Y., Hahn, M., Hamilton, D.P., Hamilton, S.A., Hanley, J., Harch, A., Hart, H.M., Hersman, C.B., Hill, A., Hill, M.E., Hinson, D.P., Holdridge, M.E., Horanyi, M., Howard, A.D., Howett, C.J.A., Jackman, C., Jacobson, R.A., Jennings, D.E., Kammer, J.A., Kang, H.K., Kaufmann, D.E., Kollmann, P., Krimigis, S.M., Kusnierkiewicz, D., Lauer, T.R., Lee, J.E., Lindstrom, K.L., Linscott, I.R., Lisse, C.M., Lunsford, A.W., Mallder, V.A., Martin, N., McComas, D.J., McNutt, R.L., Mehoke, D., Mehoke, T., Melin, E.D., Mutchler, M., Nelson, D., Nimmo, F., Nunez, J.I., Ocampo, A., Owen, W.M., Paetzold, M., Page, B., Parker, A.H., Parker, J.W., Pelletier, F., Peterson, J., Pinkine, N., Piquette, M., Porter, S.B., Protopapa, S., Redfern, J., Reitsema, H.J., Reuter, D.C., Roberts, J.H., Robbins, S.J., Rogers, G., Rose, D., Runyon, K.,

- Retherford, K.D., Ryschkewitsch, M.G., Schenk, P., Schindhelm, E., Sepan, B., Showalter, M.R., Singer, K.N., Soluri, M., Stanbridge, D., Steffl, A.J., Strobel, D.F., Stryk, T., Summers, M.E., Szalay, J.R., Tapley, M., Taylor, A., Taylor, H., Throop, H.B., Tsang, C.C.C., Tyler, G.L., Umurhan, O.M., Verbiscer, A.J., Versteeg, M.H., Vincent, M., Webbert, R., Weidner, S., Weigle, G.E., White, O.L., Whittenburg, K., Williams, B.G., Williams, K., Williams, S., Woods, W.W., Zangari, A.M., Zirnstein, E., 2015. The Pluto system: Initial results from its exploration by New Horizons. *Science* 350. <https://doi.org/10.1126/science.aad1815>
- Tegler, S.C., Cornelison, D.M., Grundy, W.M., Romanishin, W., Abernathy, M.R., Bovyn, M.J., Burt, J.A., Evans, D.E., Maleszewski, C.K., Thompson, Z., Vilas, F., 2010. Methane and Nitrogen abundances on Pluto and Eris. *ApJ* 725, 1296–1305. <https://doi.org/10.1088/0004-637X/725/1/1296>
- Trafton, L.M., 2015. On the state of methane and nitrogen ice on Pluto and Triton: Implications of the binary phase diagram. *Icarus*, Special Issue: The Pluto System 246, 197–205. <https://doi.org/10.1016/j.icarus.2014.05.022>
- Vetter, M., Jodl, H.-J., Brodyanski, A., 2007. From optical spectra to phase diagrams—the binary mixture N₂–CO. *Low Temperature Physics* 33, 1052–1060. <https://doi.org/10.1063/1.2747091>
- Wang, J., Bras, R.L., Sivandran, G., Knox, R.G., 2010. A simple method for the estimation of thermal inertia. *Geophysical Research Letters* 37. <https://doi.org/10.1029/2009GL041851>
- Woodside, W., Messmer, J.H., 1961. Thermal Conductivity of Porous Media. I. Unconsolidated Sands. *Journal of Applied Physics* 32, 1688–1699. <https://doi.org/10.1063/1.1728419>
- Zhang, X., Strobel, D.F., Imanaka, H., 2017. Haze heats Pluto’s atmosphere yet explains its cold temperature. *Nature* 551, 352–355. <https://doi.org/10.1038/nature24465>

Chapter 6

Conclusions

6.1. Summary and contributions

The icy (solid) planetary bodies in the outer fringe of the solar system, beyond the orbit of Neptune, are collectively referred to as trans-Neptunian and Kuiper Belt objects. The planetary bodies in the Kuiper Belt show a wide range of colors in optical wavelengths (Doressoundiram, 2004) and remarkably diverse albedos (Grundy et al., 2005). Understanding these bodies provides an important insight into the early history of the solar system because they are considered remnants of the formation of the solar system (Barucci et al., 2005; Wu et al., 2013). The planetary bodies in the Kuiper Belt are, thus, thought to contain chemical, dynamic, and thermal fingerprints of the solar system (Schaller, 2010). Triton (the largest moon of Neptune) and the dwarf planet Pluto are two of the interesting planetary bodies in the Kuiper Belt.

An abundance of volatile (N_2 , CH_4 , and CO) and non-volatile (H_2O) ices have been detected or inferred to be present on the surfaces of TNOs and KBOs (e.g., Cruikshank et al., 1993; Owen et al., 1993; Schmitt et al., 2017). Many of the KBOs also host non-ice materials, such as tholins, on their surfaces. The planetary bodies in the Kuiper Belt—for instance, Pluto and Triton along with others—have been identified to host volatile-supported or vapor-supported atmospheres including an active interaction with surface constituents. This interaction between the surface and atmospheric constituents of the icy bodies in the Kuiper Belt takes place through the exchange of matter and energy and is complex in nature.

The surface-atmospheric exchange of matter and energy is closely associated with the constituent materials involved (N_2 , CH_4 , CO , and H_2O ices) – their physical properties (such as solid phases and grain sizes) and thermal states. On top of that, the mechanical strengths and thermal properties of planetary surfaces are directly influenced by the grain size of planetary regolith (Gundlach and Blum, 2013). Thus, a complete interpretation of the surface-atmospheric interactions of TNOs and KBOs requires an understanding of the physical properties of the surface constituents. An accurate grain size estimation of ices on the outer solar system bodies is important for an improved understanding of the surface volatile transport and thermophysical modeling of the planetary bodies.

The surface volatile transport on icy planetary bodies is influenced by the thermal properties of the surface volatile materials (Spencer and Moore, 1992). Understanding volatile transport mechanisms and ultimately the surface-atmospheric interactions, thus, requires an accurate estimation of the thermal properties of volatile ices found on KBO and TNO surfaces. Moreover, mapping the spatial distribution of ices and their relationship with surface geology and atmospheres is very important for an improved understanding of the volatile transport models on TNOs and KBOs such as dwarf planet Pluto (Bertrand and Forget, 2016). In this thesis, we provide a recipe for investigating the physical and thermal properties of ices and mapping the geographic distribution of ice mixtures – helping in an improved understanding of volatile transport on trans-Neptunian and Kuiper Belt objects.

In *Chapter 2*, we assess the uncertainty in grain size estimation of pure CH_4 and $\text{N}_2:\text{CH}_4$ ices, the most abundant volatile materials on TNOs and KBOs. We compare the single scattering albedo

of these ices using the Mie scattering model and two other Hapke approximations – equivalent slab and internal scattering model (ISM) – at wavelengths between 1 and 5 μm . Our study reveals that the equivalent slab (Hapke slab) approximation model predicts much closer results to Mie scattering over the NIR wavelengths at a wide range of grain sizes. Owing to the Rayleigh effect on single-scattering properties, neither of the Hapke approximation models could predict an accurate grain size estimation for small particles (radii $\leq 5\mu\text{m}$). Based on this study, we recommend that future studies should favor the Mie model for unknown spectra or the Hapke slab model as an approximation when employing RTMs for estimating the grain size of volatiles on the surfaces of TNOs and KBOs in the outer solar system.

In *Chapter 3*, we evaluate the discrepancy in grain size estimation of H_2O ice (both amorphous and crystalline phases) in the outer solar system. Radiative scattering models (Mie theory and Hapke approximations) were implemented to predict the H_2O ice grain sizes at temperatures of 15, 40, 60, and 80 K (amorphous) and 20, 40, 60, and 80 K (crystalline). We compare the single scattering albedos of H_2O ice phases from the optical constants at near-infrared wavelengths. This study reveals that the Hapke approximation models predict grain size of the crystalline phase, overall, much better than the amorphous phase at temperatures of 15 – 80 K. However, the Hapke slab model predicts, in general, grain sizes much closer to that of the Mie model’s estimations while ISM predicted grain sizes exhibit a higher uncertainty.

We recommend using the Mie model for unknown spectra of outer solar system bodies to estimate the grain size of H_2O ice. When using an approximation model for RTMs, we recommend using the Hapke slab approximation model over the internal scattering model. Accordingly,

incorporating the results from *Chapter 2*, we explored which approximate model is better in predicting the grain sizes of a variety of surface ices (both volatile and non-volatile) found in the outer solar system, specifically on trans-Neptunian and Kuiper Belt objects.

In *Chapter 4*, we use the principal component reduced Gaussian mixture model (PC-GMM), an unsupervised machine learning technique, to map the geographic distribution of ices on Pluto's surface from the near-infrared observations of the LEISA/Ralph instrument onboard NASA's New Horizons spacecraft. The geographic distribution of the surface units shows a correlation with geologic features. Average I/F spectra of each unit were analyzed – in terms of the position and strengths of absorption bands of abundant volatiles such as N₂, CH₄, and CO and nonvolatile H₂O – to connect the unit to surface composition, geology, and geographic location. The distribution of surface units shows a latitudinal pattern with distinct surface compositions of volatiles – consistent with existing literature.

The implemented PC-GMM method was able to recognize local-scale variations in surface compositions of geological features on the dwarf planet. The mapped distribution of surface units and their compositions help in an improved understanding of the volatile transport mechanism on Pluto, both on global (encounter hemisphere of Pluto during New Horizons flyby in 2015) and local scales. Thus, we emphasize that the unsupervised learning (PC-GMM) used in this thesis has wide applicability and can be expanded to other planetary bodies of the solar system for mapping surface material distribution and achieving a complete understating of volatile transport modeling in particular and physical processes in general on the icy bodies at the outer solar system.

In *Chapter 5*, we propose a method to estimate thermal conductivity, volumetric heat capacity, thermal diffusivity, and thermal inertia of N_2 , CH_4 , and CO ices, and mixtures thereof in a simulated laboratory setting at temperatures of 20 to 60 K – relevant to TNOs and KBOs. To implement the method, we built a new experimental facility – named the *Outer Solar System Astrophysics Lab* – housed at the University of Arkansas. We provide detailed technical specifications of the chamber in this thesis with the objective that it can be used as a guideline for building similar cryogenic facilities in the future. We expect that the laboratory will provide a wealth of thermal (as well as spectral) data on ices that will pave the way to an improved understanding of the surface-subsurface heat flow, volatile transport mechanisms, and surface-atmospheric interactions on the planetary bodies in the outer solar system.

An improved interpretation of surface-atmospheric interactions and volatile transport mechanisms on TNOs and KBOs requires an understanding of the physical and thermal properties of the constituent ices and their geographic distribution on the planetary surfaces. In this dissertation, we presented a holistic study of the properties of ices through the implementation of widely used radiative scattering models to assess the discrepancies in grain size estimation of ices, mapped the distribution of surface compositions on Pluto by utilizing unsupervised machine learning techniques, and integrated laboratory experiments. Thus, this research was able to bring together a set of methods, tools, and techniques used in planetary science for an improved understanding of the physical and thermal properties of surface ices found in the Kuiper Belt and deciphering the surface-atmospheric interactions and volatile transport mechanisms on the planetary bodies in the outer edge of the solar system.

6.2. References

- Bertrand, T., Forget, F., 2016. Observed glacier and volatile distribution on Pluto from atmosphere–topography processes. *Nature* 540, 86–89. <https://doi.org/10.1038/nature19337>
- Cruikshank, D.P., Roush, T.L., Owen, T.C., Geballe, T.R., Bergh, C. de, Schmitt, B., Brown, R.H., Bartholomew, M.J., 1993. Ices on the Surface of Triton. *Science* 261, 742–745. <https://doi.org/10.1126/science.261.5122.742>
- Doressoundiram, A., 2004. Colour Properties and Trends in Trans-Neptunian Objects, in: Davies, J.K., Barrera, L.H. (Eds.), *The First Decadal Review of the Edgeworth-Kuiper Belt*. Springer Netherlands, Dordrecht, pp. 131–144.
- Grundy, W.M., Noll, K.S., Stephens, D.C., 2005. Diverse albedos of small trans-neptunian objects. *Icarus* 176, 184–191.
- Gundlach, B., Blum, J., 2013. A new method to determine the grain size of planetary regolith. *Icarus* 223, 479–492. <https://doi.org/10.1016/j.icarus.2012.11.039>
- Hapke, B., 1993. *Theory of Reflectance and Emittance Spectroscopy*, Topics in Remote Sensing. Cambridge University Press, Cambridge. <https://doi.org/10.1017/CBO9780511524998>
- Owen, T.C., Roush, T.L., Cruikshank, D.P., Elliot, J.L., Young, L.A., de Bergh, C., Schmitt, B., Geballe, T.R., Brown, R.H., Bartholomew, M.J., 1993. Surface Ices and the Atmospheric Composition of Pluto. *Science* 261, 745–748. <https://doi.org/10.1126/science.261.5122.745>
- Schaller, E.L., 2010. Atmospheres and surfaces of small bodies and dwarf planets in the Kuiper Belt. *EPJ Web of Conferences* 9, 267–276. <https://doi.org/10.1051/epjconf/201009021>
- Schmitt, B., Philippe, S., Grundy, W.M., Reuter, D.C., Côte, R., Quirico, E., Protopapa, S., Young, L.A., Binzel, R.P., Cook, J.C., Cruikshank, D.P., Dalle Ore, C.M., Earle, A.M., Ennico, K., Howett, C.J.A., Jennings, D.E., Linscott, I.R., Lunsford, A.W., Olkin, C.B., Parker, A.H., Parker, J.Wm., Singer, K.N., Spencer, J.R., Stansberry, J.A., Stern, S.A., Tsang, C.C.C., Verbiscer, A.J., Weaver, H.A., New Horizons Science Team, 2017. Physical state and distribution of materials at the surface of Pluto from New Horizons LEISA imaging spectrometer. *Icarus* 287, 229–260. <https://doi.org/10.1016/j.icarus.2016.12.025>
- Spencer, J.R., Moore, J.M., 1992. The influence of thermal inertia on temperatures and frost stability on Triton. *Icarus* 99, 261–272. [https://doi.org/10.1016/0019-1035\(92\)90145-W](https://doi.org/10.1016/0019-1035(92)90145-W)